NANOMECHANICS, NANOTRIBOLOGY AND FABRICATION OF FLEXIBLE MULTILAYER NANOCOMPOSITES

A Dissertation

by

MOHAMMAD MUNEER MUTLAQ HUMOOD

Submitted to the Office of Graduate and Professional Studies of
Texas A&M University
in partial fulfillment of the requirements for the degree of

DOCTOR OF PHILOSOPHY

Chair of Committee,	Andreas A. Polycarpou
Committee Members,	Jaime C. Grunlan
	M. Cynthia Hipwell
	Mohammad Naraghi
	Matt Pharr
Head of Department,	Andreas A. Polycarpou

August 2018

Major Subject: Mechanical Engineering

ABSTRACT

Polymer-based multilayer nanocomposites have become favorable material choice for many applications such as gas barriers, water membranes, optoelectronic devices, biosensors, corrosion inhibitors and energy devices. They are finding their ways as a replacement of traditional metal, silicon oxides and hard inorganic coatings. The present work is dedicated to addressing the fabrication of new polymer flexible nanocomposites and their mechanical response against normal and lateral deformation modes, known as nanoindentation and nanoscratch. Particularly, the scratch resistance of these nanocomposites is critical for many applications.

Little is known in the literature about their nanomechanics, hence reliability and durability for long-term applications. Better understanding of the nanomechanics and nanotribology of 2D multilayered thin films and 3D multilayered structures was achieved in this thesis through a series of different experiments using low and high load nanoindentation, nanoscratch and flat-punch compression. Complementary computational modeling supported the experimental findings and further explains their nano- and micromechanical behaviors.

Based on the findings of these nanomechanical experiments, functional multilayered polymeric coatings consisting of different arrangements of polymers, graphene oxide and clay were found to be potential material choices for a range of different applications such as low-friction tribological coatings, vapor/gas barriers and self-healing coatings. Furthermore, 3D silicon/polymer structures specifically under extreme deformation were found to be a potential candidate for wearable electronics and flexible microelectromechanical systems (MEMS) sensors due to the resilient and elastic behavior driven by the geometry-dependent deformation of these structures.

The last part discusses the development of a new material pertaining to the development of nanocomposites. On the quest of continuous search of 2D materials, which can act as reinforcements, a new material, Aluminum diboride (AlB_2) flakes, was introduced and discussed. High aspect ratio AlB_2 flakes is a potential reinforcement for conductive polymer nanocomposites due to the metallic conductivity in the axis parallel to the basal hexagonal plane.

In summary, the findings above focused on the mechanics and tribology of nanocomposites at the nanoscale mainly for gas barrier applications and MEMS devices. However, the knowledge can also be extended to other devices such as energy harvesting devices and membranes where tribology issues at the nanoscale are of important concerns.

DEDICATION

To my beloved parents and my siblings for their unconditional love and support

When I started writing my dissertation early 2018, a close friend was diagnosed with breast cancer. She remained strong, fought hard and kept the strong believe in God. Her fight left a very positive impact on me. This work is dedicated to Rasha and every cancer survivor.

Also, the last few years were tough worldwide with many conflicts and disputes resulting in a lot of refugees. This is dedicated to every refugee who was forced to flee his or her home.

ACKNOWLEDGEMENTS

I would like to thank my committee members Prof. Jaime C. Grunlan, Prof. M. Cynthia Hipwell, Prof. Mohammad Naraghi, Prof. Matt Pharr and Prof. Andreas A. Polycarpou for their guidance and support throughout the course of this research. Their discussions toward excellent research have motivated me to connect and bridge between different fields and tackle some of the unanswered questions about the mechanical behavior of multilayer nanocomposites. I feel fortunate and greatly honored to have the opportunity to interact with these great researchers and teachers in Texas A&M University.

Special thanks go to my Ph.D. advisor, Prof. Andreas A. Polycarpou. I have known Prof. Polycarpou for almost 8 years. I met Dr. Polycarpou first, when was the head of the department of mechanical engineering at Khalifa University in 2011. I worked closely with him to establish the first active American Society of Mechanical Engineers (ASME) student chapter in Abu Dhabi, UAE. His passionate pursuit for excellent scholarly work encouraged me to excel in my Ph.D. and learn how to conduct research with the highest academic quality. He is not only a remarkable advisor, but also a great human being, a life-time mentor from who I have learned expertise and also wisdom.

I am grateful and thankful to my colleagues in the *Microtribodynamics* research group, and the mechanical engineering department faculty and staff for making my time at Texas A&M University a great experience. Also, I want to specially thank Dr. Ali Beheshti, Dr. Tanil Ozkan and Dr. Kyriaki Polychronopoulou for their valuable training and mentoring, which helped with the advancement of work in this present thesis.

I would not have done great in College Station without the love and support from friends, who I met here in Aggieland. To name few, Dr. Amjad Assi, Bassel Daher, Moein Nazifi, Bandar Alkhudhiri, Dr. Rosanna Serafini, Nesserine Ma, Paola and Charlie Stratton, Rasha and Shwan Abdulmajid and my neighbors: Meri and Alessandro. We have met in this great station and while, we all would have to take different ways to pursue our career and life dreams, I believe we will stay in touch and reunited whenever an opportunity comes.

Part of this work was only possible through a sponsored research fellowship from Hagler Institute for Advanced Study (HIAS) at Texas A&M University. I would like to thank the institute for their generous support. Also, I would like to thank my HIAS fellow, Prof. John A. Rogers in Northwestern University for his time, mentorship and providing the training for the fabrication of 3D structures. The funding for the rest of the work was provided by the Meinhard H. Kotzebue '14 Professorship endowment in Mechanical Engineering at Texas A&M University.

As a mechanical engineering Ph.D. alumnus of Texas A&M University, I will thrive to do great wherever life takes me in my profession and career in order to bring goodness, happiness and peace to the people around me and the whole word. I will be an ambassador of my beloved school, Texas A&M, and preserve the great Aggie core values and the traditions.

Last but certainly not least, thanks to my mother, father and siblings for their love and unconditional support from the United Arab Emirates and my extended family in Jordan and Palestine. Your kind words and encouragement through my college years have motivated me to do well. I feel grateful to have you and I hope I always make you proud.

I could only say alhamdulillah "all the praises and thanks be to Allah". My faith of God has provided me with a true determination and a meaningful purpose to do the best I could in this life. I find it great to finish this acknowledgements section with a slightly-modified poem by the

Egyptian poet, Ahmad Shawqi, on education highlighting my sincere appreciation to all teachers who have taught me during my ongoing education journey.

"قُم للمعلمِ وفّهِ التبجيلا
كاد المعلمُ أن يكونَ رسولا
أعَلِمتَ أشرفَ او أجل من الذي
يبني ويُنشئُ أنفساً وعقولا
سُبحانكَ اللهم خيرَ معلم
علّمتِ بالقلمِ القرونَ الأولى
أخرجتَ هذا العقل من ظُلُماتهِ
وهَديتهُ النورَ المبينَ سبيلا
وطبعته بيدِ المعلمِ تارة
صدئ الحديدُ وتارةً مصقولا
أرسلتَ بالتوراةِ موسى مُرشدا
وابن البتول فعلّم الإنجيلا
وفجـرتَ ينبـوعَ البيانِ محمّد
فسقى الحديثَ وناولَ التنزيلا"

Translation:
“Stand for the teacher, give her/him full respect
The teacher’s rank is close to the prophet.
Can there be any person nobler than
The one who builds and nurtures souls and minds?
Glory to You God, O best instructor,
With the pen You taught the folk of yore.
You brought this mind forth from its darknesses,
And guided it a way of lucid light.
The teacher’s hand a crucible you made,
Its products ingots rusted or burnished.
Moses as a guide You sent with Torah,
So too the Virgin’s son, who taught Injil.
Muhammad’s fluent fount You caused to gush,
So human souls he quenched with scripture’s words.

CONTRIBUTORS AND FUNDING SOURCES

This thesis was completed mainly based upon supervision of my committee chair, Prof. Andreas Polycarpou, and my committee members, Prof. Jaime C. Grunlan, Prof. M. Cynthia Hipwell, Prof. Mohammad Naraghi, and Prof. Matt Pharr. The studies of 2D multilayer thin films shown in Chapters 2-5 were obtained with help of Shahla Chowdhury, Shuang Qin, Yixuan Song and Tyler Guin. The studies of 3D structures in Chapter 6 was obtained with the help of Yan Shi and Mengdi Han. The introduction of the new cleaved AlB_2 material was possible with the help of Jacob L. Meyer.

Funding of studies in Chapters 2, 3, 4 and 5 was provided from the Meinhard H. Kotzebue '14 endowment in the department of mechanical engineering at Texas A&M University. Funding of the work in Chapter 6 was provided from the Hagler Institute for Advanced Study (HIAS) at Texas A&M University. Last but not least, the research work in Chapter 7 was funded by both NSF Grant CHE-1308312 and the Meinhard H. Kotzebue '14 endowment in the department of mechanical engineering at Texas A&M University.

TABLE OF CONTENTS

ABSTRACT ii

DEDICATION iv

ACKNOWLEDGEMENTS v

CONTRIBUTORS AND FUNDING SOURCES viii

TABLE OF CONTENTS ix

LIST OF FIGURES xiii

LIST OF TABLES xix

1 INTRODUCTION AND LITERATURE REVIEW 1

- 1.1 Introduction to multilayers nanocomposites 1
- 1.2 The nanoeffect of PNC 2
- 1.3 2D PNC assembled using LbL 3
- 1.4 3D PNC assembled using Compressive Buckling 3
- 1.5 Objectives and outlines 5
- 1.6 Recommended future work 11

2 NANOMECHANICAL BEHAVIOR OF HIGH GAS BARRIER MULTILAYER THIN FILMS 13

- 2.1 Introduction 13
- 2.2 Experimental Section 15
  - 2.2.1 Materials 15
  - 2.2.2 Layer-by-layer Deposition 16
  - 2.2.3 Nanoindentation 17
  - 2.2.4 Nanoscratch 19
- 2.3 Results and Discussion 20
  - 2.3.1 Surface Roughness & Morphology 20
  - 2.3.2 Reduced Modulus and Hardness 22
  - 2.3.3 Nanoscratch 26
  - 2.3.4 High load Indentation and Scratch 29
- 2.4 Summary of Chapter 2 36

3 THE INFLUENCE OF GRAPHENE REDUCTION AND POLYMER CROSSLINKING ON IMPROVING THE INTERFACIAL PROPERTIES OF MULTILAYER POLYMERS THIN FILMS 37

- 3.1 Introduction 37

3.2 Experimental Section....40
3.2.1 Materials 40
3.2.2 Substrates 40
3.2.3 Processing 41
3.2.4 Nanoindentation 41
3.2.5 Nanoscratch.... 42
3.2.6 Shear and Adhesive Strength Measurements.... 43
3.2.7 Characterizations.... 44
3.2.8 Nanoindentation Calibration 44
3.2.9 Raman spectroscopy/X-ray photoelectron spectroscopy (XPS) 46
3.2.10 Scanning/Transmission Electron Microscopy (SEM)/(TEM) 47
3.2.11 Atomic Force Microscopy (AFM) 47
3.3 Results & Discussion....47
3.3.1 Surface Roughness & Morphology.... 47
3.3.2 Reduced Modulus and Hardness.... 52
3.3.3 Raman/XPS.... 53
3.3.4 Nanoscratch.... 56
3.3.5 Film Delamination 63
3.4 Summary of Chapter 3....67

4 IN SITU NANOMECHANICAL BEHAVIOR AND SELF-HEALING RESPONSE OF POLYMERIC MULTILAYER THIN FILMS 69

4.1 Introduction....69
4.2 Experimental Section....72
4.2.1 Materials and Processing 72
4.2.2 In Situ Wet/High Temperature Nanoindentation.... 73
4.2.3 Nanoindentation Calibration.... 75
4.2.4 Microscratch 77
4.2.5 Atomic Force microscopy (AFM) 77
4.2.6 FTIR.... 78
4.2.7 XPS 78
4.3 Results & Discussion....78
4.3.1 Self-Healing.... 78
4.3.2 Surface Roughness.... 80
4.3.3 Reduced Modulus and Hardness:.... 82
4.3.4 FTIR & XPS 90
4.4 Summary of Chapter 4....92

5 MECHANICAL BEHAVIOR OF POLYMER NANOCOMPOSITES ON STIFF AND COMPLIANT SUBSTRATES 94

5.1 Introduction....94
5.2 Methods 96
5.2.1 Materials and Processing 96
5.2.2 Substrates 97
5.2.3 AFM.... 99

5.2.4 Nanoindentation ... 99
5.2.5 Nanoscratch ... 100
5.2.6 Raman spectroscopy ... 100
5.2.7 Finite Elements Analysis (FEA) ... 101
5.3 Results & Discussion ... 102
5.3.1 Nanoindentation Experiments ... 103
5.3.2 Raman Spectroscopy ... 108
5.3.3 Nanoscratch ... 109
5.3.4 Finite Element analysis ... 114
5.3.5 Film delamination and Adhesive Strength: ... 118
5.4 Summary of Chapter 5 ... 120

6 FABRICATION AND DEFORMATION OF THREE-DIMENSIONAL MULTILAYERED KIRIGAMI MICRO-STRUCTURES ... 121

6.1 Introduction ... 121
6.2 Experimental Section ... 124
6.2.1 Materials & Fabrication ... 124
6.2.2 Mechanical characterization ... 125
6.2.3 Finite Element Analysis ... 125
6.3 Results ... 126
6.4 Summary of Chapter 6 ... 135
6.5 Supplementary movie legends ... 138

7 NEW RIENFORCMENT FOR COMPOSITES: 2D ALB$_2$ FLAKES ... 140

7.1 Introduction ... 140
7.2 Experimental Details ... 143
7.2.1 Fabrication of HAR Flakes ... 143
7.2.2 Atomic Force Microscopy (AFM) ... 144
7.2.3 Nanoindentation ... 144
7.2.4 X-ray diffraction (XRD) ... 144
7.2.5 Secondary Ion Mass Spectrometry (SIMS) ... 144
7.2.6 Atomic Layer Deposition (ALD) ... 144
7.3 Results and Discussion ... 145
7.3.1 Nanomechanical properties ... 145
7.3.2 The surface chemistry of cleaved AlB$_2$ ... 150
7.3.3 Epitaxial thin film growth ... 155
7.4 Summary of Chapter 7 ... 158

8 SUMMARY OF THESIS RESEARCH AND RECOMMENDATION FOR FUTURE WORK ... 159

8.1 Summary of the thesis ... 159
8.2 Recommendations for future work ... 164

BIBLIOGRAPHY ... 166

APPENDIX A FRAMEWORK FOR MODELLING THE NANOMECHANICAL PROPERTIES OF HIGH TEMPERATURE HFB_XC_Y COATINGS 197

A.1 Introduction...197
A.2 Methods 200
  A.2.1 Synthesis 200
  A.2.2 Nanoindentation 201
  A.2.3 Nanoscratch.. 201
  A.2.4 Analytical framework model 202
A.3 Results & Discussion..207
  A.3.1 Nanomechanical Properties.. 207
  A.3.2 Nanoscratch experiments 212
  A.3.3 Nanotribological Properties 213
A.4 Conclusion 220

LIST OF FIGURES

Page

Figure 1.1 The classification adopted in this study for nanocomposites based on their arrangements. 1

Figure 1.2 Flowchart of the research proposal, (a) simplified and (b) deatiled. 6

Figure 1.3 Multilayer thin films with exceptional gas barrier capability found to be good candidates for other applications after nanomechanical testing under different conditions. 11

Figure 2.1. Illustration of (a) LbL process and (b) bilayer structure. The procedure to build quadlayer assemblies is similar, only increasing the repeating deposition cycle to four components. 17

Figure 2.2 Scanning Electron Microscopy (SEM) image of (a) the Berkovich probe used for indention experiments and (b) a cross-sectional image of this tip. 19

Figure 2.3 Scanning Electron Microscopy (SEM) image of (a) the conospherical probe used in scratch experiments and (b) a cross-sectional image of this tip 20

Figure 2.4 Atomic Force Microscopy topography images (5×5 μm) of the multilayer thin films. Subscripts refer to the number of bilayers or quadlayers deposited. 21

Figure 2.5 TEM cross-sectional images of (a) $(PEI/PAA/PEI/GO)_5$, (b) $(PEI/MMT)_{50}$, (c) $(PEI/PAA/PEI/MMT)_{10}$ and (d) $(PEI/PAA)_{20}$. 22

Figure 2.6 Representative load–displacement curves for a single-loading of 70 μN on (a) $(PEI/PAA/PEI/MMT)_{10}$ and $(PEI/PAA)_8$ and (b) $(PEI/MMT)_{50}$ and $(PEI/PAA/PEI/GO)_{30}$. Extracted reduced elastic modulus and hardness as a function of contact depth using multiple indentations with increasing loads from 40 to 200 μN for (c) (e) $(PEI/PAA/PEI/MMT)_{10}$ and $(PEI/PAA)_8$ films and (d) (f) $(PEI/MMT)_{50}$ and $(PEI/PAA/PEI/GO)_{30}$ respectively. 25

Figure 2.7 In-situ scratch depth and residual depth (plastic deformation) for different normal loads: (a) 50 μN, (b) 100 μN, (c) 200 μN and (d) 400 μN. 28

Figure 2.8 Residual indentation profiles (2x2 μm) after 1500 μN indentation: (a) $(PEI/PAA/PEI/GO)_{30}$ (b) $(PEI/PAA)_8$ (c) $(PEI/PAA/PEI/MMT)_{10}$ and (d) $(PEI/MMT)_{50}$. . 30

Figure 2.9 Residual indentation depths for multilayer thin films indented with a 1500 μN normal load. 31

Figure 2.10 (a) Residual scratch images for $(PEI/PAA/PEI/MMT)_{10}$ and (b) residual scratch profiles with 1, 2 and 3 mN forces. 32

Figure 2.11 Residual scratch images for $(PEI/PAA)_8$ with (a) 1, (b) 2 and (c) 3 mN force and (d) residual scratch profiles with 1, 2 and 3 mN forces. 33

Figure 2.12 In-situ scratch depth and residual scratch depths of multilayer thin films scratched with high loads, (a) 1, (b) 2 and (c) 3 mN. 34

Figure 2.13 (a) Friction coefficient and (b) % elastic recovery as a function of scratch normal force for multilayer thin films. 35

Figure 3.1 Scanning Electron Microscopy (SEM) image for the nanoscratch conospherical probe with spherical tip of 870 nm radius, at (a) x250 and (b) x4,300. 43

Figure 3.2 Representative load–displacement curves for (a) Fused Quartz standard sample (b) Polycarbonate standard sample (c) Silicon substrate. 45

Figure 3.3 Height and phase images (1×1μm) of multilayer thin films for (a-b) PVAm/GO, (c-d) PVAm/rGO and (e-f) xPVAm/rGO. 49

Figure 3.4 Cross section TEM images for (a) PVAm/GO, (b) PVAm/rGO and (c) xPVAm/rGO.50

Figure 3.5 Contact Angles of a water droplet for all multilayer thin films. 51

Figure 3.6 Representative load−displacement curves for single-loading tests of 20 μN maximum load on the three different films. 53

Figure 3.7 (a) Raman and (b) C 1s XPS (c) N 1s XPS (d) O 1s XPS of the PVAm/GO, PVAm/rGO and xPVAm/rGO. 55

Figure 3.8 Residual scratch images (10x10 μm) for (a) PVAm/GO (b) PVAm/rGO (c) xPVAm/rGO after 100 μN scratch (dashed lines show the start of the scratch). 59

Figure 3.9 Scratch profile for (a) PVAm/GO (b) PVAm/rGO (c) xPVAm/rGO with a normal scratch force up to 300 μN. (d) in-situ normal desplacement versus normal load. 60

Figure 3.10 Residual scratch images for (a) PVAm/GO, (b) PVAm/rGO, (c) xPVAm/rGO (d) section profiles along the residual scratch grooves for all films showing delamination/ pile-up near the end of the scratch. 62

Figure 3.11 (a) In-situ normal displacement and (b) coefficient of friction as a function of scratch normal force up to 1 mN for all multilayer thin films. 64

Figure 3.12 AFM and SEM residual scratch images for (a-b) PVAm/GO, (c-d) PVAm/rGO and (e-f) xPVAm/rGO under a normal load of 1 mN. 65

Figure 4.1 Schematics of (a) wet nanoindentation setup and (b) HT nanoindentation setup. 75

Figure 4.2 Residual indentation images (2x2 μm^2) for (a) FQ standard sample, (c) Si sample under dry condition, and for (b) FQ, (d) Si under submerged condition in DI water. The maximum indentation load was 2 mN and 4 mN for Si sample and FQ sample respectively. 76

Figure 4.3 Load–displacement curves for silicon sample for (a) Submerged condition in DI water (b) High temperature condition ($\mathrm{T} = 120\ ^\circ\mathrm{C}$). 77

Figure 4.4 Optical images of micro-scratches (a) before and (b) after self-healing. SEM images for the start and end of the scratch (c, d) before and (e, f) after self-healing. 79

Figure 4.5 Height AFM images ($5\times5\ \mu m^2$) of the as-deposited, submerged and after-heating PEI/PAA films. 81

Figure 4.6 AFM roughness images ($5x5\ \mu m^2$) for PEI/PAA film before and during heating (step 3 and 4 respectively in Table 1). Images were taken using the Berkovich HT probe. . 82

Figure 4.7 An illustration for how to define the zero point in the load-displacement curve for PEI/PAA film under (a) Submerged condition (b) Heating condition. 84

Figure 4.8 Representative comparative load-displacement curves for the thin film during (a) as-deposited and submerged and (b) as-deposited and heating. 85

Figure 4.9 Load–displacement curves for the (a) as-deposited (b) submerged (c) heating PEI/PAA films. 86

Figure 4.10 Residual 2mN nanoindentation images ($5x5\ \mu m^2$) for the (a) as-deposited (b) submerged, (c) dry, (d) heating, (e) after-heating films, and (f) representative cross-section profiles of the residual nanoindentation marks. 87

Figure 4.11 Graphical representation of the changes in the nanomechanical properties and morphology of a thin polymeric film under different humidity and temperature conditions. 90

Figure 4.12 FTIR spectra of the PEI/PAA film under different conditions for wavenumbers of (a) 2500-4000 cm^{-1} (b) 500-2500 cm^{-1}........ 91

Figure 4.13 XPS core level spectra of (a) C1s, (b) O1s, and (c) N1s for the as-deposited and after-heating films. 92

Figure 5.1 Schematic showing both the PVAm/GO thin film on (a) Si and (b) PET substrates. . 98

Figure 5.2 (a) TEM image of PVAm/GO film on PET substrate (b) TEM image of thermally reduced PVAm/GO showing single layers of PVAm and GO. 99

Figure 5.3 Finite element model for nanoscratch on film/substrate systems........ 102

Figure 5.4 AFM roughness height image for PVAm/GO on (a) Si and (b) PET substrates....... 103

Figure 5.5 (a) Reduced modulus and (b) hardness as a function of normalized contact depth for Si-based and PET-based films........ 104

Figure 5.6 (a) Reduced modulus and (b) hardness as a function of contact depth for both films at deeper depths using Berkovich probe. 105

Figure 5.7 Representative shallow load-displacement curves of 8 μN maximum load on Si-based and PET-based films. 106

Figure 5.8 The deformation behavior of PVAm/GO film on Si and PET represents (a) compliant film on stiff substrate and (b) stiff film on compliant substrate respectively. ... 107

Figure 5.9 Raman spectra of PVAm/GO on Si and PET 109

Figure 5.10 AFM residual scratch images (10x10 μm) for PVAm/ GO on (a) Si and (b) PET under a ramp load from 0 to 300 μN (dashed lines show the start of the scratch)........ 111

Figure 5.11 (a) In-situ normal displacement and (b) coefficient of friction as a function of scratch normal force up to 300 μN for both thin films. 112

Figure 5.12 AFM residual scratch images for PVAm/ GO on PET with (a) first pass and (b) second pass........ 114

Figure 5.13 FEA contour plots of von Mises stress distribution (MPa), elastic strain, contact pressure (MPa) and shear stress (S_{12}) (MPa) for (a, c, e, g) Si and (b, d, f, h) PET. 116

Figure 5.14 SEM residual scratch images for (a) Si-based film and (b) PET-based film, and (c) coefficient of friction as a function of scratch normal force up to 1 mN. 119

Figure 6.1 (a) Conceptual illustration of the 3D kirigami structures, which were assembled from 2D precursors by compressive bukling using FEA results (scale bar is 100 μm) (b) corresponding SEM images for the 3D structures (scale bar is 30 μm). 127

Figure 6.2 Load versus displacement data for flat-punch compression of (a) Table (b) Rotated Table (c) Ring, and (d) Tent structures. 130

Figure 6.3 Snapshots taken from the recorded movies at the start of the compression, 25%, 50%, and 100% compression for the (a) Table (b) Rotated table (c) Ring (d) Tent structures. (scale bar is 30 μm). 132

Figure 6.4 SEM images taken before the start of compression, after 30-50%, and after 100% compression for the (a) Table (b) Rotated table (c) Ring (d) Tent. (scale bar is 30 μm) ... 133

Figure 6.5 FEA results for the compression of SU-8 layer in the kirigami structures (under 100% compression) showing von Mises stress (MPa, left column) and maximum principal strain (right column) for the (a) Table (b) Rotated table (c) Ring (d) Tent. The substrate and punch were removed to allow visual observation of the stress and strain contours in the structures. 137

Figure 6.6 FEA results for the compression of Si layer in the kirigami structures (up to 100% height compression) showing von Mises stress (MPa, left column) and maximum principal strain (right column) for the (a) Table (b) Rotated table (c) Ring (d) Tent. The substrate and punch were removed to allow visual observation of stress and strain contours in the structures. 138

Figure 7.1 Cross sectional SEM images for (a) as-grown and (b) cleaved AlB_2 surfaces. Scale bar is 10 μm. 145

Figure 7.2 (a) AFM of the AlB_2 flake showing a step generated after cleavage, (b) as-grown and (c) cleaved surfaces. 146

Figure 7.3 Residual indentation images and cross-section profiles (1x1 μm) after (a) 150 μN and (b) 720 μN indentation load on the cleaved sample under ambient dry conditions. 147

Figure 7.4 Representative load-displacement curves for peak indentation loads of (a) 150 μN and (b) 720 μN, for the as-grown and cleaved samples. 149

Figure 7.5 XRD for as-grown and cleaved AlB_2 flakes in (a-b) linear scale, and (c) log scale for cleaved sample. 151

Figure 7.6 Quantitative SIMS depth profiles of (a) as-grown AlB_2 and (b) cleaved AlB_2 flakes. 152

Figure 7.7 Quantitative SIMS depth profile and AFM roughness images of epitaxial grown (a) TiO_2/Si and (b) TiO_2/cleaved AlB_2. 156

Figure 7.8 AFM roughness images of the TiO_2 film deposited on (a) silicon substrate and (b) cleaved AlB_2 surface. 157

Figure A.1 Schematic for the multiple-pass scratch experiments on HfB_xC_y coating. The tip was moved back and forth. 202

Figure A.2 Schematic of quasi-equilibrium cluster distributions of stoichiometric HfB_2, HfC, and B_4C nanophases and their non-stoichiometric variants. 203

Figure A.3 Schematic for the semi-empirical mixing framework using (a) the first scenario (maximizing HfC), and (b) the second scenario (maximizing B_4C). 206

Figure A.4 Computed reduced modulus using the semi-empirical framework for the scenarios of maximizing (a) HFC and (b) B4C, and comparison with the nanoindentation results. 208

Figure A.5 Modeled results of phase percentages, which are made of different compounds/ elements in the aggregate as a function of carbon content based on their volume fractions 209

Figure A.6 E_r for HfBxCy thin films with different compositions computed and measured using the framework and nanoindentation experiments. 210

Figure A.7 Poisson's ratio and Yield Strength computed using the semi-empirical framework as a function of carbon content. 211

Figure A.8 (a) Friction coefficient an (b) elastic recovery of different HfB_xC_y thin films as a function of normal load obtained from nanoscratch experiments. 213

Figure A.9 Average normalized ER versus average H_3E_2 for HfB_xC_y thin films. 217

Figure A.10 (a) Friction coefficient and (b) contact depth as a function of the number of scratch passes using nanoscratch experiments. 218

LIST OF TABLES

Page
Table 2.1. Roughness and thickness of multilayer nanocoatings on silicon wafers. 21

Table 2.2. Nanomechanical properties and gas permeability of multilayer thin films. 26

Table 2.3. Mechanical properties of gas barrier materials. 29

Table 3.1. Elastic Modulus and Hardness for standard samples and silicon. 45

Table 3.2 List of PVAm/GO films on Si substrate. 48

Table 3.3 Nanomechanical properties of multilayer thin films[a]. 53

Table 3.4 25μN constant load scratch experiments. 58

Table 3.5 100μN constant load scratch experiments. 58

Table 3.6 Failure properties for multilayer thin films at the onset of delamination. 66

Table 4.1 Nanomechanical Properties of FQ and Si samples under dry and submerged conditions. 76

Table 4.2 AFM roughness, and nanomechanical properties of PEI/PAA films. 81

Table 5.1 Elastic Modulus and Hardness for standard sample, and Si and PET substrate.* 102

Table 5.2 Nanomechanical properties of PVAm/GO thin film on Si and PET substrates. 103

Table 5.3 25μN constant load scratch tests summary on Silicon and PET. 110

Table 5.4 100μN constant load scratch tests summary on Silicon and PET. 110

Table 5.5 Material properties of film and substrate for FEA. 115

Table 5.6 Failure properties measured at the onset of delamination. 119

Table 6.1 Comparison between kirigami structures in terms of response to mechanical deformation 130

Table 7.1 Nanomechanical properties of as-grown and cleaved AlB_2 flakes. 148

Table A.1 Elastic constants and properties of the elements and compounds in HfB_xC_y. 205

Table A.2 Nanomechanical properties of HfB_xC_y thin films measured using nanoindentation. 207

Table A.3 Nanoscratch properties of HfB_xC_y thin films (carbon content = 5%). 215

Table A.4 Nanoscratch properties of HfB_xC_y thin films (carbon content = 15%). 215

Table A.5 Nanoscratch properties of HfB_xC_y thin films (carbon content = 35%). 216

Table A.6: Comparison of HfB_xC_y with other hard tribological coatings. 220

1 INTRODUCTION AND LITERATURE REVIEW

1.1 Introduction to multilayers nanocomposites

Polymer-based Multilayered nanocomposites (PNC) have the advantage of being tunable and versatile to meet the need for functional-specific applications. The trend for these nanocomposites is moving towards scalable and cost effective material fabrication.[1] Multilayered nanocomposites can be divided to different subcategories depending on the application, materials and mechanical properties. Herein, in this thesis, we adopt two main classification: 2D and 3D nanocomposites based on their arrangement or assembly methods. (see Figure 1.1).

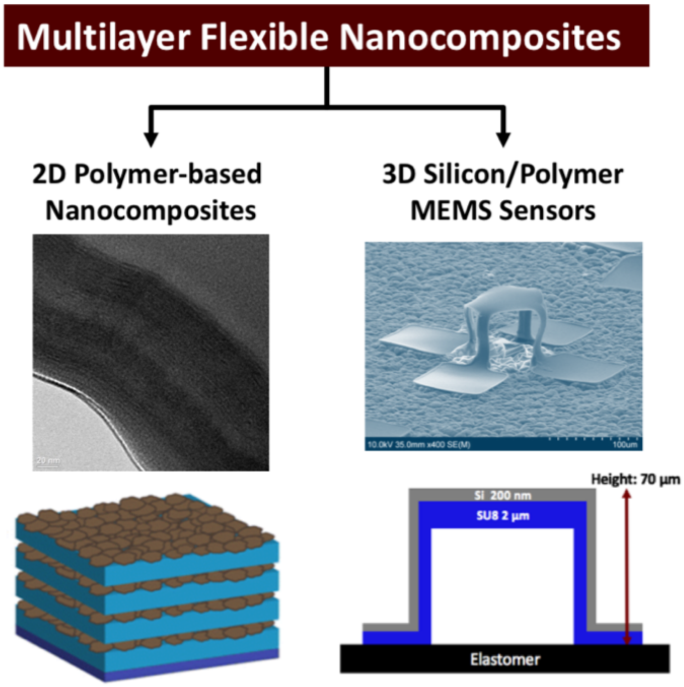

Figure 1.1 The classification adopted in this study for nanocomposites based on their arrangements.

Nowadays, polymer-based multilayer nanocomposites have become favorable material choice for many applications such as filled rubber tires, food packaging, flexible electronics and stretchable energy storages due to the unique characteristics of combining two or more materials. These hybrid materials usually consist of a polymer as a matrix and reinforcement such as silicon, clay or graphene oxide (GO). These reinforcements typically are nano-sized components to take advantage of size effect of nanoscale objects. Successfully, polymer matrices in the literature were reinforced with different inorganic and organic fillers.[2] Some examples where the polymer nanocomposites were successfully introduced are filled rubber tires, food packaging, flexible electronics and bioelectronics.[2–4]

1.2 The nanoeffect of PNC

The improved physical properties of PNC are due to the reduced size or dimensions of the fillers to the nanoscale, which are several orders of magnitudes smaller than conventional macroparticles. The surface area to volume is highly increased, when the particle size is reduced. The higher surface area leads to a higher interfacial volume between the matrix and the filler. Three different morphologies of nanoparticles or fillers are typically introduced on nanocomposites: spheres (zero-dimensional object), rods (one-dimensional object) and plates (two-dimensional object). Each nanofiller leads to different aspect ratio. It is worth to mention that the volume ratio of interface to particle changes dramatically between spheres and plates as the size of the nanoparticle is reduced. Different applications tend to require different aspect ratios. Here, we focused on plates as a reinforcement as the targeted applications such as gas barriers necessitate very low inverse aspect ratio ($h/2r$) or high aspect ratio ($2r/h$).

The properties of polymers are function of their chains' sizes. This is measured using the radius of gyration (R_g). R_g is in the order of 3-30 nm. Therefore, to achieve effective reinforcement, the size of the particles needs to be made in relative to the size of the polymer chains.[5] The smaller the particles, the larger the interface between the polymer and the particle. This results into a higher load transfer between the matrix and reinforcement leading to improved mechanical properties.[6]

1.3 2D PNC assembled using LbL

There are huge improvements in the physical and mechanical properties of polymers due to the incorporation of cost-effective low concentration (few vol%) of nanoscale fillers. Such improvements have inspired academic and industrial researchers alike. For example, researchers at Toyota Central Research showed how the modulus of nylon-6 rubber can be improved by a factor of 3 by incorporating 5 vol% of exfoliated montmorillonite (MMT) clay nanosheets.[7] These successful demonstrations turned PNC into billion-dollar global industry making different products such as automobile parts, flame retardants, packaging and protective coatings.

Two-dimensional (2D) Multilayer thin films can be synthesized using many techniques such as solvent casting, painting, spray processing, printing, spin coating, floating technique, pulsed laser deposition technique, and layer-by-layer (LbL) assembly. Compared to other techniques, the synthesis of polymer based nanocomposites using LbL technique is advantageous because it is simpler due to its flexible water-based process. This have resulted in a cheap and scalable technique, which made it possible to deposit different co-polymers and nanoplatelets such as inorganic clays and graphene. Different arrangements including bilayers and quadlayers of polymer-clay, polymer-graphene and polymer-polymer can be produced.

1.4 3D PNC assembled using Compressive Buckling

There is growing need to develop three-dimensional (3D) electronics devices due to either a requirement imposed by the application or a as a route to improve the efficiency of current 2D nanocomposites. For example, biology is inherently 3D designs. Therefore, to successfully integrate a technology with life or to mimic the nature designs, we often need to fabricate 3D electronics that meets the complexity of nature 3D designs. Also, currently, the efficiency of devices is improved through the optimization of the used material. However, there is a limitation to this route or an imposed higher cost due to using fancy materials. Popping the design of electronics from 2D to 3D provides additional material space to continue to improve the efficiency of these devices through the optimization of geometry and thickness/scale of materials. For example, 3D microelectromechanical systems (MEMS) offer vastly improved bandwidth and frequency tunability over conventional 2D MEMS structures, such as cantilevered beams and doubly clamped bridges.[8] For example, there are many advantages of creating 3D structures from 2D graphene nanoscale material, which serves as the building block. Such structures enabled novel functionalities, which are not achievable with 2D planar materials.[9]

Traditionally, the mechanics play a role in the optimization and improvement of fabrication process. In other words, as discussed previously in section 1.3, the nanomechanical experiments can be used to better understand how 2D multilayer PNC behave under normal and lateral loadings. Recently, the role of mechanics expanded to manufacturing as an approach to make new class of materials.[10] This is often called mechanics-driven manufacturing. In addition, instabilities and failures are typically viewed as threats to the durability of the material under real-life applications. Here, instead, compressive buckling is used as a route to fabricate 3D materials.

Differently to 2D PNC discussed in 1.3, complex microscale three-dimensional (3D) silicon kirigami architectures are manufactured using patterning cuts on 2D thin layers of silicon and photodefinable epoxy (SU8) deposited on elastomer substrates. Pattern cuts are defined in a way to reduce stresses and enhance flexibility (in certain orientations) in the final 3D structures. The 2D layers are patterned using photolithography and reactive ion etching (RIE) in stretched elastomer substrate such as silicone to a certain prestrain (uniaxial or biaxial and using a mechanical stretching stage). Part of the 2D patterning is to deposit a photoresist (AZ5214) in a certain bonding sites using spin casing and photolithography, which will adhere strongly to substrate using covalent surface chemical bonding. Once this prestrain is released, strong compressive lateral buckling transferred the 2D patterns intro 3D engineered structures. [11]

1.5 Objectives and outlines

The number of research related to PNC is increasing. More scholars are contributing to the understanding of how PNC works and how to manipulate their behaviors. The PNC have become a well-established field but yet the significant implementation of PNC in the industry is still ahead of us. There are few challenges to overcome, which is pervading the implementation of PNC such as large mass production, recycling, health risks and durability. In the case of durability and resistance to degradation over time, solid quantitative studies are required to encourage potential markets to implement this relatively new class of composites.

Durability is an important feature for these nanocomposites due to the nature of the applications (e.g., food packaging and electronics), which requires resistance to deformation in order to maintain the films' or structures' functionality and reliability. For example, certain applications are operated by means of mechanical contact such as touch screens and flat panel displays. In order to evaluate the mechanical properties, durability of these coatings to external normal and lateral loads and their resistance to failure and delamination, many experiments were carried out such as nanoindentation, nanoscratch and flat-punch compression. In addition, characterization techniques such as atomic force microscopy (AFM), scanning/transmission electron microscopy (SEM/TEM), Raman spectroscopy and X-ray photoelectron spectroscopy (XPS) were used to assist in further understanding the chemical and structural composition of the nanocomposites and evaluate their wear and failure.

The flowchart in Figure 1.2(a) summarizes the research ideas and the role of nanomechanics in improving the mechanical reliability of these multilayer systems. The nanomechanical testing were carried out under different conditions such as high temperature, high humidity, vacuum and room temperature to simulate real environments or due to constraints imposed by the small structures. As mentioned earlier in the case of 3D structures, mechanics play a role in both the fabrication and optimization of these structures. The fabrication and deformation of 3D structures introduces similar instabilities such as buckling but of opposite directions. Figure 1.2(b) provides detailed outline for the research proposal.

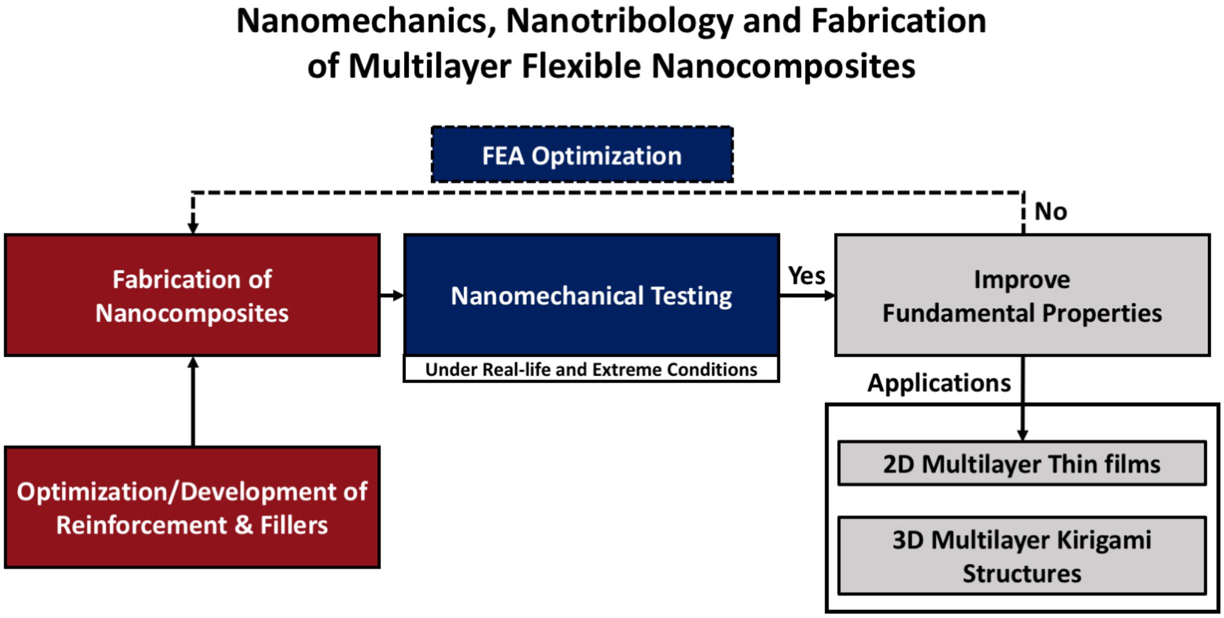

(a)

Figure 1.2 Flowchart of the research proposal, (a) simplified and (b) deatiled.

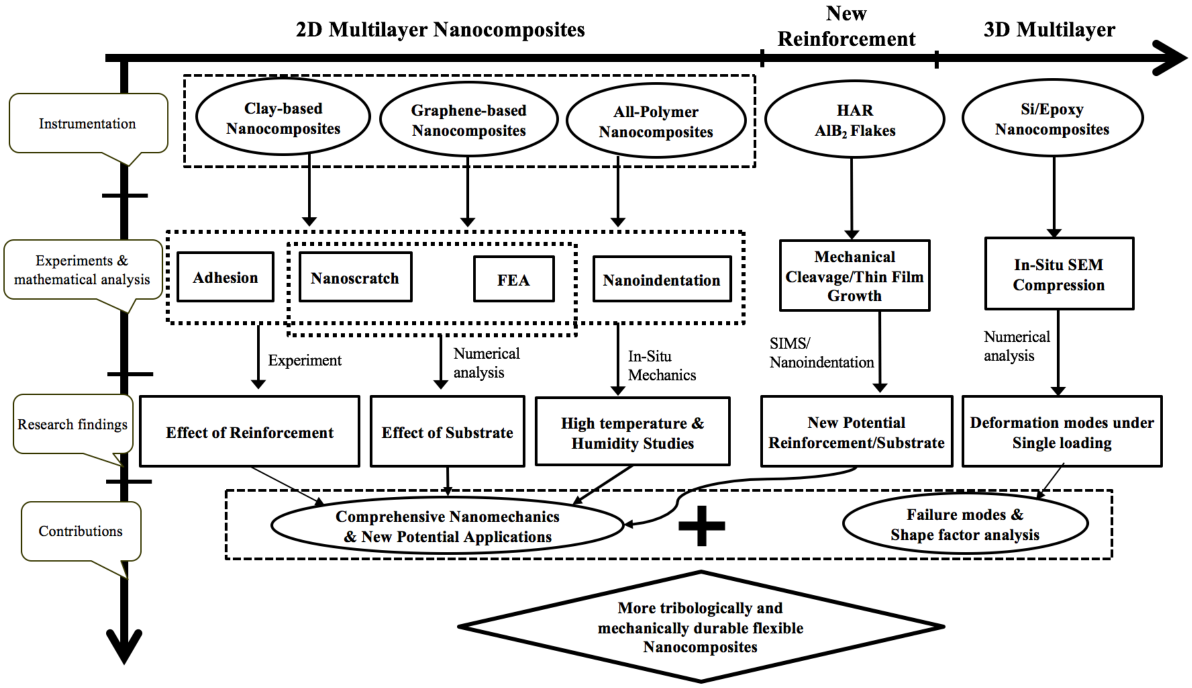

(b)

Figure 1.2 Continued.

According to the arrangement/layout of nanocomposites, the present thesis can be divided into three main parts,

(1) Nanomechanics and fabrication of 2D multilayer nanocomposites (Chapters 2-5). The studies of 2D nanocomposites cover the big portion of the present thesis, as the field of multilayer thin films is well-developed. Indeed, these 2D nanocomposites have been used in many applications. However, their durability against mechanical deformations such as scratch and their nanomechanical properties were not discussed thoroughly in the literature. Also, there is little information about their mechanical behavior as a function of reinforcements, different substrates and under different operating conditions. For these reasons, this part includes a comprehensive range of different experimental techniques including nanomechanical, chemical and imaging analysis.

Chapter 2 begins with a detailed description of the deposition method (LbL assembly), which is used for the synthesis of films in Chapters 2-5. Next, a study of the nanomechanical, nanotribological and morphological properties of five different polymer-based multilayer thin films, which are widely used as gas barriers, are presented. The films were varied based on the used reinforcement (such as clay, graphene and polymer blend) and the number of layers in each cycle (such as bilayers and quadlayers). The motivations and ideas behind the work in the next chapters (3-5) were originated based on the findings in chapter 2. For example, the clay-based films were found to be excellent choice for hard coatings due to the superior scratch resistance as compared to the other films in this study such as graphene-based films and all-polymeric films. On the other hand, the poor performance of graphene-based films against scratch led the path for the research work in chapter 3.

In Chapter 3, two extra processing steps: graphene reduction and polymer crosslinking were implemented in an effort to improve the scratch resistance of graphene-based films. Successfully, these implementations resulted in an improved adhesive and shear strength, improved mechanical properties, and lower friction coefficient of reduced graphene/crosslinked polymer films as compared to the original graphene-based film (without graphene reduction and polymer crosslinking).

All-polymer based films were found to have the lowest mechanical properties and scratch resistance as compared to the reinforced polymer nanocomposites with either clay or graphene. However, these multilayer thin films were found to have the advantage of being self-healable once a mechanical damaged is introduced on surface. To introduce the healing process for a damage, a stimulus is required such as high temperature or high humidity. Chapter 4 discusses the mechanisms behind the self-healing capability using both insitu high temperature and high humidity nanoindentation techniques. These insitu techniques were not used before in the literature. The details in how to conduct these insitu experiments are discussed in Chapter 4. They provided better insights to the role of mechanics in the self-healing process.

This part closes with Chapter 5, which focuses on the effect of the substrate on the mechanical and scratch behavior of multilayer thin films. In Chapter 2-4, the polymer nanocomposites were deposited on a Si rigid substrate to avoid any substrate effects on the nanomechanical measurements. Thus, the intrinsic properties of the films could be extracted. While, this is helpful to understand the properties of these films, it does not provide a true perception of how these films will behave on real-life applications, since these films would be deposited on a softer and more compliant substrate such as PET for the gas barrier applications. Therefore, chapter 5 highlights the behavior of film/substrate systems. Complementary finite element analysis is included to emphasize the difference in the mechanical behavior for each film/substrate system. Challenges and recommendations were discussed based on the findings and whether having the film on a stiff or compliant substrates resemble the true behavior of polymer nanocomposites in real applications.

(2) Nanomechanics and fabrication of 3D multilayer nanocomposites (Chapter 6). While coatings provide many advantages as compared to bulk materials, there is a little design space to achieve lighter and more flexible nanocomposites due to the limitation in the geometry of these composites. Popping up the design of nanocomposites from 2D to 3D provides a route to continue the enhancement of nanocomposites' properties, since it takes into account the shape factor of these composites. Chapter 6 introduces new 3D nanocomposites based on the ancient Japanese art of paper folding and cutting, known as Kirigami. Fabrication and Nanomechanics are discussed thoroughly. There is no literature for the mechanics of Kirigami or even Origami structures. Also, the discussion of the substrate role in chapter 5 continues in Chapter 6, since these Kirigami structures are deposited on a complaint elastomer substrate.

(3) Development and characterization of New Reinforcement (Chapter 7). Chapter 2 highlights different 2D polymer nanocomposites with different high aspect ratio reinforcements. Also, it showed how critical is to have a strong adhesion/load transfer between the matrix and the reinforcement. This have provided a motivation to pursue the search for new reinforcements, which can provide improved performance of multilayer nanocomposites. The last part investigates the synthesis and characterization of a new reinforcement, Aluminum diboride (AlB_2) using Nanoindentation, AFM and SIMS.

The nanomechanics and nanotribology provides a strong understanding of material behavior under study. By obtaining the nanomechanical properties measured during experiments, further information about the fundamental properties of materials was gained. Based on this knowledge, multilayer nanocomposites were found to be more mechanically robust through carrying out changes during fabrication/processing. The aim of this study is to improve the durability of PNC. In few occasions, the findings of nanomechanical properties inspired new applications for these PNC, which was not traditionally observed without nanomechanics. For example, multilayer thin films synthesized using LbL assembly, and traditionally made for high gas barrier application were found to be potential hard coatings for tribological applications, vapor barrier coatings and self-healing coatings as shown in Figure 1.3.

Part of these nanomechanics experiments were carried out at ambient conditions, while others were carried out under different conditions such as vacuum, high temperature and high humidity. In situ measurements provided better insights for certain systems, which were not attainable with ambient conditions. In addition, the nanomechanics through computational modelling can serve as a tool to optimize the fabrication processes and synthesis conditions. Therefore, a direct link between fabrication, mechanical testing and modeling is established.

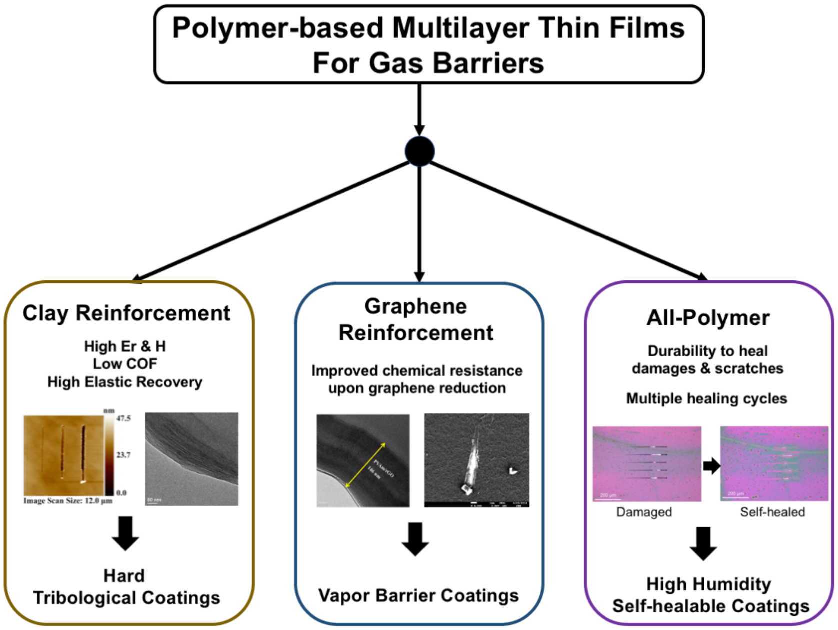

Figure 1.3 Multilayer thin films with exceptional gas barrier capability found to be good candidates for other applications after nanomechanical testing under different conditions.

1.6 Recommended future work

The mechanical behavior of a nanocomposite is dominated by the interface between the filler and the polymer matrix in case of 2D PNC and between the structure and the substrate in case of 3D PNC. Also, the importance of the interface role has become more significant due to the higher surface area to volume ratio as the nanofillers are made smaller. Therefore, more studies need to be carried out in order to understand the mechanics and physics of these interfaces. For example, time-dependent viscoelastic properties and thermomechanical response can varies widely based on the nature of this interface. As a continuation of the work presented by this thesis, one path for future work is to characterize the mechanical properties near the interface and understand how interfaces changes over time due to polymer ageing or energy dissipation under mechanical cycling or fatigue. Extraction of viscoelastic properties is important to be able to model the contact mechanics near the interface and predict the behavior of these PNC.

2 NANOMECHANICAL BEHAVIOR OF HIGH GAS BARRIER MULTILAYER THIN FILMS[*]

2.1 Introduction

The simplicity and versatility of deposition techniques, such as layer-by-layer (LbL) assembly, has caused the development of polymeric nanocoatings to flourish in the last two decades.[12,13] The most common form of LbL deposition involves alternately exposing a substrate to cationic and anionic solutions. Electrostatic attractions between the charged ingredients result in the buildup of layers. Film thickness and other properties can be easily optimized by increasing the number of deposition cycles, with optional rinsing and drying steps often used between deposition steps.[3] In addition to electrostatic attractions, hydrogen bonding,[14] covalent bonding[15] or van der Waals interactions[16] can be employed to deposit these films. Concentration,[17] ionic strength,[18] molecular weight[19] and deposition time[20] of the aqueous deposition mixtures can be adjusted to tailor multilayer structure and properties. The LbL technique has successfully incorporated multiple polymers,[21] nanoparticles,[22] inorganic clays,[23] and biological molecules.[24] Its simple and flexible water-based processing has allowed LbL assemblies to be used for drug delivery,[25,26] antireflection,[27,28] flame suppression,[29,30] and gas barrier/separation.[31,32]

Inorganic and metal oxide films are typically used to impart gas barrier to polymer substrates, but these thin films are neither stretchable nor flexible.[33] Nanobrick wall thin films, consisting of polyelectrolytes and clay nanoplatelets,[34,35] are much more flexible and can exceed the barrier of inorganic thin films. LbL-based gas barriers made with only polymers can undergo

---

[*] Reprinted with permissions from “Nanomechanical Behavior of High Gas Barrier Multilayer Thin Films” by Humood, M.; Chowdhury, S.; Song, Y.; Tzeng, P.; Grunlan, J. C.; Polycarpou, A. A. ACS Appl. Mater. Interfaces 2016, 8, 11128–11138.

modest stretching (~5%) without losing high barrier.[36,37] Even with mechanical durability playing a critical role for these packaging materials, few studies have examined the mechanical behavior of high gas barrier LbL assemblies. Nanoindentation/scratch of polymeric coatings is known to be effective for determining nanomechanical properties of both the material and the surface characteristics.[38–41] Material properties of thin films need to be measured within 10-20% of the total thickness to reduce the impact of substrate[42] and to keep the plastic deformation region within the film.[43] This requires shallow indentation, which nanoscale instruments have overcome due to sensitive force measurements of 1 nN[44] and displacement measurements of less than 1 nm.[45]

In this study, a series of polymer and polymer/platelet assemblies, known to have exceptional gas barrier,[3] were fabricated to evaluate their nanomechanical and nanoscratch behavior. These films are highly flexible,[46] dense,[32,37] transparent[3,47] and can be used for applications such as protection of flexible electronics. An understanding of the mechanical behavior of these coatings under a sliding load is developed. Available literature regarding mechanical properties of LbL assembly focused on studying the elasticity of films.[48–55] However to the best of authors' knowledge, scratch resistance has not been discussed widely for LbL multilayer thin films. Previous studies were focused on evaluation of gas barrier properties of these thin polymer multilayer films. In this case, the mechanical properties and durability to scratch resistance of four different multilayer coatings is evaluated. Nanomechanical properties and nanoscratch of these thin films were benchmarked with poly(ethylene terephthalate) (PET), which is a commonly used food packaging material.

2.2 Experimental Section

2.2.1 Materials

Branched polyethylenimine (Aldrich, St. Louis, MO) (MW ~ 25,000 g/mol) (PEI) is a cationic polymer that was dissolved into 18.2 MΩ deionized water to create a 0.1 wt% solution. The pH was adjusted from its unaltered value (~10.5) to 10 by adding 1 M hydrochloric acid (HCl). Poly(acrylic acid) (Aldrich) (MW ~ 100,000 g/mol) (PAA) is an anionic polymer that was prepared as a 0.2 wt% solution in deionized water. The pH of PAA was adjusted from its unaltered value (~3.1) to 4 by adding 1.0 M sodium hydroxide (NaOH). Anionic natural sodium montmorillonite clay (tradename Cloisite Na+) (Southern Clay Products, Inc., Gonzales, TX) was prepared as a 1.0 wt% aqueous suspension. This suspension of high aspect ratio nanoplatelets (l/d is 80 to 300)[56] was used at its natural pH (~9.7), where l and d are the thickness & diameter of the ellipsoid, respectively. Graphene oxide (GO) (aspect ratio 300-800) (CheapTubes, Brattleboro, VT) was exfoliated in deionized water via sonication (10W) for 10 minutes with a MISONIX XL-2000 tip sonicator (Qsonica, Melville, NY). A 0.1 wt% graphene oxide suspension was used as an anionic component at its unaltered pH (~3.2).

Single-side-polished (100) silicon wafers (University Wafer, South Boston, MA) were used as deposition substrates. Silicon was used as substrate to facilitate thickness and surface roughness measurements using ellipsometry (film growth characterization is discussed in recent publications)[32,37,46] and atomic force microscopy, respectively. Silicon or glass are the typical substrates for nanomechanical testing of multilayer LbL thin films.[57–60] Silicon wafers were cleaned with a 3:1 ratio of 30% hydrogen peroxide to sulfuric acid (known as piranha solution) and stored in deionized water. These substrates were then rinsed with acetone and deionized water before use. *Caution: Piranha solution reacts violently with organic material therefore it needs to* *be handled properly.* For transmission electron microscopy (TEM), samples were prepared by embedding a small piece of coated substrate (polyethylene terephthalate or polystyrene) in Epofix resin (EMS, Hatfield, PA). After curing overnight the cross-sections were cut using an Ultra 45° diamond knife (Diatome, Hatfield, PA). Samples were imaged on copper grids using a Tecnai G2 F20 (FEI, Hillsboro, OR), operated at 200 kV. For TEM characterization, 5 quadlayers of PEI/PAA/PEI/GO and 20 bilayers of PEI/PAA were deposited on substrate.

2.2.2 Layer-by-layer Deposition

Figure 2.1 illustrates the layer-by-layer assembly procedure. For the bilayer (BL) assemblies, PEI/PAA and PEI/MMT, a layer of PEI was first deposited by dipping the substrate into the solution for 5 minutes, followed by rinsing with deionized water for 30 seconds and drying with a stream of filtered air. The substrate was then dipped into PAA or MMT solution for another 5 minutes, followed by another rinsing and drying cycle. Starting from the second deposition cycle, the remaining layers were deposited using one-minute dips in each solution. For the PEI/PAA/PEI/MMT and PEI/PAA/PEI/GO assemblies, a quadlayer (QL) was completed with one more layer of PEI and nanoplatelet (following PEI/PAA) with one minute dips and all subsequent layers were also deposited with one minute immersions. All films were created with home-built robotic systems.[61,62] For each system studied, the number of cycles chosen corresponds to high oxygen barrier (permeability < 10^{-19}cm^{3}cm/(cm^2 s Pa).

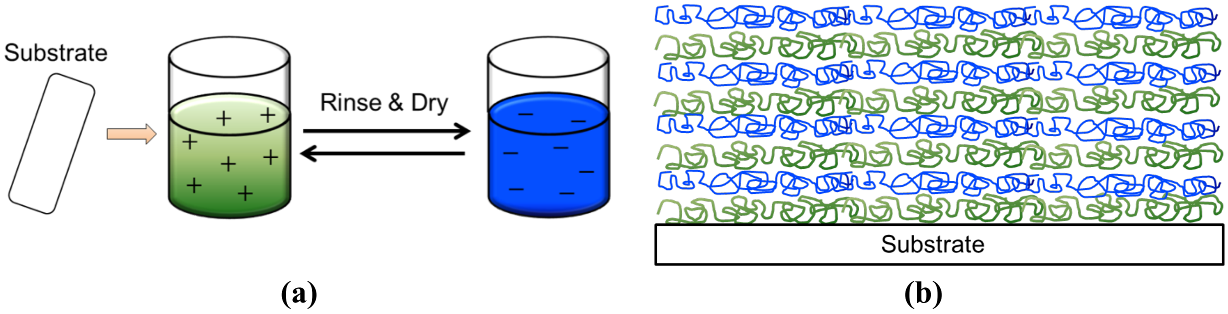

Figure 2.1. Illustration of (a) LbL process and (b) bilayer structure. The procedure to build quadlayer assemblies is similar, only increasing the repeating deposition cycle to four components.

2.2.3 Nanoindentation

Nanomechanical properties were measured using a commercial nanoindenter (Triboscope (TS) 75, Hysitron Inc., Minneapolis, MN). The maximum load and displacement are 8000 μN and 4.5 μm, respectively. A Berkovich tip (three sided pyramid), with a tip radius of ~ 150 nm (see Figure 2.2) was used for indentation. This radius was further confirmed through a technique developed by Yu et al.[63] Tip area calibration was performed on fused quartz, known as the "tip area function," to extract reduced elastic modulus and hardness measurements. A previously reported method was used,[64] which is a compliance method, where the mechanical properties are calculated based on the contact area of the probe tip to the sample under a given load. The contact depth (h_c) is the only information obtained by the indentation measurements, the tip area function correlates the contact area to the contact depth. For a perfect Berkovich tip, the area function is the geometrical function given by:[38]

$$A_c(h_c) = 24.5h_c^2 \tag{1}$$

However, due to tip imperfections, the area function more commonly takes the following form:

$$A_c(h_c) = C_o h_c^2 + C_1 h_c + C_2 h_c^{1/2} + C_3 h_c^{1/4} + C_4 h_c^{1/8} + C_5 h_c^{1/16} \tag{2}$$

where the coefficients C_1-C_5 are obtained from experimental data from the fused quartz (FQ) standard sample. To determine the coefficients, indentations at varying penetration depths (corresponding to a similar depth range as the desired measurements) were performed on a FQ sample. Since the modulus of the standard material is known, the contact area corresponding to each contact depth can be calculated using the Oliver-Pharr relation[64] and the coefficients are determined by polynomial curve fitting. Once the contact area is defined, hardness (*H*) is obtained from Eq. 3. The reduced elastic modulus (E_r) can be obtained from the unloading stiffness (S), according to Eq. 4, where β is a constant related to the geometry of the tip. Eq. 5 defines the reduced elastic modulus. It is a combination of elastic modulus of both indenter (E_i) and sample (E_s) and Poisson's ratio of both indenter (v_i) and sample (v_s):

$$H = \frac{P_{max}}{A} \tag{3}$$

$$E_r = \frac{\sqrt{\pi}}{2} \times \frac{S}{\beta\sqrt{A}} \tag{4}$$

$$\frac{1}{E_r} = (\frac{1 - {v_i}^2}{E_i} + \frac{1 - {v_s}^2}{E_s}) \tag{5}$$

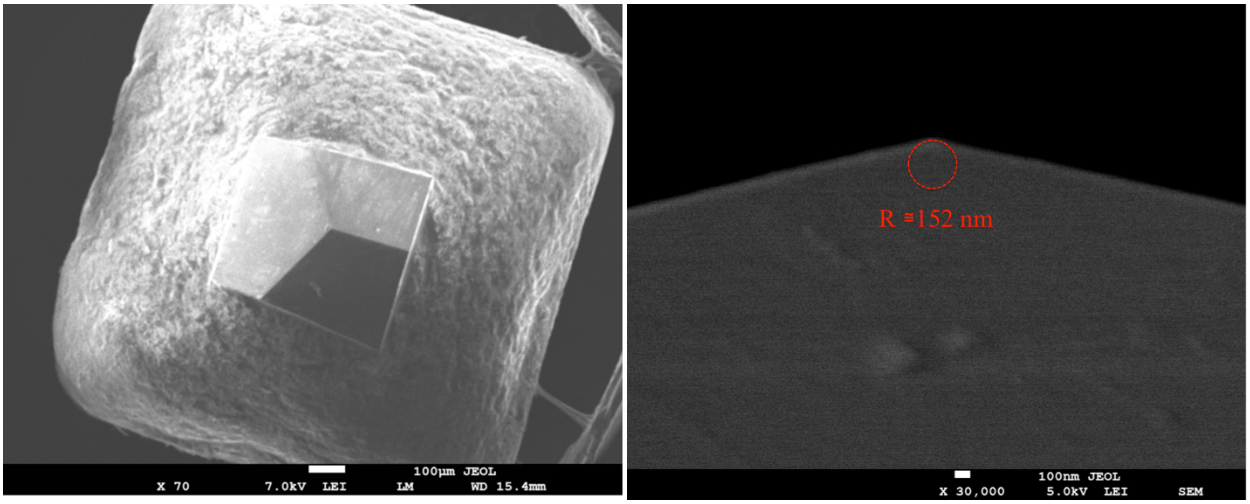

(a) **(b)**

Figure 2.2 Scanning Electron Microscopy (SEM) image of (a) the Berkovich probe used for indention experiments and (b) a cross-sectional image of this tip.

2.2.4 Nanoscratch

A nanoscratch technique was utilized using a commercial nanoindenter (TriboIndenter (TI) Premier, Hysitron Inc., Minneapolis, MN) to measure the friction, wear and elastic recovery of the multilayer coatings. To eliminate the directional effects of tip geometry, a conospherical tip (870 nm radius, see Figure 2.3) was used for the experiments.[65] The scratch measurements were performed under constant normal loads of 50, 100, 200 and 400 µN and with a sliding speed of 0.33 µm/s. The scratch length was 8 µm. At the end of each 8 µm scratch, wear depths were rescanned using the same tip to measure the residual scratch depth. This procedure also allows for an estimation of the elastic recovery of the coatings. The coefficient of friction (*COF*) was recorded from the scratch experiments. In addition, high load scratches of 1, 2 and 3 mN were performed to check the post scratch wear and assess film failure and delamination.

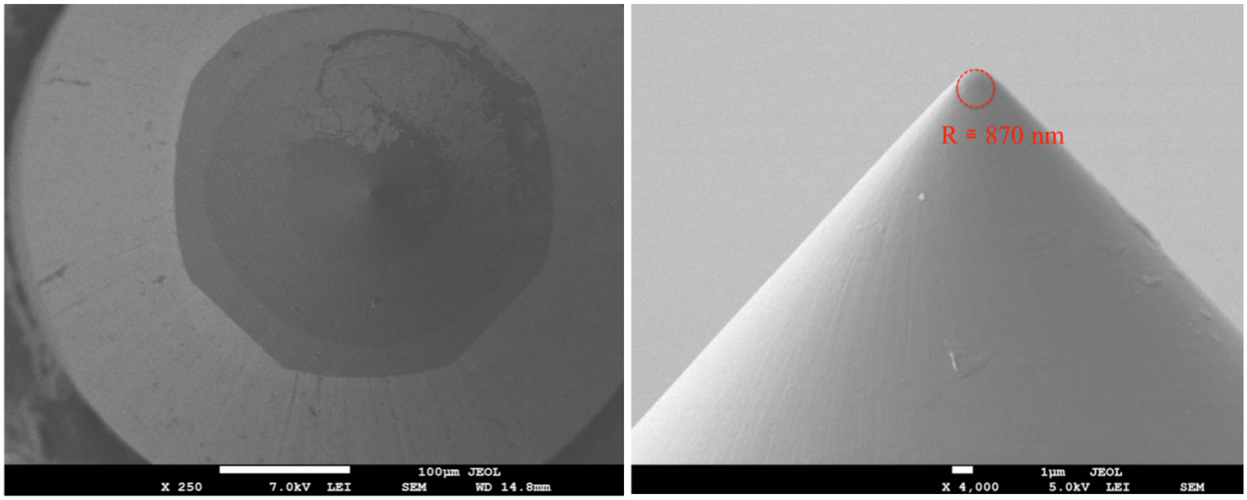

(a) **(b)**

Figure 2.3 Scanning Electron Microscopy (SEM) image of (a) the conospherical probe used in scratch experiments and (b) a cross-sectional image of this tip.

2.3 Results and Discussion

2.3.1 Surface Roughness & Morphology

Figure 2.4 shows the AFM images used to obtain root mean square (rms) roughness values that are summarized in Table 2.1 (along with a brief description of each of the coatings). The PEI/PAA film is much rougher than the multilayer films containing nanoplatelets. PEI/PAA/PEI/GO, PEI/PAA/PEI/MMT and PEI/MMT all have surface roughness values below 10 nm. Without platelets, the weak polyelectrolytes form bumpy domains that are linked to initial islands formed during the first few deposited bilayers.[66,67] High aspect ratio nanoplatelets are able to bridge islands and other defects to planarize the surfaces, thus producing smooth thin films. Cross-sectional images of these multilayer films were imaged by TEM, as shown in Figure 2.5. Clay or GO nanoplatelets appear as dark lines due to their high electron density compared to the polyelectrolyte, epoxy resin or polymer substrate, which have a lighter appearance. The wavy structure in Figure 2.5(b) was likely introduced during the TEM sample preparation. No stratified layer structure was observed in PEI/PAA all-polymer multilayer film (see Figure 2.5(c)) due to the lack of contrast between the two polyelectrolyte.

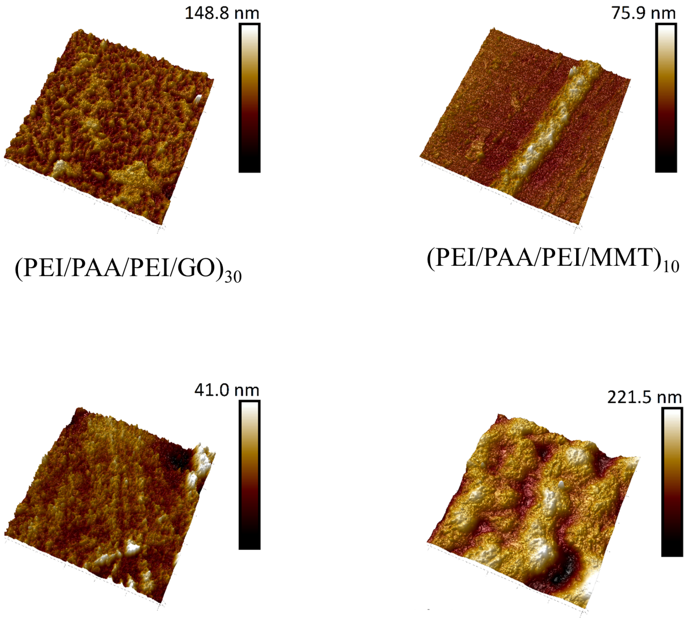

(PEI/PAA/PEI/GO)$_{30}$ (PEI/PAA/PEI/MMT)$_{10}$

(PEI/MMT)$_{50}$ (PEI/PAA)$_{8}$

Figure 2.4 Atomic Force Microscopy topography images (5×5 μm) of the multilayer thin films. Subscripts refer to the number of bilayers or quadlayers deposited.

Table 2.1. Roughness and thickness of multilayer nanocoatings on silicon wafers.

Sample	**Cycles Deposited (Bilayers or Quadlayers)**	**Description**	**Thickness (nm)**	**RMS Roughness (nm)**
PEI/PAA/PEI/GO	30	Non-clay quadlayer assembly	200	9.7
PEI/PAA/PEI/MMT	10	Clay-based quadlayer assembly	600	4.5
PEI/MMT	50	Clay-based bilayer assembly	400	3.6
PEI/PAA	8	All-polymer bilayer assembly	450	22.7

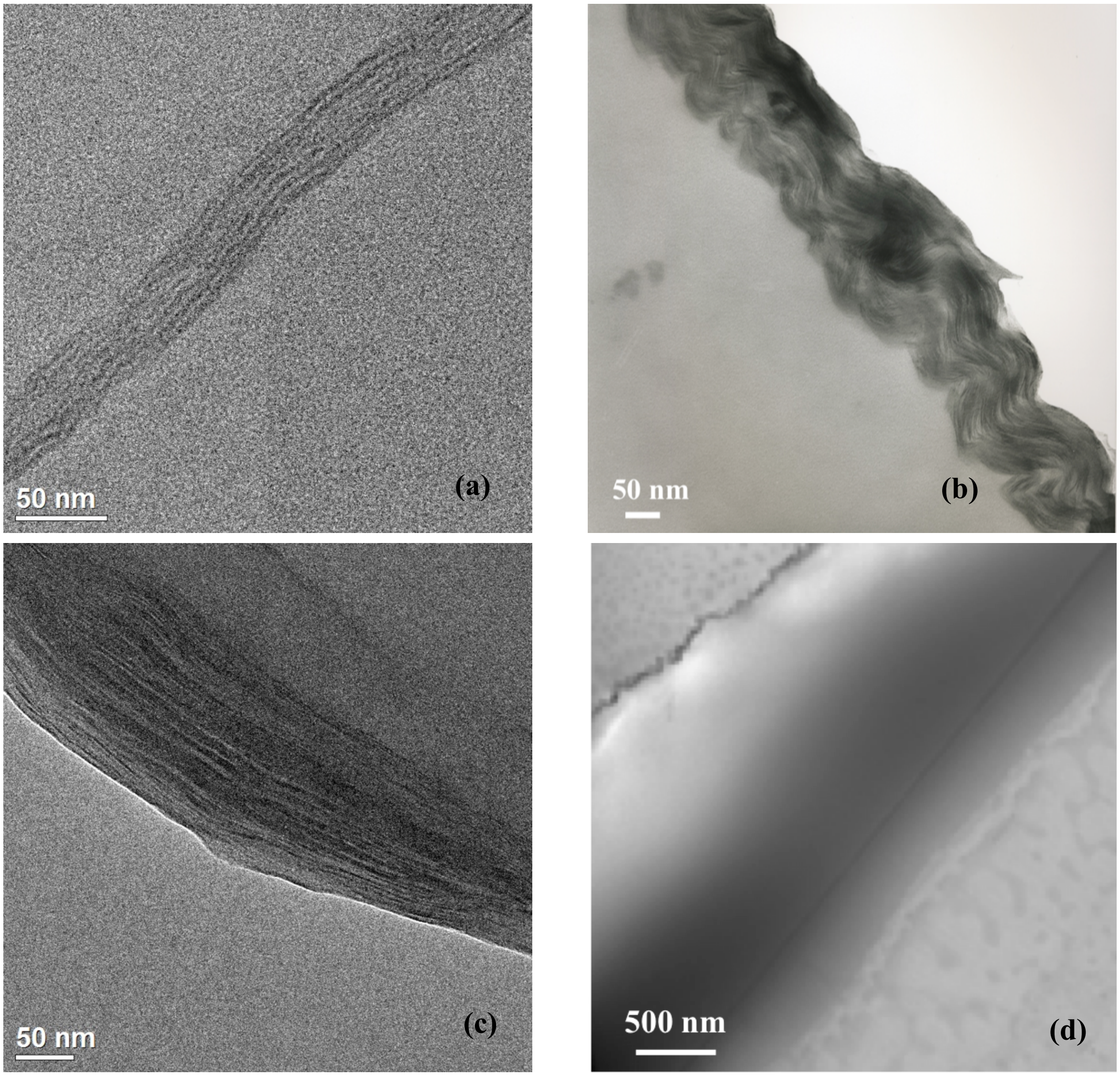

Figure 2.5 TEM cross-sectional images of (a) $(PEI/PAA/PEI/GO)_5$, (b) $(PEI/MMT)_{50}$, (c) $(PEI/PAA/PEI/MMT)_{10}$ and (d) $(PEI/PAA)_{20}$.

2.3.2 Reduced Modulus and Hardness

The area function was determined using multiple indentations, from 50 to 700 μN, on the fused quartz standard. It was calibrated for a range of contact depths between 17 and 162 nm. Multiple indentations, with constant step loads of 40 μN, starting from 40 μN and going up to 200 μN, were employed and the depth of penetration was kept below 20% of the total film thickness to avoid substrate effects.[43] Figure 2.6(a-b) shows representative load-displacement curves using a single load function, with a maximum load of 70 μN for multilayer thin films. Figure 2.6(c-f) depicts the variation of reduced elastic modulus and hardness with contact depth. $(PEI/PAA/PEI/MMT)_{10}$ exhibited less variability as a function of coating thickness relative to the $(PEI/PAA)_8$ coating because the latter film is five times rougher. When the film's roughness is more than 5% of the indentation depth, surface roughness introduces uncertainties in the measurements.[38,39]

$(PEI/PAA/PEI/GO)_{30}$ and $(PEI/MMT)_{50}$ have maximum indentation depth half of $(PEI/PAA/PEI/MMT)_{10}$ and $(PEI/PAA)_8$ under same applied load. This indicates that these two multilayer films are harder to penetrate under this indentation load range. Residual indentation profiles were scanned for multilayer thin films using same tip and there was no pile up taking place for this indentation load range. Table 2.2 summarizes the reduced modulus and hardness properties for all four multilayer thin films tested. $(PEI/PAA/PEI/GO)_{30}$ and $(PEI/MMT)_{50}$ have the highest reduced modulus (E_r = 38 GPa) and hardness values (H =1.4-1.65 GPa), while $(PEI/PAA/PEI/MMT)_{10}$ and $(PEI/PAA)_8$ are about half of these values. One possible explanation for the lower values E_r and H for MMT-based quadlayers is due to a decrease in clay concentration.[3]

$(PEI_{10}/PAA_4)_8$ has high E_r and *H as an* all-polymer multilayer thin film, which suggests glassy behavior at room temperature. Its mechanical properties are comparable to some reported polymer-only barrier LbL films such as $(PAH_{3.5}/PAA_{3.5})_{20}$ (E_r=17.0±4.0 & H=0.80±0.10)[54]. PEI_{10}/PAA_4 has a greater film growth rate (8 bilayers resulted in a film of 450 nm while 20 bilayers of PAH/PAA yielded a film of 100 nm). This is due to the effective crosslink density and polymer interdiffusion because of the low charge of both PEI and PAA in PEI_{10}/PAA_4, while PAH is fully charged in $PAH_{3.5}/PAA_{3.5}$ system.[46,54] As a result, a scrambled salt structure with low mobility and reduced free volume is formed for PEI_{10}/PAA_4, so it exhibits more resistance to axial deformation than $PAH_{3.5}/PAA_{3.5.}$ Table 2.2 shows gas permeability values for three of the four multilayer thin films. Clay-based films show superior gas permeability due to the extremely tortuous path for oxygen. All of these films have very low permeability relative to SiO_x.[31] The advantage of graphene-based film is its capability to maintain a strong gas barrier in humid condition once graphene is reduced (graphene reduction makes the film more hydrophobic).[68] Also, recent finding showed enhanced mechanical properties with graphene reduction[69].

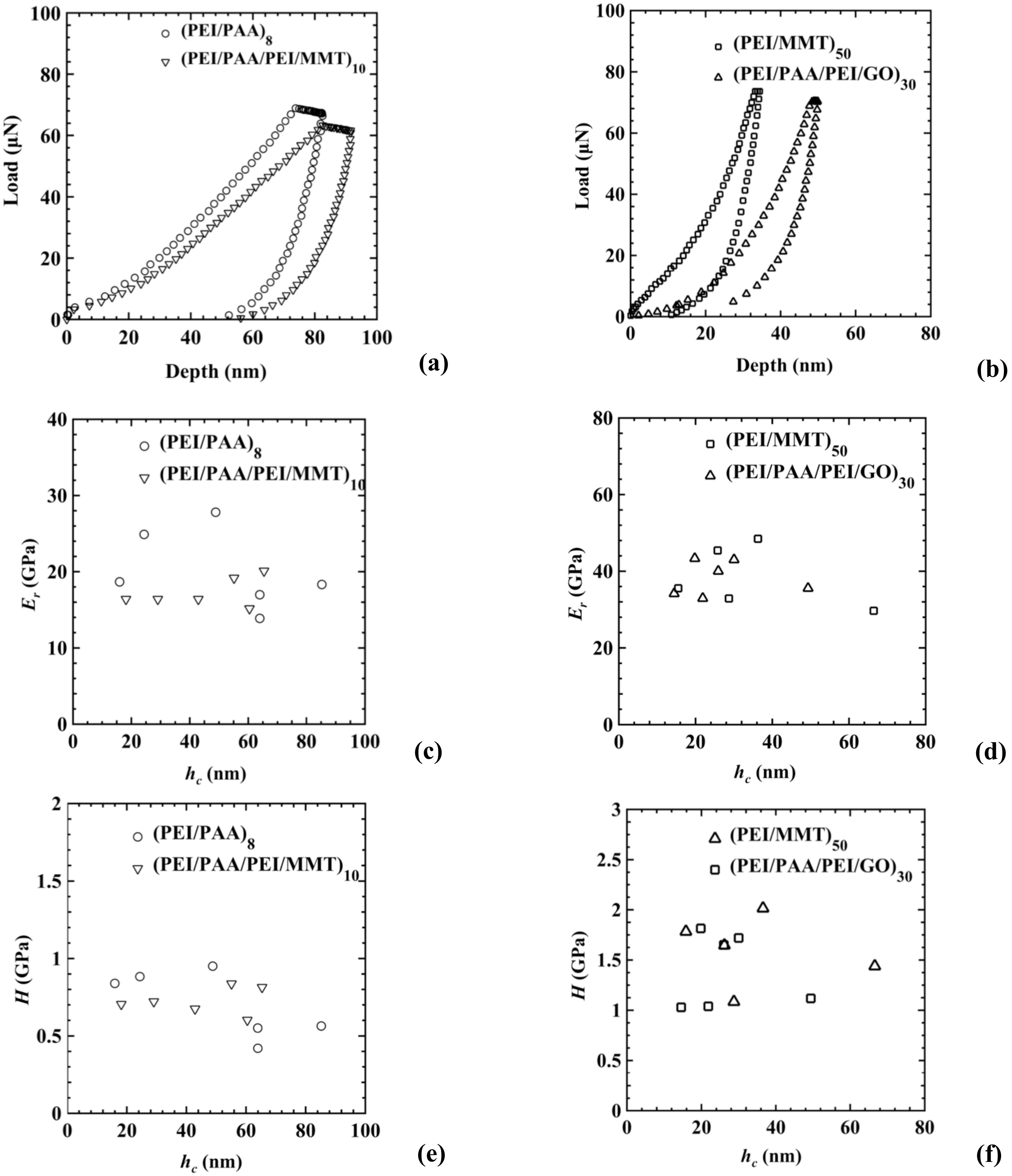

Figure 2.6 Representative load–displacement curves for a single-loading of 70 μN on (a) (PEI/PAA/PEI/MMT)$_{10}$ and (PEI/PAA)$_8$ and (b) (PEI/MMT)$_{50}$ and (PEI/PAA/PEI/GO)$_{30}$. Extracted reduced elastic modulus and hardness as a function of contact depth using multiple indentations with increasing loads from 40 to 200 μN for (c) (e) (PEI/PAA/PEI/MMT)$_{10}$ and (PEI/PAA)$_8$ films and (d) (f) (PEI/MMT)$_{50}$ and (PEI/PAA/PEI/GO)$_{30}$ respectively.

Table 2.2. Nanomechanical properties and gas permeability of multilayer thin films.

Coating	**Reduced modulus**, E_r **(GPa)**	**Hardness,** H **(GPa)**	***COF*** **at 100 µN scratch load test**	**Maximum scratch depth (nm) [% ER at 100 µN scratch load]**	**Film's Permeability (x10^{-16} cm^3 cm/(cm^2 s Pa))**
$(PEI/PAA/PEI/GO)_{30}$	38±5.0	1.4±0.35	0.18±0.019	47 [83%]	*
$(PEI/PAA/PEI/MMT)_{10}$	17±3.0	0.74±0.10	0.12±0.015	11 [90%]	<0.000009[3]
$(PEI/MMT)_{50}$	38±4.0	1.65±0.30	0.11±0.008	9 [98%]	<0.0000044[37]
$(PEI/PAA)_8$	20±3.5	0.75±0.20	0.31±0.019	123 [78%]	<0.000048[46]

* Just five quadlayers of chitosan/PAA/chitosan/GO have an oxygen permeability of ~ 10^{-19} cm^{3}cm/(cm^2 s Pa),[70] so $(PEI/PAA/PEI/GO)_{30}$ is reasonably expected to have similar or lower permeability than $(PEI/PAA/PEI/MMT)_{10}$.

2.3.3 Nanoscratch

Scratch experiments were used to study the frictional behavior, elastic recovery and wear resistance of the multilayer thin films using constant normal loads of 50, 100, 200 and 400 µN and a constant sliding velocity of 0.33 µm/s. Once each scratch experiment was performed, scratch depths were rescanned using the same tip to measure the residual scratch depth. Table 2.2 summarizes the *COF* values and % elastic recovery for each film studied. The low *COF* and high recovery for $(PEI/MMT)_{50}$ are superior to low-friction polymeric coatings. For example, epoxy/carbon nanostructures have *COF* of about 0.15.[71] Also, $(PEI/MMT)_{50}$ shows better mechanical behavior than carbon fiber-reinforced polyetheretherketone (PEEK), used for medical applications (E_r = 3.5 GPa, H = 0.12 GPa, and *COF* increases up to 0.3 once scratched with 100 µN scratch force).[72] Nanoscratch experiments were also carried out for hafnium borocarbide,

(HfB_xC_y) using the same testing setup, scratch forces and diamond tip used here. $(PEI/PAA/PEI/MMT)_{10}$ and $(PEI/MMT)_{50}$ showed similar low friction behavior to this ultra-hard ceramic coating (E_r = 140 GPa, H = 12.5 GPa, COF = 0.10-0.11, at 15 at.% carbon content).[73]

The % elastic recovery of films was measured after each scratch test. Figure 2.7 shows the initial and residual scratch depth values. For the 50 to 400 μN load regime, films $(PEI/MMT)_{50}$ and $(PEI/PAA/PEI/MMT)_{10}$ have the lowest in-situ depth of penetration. For $(PEI/MMT)_{50}$, it is less than 25 nm or 7% of the film thickness, with the % elastic recovery being 93-97% (accompanied by highly stable recovery). $(PEI/PAA/PEI/MMT)_{10}$ has slightly lower scratch depths and recovery (90-93%) compared to $(PEI/MMT)_{50}$. $(PEI/PAA/PEI/GO)_{30}$ depth of penetration is 35-70 nm, or 18-35% of film thickness (recovery being 80-83%). $(PEI/PAA)_8$ shows scratch depth higher than 100 nm for all scratch forces while maintaining high recovery (68-84%). This is due to the film containing only polymers. All multilayer thin films, except $(PEI/PAA)_8$, maintained stable recovery for low load scratch. Overall, the $(PEI/MMT)_{50}$ exhibited exceptional performance. This coating is known to have a nanobrick wall structure.[37] It shows high wear resistance and a high elastic recovery, low COF and high hardness and reduced elastic modulus, while maintaining a smoother surface than $(PEI/PAA/PEI/GO)_{30}$.

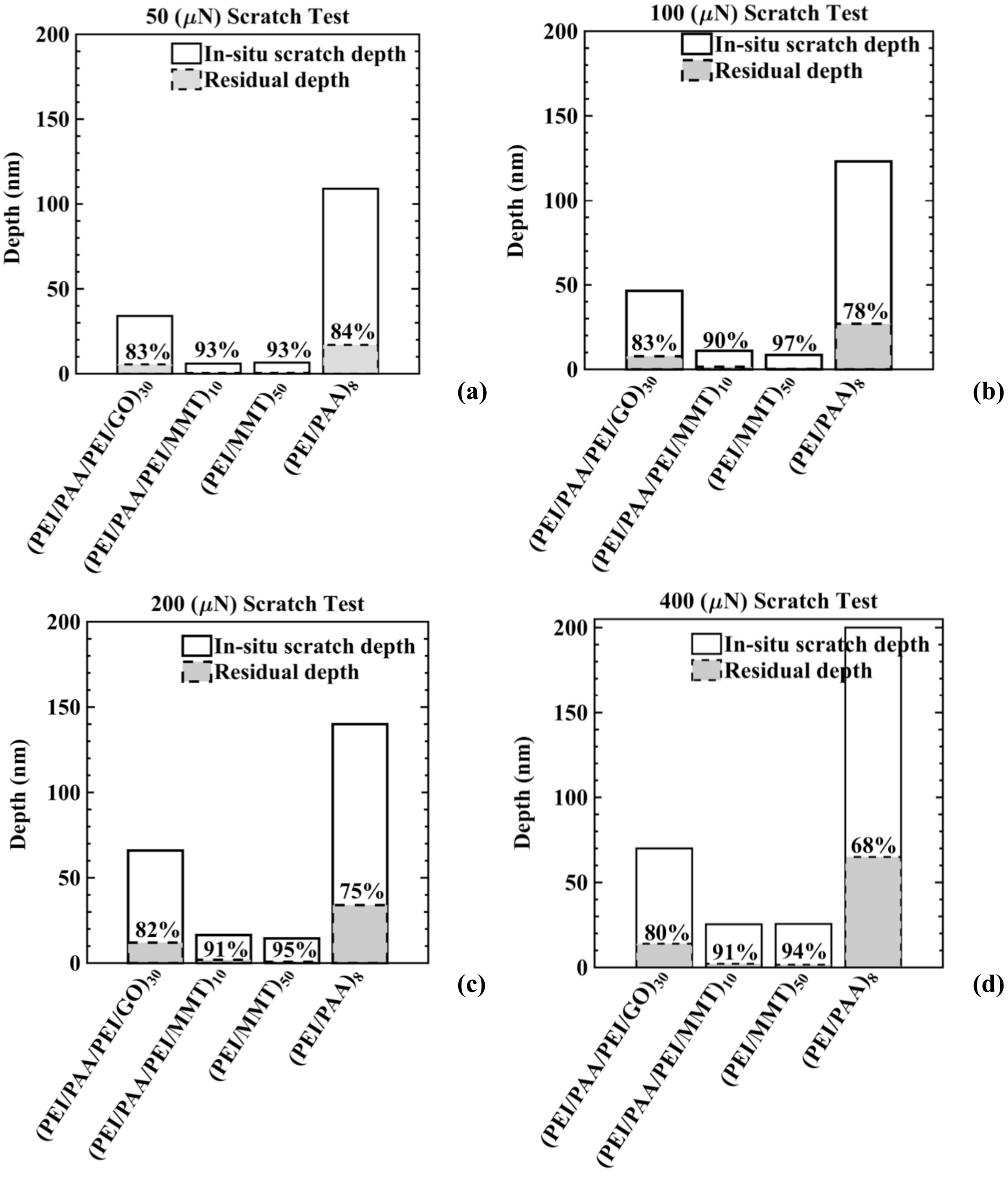

Figure 2.7 In-situ scratch depth and residual depth (plastic deformation) for different normal loads: (a) 50 μN, (b) 100 μN, (c) 200 μN and (d) 400 μN.

The elastic modulus and hardness of $(PEI/PAA)_{10}$ (23.4 ± 5.7 GPa and 0.7 ± 0.3 GPa, respectively) reported previously agrees well with the measured values in this work.[74] $(PEI/PAA)_8$ was found to have a relatively lower elastic modulus, but the results agree in general. Priolo et al. found that $(PEI/MMT)_{40}$ had a lower reduced elastic modulus and hardness of about 15 and 0.8 GPa, respectively than $(PEI/MMT)_{50}$.[37] Table 2.3 compares the properties of $(PEI/MMT)_{50}$ to PET film with and without a 50 nm coating of SiO_x. $(PEI/MMT)_{50}$ shows superior mechanical properties to uncoated PET (12 μm thick) and slightly lower *COF* and surface roughness. In addition to outstanding mechanical properties, these nanobrick wall films were found to have an oxygen transmission rate 67 times lower than PET.[37]

Table 2.3. Mechanical properties of gas barrier materials.

Coating	Thickness (nm)	RMS roughness (nm)	Reduced modulus, E_r (GPa)	Hardness, H (GPa)	*COF*
$(PEI/MMT)_{50}$	400	3.63	38.0±4.0	1.65±0.30	0.11
Uncoated PET[75,76]	12,000	4	3.0±0.5	0.30±0.10	0.30
SiO_x/PET[75,77]	12,050	0.6	5.7-6.7	0.39-0.47	0.25

2.3.4 High load Indentation and Scratch

High load indentation experiments were performed at 1500 μN with the same Berkovich tip used to obtain reduced modulus and hardness. The residual indentation marks were measured using the same tip and are shown in Figure 2.8, with data summarized in Figure 2.9. $(PEI/PAA/PEI/GO)_{30}$ and $(PEI/PAA)_8$ show high residual indentation depths (100 – 145 nm). Both films also exhibit pile-ups around the indentation, which is typical for polymeric coatings such as poly(methyl methacrylate)[78] and polytetrafluoroethylene/pyrrolidone[38] coatings. Under high load indentation, the plastic deformation becomes irreversible, where some polyelectrolyte multilayers become decoiled. This can result in an increase in the polarity of polyelectrolytes.[79] (PEI/PAA/PEI/MMT)$_{10}$ and (PEI/MMT)$_{50}$ exhibit shallower residual indentation depths at this load (about 30 nm deep) and show no pile-up behavior. The observed sink-in behavior is similar to materials that exhibit hard brittle behavior.[43]

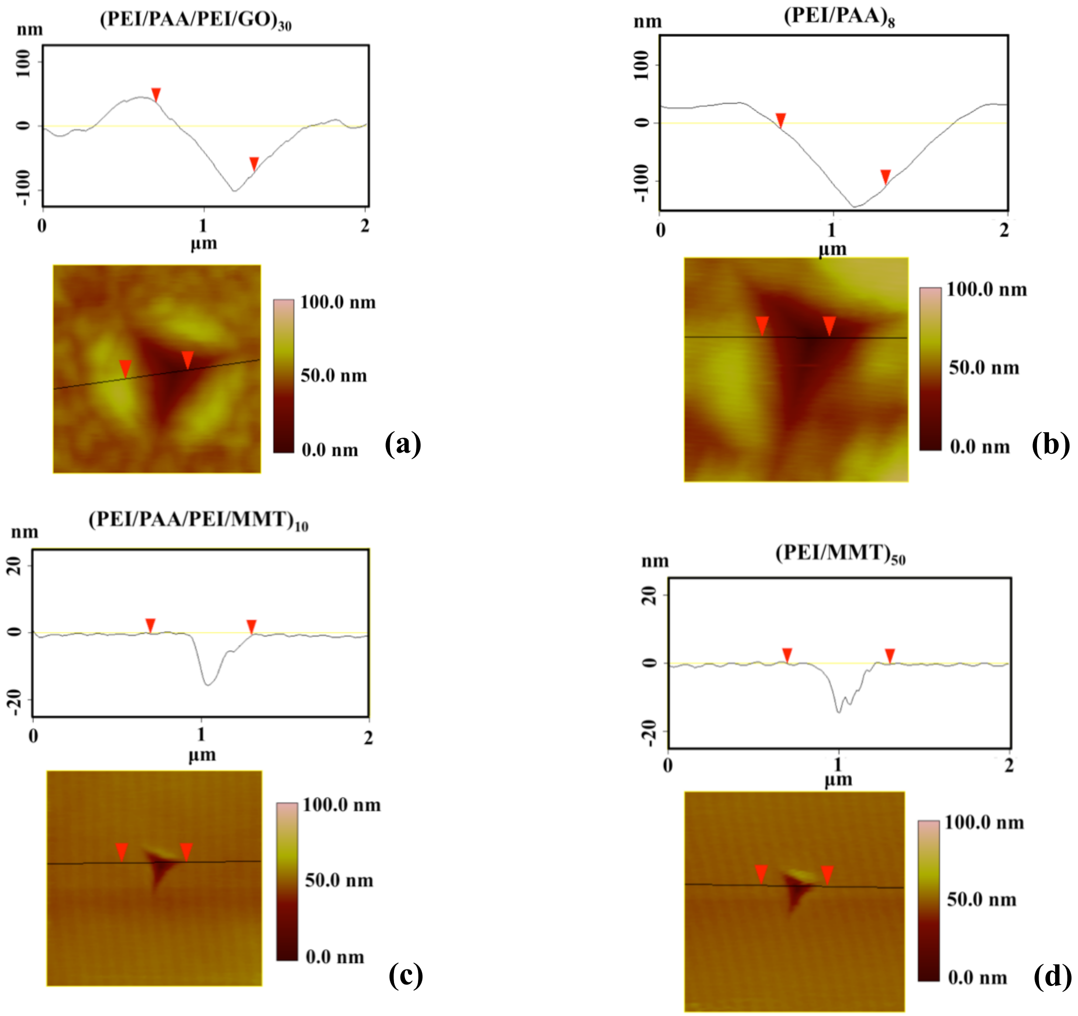

Figure 2.8 Residual indentation profiles (2x2 µm) after 1500 µN indentation: (a) (PEI/PAA/PEI/GO)$_{30}$ (b) (PEI/PAA)$_{8}$ (c) (PEI/PAA/PEI/MMT)$_{10}$ and (d) (PEI/MMT)$_{50}$.

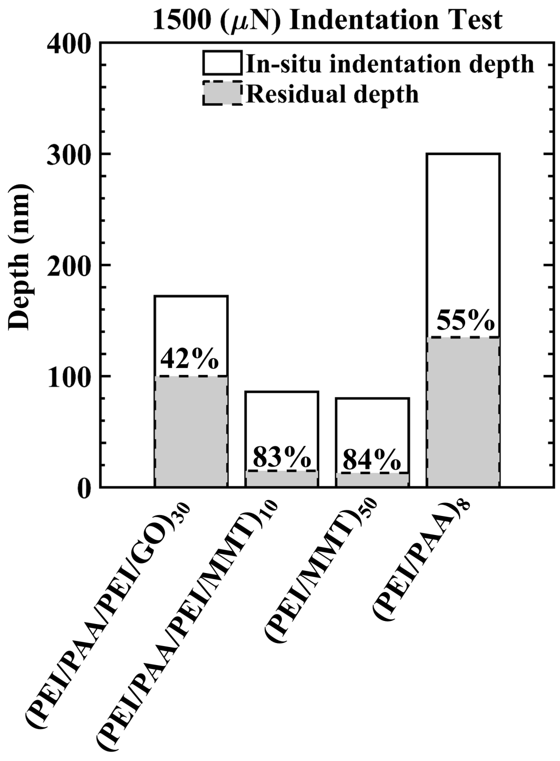

Figure 2.9 Residual indentation depths for multilayer thin films indented with a 1500 μN normal load.

High load scratch experiments were performed at 1, 2 and 3 mN using the same conospherical tip. The residual scratches were scanned for the penetration depth and the pattern of the scratch groove, as shown in Figures 2.10 and 2.11 for $(PEI/PAA/PEI/MMT)_{10}$ and $(PEI/PAA)_8$, respectively. Both $(PEI/PAA/PEI/GO)_{30}$ and $(PEI/PAA)_8$ exhibited pile up behavior followed by visible deformation around the scratch mark, which made it impossible to scratch the same location twice. In addition, these films have high residual scratch depths, as shown in Figure 2.12. Elastic recovery decreases for these coatings as scratch load increases. Film penetration clearly took place for $(PEI/PAA/PEI/GO)_{30}$ and $(PEI/PAA)_8$ films as the residual scratch depth exceeded the film thickness at 1mN and at 2mN, respectively. Among all the multilayer thin films, $(PEI/PAA/PEI/MMT)_{10}$ and $(PEI/MMT)_{50}$ are exceptional, maintaining remarkable wear resistance and elastic recovery with increasing scratch load. Their residual scratch depths were below 30 nm, with no significant pile-ups. They did not show any distortion of the surrounding area, so it was possible to do multiple scratches at the same location. Even though, non-clay based multilayer thin films such as $(PEI/PAA/PEI/GO)_{30}$ and $(PEI/PAA)_8$ have similar E_r and H to $(PEI/MMT)_{50}$ and $(PEI/PAA/PEI/MMT)_{10}$, respectively, their deformation behavior against an applied lateral load were very different. The superior scratch-resistant behavior of MMT-based LbL films is due to few factors: (1) MMT platelets act like a reinforcement in the polymeric matrix (E = 175 GPa),[80] (2) polyelectrolytes and MMT form strong hydrogen bonds,[81] (3) a highly aligned laminate structure, which acts as a stress damping preventing stress from reaching deeper layers of polymers,[82] and (4) clay-based films have smoother surface roughness compared to other multilayer thin films.

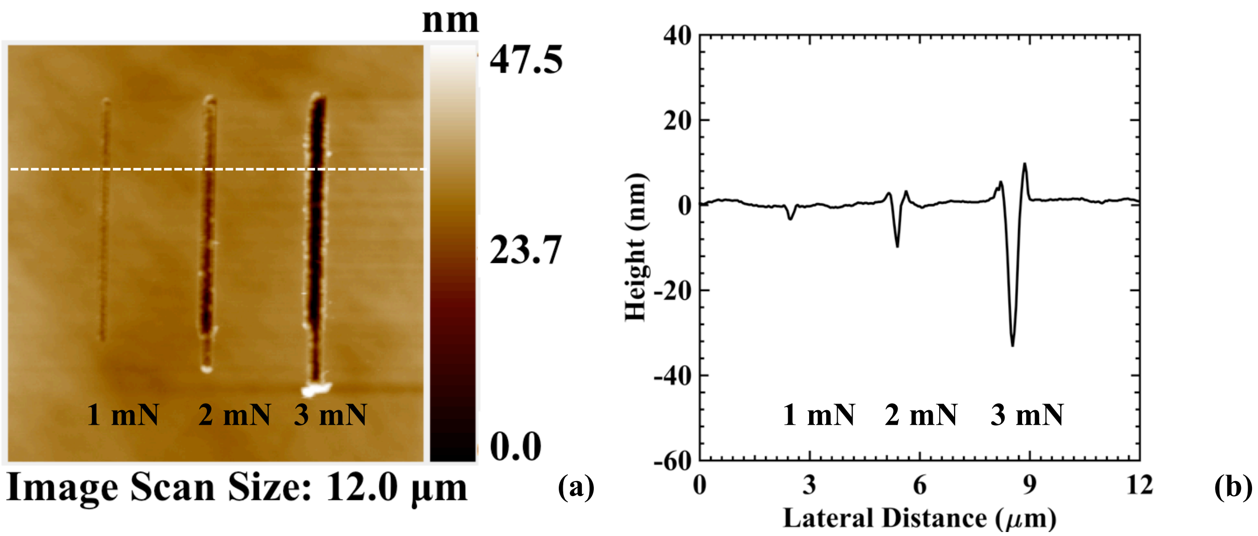

Figure 2.10 (a) Residual scratch images for $(PEI/PAA/PEI/MMT)_{10}$ and (b) residual scratch profiles with 1, 2 and 3 mN forces.

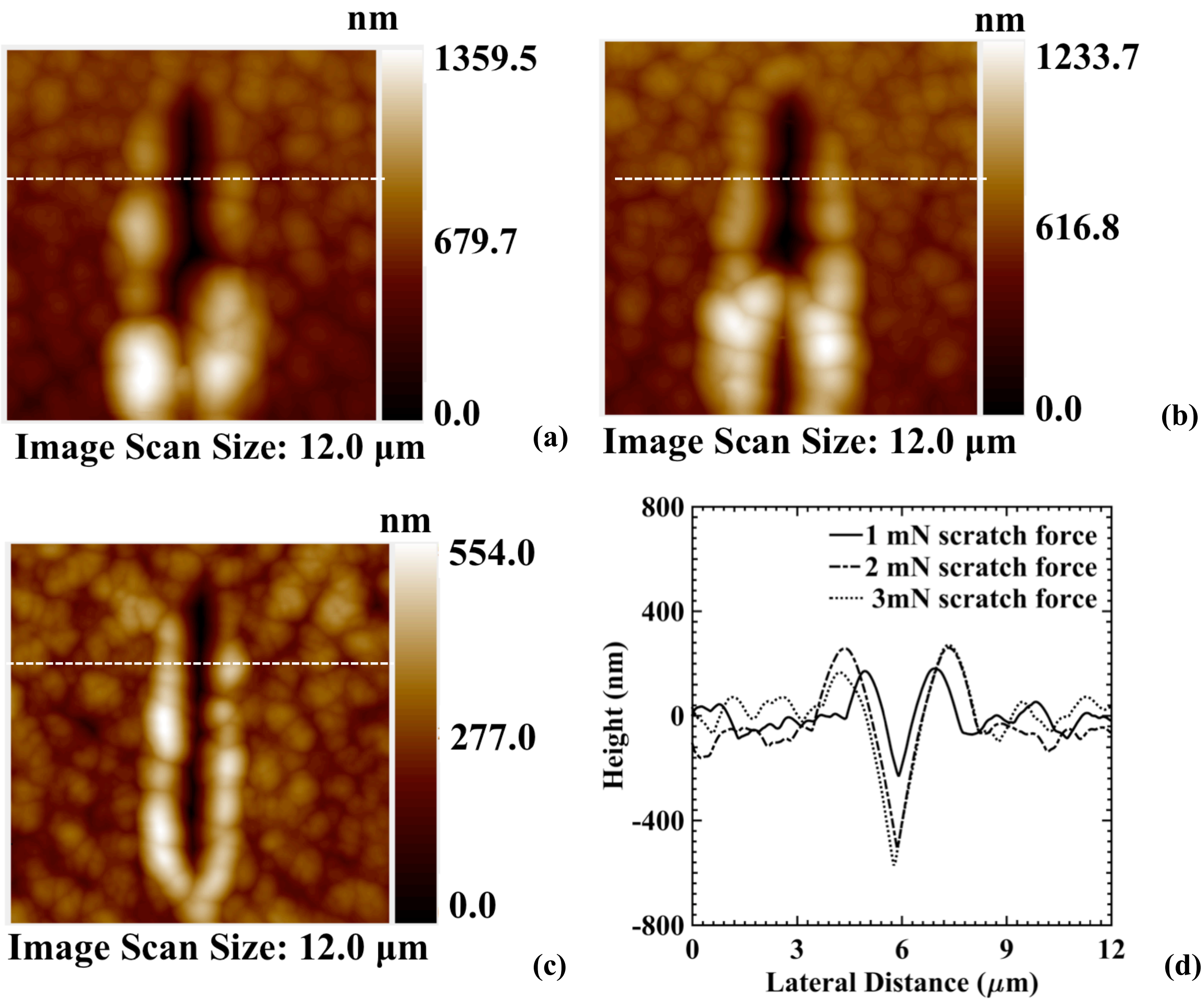

Figure 2.11 Residual scratch images for $(PEI/PAA)_8$ with (a) 1, (b) 2 and (c) 3 mN force and (d) residual scratch profiles with 1, 2 and 3 mN forces.

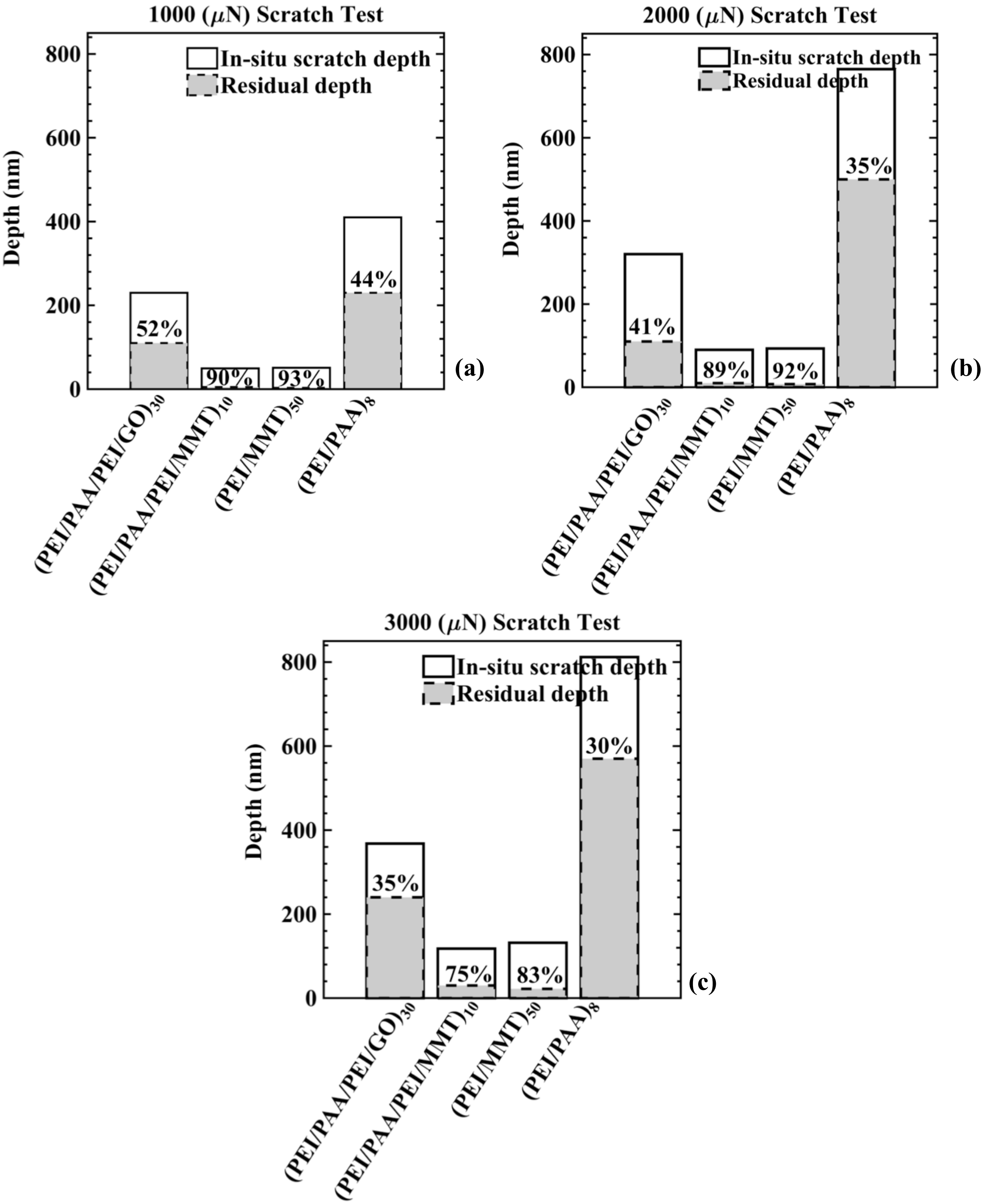

Figure 2.12 In-situ scratch depth and residual scratch depths of multilayer thin films scratched with high loads, (a) 1, (b) 2 and (c) 3 mN.

To evaluate the failure and possible delamination of the films using the scratch technique, *COF* and % elastic recovery are plotted as a function of scratch force in Figure 2.13. Additional scratch tests with various forces were carried out to obtain more information. With increasing load, the *COF* increases for (PEI/PAA/PEI/GO)$_{30}$ and (PEI/PAA)$_{10}$ by more than 100% and elastic recovery decreases by half. For (PEI/MMT)$_{50}$ and (PEI/PAA/PEI/MMT)$_{10,}$ *COF* increases by less than 0.1 and % elastic recovery remains almost constant for most applied loads. Critical transitions happen for the (PEI/PAA/PEI/GO)$_{30}$ and (PEI/PAA)$_{10}$ at about 750 µN, with a significant drop in the recovery accompanied by an increase in the *COF*. At this load, the scratch depth reaches the film thickness of (PEI/PAA/PEI/GO)$_{30}$ (scratch depth = 207 nm) and the tip starts to scratch the silicon substrate. The scratch depth exceeds 72% of film thickness of (PEI/PAA)$_{10}$ (scratch depth = 325 nm). (PEI/MMT)$_{50}$ and (PEI/PAA/PEI/MMT)$_{10}$ have a transition at a higher load of 2500 µN with a smaller drop in elastic recovery. To confirm exact transitions, a ramp load type scratch test is required to find the critical force where the transition takes place.

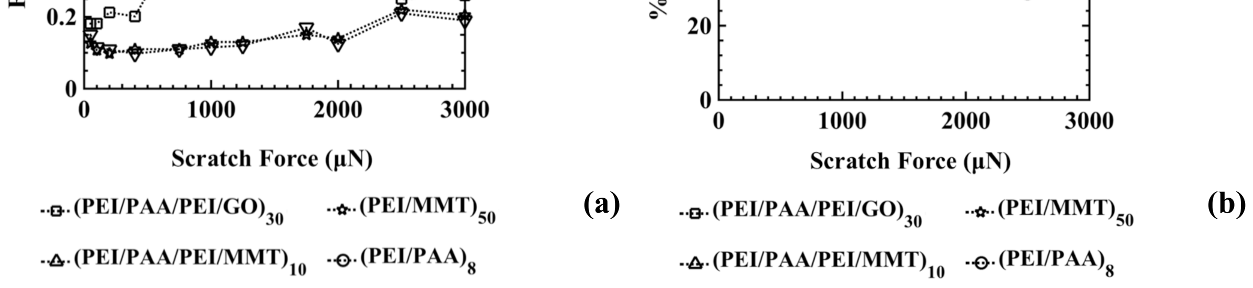

Figure 2.13 (a) Friction coefficient and (b) % elastic recovery as a function of scratch normal force for multilayer thin films.

2.4 Summary of Chapter 2

Multilayer coatings were manufactured using LbL assembly for various packaging applications. In addition to being moderately stretchable gas barriers, these coatings exhibited mechanical properties superior to PET and other low-friction polymeric coatings. Nanoindentation and scratch experiments were carried out to obtain the mechanical behavior of these coatings and their wear characteristics. Clay-based assemblies, $(PEI/MMT)_{50}$ and $(PEI/PAA/PEI/MMT)_{10}$, exhibit superior scratch resistance compared to other multilayer thin films. In particular, $(PEI/MMT)_{50}$ shows the best performance. It has a smooth surface with low rms roughness (3.63 nm) and friction coefficient (0.11). Its reduced elastic modulus (38 GPa) and hardness (1.65 GPa) are comparatively high amongst polymeric coatings. It also showed very low depth of penetration during scratch and had an outstanding elastic recovery of > 93% for low load scratch and above 84% for high scratch load. At high load indentation/scratch this film exhibited shallow indentation/scratch depths with almost no distortion in the surrounding area. This excellent mechanical behavior makes such a thin film a favorable candidate for hard coating applications. Next chapter investigates the influence of graphene reduction and polymer crosslinking in the mechanical behavior of these multilayer thin films.

3 THE INFLUENCE OF GRAPHENE REDUCTION AND POLYMER CROSSLINKING ON IMPROVING THE INTERFACIAL PROPERTIES OF MULTILAYER POLYMERS THIN FILMS[*]

3.1 Introduction

Graphene, a one-atom thick 2D dimensional material, has unique electrical,[83] mechanical,[84] thermal,[85] optical,[86] chemical[87] and biocompatibility characteristics.[88] Conventionally, graphene is produced using chemical vapor deposition (CVD),[89] however this technique is costly and difficult to scale up for commercial applications.[90] In addition, it introduces structural defects and contamination into graphene sheets, and a lack of uniformity over large surface areas. This leads to a major issue for many applications, which requires high quality continuous defect-free graphene sheets such as gas barriers,[91] water membranes,[92] optoelectronic devices,[93] biosensors,[94] corrosion inhibitors,[95] energy devices,[96] and nanocomposites.[97]

Hybrid graphene-based multilayer thin films consisting of graphene and polymer shows improved unique properties due to the incorporation of materials with diverse functionalities, which is promising for the aforementioned applications. There are many techniques for fabricating thin multilayer films, such as: solvent casting,[98] painting,[99] spray processing,[100] printing,[101] spin coating,[102] floating technique,[103] pulsed laser deposition technique,[104] and layer-by-layer (LbL) assembly.[31] Compared to other techniques, the synthesis of graphene-based nanocomposites using LbL technique is advantageous because it is simpler, reproducible due to the highly ordered

---

[*] Reprinted with permissions from "Influence of Graphene Reduction and Polymer Cross-Linking on Improving the Interfacial Properties of Multilayer Thin Films" by Humood, M.; Qin, S.; Song, Y.; Polychronopoulou, K.; Zhang, Y.; Grunlan, J. C.; Polycarpou, A. A. ACS Appl. Mater. Interfaces 2017, 9, 1107–1118.

structure, and scalable through linear or exponential thickness growth.[67,105]

It is possible to use LbL method to deposit graphene oxide (GO) because of its solubility in water. Its molecules can easily intercalate through the graphene layers due to the interlayer distance of less than 1 nm.[106] Therefore, GO is easily dispersed using aqueous processing (contains carboxylic acid groups which introduce negative charges once exfoliated in water).[47] The graphene is held within the LbL assembly by electrostatic interactions, hydrogen bonding and van der Waals interactions. Usually electrostatic interaction is the driving force for stacking graphene/polymer multilayer structures. In addition, on the interface of graphene/polymer, the functional groups and the π-π stacking are held by hydrogen bonding and van der Waals respectively.[107]

Although graphene shows several unique properties, there is a major challenge for effective graphene reinforcement in nanocomposites: the weak interface bonding for graphene with different substrates such as metals and polymers. This is due to the weak Van der Waals forces, which govern the adhesion of graphene.[108] This is overcome by adding a layer of a polymer to adhere to substrate instead.[109] Therefore, this drawback results in limitations in performance and applications for these nanocomposites.[110] In a recent study, we showed a comparison of different polymer nanocomposites such as montmorillonite (MMT) clay and graphene (GO) based multilayer thin films. Polyethylenimine (PEI)/ Poly(acrylic acid) (PAA)/PEI/GO system showed twice-stronger mechanical properties of reduced elastic modulus (E_r) and hardness (H) than PEI/PAA/PEI/MMT. This shows effective load transfer in the normal direction due to strong π–π stacking, electrostatic interaction and hydrogen bonding. However, the load transfer through lateral direction using scratch tests was less appealing for graphene-based multilayer films. It showed higher coefficient of friction, highly visible and wider scratches, lower elastic recovery and deeper scratch depths.[111]

Scratch resistance of these nanocomposites is critical for many applications.[112] For example, optoelectronic devices such as flat panel displays and touch screens are operated by means of mechanical friction. Others are subjected to mechanical erosion and scratch as part of their normal operation such as solar cells and membranes.[113,114] The stable operation of coatings requires strong adhesion to substrate in order to sustain long-term durability against repeated sliding process.

To improve the scratch resistance of graphene based nanocomposites, two steps are suggested here. First, thermal reduction (at a temperature less than 200 °C) changes GO from an electric insulator to being electrically conductive due to the partial restoration of hybridized sp^2 carbon bonds. Once graphene oxide is reduced, it turns from transparent to opaque film.[68] Thermal reduction was found to improve the interfacial bonding, thermal conductivity, mechanical properties, and restore some of the properties of graphene sheets.[115]

Next, polymer covalent crosslinking of multilayer thin films improves the thermal stability,[116] mechanical properties[117] and chemical resistance.[69] The influence of crosslinking depends on the density of crosslinks.[118] In the case of poly(vinyl alcohol) (PVA), increasing the crosslinking density shows 20% increase in properties such as storage modulus, glass transition temperature and hardness, because of increases in the chain rigidity, which results in restriction of chain mobility.[116]

Although the electrical,[119] mechanical,[120] and chemical properties[121] of polymer/GO thin films are actively pursued, there is lack of fundamental knowledge on the effects of GO reduction and polymer crosslinking on the mechanical/scratch/wear behavior of these films.[122,123] In order to improve the surface reliability of GO-based LbL films, the mechanical properties and scratch resistance are of significant importance. Nanoindentation and nanoscratch experiments are an effective way to measure these properties.[38,40,124] The hardness and elastic modulus can be obtained through Oliver-Pharr method.[64] In addition, scratch testing is typically used to measure the friction coefficient and gain insight on the interfacial shearing required for both single layer and multilayered coating removal.[125–127]

In the present study, polyvinylamine/graphene oxide (PVAm/GO) multilayer thin films, deposited on silicon (Si) substrates, are evaluated and characterized using different techniques. To understand how graphene reduction and polymer crosslinking improve the mechanical behavior and interfacial bonding, nanoindentation and scratch experiments are employed using original (PVAm/GO), reduced (PVAm/rGO), and reduced and crosslinked (xPVAm/rGO) films.

3.2 Experimental Section

3.2.1 Materials

Polyvinylamine (PVAm) (95% hydrolyzed, M = 340 kDa, trade name Lupamin 9095, BASF, Ludwigshafen, Germany) was dialyzed three times for 24 hours in 18.2 MΩ DI water using cellulose dialysis tubing (M_{cutoff} = 14 kDa, Sigma Aldrich, St. Louis, MO), and then diluted to 0.1 wt% and adjusted to the desired pH using 1 M NaOH or HCl (Sigma). Graphene oxide (Graphenea, Cambridge, MA) was diluted to a 0.1 wt% suspension in DI water and dispersed with 10 minutes of 15 W tip sonication.

3.2.2 Substrates

(1 0 0) silicon wafers were cleaned using successive rinsing of acetone, methanol, and DI water and a 10 minute air plasma cleaning treatment (Harrick Plasma, Ithaca, NY). For transmission electron microscope (TEM) characterization, polyethylene terephthalate (PET) films (179 µm, ST505, Dupont-Teijin, Chester, VA) were cleaned by rinsing multiple times with DI water, methanol, and air, followed by corona treatment (BD-20C Corona Treater, Electro-Technic

Products Inc., Chicago, IL) for improved film adhesion.

3.2.3 Processing

The nanofilms were deposited via LbL assembly, alternately exposing the substrate to the PVAm and GO solutions and rinsing thoroughly with DI water and drying with filtered air between depositions. The first dips into the solutions were 5 min, while subsequent depositions were 1 min. Thermal reduction of the multilayer thin films was performed in air at 175˚C for 90 min following deposition. The heat treatment takes place below the melting temperature of PVAm. PVAm moiety starts to decompose between 300-450 °C.[128] Crosslinking of the multilayer thin films was performed after reduction by soaking in 1 vol% aqueous glutaraldehyde (Sigma) for 60 min, followed by soaking in 0.1 M sodium borohydride (Sigma) in ethanol for 60 min. After crosslinking, these films were rinsed thoroughly with ethanol and DI water, and finally dried at 70˚C for 5 min. The thicknesses of the films were measured on (1 0 0) silicon wafers with a P-6 profilometer (KLA-Tencor, Milpitas, CA). Notation of these films is as follows: PVAm/GO for the original film, PVAm/rGO for the film following GO reduction and xPVAm/rGO for the film following GO reduction and crosslinking.

3.2.4 Nanoindentation

Nanoindentation experiments were performed using a Triboscope (TS) 75 instrument (Hysitron Inc., Minneapolis, MN). A sharp 90° diamond cube corner probe was used to obtain measurements in a wide range of contact depths (5-40 nm). The mechanical properties of PVAm/GO films are found based on the contact area (A_c), which is related to contact depth (h_c) through the tip area function (see Equation 1).[64] A fused quartz standard sample with known properties is used for calibration. The area function of each tip can be expressed as follows:

$$\text{Area function } (A_c) = C_o h_c^2 + C_1 h_c + C_2 h_c^{1/2} + C_3 h_c^{1/4} + C_4 h_c^{1/8} + C_5 h_c^{1/16} \qquad (1)$$

where C_1-C_5 are curve-fit coefficients, which are related to tip imperfections, and C_o equals to 2.598 for a cube corner (90°) probe, and h_c is the contact depth. To define a precise area function for this study, the indentation depth range on fused quartz has to match the depth of less than 20% of the total thickness of the samples with unknown properties (PVAm/GO films). The coefficients C_1-C_5 are determined by conducting indentation experiments at variable penetration depths. To ensure the accuracy of the area function, the elastic modulus and the hardness of polycarbonate and silicon were measured with the determined area function and compared with known values. The detailed indentation is included in the supporting information (see Table 3.1 and Figure 3.2).

The reduced modulus and hardness of each PVAm/GO sample were then extracted using the Oliver-Pharr method[64]. Different indentations were applied with maximum indentation forces of 1 to 20 μN to maintain indentation depths less than 20% of the total film thickness to avoid substrate effects.[43] The load function includes a holding time of 2 seconds on the peak load to reduce the influence of viscoelasticity of the polymeric films.[40] Moreover, to characterize the hardness of the material within its plastic deformation region there should be no significant residual-indentation pile-up.[43]

3.2.5 Nanoscratch

The nanoscratch experiments are carried out using a commercial indenter (TriboIndenter (TI) Premier, Hysitron Inc., Minneapolis, MN) to study the frictional behavior of PVAm/GO multilayer thin films. Figure 3.1 shows the conospherical probe with a tip radius of 870 nm, which is used for the nanoscratch experiments. To study the different friction regimes (such as adhesive and plowing), scratch experiments were performed under various constant, and ramp normal loads of 25, 100 and 300 μN with a fixed sliding speed of 0.67 μm/s. Different sliding speeds were examined initially and friction coefficient was found to change slightly with different sliding speeds, which corroborates with findings in the literature.[65,129,130] These normal loads are chosen to keep the scratch depths within the film's thickness. The scratch length was kept to 6 μm. Before and after each scratch experiment, a height scan is performed using the same tip to measure the initial topography and the residual scratch depth. The coefficient of friction (COF) is recorded for each experiment by dividing the lateral load over the normal scratch load. To evaluate the films' delamination precisely, a high scratch ramp load of 1 mN was performed using the nanoscratch probe.

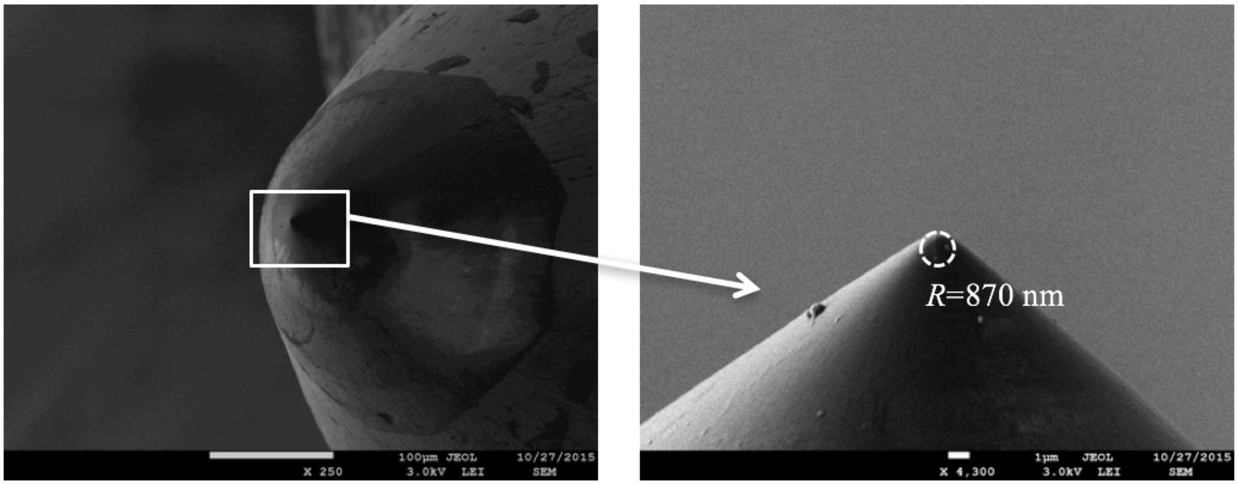

(a) **(b)**

Figure 3.1 Scanning Electron Microscopy (SEM) image for the nanoscratch conospherical probe with spherical tip of 870 nm radius, at (a) x250 and (b) x4,300.

3.2.6 Shear and Adhesive Strength Measurements

Shear (τ_c) and adhesive (σ_a) strengths, which are required to delaminate a thin film at the film-substrate interface are calculated using methods developed by Ashcroft and Derby, and Laugier respectively.[125,131]

$$\text{Shear Strength } (\tau_c) = \sqrt{\frac{H_s P_c}{\pi\left(r^2 - \frac{P_c}{\pi H_s}\right)}} \tag{2}$$

$$\text{Adhesive Strength } (\sigma_a) = \frac{2P_c}{\pi d_c^2}\left[(4 + \nu_s)\frac{3\pi\mu}{8} - (1 - 2\nu_s)\right] \tag{3}$$

Where τ_c is a function of the substrate hardness (H_s), the critical contact pressure/load, which is required for film delamination (P_c) and tip radius (r=870 nm), σ_a is a function of scratch groove width (d_c), coefficient of friction measured during the experiment (μ), P_c, and the substrate Poisson's ratio (ν_s). Si (1 0 0) has an anisotropic Poisson's ratio varying between 0.064 and 0.279. In this work Si is assumed to be isotropic and linearly thermoelastic ($\nu_s = 0.22$).[132,133]

3.2.7 Characterizations

Different imaging techniques such as scanning/transmission electron microscopy (SEM)/(TEM) and atomic force microscopy (AFM) were performed to evaluate the films' morphology, thickness and residual scratch deformation. Also, chemical analysis tools such as Raman spectroscopy/X-ray photoelectron spectroscopy (XPS) were used to better understand how the chemical structure, bonding and composition of these multilayer thin films change with graphene reduction and polymer crosslinking and their influence in the mechanical behavior of these films. Details of these techniques are provided below.

3.2.8 Nanoindentation Calibration

By performing multiple indentation experiments on a fused quartz standard sample with known properties, reduced elastic modulus (E_r) = 69.6 GPa (±5%), hardness (H) =9.3 GPa (±10%), the area function was determined with various coefficients as function of indentation depth. Multiple loads were applied to measure the reduced elastic modulus and hardness throughout the calibrated indentation range. Once the area function of cube corner tip is found, multiple indentations were carried out in both fused quartz and polycarbonate (PC) standard samples with known properties, E_r = 3.10 GPa (±10%), H =0.18 GPa (±10%), to verify the calibration (see Table 3.1).

Furthermore, the mechanical properties of the substrate were found using multiple indentation experiments and the results are summarized in Table 3.1. Results are consistent with the literature.[134] Figure 3.2 presents load–displacement curves for different indentation loads on the fused quartz and polycarbonate standard samples, and the silicon substrate. All indentation experiments were kept within the calibrated contact depth range on fused quartz.

Table 3.1. Elastic Modulus and Hardness for standard samples and silicon.

Substrate	**E_r (GPa)**	**H (GPa)**
Fused Quartz	70.10±1.32	9.42±0.28
Polycarbonate	3.24±0.26	0.23±0.01
Silicon Substrate (Si)	163.14±10.78	13.33±0.68

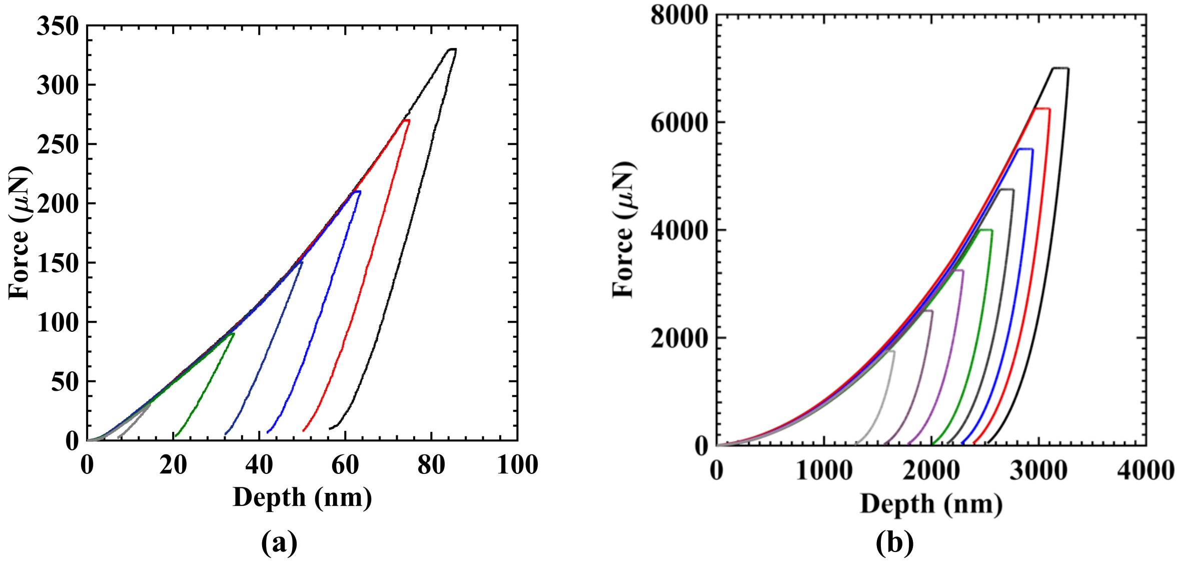

(a)

(b)

Figure 3.2 Representative load–displacement curves for (a) Fused Quartz standard sample (b) Polycarbonate standard sample (c) Silicon substrate.

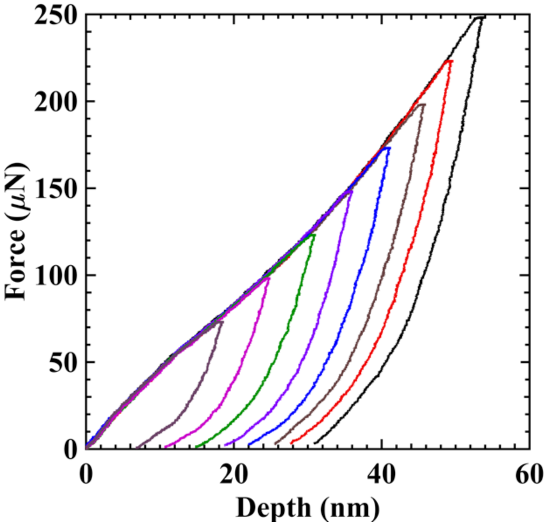

(c)

Figure 3.2 Continued.

3.2.9 Raman spectroscopy/X-ray photoelectron spectroscopy (XPS)

Raman experiments were performed using a Raman confocal microscope made by Horiba Ltd (Jobin-Yvon LabRam). The pinhole diameter is 200 nm and the objective lens is 100x, making the spatial resolution of the beam 3.7 μm. The laser wavelength is 633 nm and the exposition time is 15s with 5 accumulations for each test. X-ray photoelectron studies were performed using an Omicron ESCA system equipped with a monochromatic MgKα X-ray source (1253.6 eV) and operated at 300 W. Samples were analyzed under vacuum ($P < 10^{-8}$ Torr), whereas survey scans and high-resolution scans were collected using pass energies of 40 eV, respectively. Binding energies were referred to the C 1s binding energy at 284.6 eV. The samples' exposure to air was minimized to avoid any oxidation. A low-energy electron flood gun was employed for charge neutralization. Prior to XPS measurements, the films were mounted on stubs and put into the entry-load chamber to pump overnight.

3.2.10 Scanning/Transmission Electron Microscopy (SEM)/(TEM)

The deformation patterns of thin films under nano/microscratch testing were examined using SEM (operating voltage = 3 kV). In addition, SEM is used to evaluate parameters such as scratch width and critical events such as coating delamination and stick-slip motion. For TEM, the samples were prepared by embedding a small substrate of either polyethylene terephthalate or polystyrene in an Epofix resin (EMS, Hatfield, PA). The samples are left to cure overnight and then cross sections were cut using an Ultra 45° diamond knife (Diatome, Hatfield, PA). Samples were imaged on copper grids using a Tecnai G2 F20 (FEI, Hillsboro, OR), operated at 200 kV.

3.2.11 Atomic Force Microscopy (AFM)

The surface roughness is measured using Dimension Icon AFM (Bruker, Billerica, MA). AFM mode is set to tapping mode. AFM silicon tip (HQ:NSC35/AL BS) is obtained from (MikroMasch, Watsonville, CA), and it has a radius of 8 nm, resonance frequency of 150 kHz and force constant of 5.4 N/m. In order to obtain high quality images, the scanning rate was set to 0.5 Hz with 512 samples per line. The conospherical scratch tip is used for in-situ characterizations of residual scratch images.

3.3 Results & Discussion

3.3.1 Surface Roughness & Morphology

Table 3.2 lists the three PVAm/GO films under study, namely PVAm/GO, PVAm/rGO (reduced), and xPVAm/rGO (crosslinked). The film thickness was kept constant by varying the deposition layers for each film. Thermal reduction of GO reduces the film thickness by 35% due to both the removal of oxygen from GO surface and the reduction of GO nanoplatelet wrinkles.[68,69] Therefore, more layers were required for the films to be reduced to yield a similar film thickness as the initial film. On the other hand, crosslinking was found to slightly increases the film thickness due to the added volume of glutaraldehyde.[69] The heat treatment does not cause any thermal degradation of the polymer based upon TGA results of PVAm in literature.[54] Others attempted to understand how the graphene reduction alters the morphology or thickness of host polymers but did not detect any measurable changes with these polymers.[135,136]

Each cycle of graphene and PVAm yielded a thickness of 5 nm for the initial film, PVAm/GO, based on the linear relationship between the film thickness and the number of deposited bilayers. If graphene layer is expected to have a thickness of about 0.8-1 nm before reduction,[137] then PVAm layer is about 4 nm thick. Figure 3.3 shows AFM height and phase images for all films (average root-mean-square (*Rq*) roughness values are reported in Table 3.2 with standard deviation). Five areas of (1x1 μm) were scanned for each sample in different surface locations and Rq roughness was found to be consistent. The film becomes smoother with graphene reduction and polymer crosslinking as the phase images clearly show in Figures 3.3(d, f). The initial film (see Figures 3.3 (a, b) is wrinkled and rougher. The graphene reduction shrinks GO platelets making them thinner due to the partial removal of oxygen-containing groups.[115]

Table 3.2 List of PVAm/GO films on Si substrate.

Film[a]	**Layers**[b]	**Description**	**Thickness**[c] **(nm)**	**Average RMS Roughness**[d] **(nm)**
PVAm/GO	29	Polymer/graphene	144	5.75±0.56
PVAm/rGO	47	Polymer/reduced graphene	146	4.60±0.55
xPVAm/rGO	42	Crosslinked polymer/ reduced graphene	147	4.38±0.40

[a] all multilayer films are bilayer assembly [b] as defined by the film deposition process
[c] thickness was measured using TEM images [d] based on 1x1 μm AFM measurements

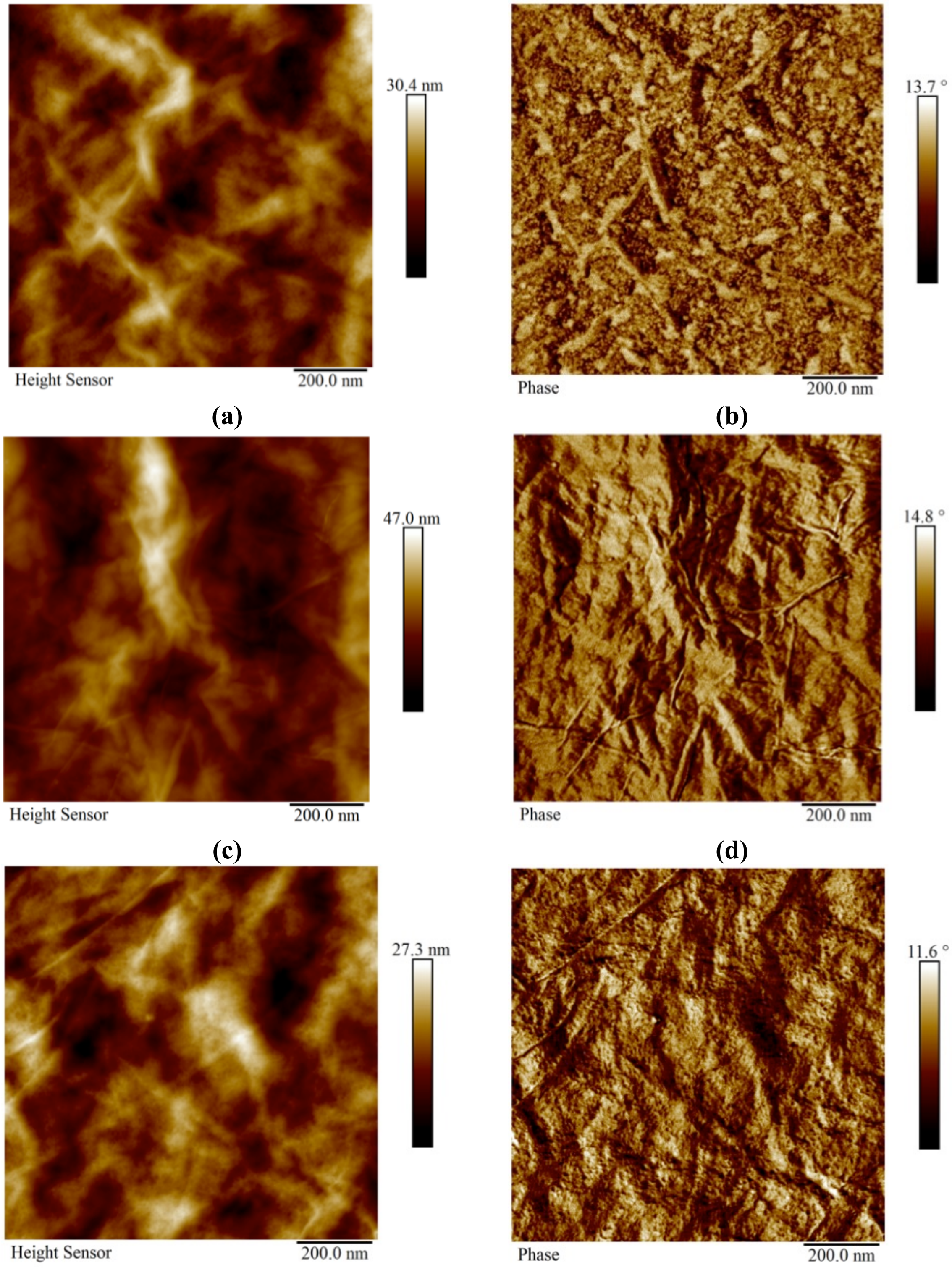

(a) **(b)**

(c) **(d)**

(e) **(f)**

Figure 3.3 Height and phase images (1×1µm) of multilayer thin films for (a-b) PVAm/GO, (c-d) PVAm/rGO and (e-f) xPVAm/rGO.

The TEM images in Figure 3.4 show the cross-sectional area of the films with a nominal thickness of 150 nm. In general, the multilayer thin films are highly ordered with nanoscale uniformity, which is an advantage of the LbL technique. It is hard to see the layering in the PVAm/GO due to the small contrast between different layers. Once reduced, the layers become clear as a result of removing some of the moisture and oxygen-containing groups.[115] Interestingly once the film is crosslinked, xPVAm/rGO shows less contrast between bilayers than PVAm/rGO. Crosslinking tends to oxidize the films again.

Contact angle (*CA*) measurements were performed using a water droplet. Figure 3.5 shows similar trend to TEM cross-section images. PVAm/GO film shows hydrophilic behavior (*CA*=85°), while PVAm/rGO film shows hydrophobic behavior (*CA*=97°), and finally xPVAm/rGO exhibits more hydrophilic behavior than the original film (*CA*=70°). Most likely this is due to the fact that the hydrophilic glutaraldehyde makes the polymeric crosslinked matrix (xPVAm) more hydrophilic, where the rGO is highly immobilized as hydrophobic unit.

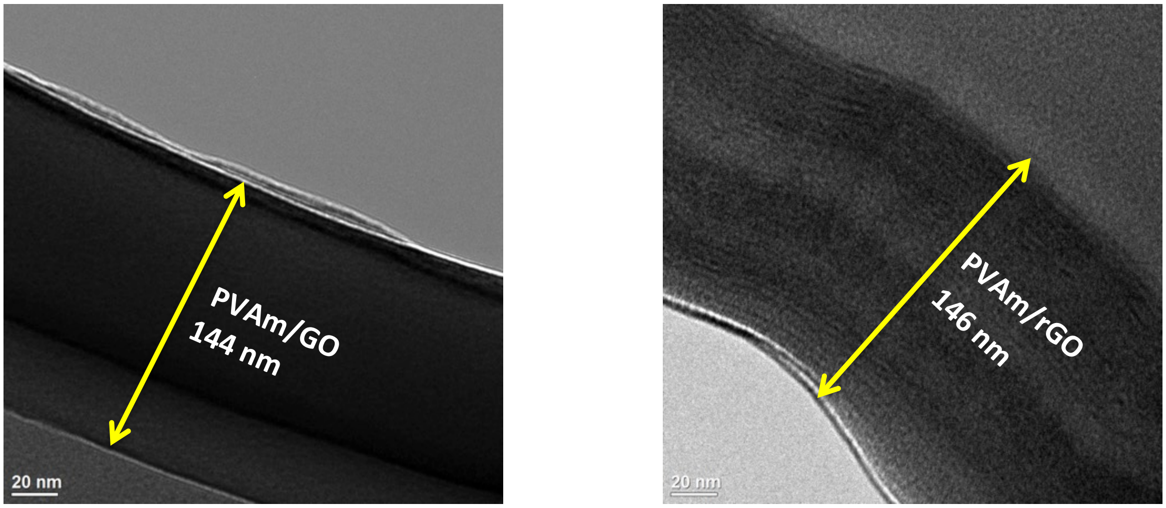

(a) **(b)**

Figure 3.4 Cross section TEM images for (a) PVAm/GO, (b) PVAm/rGO and (c) xPVAm/rGO.

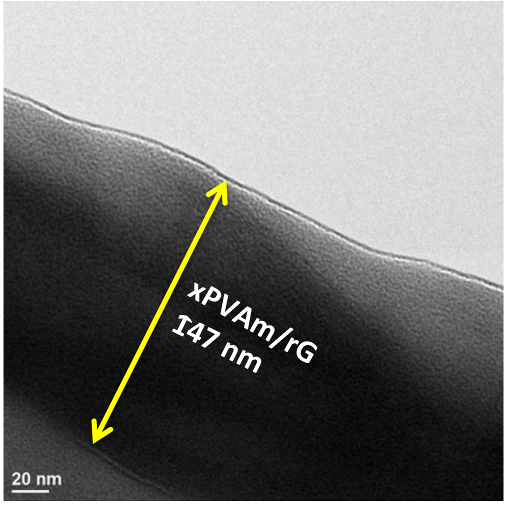

(c)

Figure 3.4 Continued

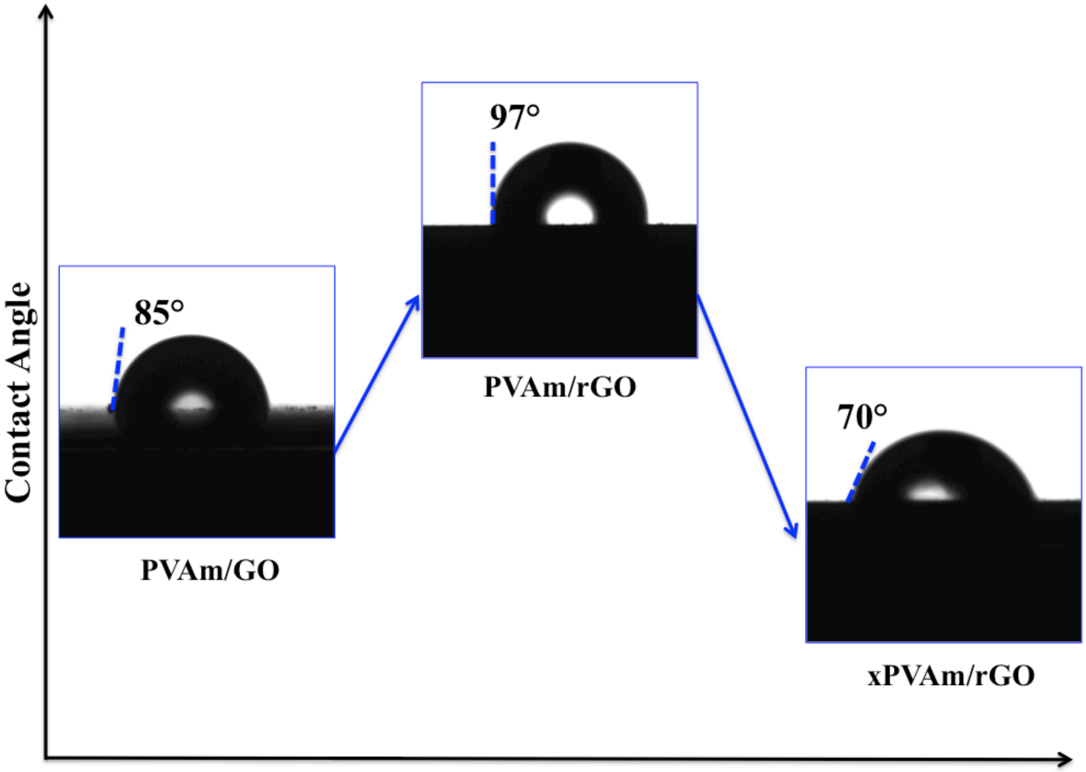

Figure 3.5 Contact Angles of a water droplet for all multilayer thin films.

3.3.2 Reduced Modulus and Hardness

Indentation forces were applied increasingly from 1 to 20 μN using 90-degree cube corner tip on different sites for each sample. The indentation depth did not exceed 20% of the thickness of the films in all indentation experiments. The 20% thickness is chosen as a limit based on previous studies. This is confirmed here as well, where the substrate effect starts to appear deeper than 20% of the film thickness.

Table 3.3 shows the statistical results of the elastic modulus and hardness of PVAm/GO films. PVAm/GO has the lowest values for both E_r and H. Graphene reduction contributes significantly to an increase of 60-70% in both E_r and H. Graphene reduction leads to a decrease in the interlayer spacing between graphene sheets to about one third (≅0.3 nm) because of fractional removal of the oxygen-containing groups, as was proved by XPS and Raman studies (presented below).[137] This is anticipated to yield an increase in the mechanical properties because of the denser structure of graphene sheets. Furthermore, a large aspect ratio of the graphene sheets, and a strong interfacial adhesion due to H-bonding between graphene and PVAm layers can explain the obtained mechanical properties. PVAm crosslinking show a slight increase in the E_r and H values when compared to PVAm/rGO. While polymer crosslinking did not show a significant effect on the mechanical properties of the films, it is successfully maintaining these properties at the same values.

Representative load-displacement curves for all multilayer layer thin films are shown in Figure 3.6. There were no detectable residual indentation marks under this range of indentation loads, which indicates no significant plastic deformation during indentation experiments. In addition, there was no substrate effect on the E_r and H values for the three films within 20% of film thickness up to 20 μN indentation force.

Table 3.3 Nanomechanical properties of multilayer thin films[a].

Film	E_r **(GPa)**	H **(GPa)**
PVAm/GO	16.08±3.94	1.26±0.307
PVAm/rGO	25.65±4.50	2.12±0.269
xPVAm/rGO	26.94±4.96	2.15±0.282

[a] ± values are ± one standard deviation

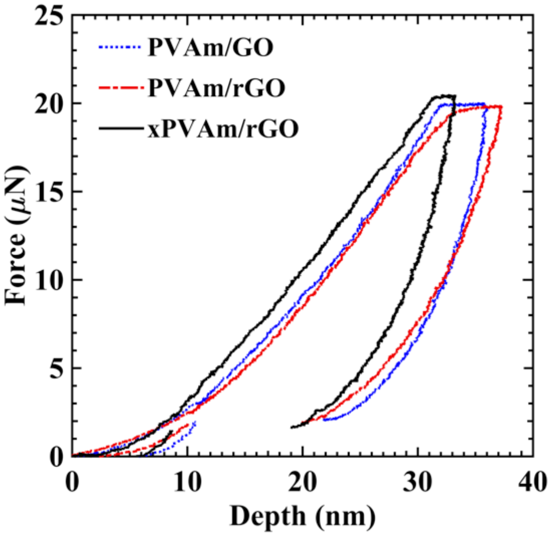

Figure 3.6 Representative load−displacement curves for single-loading tests of 20 μN maximum load on the three different films.

3.3.3 *Raman/XPS*

Raman spectroscopy is a non-destructive tool for characterizing graphene. Graphene typically exhibits three main Raman active modes, D-band (1300cm^{-1}), G-band (1600 cm^{-1}), and two-dimensional modes (not presented here), each having different physical origins.[138] Raman spectra of PVAm/GO, PVA/rGO and xPVAm/rGO films are shown in Figure 3.7(a), recorded using 633 nm laser irradiation. The I_D/I_G ratio is reduced in the case of PVAm/rGO compared to the original PVA/GO film. This suggests that new (or more) graphitic domains are formed and the sp^2 carbon species population is increased after the reduction process described above, showing good reduction efficiency which is preserved following the crosslinking process.[139]

X-ray photoelectron spectroscopy (XPS) was used to investigate the chemical structure and composition of the films and also to confirm the results obtained by Raman. Figure 3.7(b) presents the C1s core level spectra of PVAm/GO, PVAm/rGO and xPVAm/rGO films. The C1s spectrum of the original PVAm/GO signal shows two distinct peaks. This can be ascribed to the oxygen-containing functional groups. In particular, contributions from sp^2 (284eV), sp^3 (284.8 eV), and C-O (286.8 eV) can be seen.[115,140]

After GO reduction the intensity of the peak at 286.8 eV drops, reducing to a shoulder, indicating the consumption of the particular oxygen-containing groups during the GO reduction process. This also supports the existence of more sp^2 carbon in graphite environment, as discussed earlier in Raman studies. Also, after reduction of GO, a small peak at 288.2 eV is emerging corresponding to C=O chemical species. The CC/CO intensity ratio for the reduced and the crosslinked materials is much higher compared to the one for the original film, where CC is the summation of C-C and C=C, whereas CO is the summation of all combinations of carbon and oxygen atoms. The oxygen containing groups are potential reaction sites for covalent bonding with the polymer layer. Though, the oxygen-containing functional groups are removed by thermal reduction of GO. In such a way, a restoration of the aromatic network in graphene is taking place. Due to the strong π-π interaction between layers of rGO an unavoidable agglomeration can happen. Nevertheless, the presence of PVAm, the protonation of which can be tailored through pH (polycationic in this study), seems that can tailor the sensitive balance between hydrogen bonding, hydrophobic interactions and electrostatic interactions.[141]

By comparing the peaks that correspond to the PVAm/rGO and xPVAm/rGO films, a small shift from 284.3 to 284.7 eV can be noticed. This corroborates with more oxidized environment in the crosslinked film. The intensity of the sp^2 carbon peak (~284 eV) is lower, whereas the C-O peak at ~286 eV remains of low intensity, showing the preservation of the reduced environment of carbon following crosslinking, possibly because the oxidized carbon species participate in the crosslinking with amino groups from the glutaraldehyde agent.

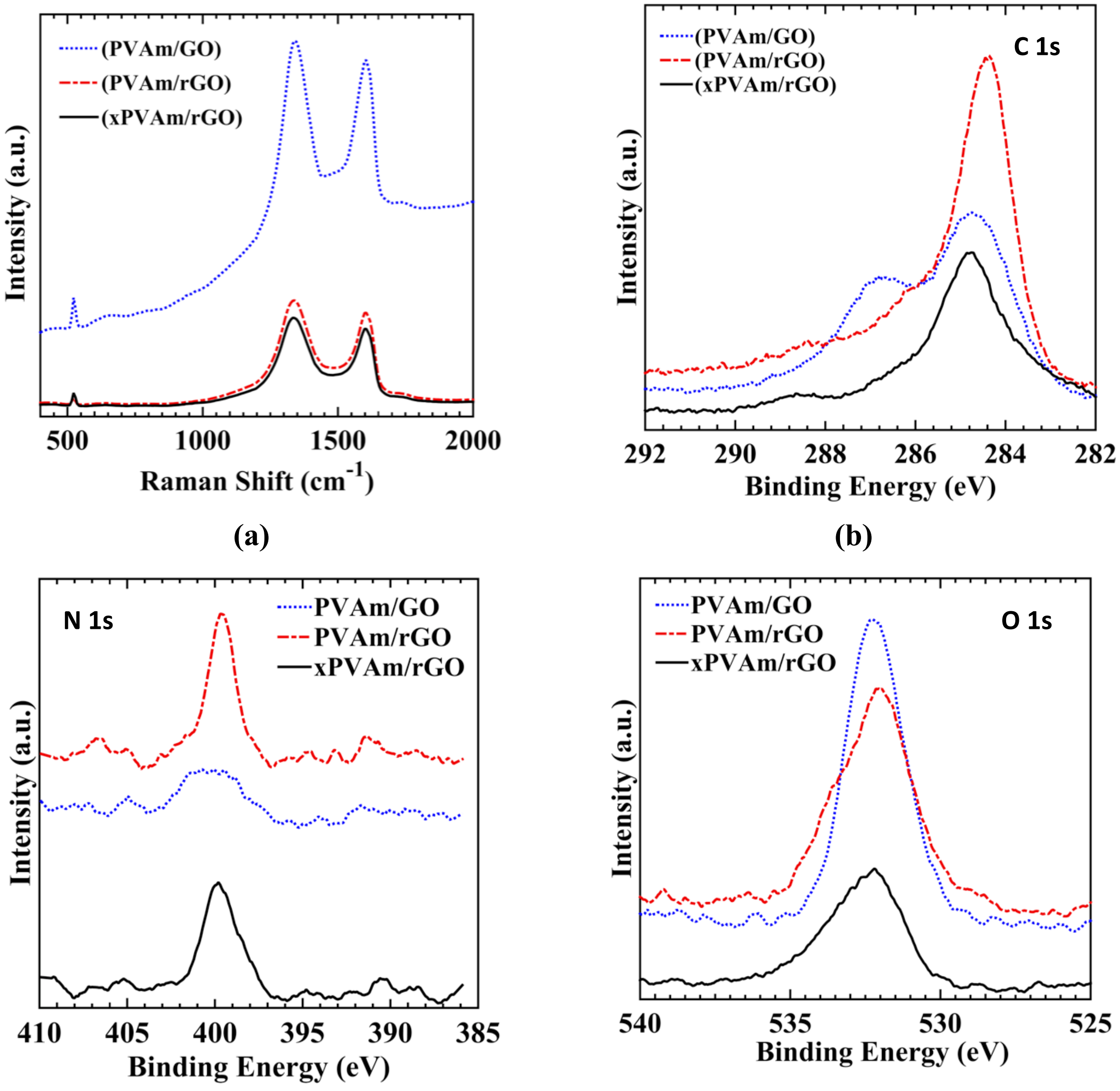

(a)

(b)

(c)

(d)

Figure 3.7 (a) Raman and (b) C 1s XPS (c) N 1s XPS (d) O 1s XPS of the PVAm/GO, PVAm/rGO and xPVAm/rGO.

The XPS N1s spectra (Figure 3.7(c)) of the PVAm/GO is a rather broad peak corresponding to N species such as R-NH_2 (398.6 eV), NH-C=O and/or R-NH-R (400 eV) and R-NH_2 (402 eV).

The N species NH-C=O and/or R-NH-R at 400 eV still exist in the case of PVAm/rGO (reduction) and xPVAm/rGO (reduction and crosslinking) at an even higher population as it is designated by the higher intensity of the peaks. Thus, a restructuring of the PVAm/GO can be suggested as a result of reduction and crosslinking processes.[142] This restructuring in PVAm/rGO and xPVAm/rGO is most likely due to the fact that covalent bonding is taking place between the two components of the multilayer thin film: PVAm and GO. Particularly, the crosslinking with glutaraldehyde changes the original PVAm chain by forming covalent bonds at different points of the chain and some acetal bridges. This reduces the rigidity of the multilayer thin film. In general, due to the crosslinking, there are 3 competitive phenomena: (i) size reduction of the existing polymer network due to hydrogen bonding; (ii) chemical network formation with moieties of the crosslinker (as seen in N1s XPS peak at 400eV); and (iii) introduction of flexible chain parts due to the particular structure of the crosslinker. The crosslinking increases the crystallinity and the latter improves the hardness and reduced elastic modulus.

The O1s core level spectra, shown in Figure 3.7(d), has contributions from oxygen double-bonded to carbon (O=C, 531.7 eV), oxygen single-bonded to carbon (O-C, 532.5 eV, peak maximum), hydroxyl group bonded to carbon (533 eV) and carboxylic group (535.3 eV).[142] The C-OH and carboxylic (OH-C=O) group species appeared to be of higher concentration after reduction and crosslinking processes.

3.3.4 Nanoscratch

Scratch experiments were carried out using low (25 and 100 μN) and high (300 and 1000 μN) normal loads, to capture different friction regimes and deformation mechanisms. In its simplest form, friction consists of two parts: adhesive and plowing friction (see Equations 4, 5 for plowing friction for a spherical asperity). Besides adhesion and plowing, elastic deformation and hysteresis play a role with scratching polymers.[127,143]. For 25 μN normal load experiments, there was no visible scratch after each experiment and thus elastic recovery is estimated to be 100 % for all films. Table 3.4 shows the results of these experiments. The adhesive part of the friction coefficient (μ_a) dominates and it is higher in the case of PVAm/GO. Adhesive friction results in shear failure of asperities. For the scratch depth and friction coefficient, they decrease with graphene reduction and polymer crosslinking possibly due to denser and more immobilized structure (as described earlier). Also, the friction coefficient drop could be attributed to the increase of sp^2 carbon species following the reduction process. In addition, the reduction of oxygen species was found in the case of rGO films. This deoxygenation corroborates with a lower surface energy leading to lower COF (supported by the XPS and Raman studies).

The 100 μN normal force scratch experiments, result in residual scratch depths, which are measured using the same tip. The PVAm/GO shows twice higher μ compared to xPVAm/GO. This increase in friction could be due to two reasons:

First, plowing friction is also involved in this case. Plowing friction takes place when a harder asperity plows a softer surface. For a scratch of a spherical asperity, ploughing friction coefficient (μ_d) equals:

$$\text{Ploughing friction coefficient } (\mu_d) = 0.6\times\sqrt{\frac{h}{R}} \text{ or } \frac{4}{3\pi}\times\frac{r}{R} \tag{4}$$

$$\text{In a simplified form, the total friction coefficient } (\mu) \approx \mu_a + \mu_d \tag{5}$$

where R is the tip radius (R=870 nm), $2r$ is the in-situ groove width and h is the in-situ scratch depth (see Table 3.5).[144] Since $R>>h$ and h is similar for the three films, the plowing friction component ranges from $\mu_d = 0.145$ for PVAm/GO to $\mu_d = 0.136$ for xPVAm/rGO. The total μ for xPVAm/rGO is similar to μ_d, which indicates a small adhesive part. However, the total μ for PVAm/GO and PVAm/rGO is higher, this suggesting higher adhesive friction for these films.

Second, PVAm/GO exhibits lower residual depth and higher elastic recovery for this force range due to the high influence of elastic deformation and hysteresis (known as elastic limit) on the scratch behavior. Even though, PVAm/rGO and xPVAm/rGO are easier to initiate a scratch with lower elastic recovery for this load range, they maintain a stable scratch, particularly in the case of xPVAm/rGO film. This is most likely due to the stiff and dense structure of the film following reduction and crosslinking. Figure 3.8 shows the influence of the elastic deformation mechanism in the three films. The scratch is hardly visible in the case of PVAm/GO because of the high recovery. This suggests that PVAm/rGO and xPVAm/rGO show more plastic deformation than the original film, PVAm/GO.

Table 3.4 25µN constant load scratch experiments.

Film	In-Situ Scratch Depth (nm)	Residual Depth (nm)	Recovery	Friction Coefficient
PVAm/GO	25	0	100%	0.80
PVAm/rGO	18	0	100%	0.52
xPVAm/rGO	15	0	100%	0.35

Table 3.5 100µN constant load scratch experiments.

Film	In-Situ Scratch Depth (nm)	Residual Depth (nm)	Recovery	Friction Coefficient
PVAm/GO	51	3	95%	0.25
PVAm/rGO	47	18	62%	0.19
xPVAm/rGO	45	10	78%	0.13

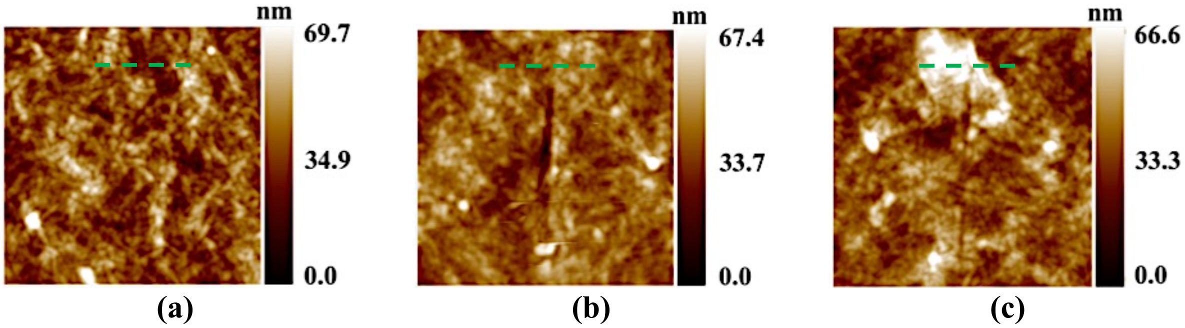

Figure 3.8 Residual scratch images (10x10 μm) for (a) PVAm/GO (b) PVAm/rGO (c) xPVAm/rGO after 100 μN scratch (dashed lines show the start of the scratch).

To gain insight in the wear and delamination behavior of the films, ramp load scratch experiments were also performed. Each experiment consists of an initial scan for topography (pre-scan), then the normal load is increased linearly (ramp load), and finally a post scan is performed to measure the residual scratch depth. Once the test is completed, the residual scratch image is scanned using the same tip. Figure 3.9 shows the scratch profiles obtained for the multilayer thin films.

There are three scratch regimes, which a material can exhibit under combined loading: elastic contact, plastic deformation (plowing) and severe deformation with wear debris. The elastic contact dominates the behavior of PVAm/GO film (see Figure 3.9(a)). Therefore, the film only exhibits the first regime. Once a critical load is reached, this film experiences delamination and material transfer. The material transfer ahead of the tip is due to elastic deformation (hysteresis), which occurs in polymers due to their viscoelastic nature.[112] PVAm/rGO and xPVAm/rGO films experience plowing deformation as the post-scan shows residual deformation in Figures 3.9(b, c). Crosslinking tends to recover most of the scratch depth and the plowing part of friction is well maintained till the end of the applied normal load. The xPVAm/rGO film is the only film that does not exhibit a surface rupture and only has material transfer at the end of the applied scratch. The results of Figures 3.9 (a, c) agree with the findings of the constant load scratch experiments (see

Figure 3.8 and Table 3.5).

Material pile up takes place in all graphene reinforced PVAm films because of the weak GO interfacial bonding, which causes the material build up in front of the tip and due to the polymer molecular mechanisms such as crazing, where new surfaces are created as a result, and higher entanglement density around the indentation site.[127]

Figure 3.9(d) shows the in-situ normal displacement as a function of applied normal load. Once increasing the applied load, the PVAm/GO film shows transition in the frictional behavior reaching delamination. The normal displacement of PVAm/GO film drops faster than the other two films where the first drop is due to the elastic deformation in the film. The other two films did not reach delamination under this normal scratch force.

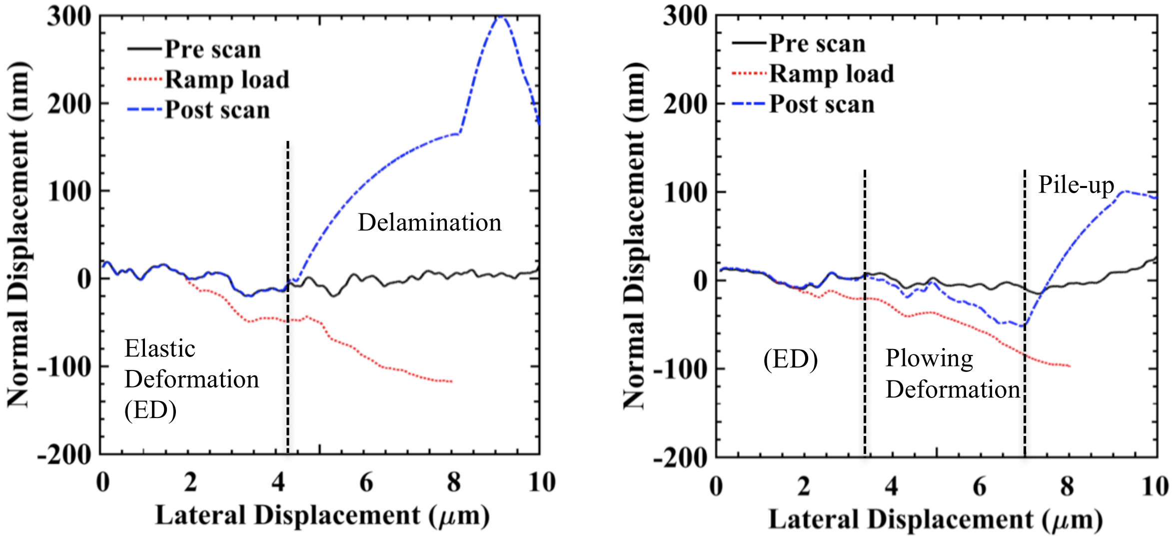

(a) (b)

Figure 3.9 Scratch profile for (a) PVAm/GO (b) PVAm/rGO (c) xPVAm/rGO with a normal scratch force up to 300 μN. (d) in-situ normal desplacement versus normal load.

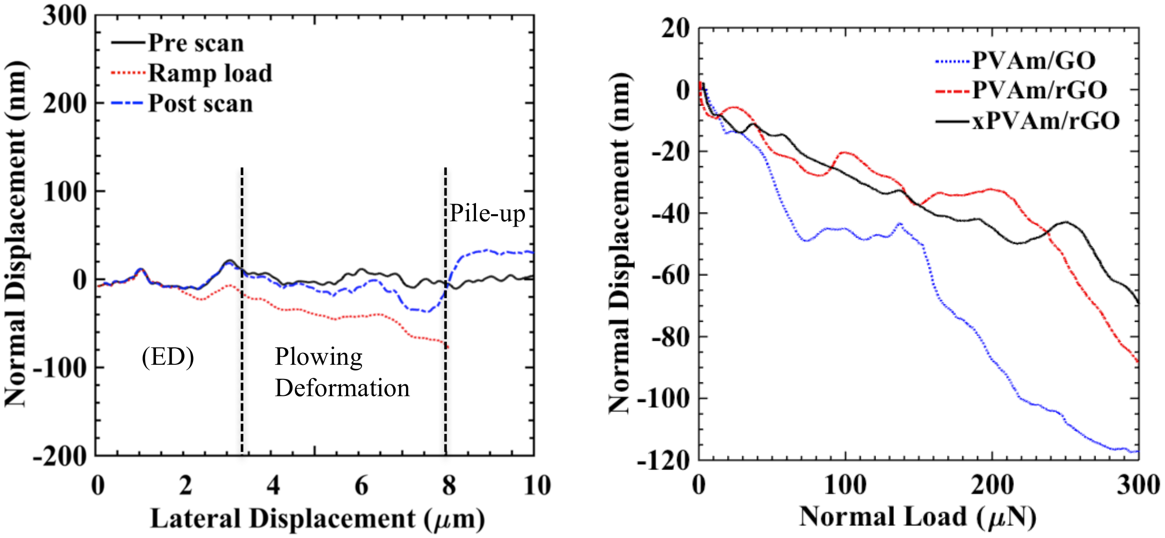

(c) **(d)**

Figure 3.9 Continued.

Residual scratch images and cross section residual depth are shown in Figure 3.10 for all multilayer thin films studied herein. Clearly, there is a major difference between the three films. The original film, PVAm/GO shows faster growth in the scratch width ending with a surface failure. The material transfer (380 nm) ahead of the tip is more than twice the film thickness. This is due to the creation of new surface on the sides of the scratch groove with a smaller stress magnitude than beneath and ahead of the tip, which are under high hydrostatic/ compressive stress. Therefore, the post recovery is smaller in the sides of the groove.[112] PVAm/rGO shows smaller residual depth and width of the scratch groove. However, it experiences material transfer on the sides and at the end of the groove. The xPVAm/rGO film shows the highest scratch resistance with the smallest groove and no visible residual material transfer/pile-up. The elastic recovery is higher for PVAm/rGO and xPVAm/rGO films and particularly for the later.

The improved scratch behavior of PVAm/rGO and xPVAm/rGO films is due to: (1) film with higher hardness (70% increase) is expected to show better scratch resistance,[145] (2) plowing friction coefficient increases with scratch groove width (2*r*) therefore PVAm/GO film exhibits higher plowing friction, (3) PVAm/GO film has a dominant *π–π* stacking bonding, while the PVAm/rGO and xPVAm/rGO films have stronger covalent bonds,[146] (4) higher density of layers after graphene reduction where GO layer is becoming more dispersed (less aggregated), which is essential for better load transfer to the PVAm matrix from graphene fillers, (5) smoother surface because of the increase of sp^2 carbon species (XPS and Raman studies) and (6) according to the N1s XPS, functionalization of GO with PVAm took place. The linkages of the GO with the PVAm may act as suppressers for the scratch failure in the direction of the test.

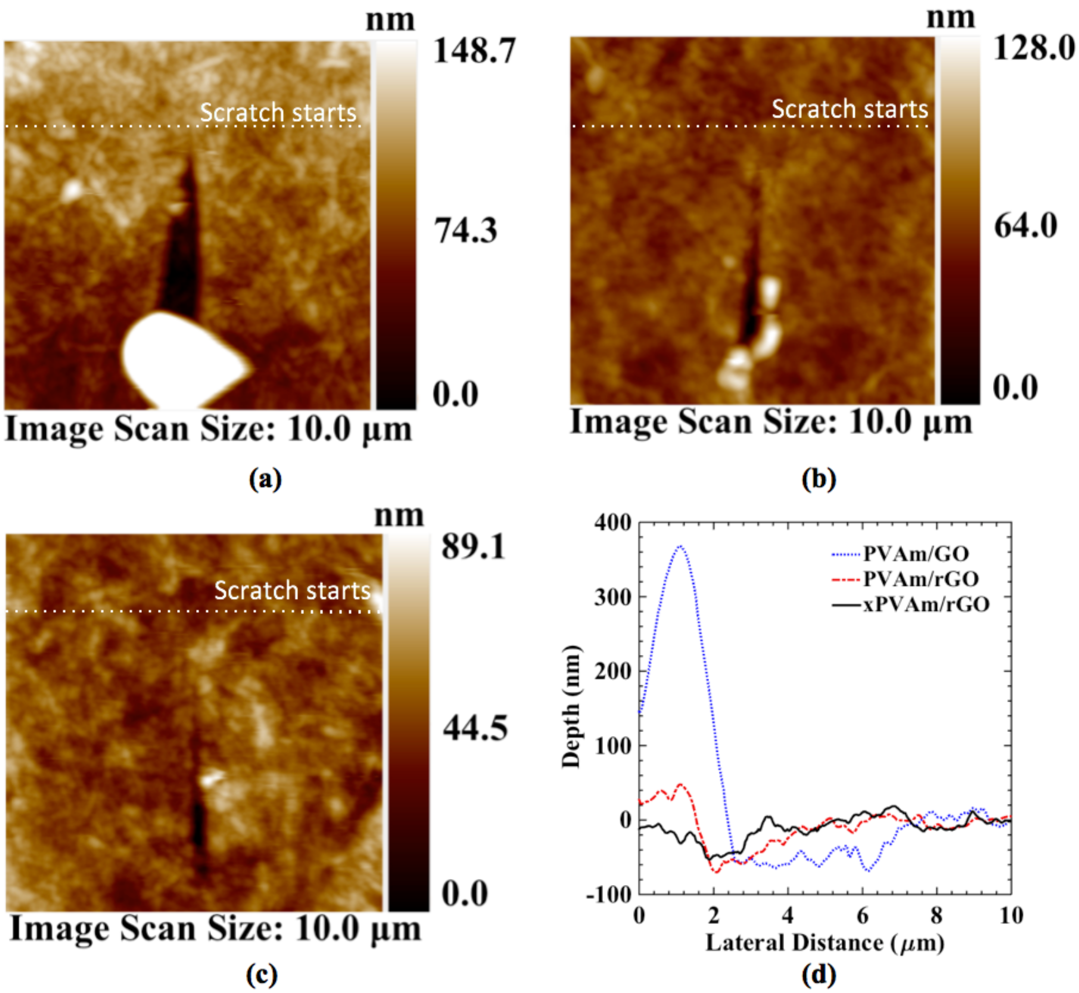

Figure 3.10 Residual scratch images for (a) PVAm/GO, (b) PVAm/rGO, (c) xPVAm/rGO (d) section profiles along the residual scratch grooves for all films showing delamination/pile-up near the end of the scratch.

3.3.5 Film Delamination

Reduced elastic modulus, hardness and friction coefficient have been used to evaluate the mechanical properties of film/substrate assemblies. To further evaluate the effectiveness of this thin film system, quantitative analysis is also performed. Ramp-load scratch experiments can be used to initiate film delamination. The scratch force is increased linearly to reach the critical load (P_c). P_c is defined as the load required to rapture/ delaminate the film and identified by a sudden change in the normal displacement.[126] The critical load can be used to measure the shear and adhesive strengths at the coating-substrate interface. Interfacial stress transfer is an important factor to study.[147] 1 mN Ramp load scratch experiments were carried out to extract these properties. This scratch force was found to be sufficient to cause coating removal for the three films. To confirm these findings, the experiments were performed 10 times each and the results were found to be repeatable.

Figure 3.11 depicts COF and normal displacement as a function of normal scratch force. The films exhibit similar COF for normal forces higher than 600 μN as they reach the substrate properties due to the coating removal. Ciritical load and friction cofficient are labeled in Figure 3.11(a, b).

The fluctuation in the friction coefficient (see Figure 3.11 (b)) is due to stick-slip motion (also known as Schallamach waves),[148] which is a typical phenomenon when scratching polymers due to the large elastic and viscoelastic deformation. The amplitude of fluctuations is lower for xPVAm/rGO, compared to the other two films. Therefore, it shows less rubbery behavior (viscoelastic behavior) and more ductile behavior than the other films. The stick-slip motion is a function of adhesive or interfacial friction. Therefore, PVAm/GO is expected to show higher stick-slip motion and more material transfer due to high adhesive friction.

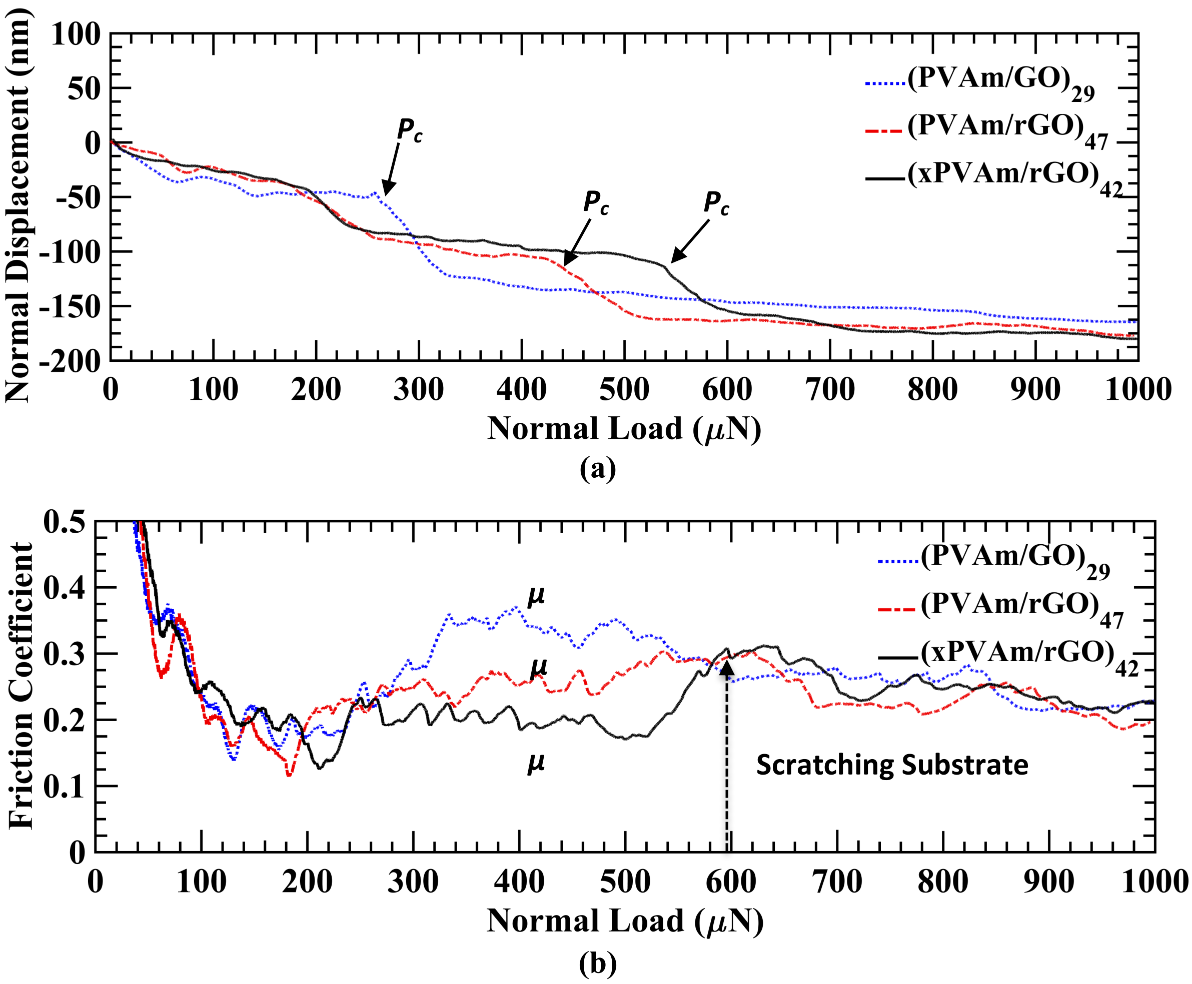

Figure 3.11 (a) In-situ normal displacement and (b) coefficient of friction as a function of scratch normal force up to 1 mN for all multilayer thin films.

The residual scratch width is extracted from SEM images once the critical load is reached (see dashed lines in Figures 3.12 b, d, f). PVAm/GO experiences side surface raptures and fast widening in the scratch groove and more material pile up ahead of the tip due to stick-slip motion. Also, film delamination happens earlier than the other two films. The scratch groove width at the start of the scratch experiment is ranked from smallest to largest as we move from the xPVAm/rGO, to PVAm/rGO to PVAm/GO. Particularly xPVAm/rGO film has a groove much smaller than the tip radius. This is an indication of instantaneous elastic recovery, which reduces the groove width while scratching is carried out. On the other hand, PVAm/GO has an initial scratch width equal to the tip radius. Thus, it shows little or no elastic recovery.

Table 3.6 summarizes the failure/ delamination properties for these films. Using Equations 2 and 3, σ_a and τ_c are calculated. Adhesive and shear strengths are 138% and 48% higher for the xPVAm/rGO film than the PVAm/GO original film. The improvement of adhesive strength is due to graphene reduction. Crosslinking yields substantial improvement in the shear strength. A possible explanation is considering that failure is happening through cavities formation. Once cavities are formed, the stress is sustained by fibrils, a phenomenon very much alike the crazing in polymers. Graphene oxide increases the stiffness and the strength of the polymer, resulting in cavity formation at higher values of stress, whereas fibrils are becoming more resistant to deformation. Also, the covalent bond between rGO and xPVAm and a possible entanglement of xPVAm chains happening during the crosslinking may enhance the stress transfer and shear strength. Shear strength of all PVAm/GO films is comparable to ultra-hard ceramic coatings such as HfB_2 on silicon (τ_c=4.3 GPa).[126] However, the adhesive strength is much smaller due to the viscoelastic nature of polymer and weak GO bonding ($\sigma_a = 1.1$ for as-deposited HfB_2 films).

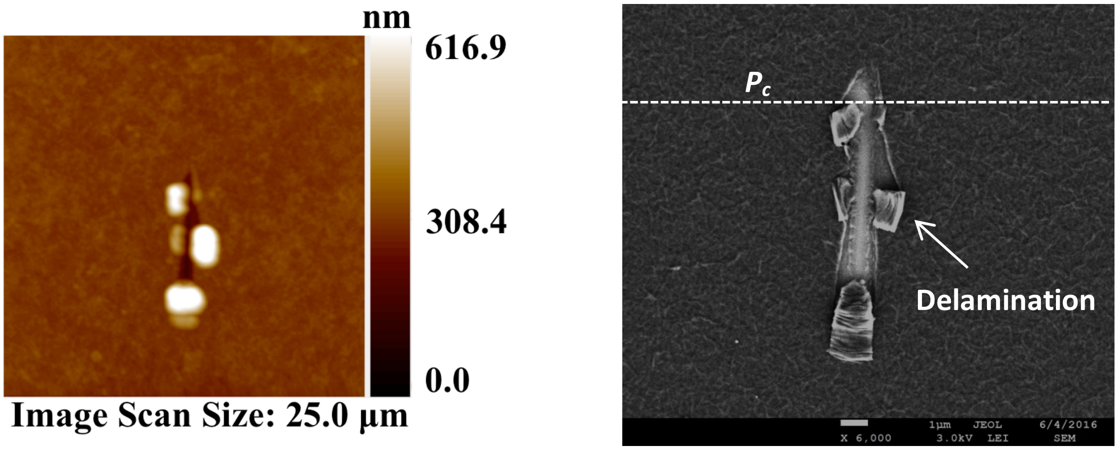

(a) (b)

Figure 3.12 AFM and SEM residual scratch images for (a-b) PVAm/GO, (c-d) PVAm/rGO and (e-f) xPVAm/rGO under a normal load of 1 mN.

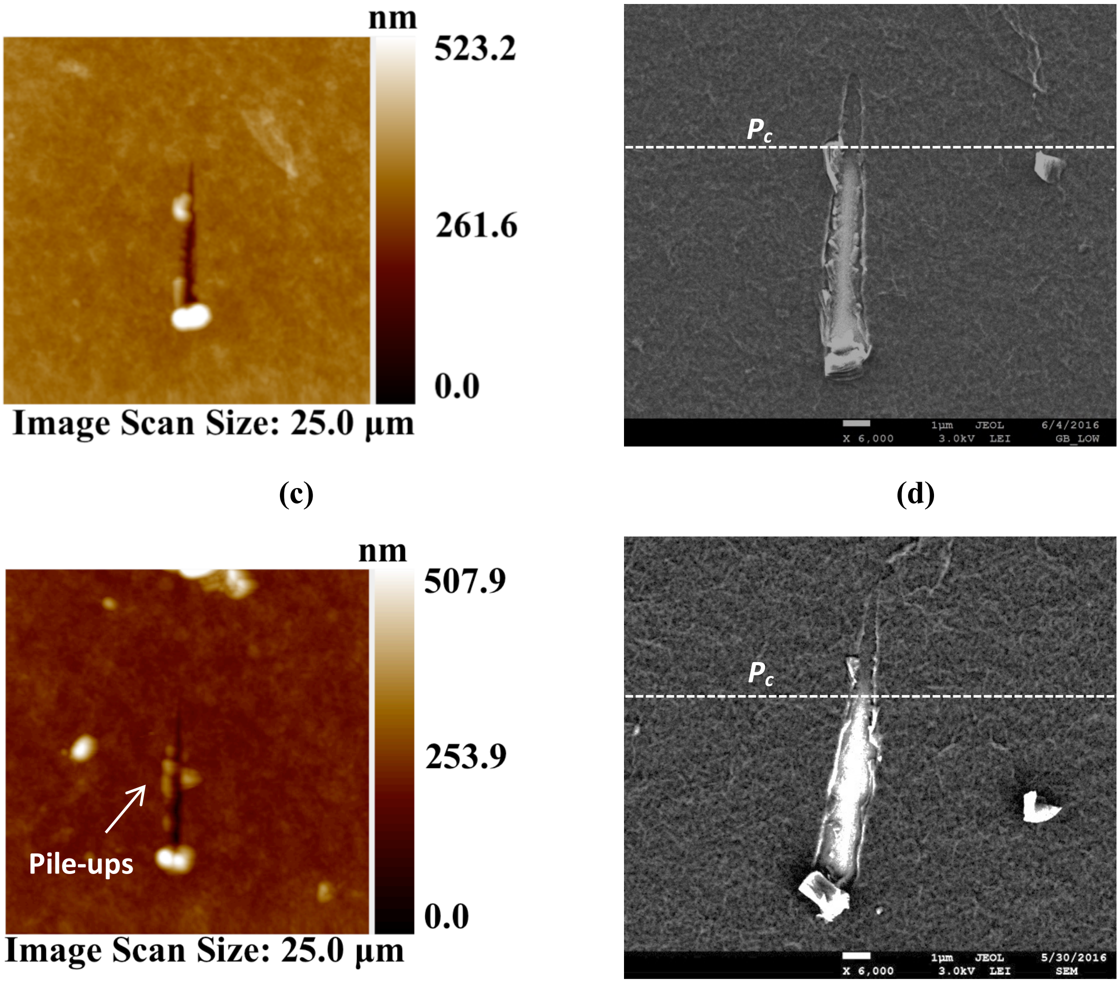

(c) **(d)**

(e) **(f)**

Figure 3.12 Continued.

Table 3.6 Failure properties for multilayer thin films at the onset of delamination.

Sample	Critical load (P_c) (µN)	Penetration depth at P_c (nm)	Friction Coefficient (μ)	Adhesive Strength (σ_a) (GPa)	Shear Strength (τ_c) (GPa)	Scratch width at P_c (d_c) (µm)
PVAm/GO	250	50	0.35	0.13	4.22	1.19
PVAm /rGO	450	140	0.25	0.29	5.66	0.82
xPVAm /rGO	550	130	0.20	0.31	6.26	0.70

3.4 Summary of Chapter 3

Polymer/graphene multilayer thin films are a favorable material choice for many applications due to their attractive characteristics. One challenge is to make durable and strong thin films with strong adhesion to the substrate. Graphene's common drawback of weak interfacial bonding, which leads to weak adhesion and coating failure, has been successfully overcome in the present study. To do so, graphene reduction and polymer crosslinking were added to the synthesis process and their impact on the mechanical properties of PVAm/GO films was investigated.

Nanoindentation and nanoscratch techniques were used to measure the mechanical properties of these films, and Raman and XPS techniques were employed to explain the chemical structure of the films following the aforementioned processes. In particular, Raman and XPS studies showed the existence of more sp^2 carbon in graphite environment after GO reduction and GO reduction followed by crosslinking. Also, after reduction of GO, a small peak at 288.2 eV emerged corresponding to C=O chemical species. The CC/CO intensity ratio for the reduced and the crosslinked materials is higher compared to the original film, where CC is the summation of C-C and C=C, whereas CO is the summation of all combinations of carbon and oxygen atoms.

Graphene reduction leads to an improvement of 60-70% increase in the mechanical properties (reduced elastic modulus and hardness) and 120% increase in the adhesion strength compared to the unreduced PVAm/GO films. Crosslinking PVAm units using glutaraldehyde, results in improvement of the tribological behavior, namely 50% reduction in the friction coefficient, 50% increase in the shear strength, high elastic recovery and less scratch visibility. Crosslinking increases the interfacial interaction between the polymer matrix and the organic filler, graphene. Here, the interfacial adhesion between the PVAm/GO and Si substrate is studied. Further studies are required to understand how the layer thickness of LbL deposition, the substrate hardness and the interfacial adhesion between coating layers influence the mechanical properties and scratch resistance. Graphene reduction and polymer crosslinking leads to more durable and stronger thin polymer films. When combined with other characteristics of polymer crosslinking and graphene reduction such as better chemical resistance, smoother surface, improved thermal stability and electrical conductivity, these two techniques can improve the surface reliability of polymer/graphene nanocomposites, thus making them potential candidates for applications where resistance to mechanical contact and scratch is required. Next chapter extends in the role of polymer crosslinking in the self-healing mechanism of all-polymer multilayer thin films.

4 IN SITU NANOMECHANICAL BEHAVIOR AND SELF-HEALING RESPONSE OF POLYMERIC MULTILAYER THIN FILMS*

4.1 Introduction

Living organisms such as human skin have the fascinating property of self-healing, and this has inspired innovative ideas by the scientific community towards the design and fabrication of elegant materials, which demonstrate self-healing capability.[149] A self-healing material has the ability to heal damage and restore its properties, mainly mechanical properties.[150] Such a property has made them attractive candidates for many applications, including optics,[151] catalysis,[152] gas barriers,[153] electronics,[154] membranes,[155] corrosion resistance,[156] and electrodes for lithium ion batteries.[157] There are two types of self-healing materials: extrinsic and intrinsic, based on how the self-healing is stimulated.[158] Examples of extrinsic self-healing includes healing agents or nanoparticles,[159] which are embedded in the assembly of the coating, and can undergo phase separation. However, these particles or healing agents have a limitation to continue to heal the same area over a cycle of damage without re-supplying additional healing agents through spray or deposition.[160]

Alternatively, intrinsic self-healing is a property of many materials, including some polymers, which can repair themselves. This can take place using reversible chemical bonds either within the polymer matrix, or with physical interaction with certain surrounding environments.[161] The first is known as autonomic and the latter as non-autonomic self-healing, since it requires to have an external stimulus such as light, humidity and heat.[162,163] The autonomic self-healing has a

---

*Reprinted with permissions from "In Situ Nanomechanical Behavior and Self-Healing Response of Polymeric Multilayer Thin Films." by Humood, M.; Polychronopoulou, K.; Song, Y.; Grunlan, J. C.; Polycarpou, A. A. Polym. (United Kingdom) 2017, 131, 169–178.

limitation to certain chemical reactions and typically the dangling chains interact with one side of a deep scratch and not across the gap.[164] This would lead to a partial self-healing, as compared to complete self-healing. On the other hand, non-autonomic self-healing such as immersing the polymer in water leads to quick full recovery of a damaged area due to the fact that the polymer matrix turns to a hydrogel.[165] Hydrogels are crosslinked 3D polymer networks, which are swollen with water.[166] Likewise, heating the polymer over its glass transition (Tg) allows the material to rearrange itself to heal a damage.[167]

Different synthesis methods were developed to fabricate healable polymeric films such as chemical grafting and layer-by-layer (LbL) assembly.[168,169] The fabrication of the films through layer-by-layer (LbL) assembly is well-established, where the polyelectrolytes exhibit high chain mobility when subjected to external stimuli.[170,171] This allows the polymeric chains to reshuffle and initiate self-healing. Due to the high diffusion rate, free volume increases, whereas low values of Young's modulus are reported for the same reason.

The precise measurement of the mechanical properties for the self-healable films are of significant interest to better understand and improve the self-healing process.[172–175] Indeed, the *in situ* characterization of submerged samples in liquid media is essential for biological and soft samples, such as hydrogels and tissues, and it is known as in-vitro characterization.[176] Similarly, immersed polymers are interlinked with water molecules and therefore, their properties are expected to be different than in the dry ambient condition.[177,178] Water adsorption of polymers results in effects such as plasticization, leaching of unreacted functional groups, structural damage, chemical degradation, and oxidation.[179,180] Therefore, the changes in the mechanical properties due to humid environments are important. For example, Nylon 6, due to its polar nature, absorbs water, which results on a plasticization due to a decrease in hydrogen bonds in the amorphous part of the polymer.[181,182] In addition, water is known to be a strong plasticizer of polyelectrolyte complexes.[183]

Nanoindentation has been widely used to extract the mechanical properties for polymeric multilayer thin films.[111,127,184,185] However, limited measurements have been reported regarding the effect of swelling in solutions such as water and the liquid-solid interface.[49] Little attention has been paid to measure the *in situ* mechanical changes of polymers once being immersed in water. In addition, most of the literature, which reported measurements of reduced modulus for polymeric films in wet conditions, were done using AFM nanoindentation.[186–189] AFM nanoindentation is less accurate than direct force/displacement measurements using instrumented nanoindentation techniques, due to the change in the shape of AFM cantilevers during experiments, which leads to significant errors in the measured modulus.[190,191]

The physical models for the chain relaxation of multilayered LbL-assembled films such as PEI/PAA under different stimuli have been shown in earlier works and by others in the literature.[192,193] In this work, we report precise measurements of reduced modulus and hardness for a self-healing polymeric multilayer thin film, PEI/PAA under dry and high humidity conditions. The measurements were performed using wet nanoindentation technique. The water was found to have two coupling effects on the thin film, which were studied herein: (1) the coupling effect of water and swelling behavior of the polymer and (2) the coupling effect of water and surface roughness. The first effect is found to be reversible once the polymer is dried (de-swelled) at room temperature (RT) conditions for 24 h. The second effect required additional heating to restore the surface roughness of the as-deposited film. Therefore, HT nanoindentations were also carried out to better understand the *in situ* changes during the heating process.

4.2 Experimental Section

4.2.1 Materials and Processing

Multilayer thin films were prepared using alternating deposition of LbL assembly method. Both branched PEI (Mw≈25,000 g/mol, ρ=1.10 g/cm^3) and PAA (Mw≈100,000 g/mol, ρ=1.20 g/cm^3) were obtained from Sigma-Aldrich (Milwaukee, WI). PEI acts as a cationic polymer and was dissolved in DI water to create a 0.1 wt% solution, while PAA acts as an anionic polymer and was prepared as 0.2 wt% solution in DI water. The pH of PEI and PAA solutions were adjusted to 10 and 4 using 1 m HCl and 1 m NaOH, respectively.

Single-side polished (100) silicon wafers (University Wafer, South Boston, MA) were used as substrates for deposition and nanomechanical testing. Silicon wafers were cleaned using piranha solution. They were cleaned again with acetone and DI water before use. *Caution: Piranha solution should be handled with care since it reacts violently with organic materials.*

LbL deposition was carried out using a home-built robotic dipping system. For the first bilayer cycle, the Si substrate was dipped into PEI and PAA solution for 5 minutes each. Between both dipping steps, the sample was rinsed with DI water and dried with filtered air. The rest of the deposition cycles were similar but with 1 min dipping in both solutions. Eight bilayer deposition cycles yielded a PEI/PAA multilayer thin film of 700 nm thickness. The film thickness was measured using a P-6 Stylus Profiler (KLA-Tencor, Milpitas, CA). *In situ* film thickness under wet and HT conditions were measured in an earlier work.[153] Immersing the film on DI water increased the film thickness by 52%, while, heating the wet film at elevated temperature restored the original film thickness. The period of self-healing was set to 24 hr in this study, however a 10-min period was found sufficient to heal the mechanical damage of 8 bilayers of PEI/PAA thin film.[194]

4.2.2 In Situ Wet/High Temperature Nanoindentation

In order to understand the changes in the mechanical behavior of these thin films during each step of the self-healing process, *in situ* nanomechanical testing was used to measure the changes in the mechanical properties. A Berkovich fluid cell probe with a tip radius of 150 nm was used for all experiments at RT. A fluid cell probe has an extended shaft of additional 4 mm, compared to a standard Berkovich probe and a thicker shaft diameter to reduce the influence of water forces. This was designed as such in order to help reduce the meniscus forces in water. Therefore, the probe could penetrate the water and stop at the surface of the sample once contacted. In addition, the longer shaft is expected to prevent the housing of the transducer or the piezo scanner from contacting the water or the container's walls. A special stage made of Teflon was used for wet nanoindentation. The sample was sandwiched between the top and bottom of the stage. An O-ring was used to seal the sample and four screws were used to tighten the top and bottom parts of the stage. Figure 4.1(a) shows a schematic for the wet nanoindentation setup.

For submerged experiments, the film was immersed in DI water for 24 hours before carrying out the experiments. This allowed the swelling behavior to stabilize. The experiment started with the probe out of contact with the sample or water. In order to determine the contact point of the sample, the probe was lowered slowly using a 15 μN setpoint force. Once the surface was found, the setpoint force was lowered to 2 μN, and the tip was moved to a new position before the start of experiments. Before each experiment began, a holding segment of 20 s was used to reduce drift. Then, the probe was lifted 180 nm out of contact and penetrated slowly back to help identify the starting contact point in the load-displacement curve. For nanoindentation of dry samples, a smaller lift height of 25 nm was found to be sufficient.

Once all wet nanoindentation experiments were performed, the thin film was placed to dry for 24 hours at RT conditions in a dry-box desiccator. Then, it was dried in a vacuum oven at 120 ℃ for 24 h. HT drying was found essential to reconstruct the surface roughness of the multilayer thin film. To simulate the HT drying process, HT nanoindentation experiments were done. A similar Berkovich tip in terms of shaft length and tip diameter was used, but this time with a special ceramic holder to reduce thermal drifts. Nanoindentation depths for all experiments were kept in the range of 40-120 nm (5-15% of the film thickness). The heating stage, xSol (Bruker, Minneapolis, US), has a fast PID control, 4 temperature sensors, dual resistive heating elements and DI water cooling system to achieve fast heating/cooling, and uniform heating on the surface of the sample. The sample was sandwiched in a thermally stable microenvironment which was in the presence of a gas mixture of 5% Hydrogen and 95% Helium to reduce oxidation at elevated temperatures (See Figure 4.1(b)).

The mechanical properties were measured using a commercial indenter, TI Premier (Bruker, Minneapolis, US), and the experiments were carried out using load-control mode. To reduce the creep deformation, various holding segments and rates of loading and unloading were carried out. For all experiments, 5 s time periods for loading and unloading and 2 s dwell time at maximum nanoindentation load were used. The hardness (H) and reduced elastic modulus (E_r) were obtained from the first one-third of the unloading curve according to the Oliver and Pharr method, which was found to be applicable as well for submerged experiments.[64]

The nanoindentation calibration for different Berkovich probes was provided in the supporting information. In addition, a proof of concept for wet nanoindentation was provided for fused Quartz (FQ) and Si samples, which are insensitive materials to DI water. Figure 4.2 and Table 4.1 showed that both samples had similar properties in dry and submerged conditions. The is due to FQ and Si being both smooth samples, and known to be non-reactive with DI water at low temperatures and low pressures. Furthermore, representative load-displacement curves were provided for Si substrate for submerged and HT conditions in Figure 4.3. HT nanoindentation experiments of Si substrate were carried out at 120 °C.

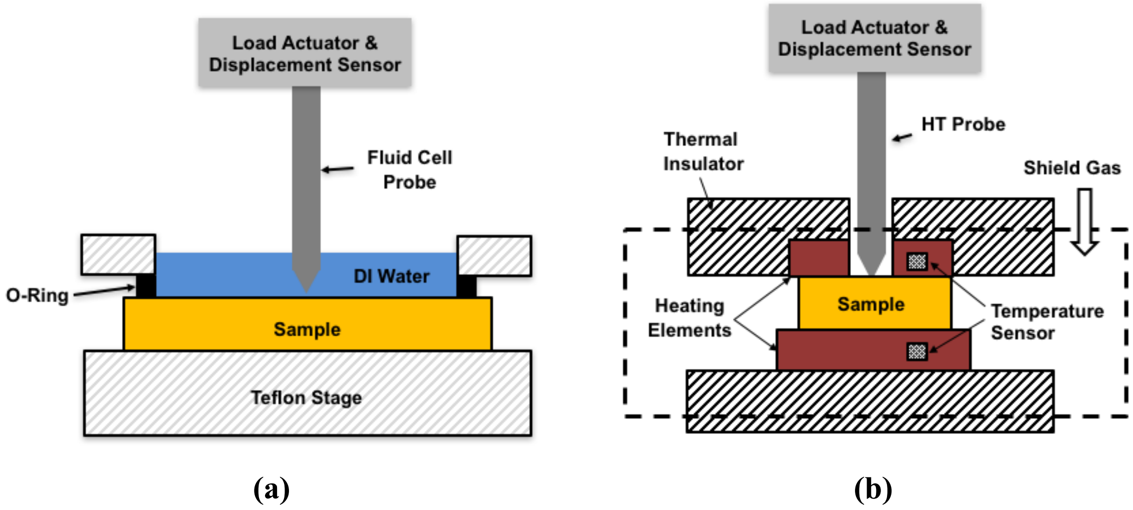

Figure 4.1 Schematics of (a) wet nanoindentation setup and (b) HT nanoindentation setup.

4.2.3 Nanoindentation Calibration

The indenter probe was calibrated using a standard fused quartz (FQ) sample. The calibration was performed under room temperature dry (25% humidity) and submerged condition in DI water (100% humidity). Since FQ sample is water-insensitive, both conditions give similar mechanical properties. Once the area function was calibrated according to the Oliver-Pharr method, additional experiments were carried out on the silicon sample (Si). Figure 4.2 shows the residual nanoindentation images for FQ and Si samples in both dry and wet conditions. These residual nanoindentation’ marks were found to be similar for both samples under both conditions. A series of 20 nanoindentations were carried out to determine the mechanical properties, which are reported in Table 4.1. The Si sample shows slightly lower properties in submerged condition due to the formation of a thin protective layer of silicon dioxide. The effect of water molecules is to decrease the variability of the mechanical properties in submerged conditions for the silicon sample.

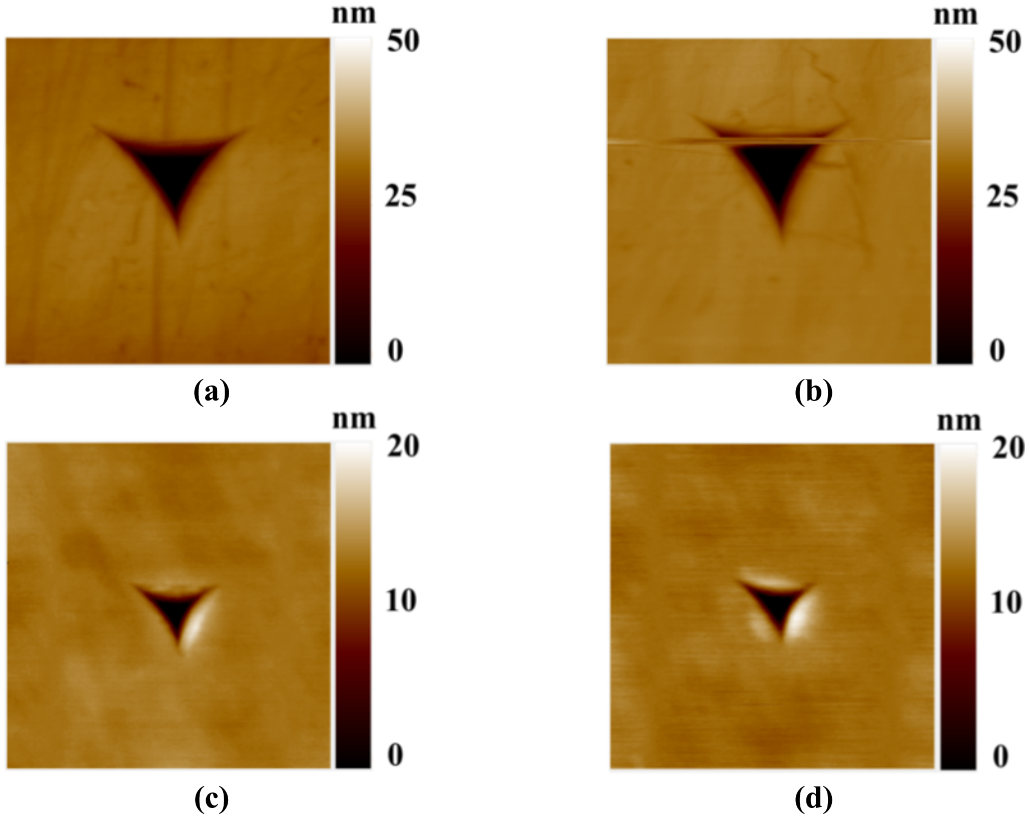

(a) (b) (c) (d)

Figure 4.2 Residual indentation images (2x2 μm^2) for (a) FQ standard sample, (c) Si sample under dry condition, and for (b) FQ, (d) Si under submerged condition in DI water. The maximum indentation load was 2 mN and 4 mN for Si sample and FQ sample respectively.

Table 4.1 Nanomechanical Properties of FQ and Si samples under dry and submerged conditions.

Sample	E_r **(GPa)**/ *Dry*	E_r **(GPa)**/ *Submerged*	***H*** **(GPa)**/ *Dry*	***H*** **(GPa)**/ *Submerged*
FQ	69.64±0.89	68.90±2.00	8.68±0.25	8.71±0.63
Si	163.14±10.78	161.77±2.41	13.33±0.68	12.61±0.44

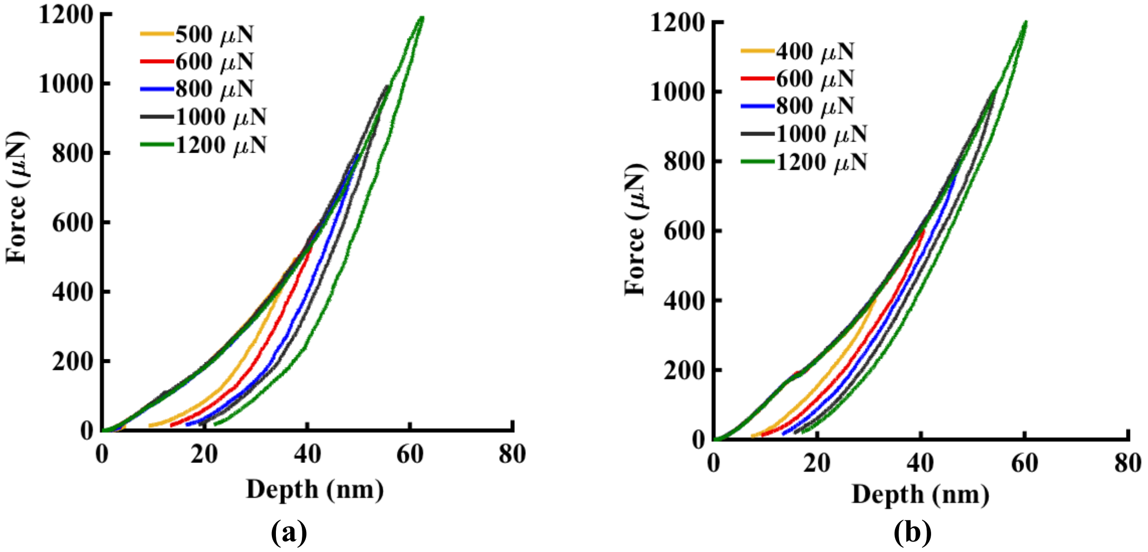

Figure 4.3 Load–displacement curves for silicon sample for (a) Submerged condition in DI water (b) High temperature condition ($T = 120$ ℃).

4.2.4 Microscratch

To demonstrate the self-healing property of PEI/PAA thin films, a 2D force transducer was used with the same TI Premier indenter to scratch the thin film. A diamond conospherical probe with tip radius of 4.3 µm was used to scratch the multilayer thin films. The normal ramp scratch force was 10 mN and the scratch length was set to 600 µm. The scratch experiments were repeated 5 times, to ensure repeatability.

4.2.5 Atomic Force microscopy (AFM)

The changes in the surface roughness were measured using a Dimension Icon AFM (Bruker, Billerica, MA). AFM tapping mode was used. The scan rate is set to 0.5 Hz with 512 samples per line. AFM silicon tip with a nominal tip radius of 8 nm, force constant of 5.4 N/m and resonance frequency of 150 kHz was used. For AFM liquid imaging, the AFM mode was changed to *ScanAsyst-Fluid,* and a silicon-nitride tip was used instead with a smaller force constant of 0.7 N/m to protect the soft polymer sample and tip from damage.

4.2.6 FTIR

A Thermo Nicolet 380 FTIR spectrometer was used to obtain FTIR measurements. The diamond tipped attenuated total reflection stage was utilized to obtain the spectra for all thin films. The background data was collected first and then subtracted from all measurements. The spatial resolution was 4 cm^{-1} and the number of scans was 64.

4.2.7 XPS

XPS studies were performed using an Omicron ESCA system equipped with a monochromatic MgKα X-ray source (1253.6 eV) and operated at 300 W. Samples were analyzed under vacuum ($P < 10^{-8}$ Torr), whereas survey scans and high-resolution scans were collected using pass energy of 40 eV. Binding energies were referred to the C 1s binding energy at 284.6 eV.

4.3 Results & Discussion

4.3.1 Self-Healing

To demonstrate the self-healing property for PEI/PAA films using humidity as a stimulus, microscratch experiments were carried out to make scratches on the coating surface. The films were scratched with an increasing normal force up to 10 mN. This maximum force was chosen, because it initiated delamination of the thin film. This helps to identify the location of scratches after self-healing, as the thin film would not heal upon a complete removal. The 10 mN normal force yielded scratches with average depth and width of 645 nm and 4.8 μm, respectively. The delamination took place in the last one third of each scratch. The scratches before self-healing are shown in Figure 4.4(a) using optical microscopy. After scratch experiments were carried out, the film was submerged in DI water for 24 hours to activate the self-healing property of the thin film. Subsequently, the film was removed from DI water and left to dry in a dry-box desiccator for another 24 h. The film after self-healing was scanned again using SEM, and it showed a complete recovery of the damaged area due to the scratch, as shown in Figure 4.4(b). Figures 4.4(c-f) show the scratches at the beginning and end points before and after self-healing. These images were taken using JSM-7500F (JEOL USA, Peabody, MA) scanning electron microscope (SEM) after coating with a 7 nm of Pt/Pd.

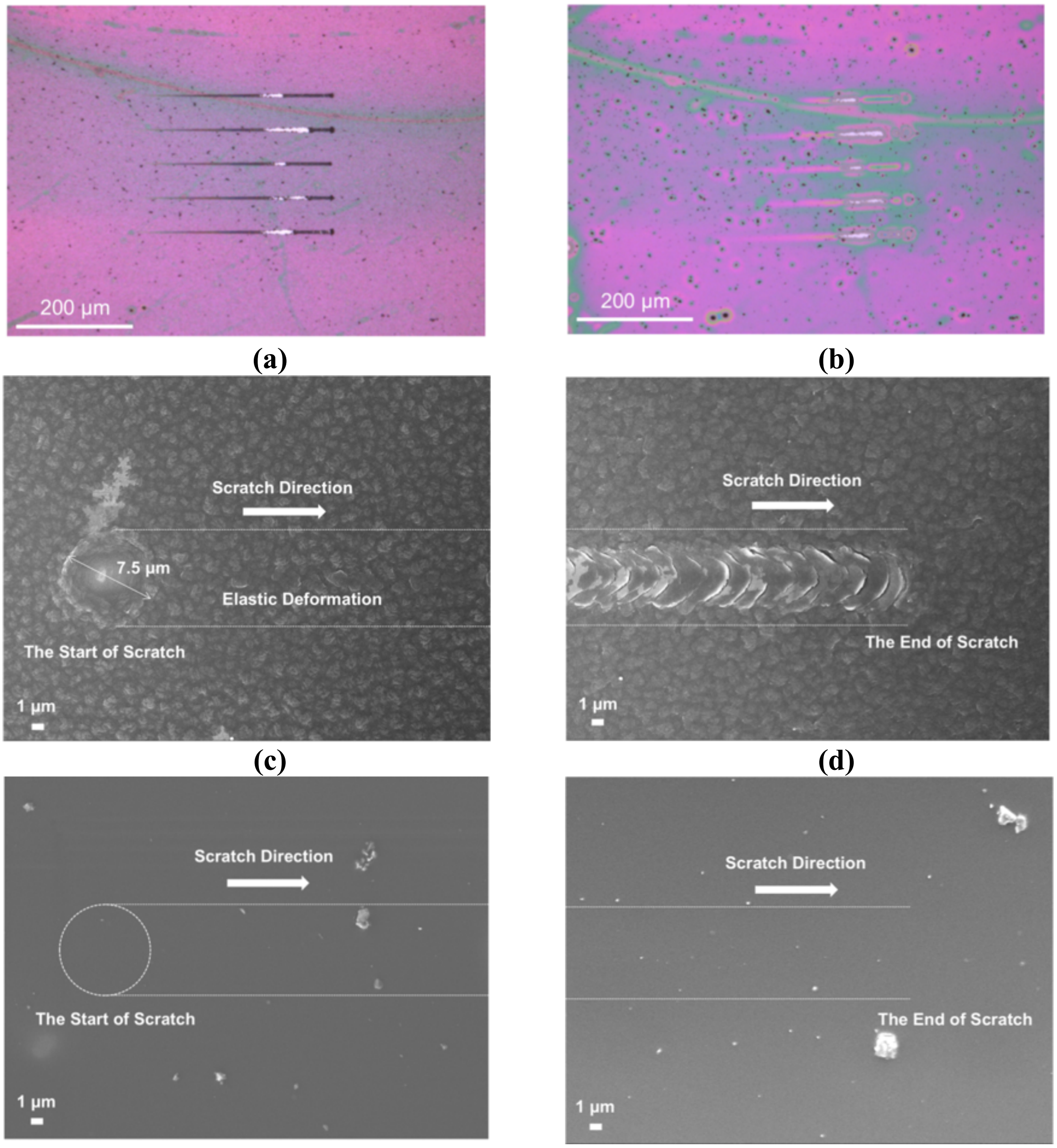

(a) **(b)**

(c) **(d)**

(e) **(f)**

Figure 4.4 Optical images of micro-scratches (a) before and (b) after self-healing. SEM images for the start and end of the scratch (c, d) before and (e, f) after self-healing.

4.3.2 Surface Roughness

Film surface roughness was measured using AFM. Four measurements were performed and the average values of *Rq roughness* are provided in Table 1. The AFM height roughness images are shown in Figure 4.5 for the as-deposited, submerged, and after-heating films. Initially, the surface of PEI/PAA film was rough showing deep pores/voids, which is typical for a polymeric multilayer thin film.[111] Once submerged in water for a day under a humidity condition of nearly 100%, the surface topographical features were swollen with water leading to a drop of *Rq* roughness to 1.4 nm (see Figure 4.5). Some of the water was diffused into the film (known as swelling water) and the rest was immobilized or confined at the rough surface layer (known as void water). After drying the film at RT, the Rq roughness remained similar to the submerged film. This was likely because the hydrophilic PEI/PAA film kept the void water, which filled the pores or free volume. These pores were initially filled with air in the as-deposited film.[195,196] Other researchers have reported that the hydrophilic PE film still had as much as 7% water in the voids inside the film after drying at room temperature.[197] To restore the original roughness, the film was dried at a temperature higher than its glass transition ($T_g \approx 100$ ℃)[46] in a vacuum oven for 24 hours. Roughness measurements were carried out afterwards and found to be similar to the as-deposited film (see process step 5 in Table 1). Heating at 120 ℃ forced the void water to evaporate, leading to a restoration of the roughness features. Therefore, the *Rq* roughness was recovered by annealing the film at HT. Note that the roughness measurements in step 4 were performed using the nanoindenter probe, which has a larger tip radius than the AFM probe.

However, the recovery of surface roughness after heating and the water removal did not yield a roughness identical to the as-deposited film. The thermally activated drying resulted in the growth of the peaks followed by a coalescence of these peaks. The film decreased its total free energy by reducing the tension of these features (peaks or voids). Therefore, these coalescences were dominated by shear between the lamellae.[198] In addition to diffusion driven-process, heating the film resulted in a thermal crosslinking of amine groups from PEI and carboxylic acid groups from PAA, which led to a smoother overall surface.[199]

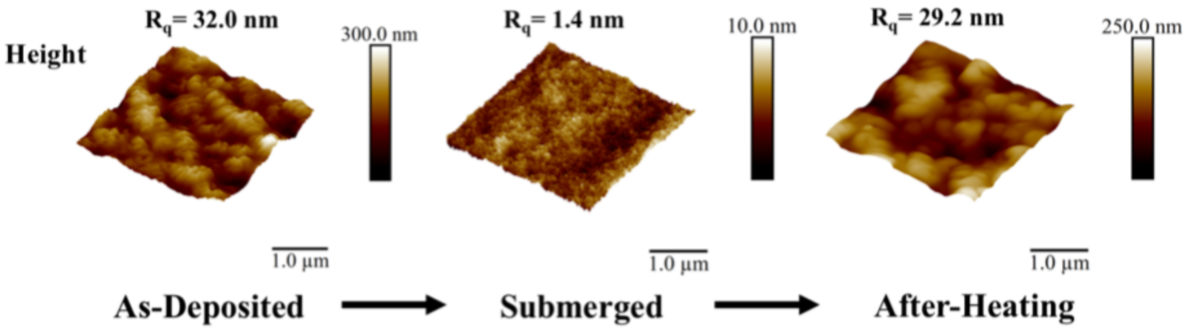

Figure 4.5 Height AFM images (5×5 μm^2) of the as-deposited, submerged and after-heating PEI/PAA films.

Table 4.2 AFM roughness, and nanomechanical properties of PEI/PAA films.

#	**Process Step**	***Humidity***	***Rq Roughness* (nm)**	**E_r (GPa)**	***H* (GPa)**
1	As-Deposited	~25%	31.8±1.9	14.80±3.12	0.44±0.11
2	Submerged	~100%	1.4±0.1*	0.54±0.12*	0.03±0.01*
3	Dry	~25%	1.3±0.2	14.98±0.94	0.44±0.06
4	Heating	<5%	6.8±0.3*	22.66±1.44*	0.76±0.02*
5	After-Heating	~25%	29.2±3.4	18.47±1.15	0.57±0.03

***In situ* measurements using either wet or HT AFM/nanoindentation**

To demonstrate the *in situ* recovery of roughness features, roughness height images were obtained before and during the *in situ* HT nanoindentation (see Figure 4.6). The surface roughness was scanned initially at RT after drying the thin film (step 3). Then, the film was heated to a temperature of 120 °C. Once heating reached a steady state after 15 min, the same surface roughness was scanned again at high temperature. The growth of peaks or pores was captured during this process with an increase in the *Rq roughness* to 6.8 nm. For a full reconstruction of peaks, the sample was heated for a longer annealing time such as 24 hours.

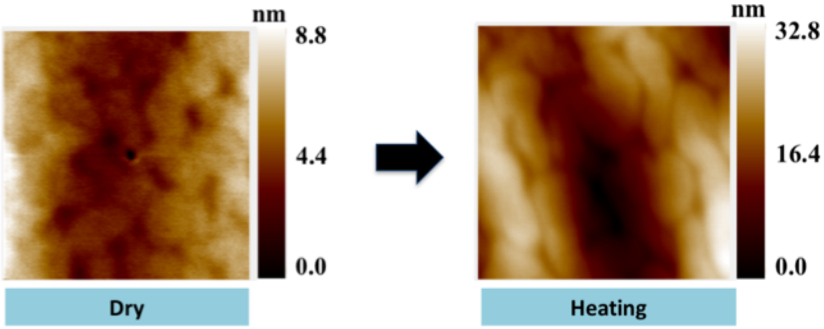

Figure 4.6 AFM roughness images (5x5 μm^2) for PEI/PAA film before and during heating (step 3 and 4 respectively in Table 1). Images were taken using the Berkovich HT probe.

4.3.3 Reduced Modulus and Hardness:

The mechanical properties were measured during each step of the healing process, and they are provided in Table 1. Humidity measurements were estimated for every process step similar to the conventions used in the literature.[183] For the as-deposited film, the mechanical properties and roughness measurement of 8 bilayers of PEI/PAA were similar to the ones reported in the literature for this thin film under similar conditions.[111] Once immersed in DI water (~100% humidity), the thin multilayer film became much softer, where roughness, modulus and hardness were reduced by about 100%. This is due to the plasticization of the PEI/PAA, where the water molecules broke the bonding between PEI and PAA. The hydrophilic film was swollen with a behavior similar to hydrogels. The internal ionic bonds were controlled by ionization ratio and charge density, which changes in water. This resulted in the breakage of the ionic bonds lowering the activation energy for diffusion, which allows the polyelectrolyte chains to shuffle freely.[200,201]

The film was left to dry overnight in a dry ambient room (see process step 3 in Table 1).

Once dried, the mechanical properties were found to be similar to the as-deposited film but with lower standard deviation for both the reduced modulus and hardness values. The ionic and hydrogen bonding were both recovered once dried in air, which led to the increase in the stiffness of the film again.[74,202] The lower standard deviation was due to the film surface becoming smoother, which reduced the deviation in the measurements.

Then, HT nanoindentation was carried out to better understand the recovery of the roughness mechanism using high temperature drying. Heating the polymeric film was found to increase its reduced modulus and hardness by 50 and 70%, respectively. This improvement was due to the following reasons: (1) the surface chemical reactions and molecular rearrangement (as indicated by XPS later). (2) The reduction of the free volume leading to a restricted motion of the polyelectrolyte chains (denser structure). (3) The thermal crosslinking and formation of new covalent bonding.[203] Once, the polymeric film was cooled down to RT (see process step 5 in Table 1), its mechanical properties were reduced but remained higher than as-deposited film. This showed that this enhancement, which took place during the heating treatment, was permanent.

Figure 4.7 shows the capillary forces in the force-displacement curve for different steps (below zero). A higher lift height of 180 nm was required to precisely find the contact point of load-displacement curve for the submerged sample. In the case of the RT and HT experiments, a lower lift height of 25 nm was sufficient to determine the zero-contact point in the load-displacement curve.

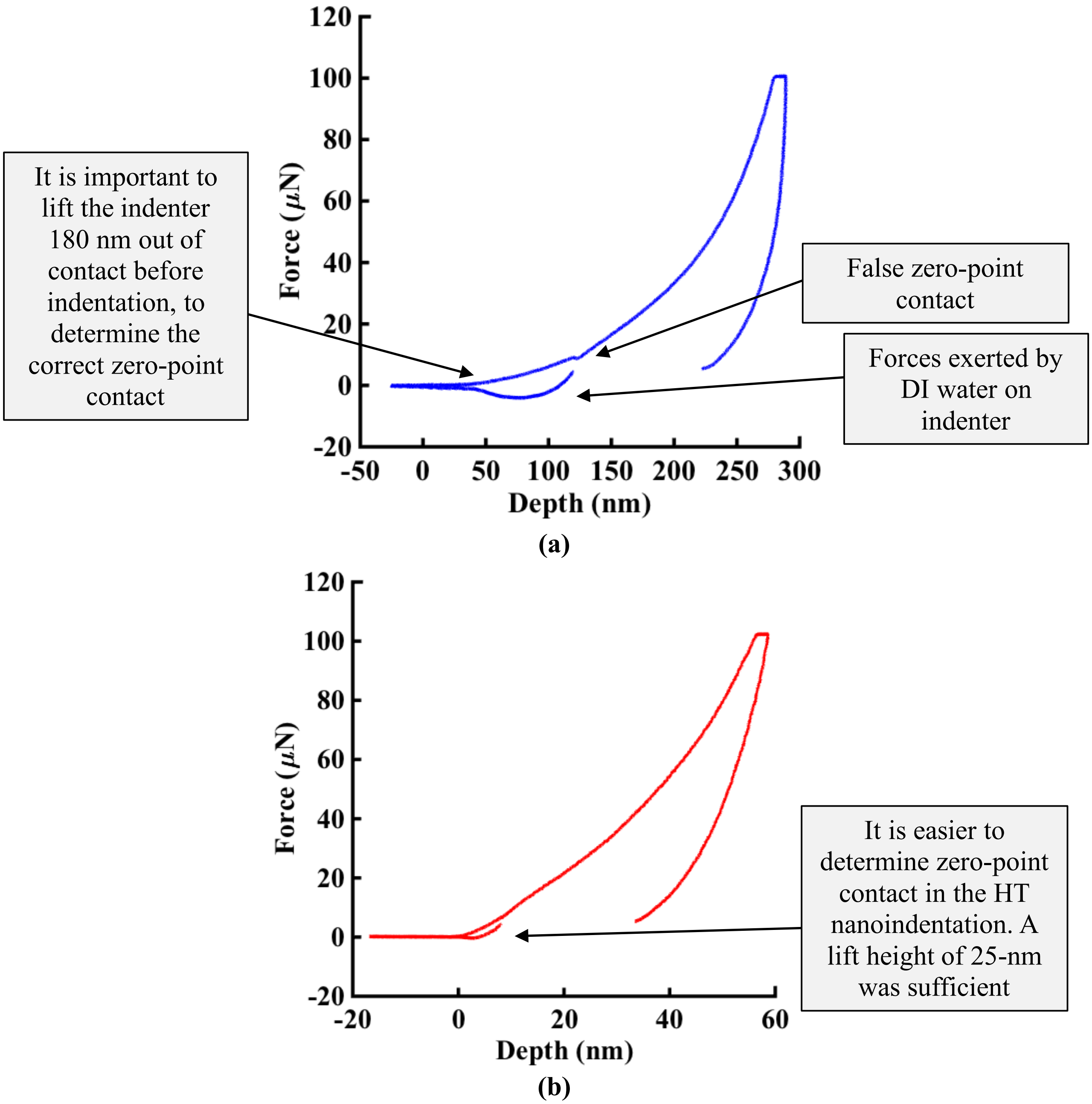

Figure 4.7 An illustration for how to define the zero point in the load-displacement curve for PEI/PAA film under (a) Submerged condition (b) Heating condition.

The load-displacement curves in Figure 4.8 shows two opposite trends for the film during the *in situ* submerged and the HT experiments, as compared to the as-deposited film. In case of the submerged experiment, the film was much softer, while it became harder to penetrate at HT. The opposite trend was due to the changes in the free volume between both the submerged and HT conditions. Immersing the film in DI water yielded an enlargement of free volume, while heating the film resulted in a reduction of free volume and a higher densely packed molecular arrangement.[204–206] Therefore, the amount of free volume of a polymer was found to be closely linked to the mechanical properties of PEI/PAA thin film. The hydrophilic PEI/PAA film, when in contact with water, expands. The breakage of bonding enhanced the mobility of the chains (diffusion) and hence the stiffness.[192,193] Figure 4.9 provides additional load-displacement curves for as-deposited, submerged and heated PEI/PAA films.

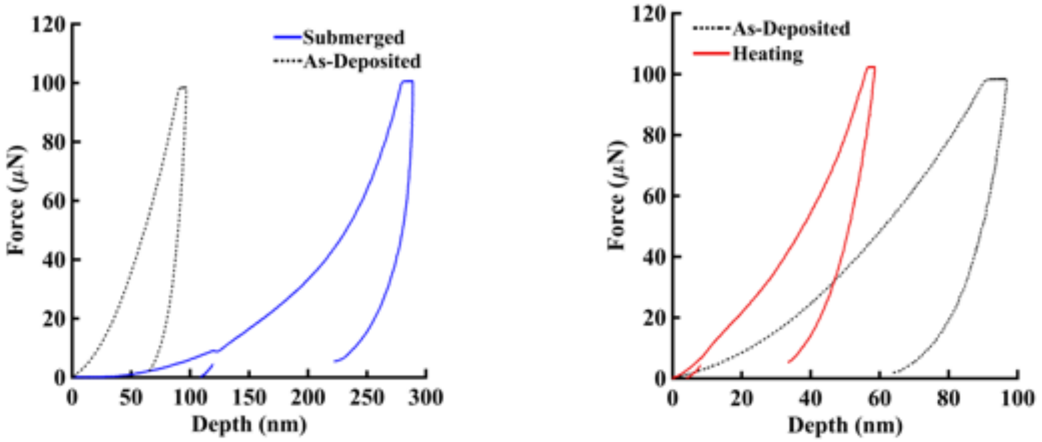

(a) (b)

Figure 4.8 Representative comparative load-displacement curves for the thin film during (a) as-deposited and submerged and (b) as-deposited and heating.

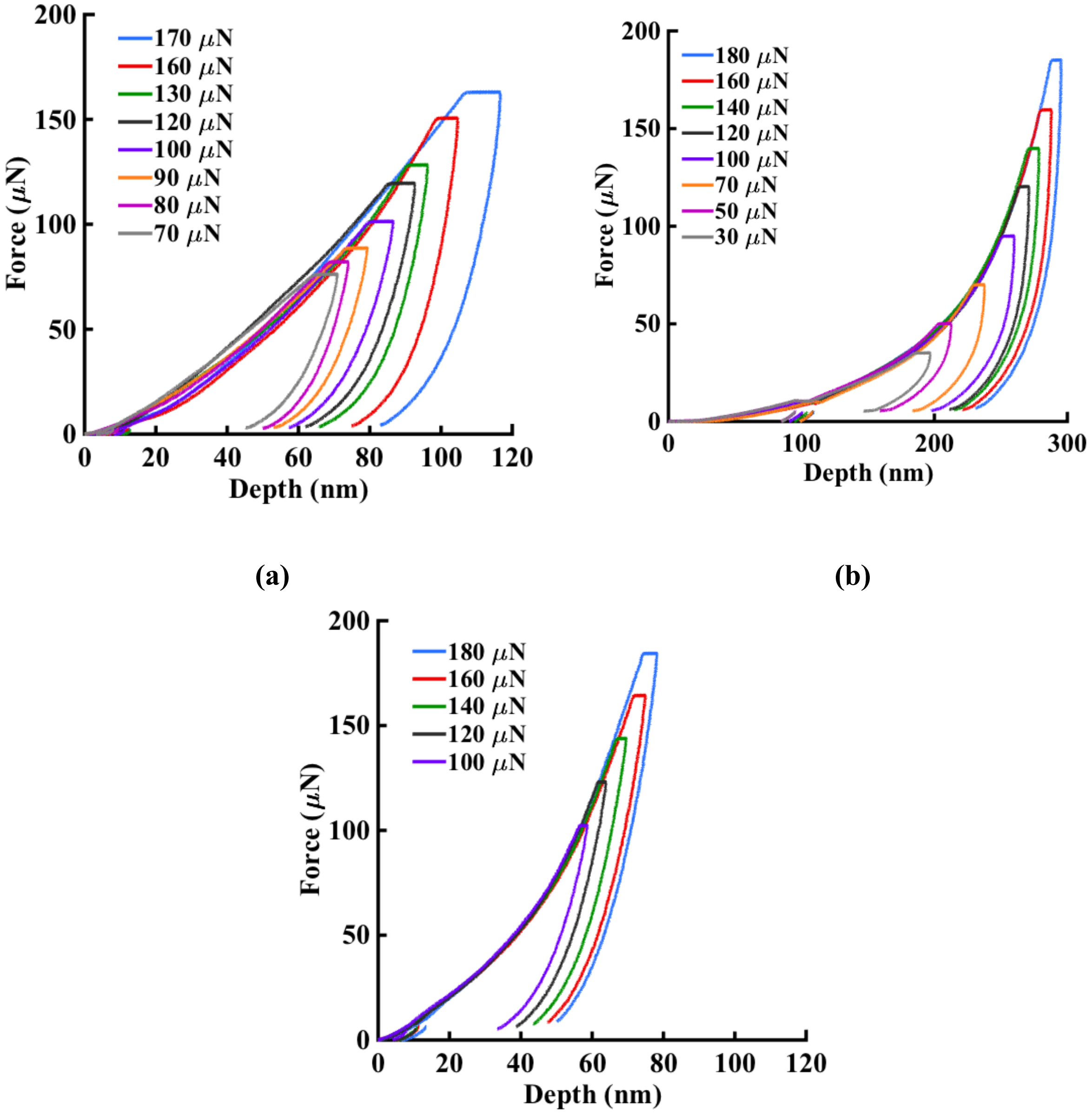

(a) **(b)**

(c)

Figure 4.9 Load–displacement curves for the (a) as-deposited (b) submerged (c) heating PEI/PAA films.

Figure 4.10 shows the residual nanoindentation marks and profiles for the self-healing steps using a maximum nanoindentation force of 2 mN. The residual nanoindentation mark was surrounded by rough features for the as-deposited film. Immersing the thin film in DI water made the nanoindentation area about eight times bigger with a residual nanoindentation depth almost twice than that of the as-deposited film. The bigger residual nanoindentation mark was due to both the softening of the polymer, as discussed earlier, and the rough surface of the as-deposited film, where liquid molecules were confined in the narrow valleys of the surface roughness leading to a larger nanoindentation depth.[207] Drying the film at RT made the contact area and depth smaller, but it still remained larger than the as-deposited film. *In situ* HT nanoindentation showed the *in situ* formation of topographical features. The nanoindentation residual area became as small as the as-deposited film, but with lower residual depth due to the film becoming stiffer and harder to penetrate. The after-heating film resembled the behavior of as-deposited film with minor differences due to the coalescence of roughness features and the formation of covalent bonding.

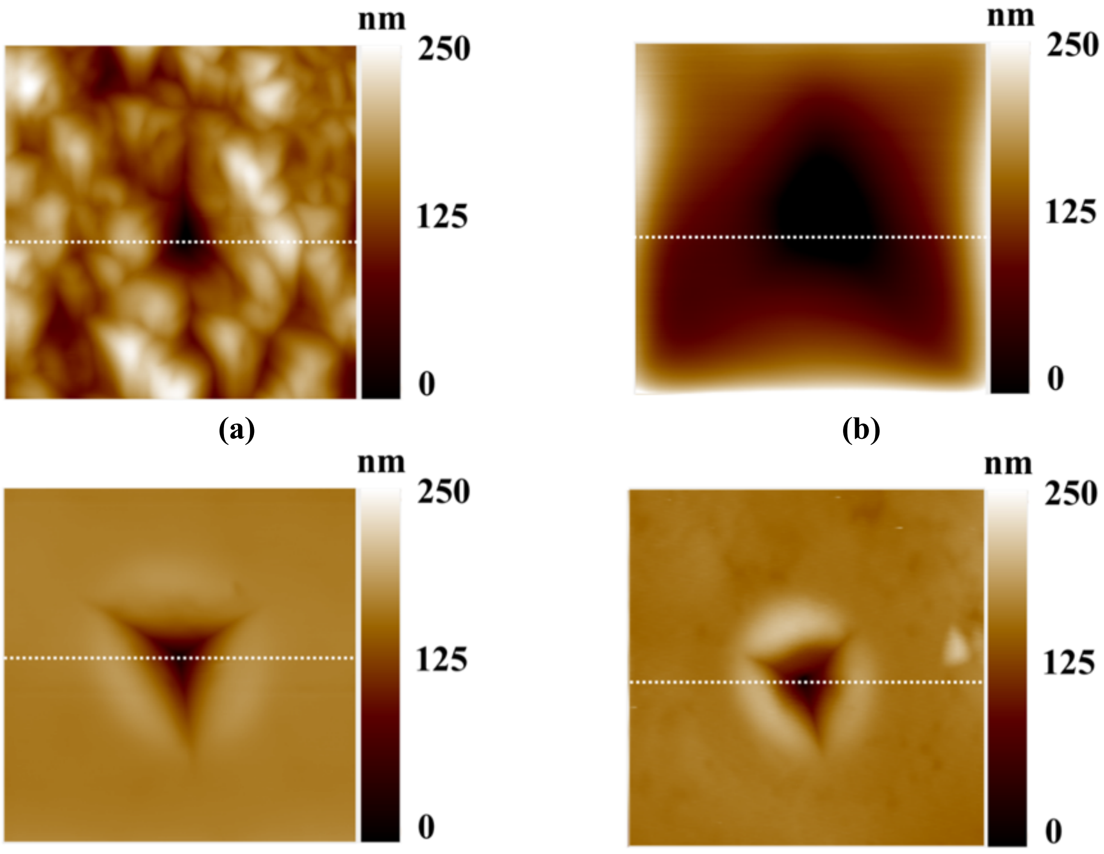

(a) (b) (c) (d)

Figure 4.10 Residual 2mN nanoindentation images (5x5 μm^2) for the (a) as-deposited (b) submerged, (c) dry, (d) heating, (e) after-heating films, and (f) representative cross-section profiles of the residual nanoindentation marks.

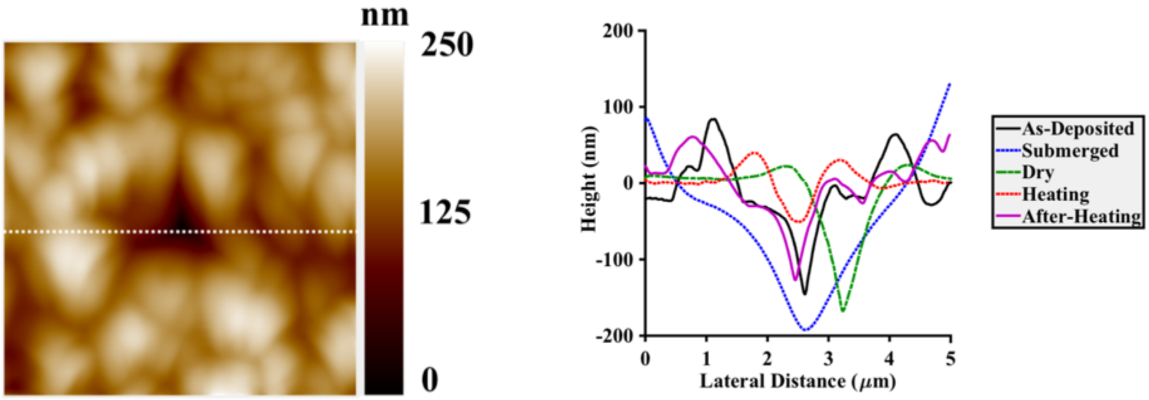

(e) (f)

Figure 4.10 Continued.

The influence of water plasticization on the PEI/PAA films influenced both bulk and surface properties. This process is summarized schematically in Figure 4.11. In terms of mechanical properties, they were recovered after drying the film at RT for 24 h (humidity ≈ 25%) due to quick rehydration and recovery of the initial thickness of the film. However, the surface properties such as roughness did not recover after the same period. The multilayer thin film had immobilized water molecules within the pores of surface roughness, which were not removed by simple drying at RT. Therefore, there was a need for a second external high energy stimulus such as drying at higher temperature (humidity < 5%) to reach complete desorption of the moisture and force the leaching of water molecules. Water molecules were bonded to PEI/PAA and therefore an external stimulus, such as heat, was required to break this bonding. Similar results were observed with adhesive joints, when subjected to moisture absorption.[208]

Furthermore, as mentioned earlier, the water absorbed by the polymeric film can be divided into either void water or swelling water. The absorbed water can influence both the bulk and the surface of the polyelectrolyte multilayers film.[209] The water can be immobilized on the surface or diffuse into the polymer film. Upon drying the film at room temperature conditions, the swelling water evaporates and the film de-swells. However, the immobilized water, which is trapped on the voids of the surface roughness would require heating. The rougher surface will swell in a more pronounced way than the smooth surface because it can contain more immobilized water.

The recovery of mechanical properties such as E_r and H with 24-hours drying at ambient condition was driven by the relaxation of ionic bonding after partial removal of water. However, electrostatic assemblies with ionic bonding is known to lose some of their structural integrity when absorbing water.[210] Therefore, more energy in the form of heating was required to reconstruct the surface roughness of the film. During heating, additional strong covalent bonding was formed at HT.[211] Once cooled down to RT, the thin film had higher reduced modulus and hardness than as-deposited film due to the film being ionically bonded with new physical crosslinks. The incorporation of covalent crosslinks resulted in an improved mechanical properties, higher resistance to deformation and increased self-healing efficiency.[212,213] The PEI/PAA thin films showed satisfactory stability for repeated exposure in water**.** In a recent study, the swelling-drying process was repeated ten times and it was found to be reversible without damaging the multilayer nano coating.[153] In addition, other researchers have showed similar findings for liquid water.[197]

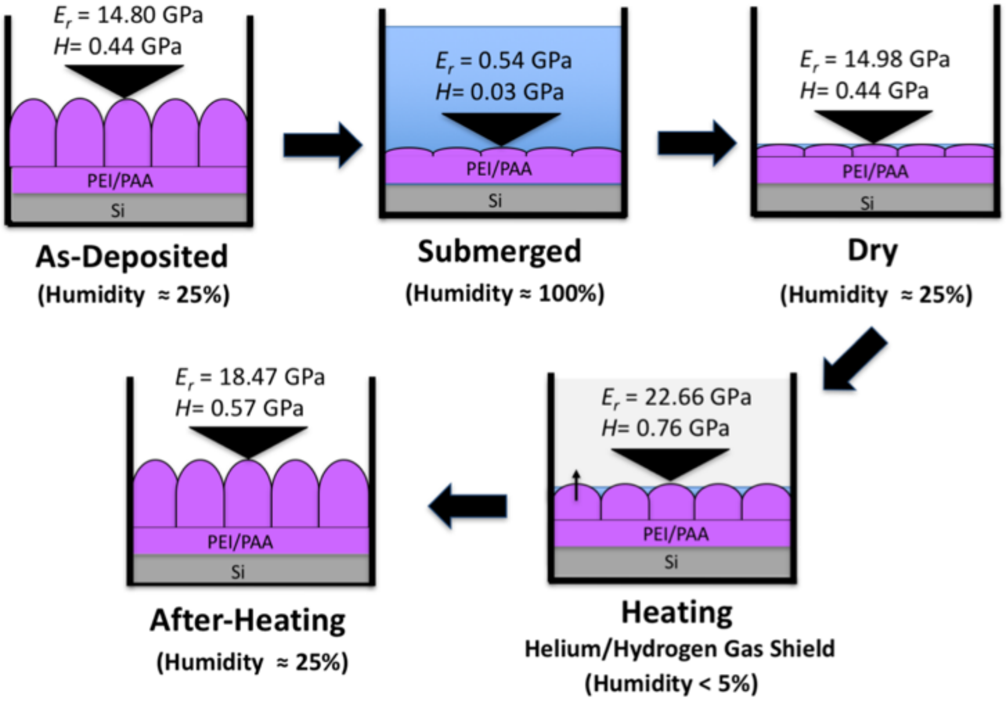

Figure 4.11 Graphical representation of the changes in the nanomechanical properties and morphology of a thin polymeric film under different humidity and temperature conditions.

4.3.4 FTIR & XPS

The chemical structure of PEI/PAA films was identified using FITR, as shown in Figure 4.12. Characteristic peaks of PEI at 3272 cm^{-1} (–N–H stretching), 2940–2830 cm^{-1} (–C–H stretching), 1576 cm^{-1} (–N–H bending), 1465 cm^{-1} (–C–H bending) and 1350–1000 cm^{-1} (–C–N stretching) were found in the spectra. The peak at 1656 cm^{-1}, which corresponded to the stretching band of –C=N, indicated the Schiff reaction between the amine groups of PEI and aldehyde groups. The peak of stretching vibration of –N–H which typically appears at 3272 cm^{-1} in the spectrum of PEI, transferred to 3424 cm^{-1} in the case of the composite film. For PAA, typical absorption bands of acrylate monomer at 1727, 1635 and 810 cm^{-1} were assigned to C=O stretching, C=C vibration and =CH alkene twisting absorptions, respectively. By comparing the FTIR spectra of the as-deposited and the after-heating films, it could be concluded that none of the chemically functional groups had been deteriorated due to the self-healing process that took place.

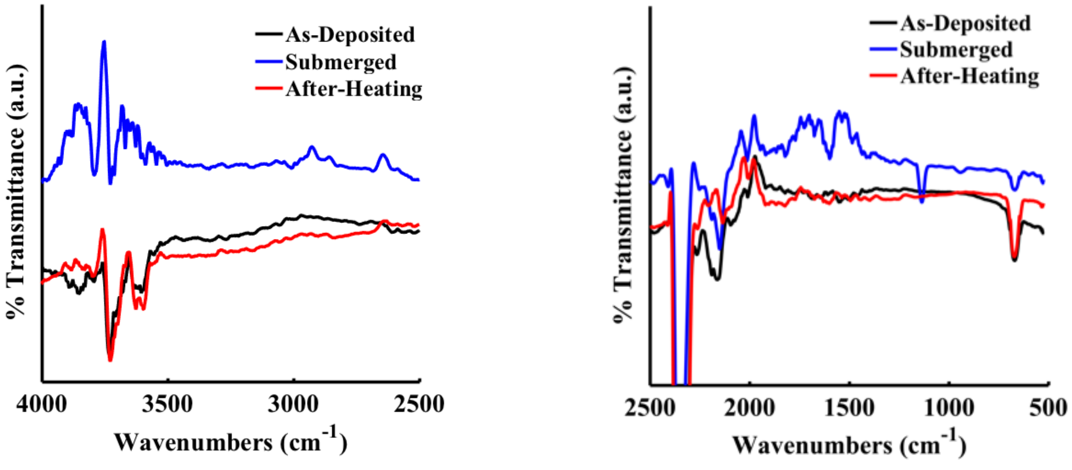

(a) **(b)**

Figure 4.12 FTIR spectra of the PEI/PAA film under different conditions for wavenumbers of (a) 2500-4000 cm^{-1} (b) 500-2500 cm^{-1}.

Using XPS analysis, in the C1s spectrum (Figure 4.13(a)), the major peak at 284.6 eV corresponded to C-C bond, whereas there was a contribution at 288 eV corresponding to C=O bonding environment (ketones environment). In the O1s core level spectrum (Figure 4.13(b)), the peaks could be analyzed to the contributing peaks from 530, 531 and 532 eV corresponding to C-O, which shifted to 533 eV (C=O bond). The O1s peak of the as-deposited film was shifted to higher binding energies, as compared to the after-heating film. This corroborated for the presence of more oxidized species in the as-deposited film, which could be traced on the surface of the analyzed film. This could be interpreted either as the more oxidized species have been ‘sacrificed’ in the healing process or that the healing process was accompanied by a reaction that led to the formation of less oxidized species or a diffusion of the more oxidized species towards the bulk (inwards diffusion from the surface to the bulk that happened on the course of the healing process). The later scenario was adopted as diffusion was anticipated to play a key-role in the self-healing process.

The species that most actively had participated in the healing process are the N-containing species. Since the FTIR studies did not show any functional group forming or disappearing from the surface with the heat treatment, the most predominant mechanism of N-species participating in the healing could be considered through the mechanism of molecular re-orientation and diffusion. The latter was taking place during the self-healing process to such extent that the N-containing polymer chains were diffusing in greater depths (from the surface to the sub-surface) and covered by the self-healed layer. This explained the deterioration of N-containing species into the healing process due to their migration to greater depths (see Figure 4.13(c)). The N1s peak could be analyzed into two contributions in 399 and 401 eV species, which were contributing to NH and NH^{3+} species.

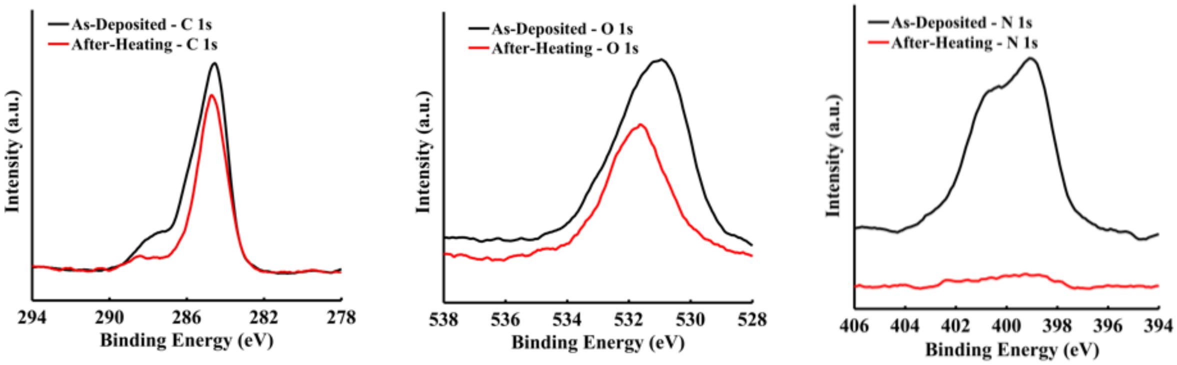

(a) **(b)** **(c)**

Figure 4.13 XPS core level spectra of (a) C1s, (b) O1s, and (c) N1s for the as-deposited and after-heating films.

4.4 Summary of Chapter 4

In situ wet and HT nanoindentation techniques were used to measure the nanomechanical properties and to gain further knowledge about the self-healing process of the polymeric multilayer thin film, PEI/PAA. These techniques were successful in measuring the changes in the mechanical behavior and topography of the film, which occur during the self-healing process. The complete self-healing of polymeric films back to the condition of as-deposited film (measured using nanomechanical properties of *Er* and *H*) and surface shape (measured using surface roughness) required multiple stimuli such as a change in relative humidity and temperature. The mechanical behavior of the polymeric film undergoing high humidity and temperature was different. The immersion in DI water led to the swelling of the polymer and softening of the thin film, while heating led to a stiffer surface due to the thermally induced molecular rearrangement and diffusion of species toward the surface (O-species) or toward the deeper depths (N-species). No functional groups were consumed during the self-healing process.

5 MECHANICAL BEHAVIOR OF POLYMER NANOCOMPOSITES ON STIFF AND COMPLIANT SUBSTRATES

5.1 Introduction

Polymer multilayer thin films, also known as polymer nanocomposites, have been successfully used for many applications such as flame suppression,[214] anti-reflection,[215] organic electronics,[216] gas and vapor barriers,[217] self-healing coatings,[218] tribological coatings,[219] and in drug delivery.[220] These films are typically deposited using spin casting,[221] plasma deposition,[222] spray processing ,[223] 3D printing,[224] and layer-by-layer (LbL) assembly.[225] The last is known to be tunable, versatile, simple and scalable.[199] Also, due to the nature of the deposition through exposing a charged substrate to cationic and anionic solutions, the technique results in thin films, which are bonded strongly to the substrate through electrostatic attraction,[226] ionic and hydrogen bonding,[153] and covalent bonding using thermal or chemical crosslinking.[199]

Mechanical properties play a critical role in the durability of polymeric thin films. For example, scratching a thin film reduces its functionality for gas barrier application as the gas would find an easier path to escape.[69] Therefore, an understanding of the nanomechanical behavior of these films is essential. It is often challenging to test free-standing nano-thick films using tensile testing.[227] Another challenge is to make freestanding nanoscale LbL films.[183] Nanoindentation stands out as an effective technique to extract the intrinsic properties of thin films. Thin films are deposited on substrates to provide support during the experiments, where compressive forces are being applied. Nanoindentation measurements need to be carried out within 10-20% of the film thickness to reduce the influence of substrate properties and maintain the deformation locally within the film. This rule is found to work well when the substrate is stiffer than the thin film.

Therefore, multilayer thin films are typically deposited on stiffer substrates such as silicon or glass for nanoindentation experiments.[57–60]

However, the "10% rule" was found to fail when the substrate is more compliant than the deposited thin film.[42] Also, the 10% rule is hard to maintain for very thin films, e.g., thinner than 100-200 nm as indents need to be performed in shallower depths less than 10-20 nm.[228] Yet, it is essential to understand how thin films behave when deposited in compliant substrates. Typically for many applications such as gas barriers,[229] bioelectronics,[230] flame retardant [231] and drug delivery,[232] the multilayer LbL films are deposited on compliant substrates. For example, polymer/ platelet assemblies are deposited on PET, which is a commonly used food packaging material.[31]

Studying thin films on rigid substrates provides an insight for the intrinsic properties of the thin films. However, the interface and the deformation behavior could be different when a thin film is deposited on different substrates, as the interfacial properties between the film and substrate influence the mechanical response of these films. In the case of Poly(methyl methacrylate) (PMMA) films, it was observed that films get stiffer in depths close to the silica substrate. This higher stiffness is measured through an increase in the elastic modulus and glass transition temperature, which highlights the origin of the increase, namely confinement in the polymer chain dynamics.[228] However, more compliant substrates with stiffness similar to the film could result in a different mechanical behavior for the film and possibly different polymer chain dynamics for the thin film. Furthermore, the compliant substrate could result in lower reduced modulus, and it would dominate the behavior of the film.[233,234] Lastly, when the substrate is significantly more compliant, buckling, cracks and delamination of the relatively stiffer thin film due to the large elasticity mismatch can take place during nanomechanical testing.[235]

In this study, the nanomechanical properties of Polyvinylamine (PVAm)/Graphene oxide (GO) deposited on two distinctly different substrates, namely Si and PET, were measured using nanoindentation and nanoscratch. In a recent study, different polymer multilayer thin films including all-polymer and polymer/platelet assemblies were studied using nanoindentation.[111] These thin films were deposited on rigid silicon wafers and the intrinsic thin film modulus and hardness were successfully measured. To the best of the authors' knowledge, the nanomechanical properties of LbL multilayer thin films on compliant substrates such as PET have not been measured using nanoindentation and nanoscratch. Typically, coatings for gas barriers applications are deposited on a compliant substrate such as poly(ethylene terephthalate) (PET).

Herein, an understanding of the nanomechanical and interfacial behavior of these thin films on different substrates was developed. The behavior of PVAm/GO, deposited on Si and PET was found to represent a compliant film on stiff substrate and stiff film on compliant substrate, respectively. In the case of PVAm/GO on Si, the "10% rule" holds, and it is possible to measure the intrinsic properties of the thin film. However, extracting the mechanical properties of the thin film on PET was found to be challenging. In terms of scratch experiments, both film/substrate systems exhibited different behaviors due to the difference in the compliance of the substrate and the adhesive strength at the interface. Complementary computational modeling further explained the different scratch behavior for both systems.

5.2 Methods

5.2.1 Materials and Processing

The LbL assembly in this study consists of alternately depositing PVAm (95% hydrolyzed, M = 340 kDa, trade name Lupamin 9095, BASF, Ludwigshafen, Germany) and GO (Graphenea, Cambridge, MA). First, PVAm was dialyzed three times for 24 hours in 18.2 MΩ DI water using cellulose dialysis tubing (M_{cutoff} = 14 kDa, Sigma Aldrich, St. Louis, MO). Then, both materials were diluted in DI water to 0.1 wt %. Later, PVAm was adjusted to the desired pH using 1 M NaOH or HCl (Sigma). While, GO was dispersed well using 15 W tip sonication. Before each deposition of either PVAm or GO, the thin film is rinsed with DI water and dried with filtered air. The cycle was carried out using a home-made robotic system and it was continuously running till the desired thickness was reached. The thickness increased linearly with the number of bilayers, therefore 29 layers of PVAm/GO yielded a film thickness of 150 nm. The recipes for the deposition of PVAm/GO multilayer thin film using LbL were adopted from a recent work by the authors.[236]

5.2.2 Substrates

The single-side polished (100) Si wafer (University Wafer, South Boston, MA) and the PET films with a thickness of 179 μm (ST505, Dupont-Teijin, Chester, VA) were used as deposition substrates and for nanomechanical testing. Prior to film deposition using LbL, the surface of the substrate was cleaned and oxidized to promote a surface charge in order for the first PVAm layer to adhere through ionic interactions. For Si, it was cleaned using acetone, methanol and DI water followed by 10 min air plasma treatment (Harrick Plasma, Ithaca, NY). The plasma was primarily oxygen plasma, and oxidized the silicon to silicon oxide and silicon hydroxide groups.[237] The active oxidative species in this case are atoms of oxygen rather than molecular oxygen. As the Si oxidation proceeds converting Si into SiO_2, diffusion of atomic oxygen through SiO_2 takes place .[238]

In the case of PET, it was cleaned with rinsing in DI water, methanol and air, multiple times. Finally, it was treated using corona treatment (BD-20C Corona Treater, Electro- Technic Products Inc., Chicago, IL). This treatment was used to create a net oxygen imbalance on the PET surface. This cleaning technique is used typically in packaging to help ink adhere to a PET substrate.

Figure 5.1 shows the schematic for the growth of the thin film of PVAm/GO on both substrates. The horizontal lines in Figure 5.1 (a, b) represent the bi-layers. Figure 5.2 illustrates the cross-sectional images using transmission electron microscopy (TEM) for PVAm/GO on PET. Due to the small contrast between PVAm and GO, it was hard to see the different layers of the thin film. To enhance the contrast, thermal reduction at 175 ℃ was used to remove the moisture and some of the oxygen-containing groups. Figure 5.2(b) shows the reduced thin film. The thin film was highly ordered and uniform at the nanoscale. Also, the film thickness on Si and PET was measured using a Tencor profilometer and cross-checked with the TEM cross-sectional images.

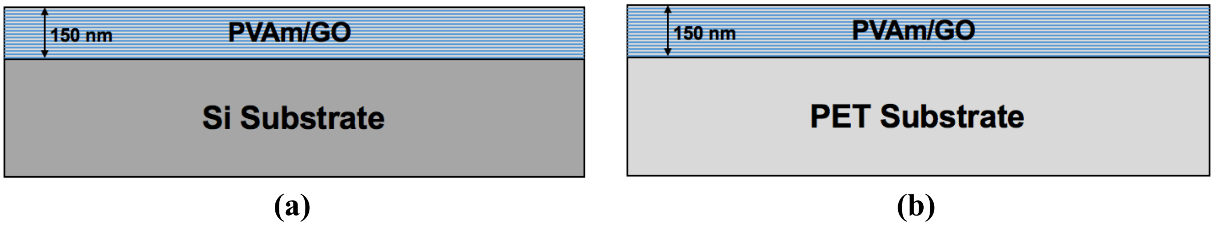

(a) **(b)**

Figure 5.1 Schematic showing both the PVAm/GO thin film on (a) Si and (b) PET substrates.

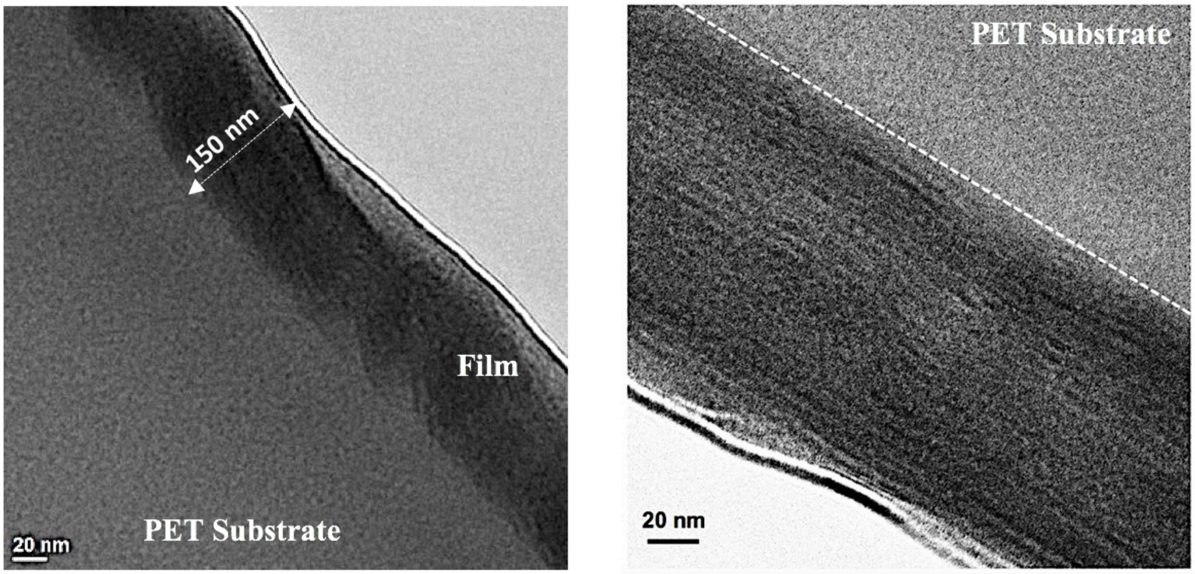

(a) **(b)**

Figure 5.2 (a) TEM image of PVAm/GO film on PET substrate (b) TEM image of thermally reduced PVAm/GO showing single layers of PVAm and GO.

5.2.3 AFM

Atomic force microscopy (AFM) was performed using a Dimension Icon AFM (Bruker, Billerica, MA) to measure the root-mean-square (Rq) roughness of the film on both substrates. The scan area was 5x5 µm. AFM silicon tip with a nominal radius of 8 nm and resonance frequency of 150 kHz was used. The scanning rate was set to 0.5 Hz to obtain high quality images.

5.2.4 Nanoindentation

Nanomechanical experiments were carried out using a TriboIndenter (TI) Premier, (Hysitron Inc., Minneapolis, MN). To extract data at very shallow depths, an ultra-sharp cube corner indenter was used for the nanoindentation measurements.[239] First, the nanoindenter system need to be calibrated, which is known as the contact area function of the tip. The contact area (A_c) is related to the contact depth (h_c) through the Oliver and Pharr method, where the contact area function is:

$$A_c = C_o h_c^2 + C_1 h_c + C_2 h_c^{1/2} + C_3 h_c^{1/4} + C_4 h_c^{1/8} + C_5 h_c^{1/16} \quad (1)$$

C_1-C_5 are curve-fit coefficients, which are related to tip imperfections and C_o equals 2.598 for a 90º cube corner tip. C_1-C_5 coefficients were found experimentally by performing a series of nanoindentations on a standard fused quartz (FQ) sample with known properties of reduced modulus (E_r) = 69.6 GPa (±5%), and hardness (H) =9.3 GPa (±10%). In this work, 100 nanoindentations were performed on FQ and the contact area was calibrated for contact depths of 5-50 nm, using a standard transducer.

5.2.5 Nanoscratch

The nanoscratch experiments were carried out using the same TriboIndenter Premier (Hysitron Inc., Minneapolis, MN) to study the frictional behavior of PVAm/GO thin films on Si and PET. Two different scratch experiments were performed: (a) constant normal loads of 25, 100 μN and (b) a ramp normal load up of 300 μN. The sliding speed and scratch length were kept at 0.67 μm/s and 6 μm. To calculate the elastic recovery, a height scan was performed using the same tip to measure the initial topography and the residual scratch depth. The coefficient of friction (COF) was measured for each experiment by dividing the friction over the normal force.

5.2.6 Raman spectroscopy

Raman experiments were carried out to get an insight of the structural similarities of the two films during their growth process. For this purpose, a Raman confocal microscope made by Horiba Ltd (Jobin-Yvon LabRam) was used. The pinhole diameter is 200 nm and the objective optical lens is 100x, making the spatial resolution of the beam 3.7 μm. The laser wavelength was 633 nm and the exposition time was 15 s with 5 accumulations for each test at room temperature. Experiments were repeated 2 times to ensure repeatability.

5.2.7 Finite Elements Analysis (FEA)

To understand the stress/strain distributions, contact pressure and the onset of yielding for both systems under nanoscratch process, FEA was carried out. The behavior was restricted to elastic analysis and it was implemented using a commercial code, ABAQUS. The PVAm/GO film was modeled as a homogenous single layer material, where the multilayers were well bonded to each other neglecting the interfacial properties between each layer. Likewise, both Si and PET were modeled as homogenous materials. Fully bonded condition is also assumed between the substrate and the film. A constant load of 100 μN in the vertical direction was applied. Then, the indenter moved to the right while maintaining the same normal load. The indenter was modeled as a half sphere using an analytical rigid surface with a conospherical tip radius of 870 nm. Due to the symmetry across the *xy* plane, only half of the geometry was considered to save computational power (see Figure 5.3). Boundary conditions were applied to restrict the movement in the y-direction at the bottom of the substrate. Similarly, the x-movement was restricted in the left and right of the film and the substrate. A biased mesh towards the surface was used to increase the density of the mesh near the surface and the interface between the film and the substrate.

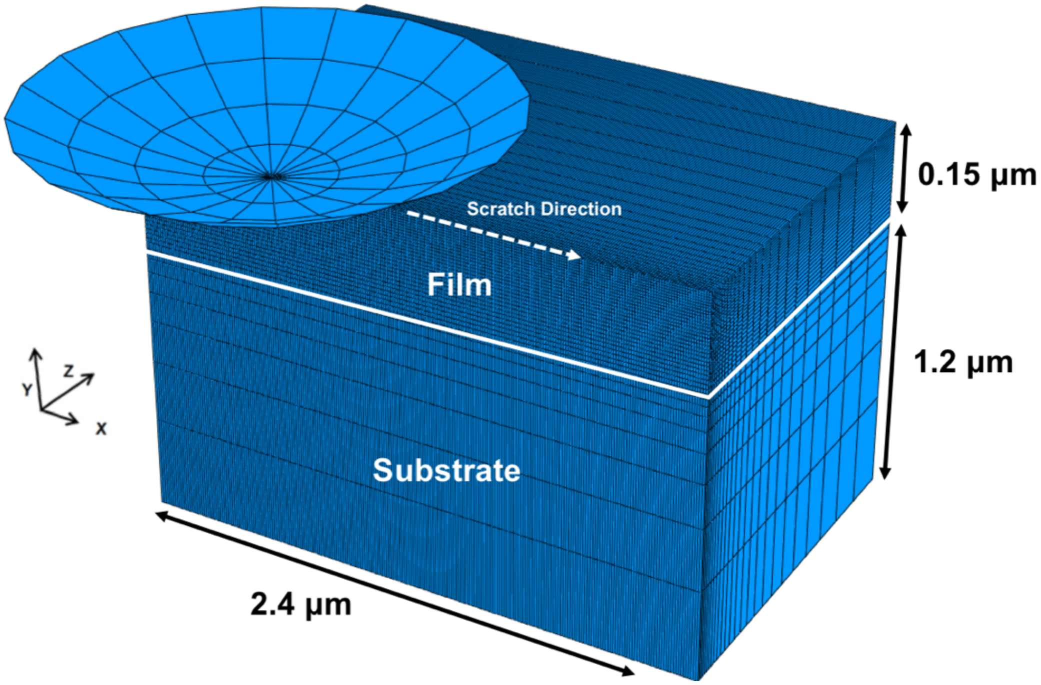

Figure 5.3 Finite element model for nanoscratch on film/substrate systems.

5.3 Results & Discussion

The average values of the elastic modulus and hardness for the Si and PET substrates were first obtained (Table 5.1). All nanoindentation experiments were kept within the calibrated contact depth range on FQ. The obtained properties (reduced modulus and hardness) for both Si and PET agree with reference data.[134,240] The silicon substrate is much stiffer and harder than the PET substrate. Therefore, the nanomechanical and nanotribological behavior of the thin film on Si and PET is expected to be different due to the effect of the substrate.

Table 5.1 Elastic Modulus and Hardness for standard sample, and Si and PET substrate.*

Substrate	E_r (GPa)	H (GPa)
Si	169.00±9.56	12.01±0.87
PET	4.22±0.49	0.22±0.04

*Error bars show ±1 standard deviation

5.3.1 *Nanoindentation Experiments*

The film thickness, roughness, E_r and H were extracted for PVAm/GO film on both substrates and are given in Table 5.2. Both cases were found to have similar R_q values, and the AFM height images of the surface roughness are shown in Figure 5.4. The average film thickness was measured to be ~150 nm using TEM and, it was also checked using a contact profilometer. Therefore, the surface roughness and film thickness on both films are similar, as desired, making the substrate as the only difference between both films. The reduced modulus and hardness of PVAm/GO film on Si was 2 and 1.3 times higher than the PVAm/GO film on PET. The mechanical properties were extracted from depths between 10-20% of the film thickness.

Table 5.2 Nanomechanical properties of PVAm/GO thin film on Si and PET substrates.

Thin film	Substrate	Thickness (nm)*	*Rq* Roughness** (nm)	E_r (GPa)	H (GPa)
PVAm/GO	Si	150	8.58	12.08±2.81	1.04±0.35
PVAm/GO	PET	150	8.98	5.89±1.64	0.78±0.39

*Film thickness was measured using Tencor profilometer

** Rq roughness are based on 5 × 5 μm AFM measurements.

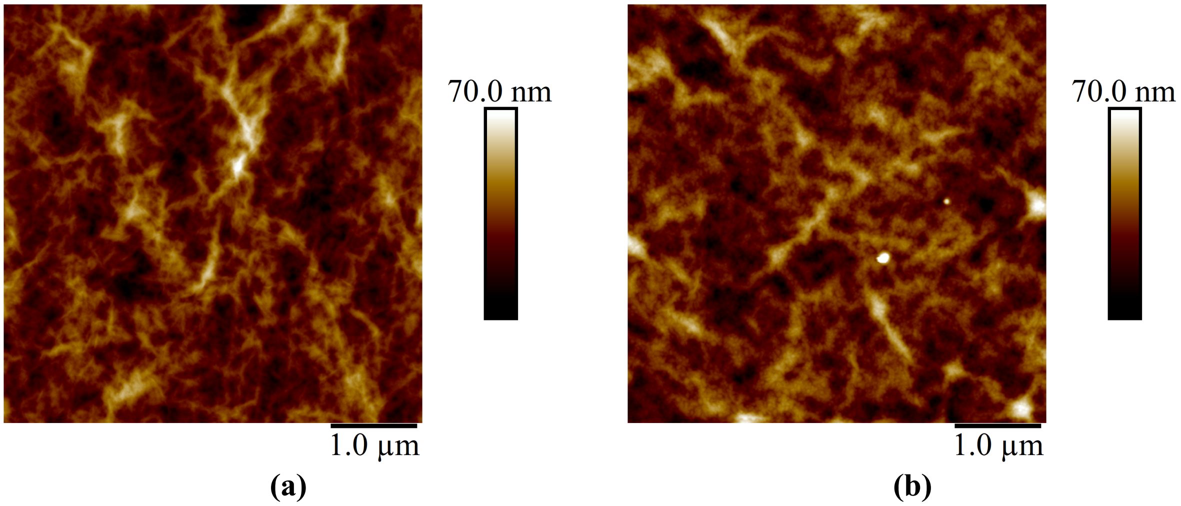

(a) **(b)**

Figure 5.4 AFM roughness height image for PVAm/GO on (a) Si and (b) PET substrates.

Figure 5.5 shows the reduced modulus and hardness as a function of contact depth per film thickness for both Si-based and PET-based films. The reduced modulus shows higher mismatch in stiffness behavior for both films. Beyond the 15% film thickness for the Si-based film, the substrate-effect resulted on a sharp increase in the modulus. While Si-based film showed a clear change due to the substrate-effect, the PET-based film did not show a clear change in the reduced modulus with increasing depth. However, both films show clear trends for hardness, where the Si-based film showed increasing hardness, similar to the reduced modulus. The Si-based film showed more scattering data potentially due to a more disorder in the carbon material, as was proved by Raman studies (presented below). On the other hand, the PET-based film showed a decreasing hardness with contact depth, which is to be expected as PET is softer. To confirm this observation, a Berkovich probe was also used to induce deeper nanoindentations. The data was plotted in semi-log scale and provided in Figure 5.6. The lower Young modulus for PET-based film was dominated by the bending of the compliant substrate at both shallow and deeper penetrations. However, the hardness was dominated by the film at shallow depths and the bending of the substrate at higher depths.[241] This lead to a rapid decay of hardness as the probe broke into deeper layers of the film.

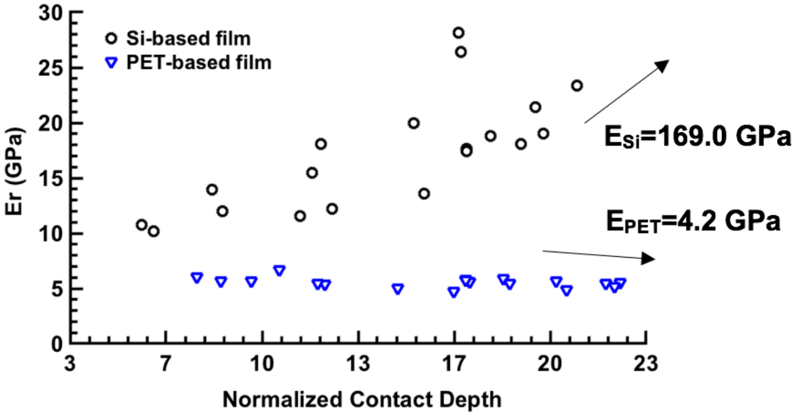

(a)

Figure 5.5 (a) Reduced modulus and (b) hardness as a function of normalized contact depth for Si-based and PET-based films.

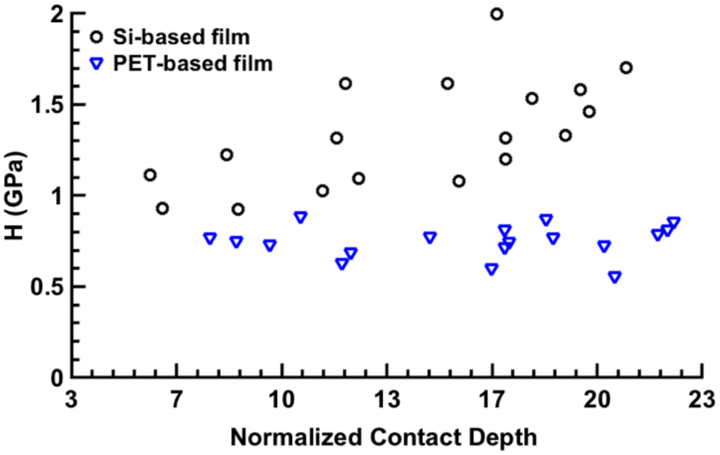

(b)

Figure 5.5 Continued.

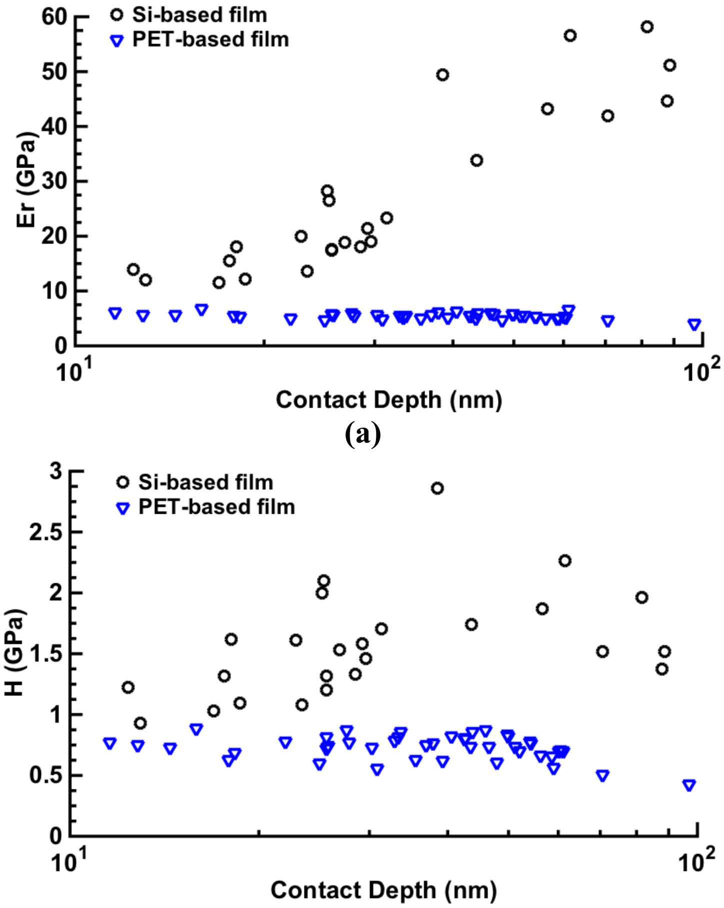

(a)

(b)

Figure 5.6 (a) Reduced modulus and (b) hardness as a function of contact depth for both films at deeper depths using Berkovich probe.

Representative load-displacement curves for the two multilayer thin films on both substrates are provided in Figure 5.7. The PET-based film showed softening behavior once nanoindentation force increased, as compared to the Si substrate film. Such behavior is usually observed, when there is a layered material, which has different phases. Each phase has a different load-carrying capability. Similar behavior is seen in layered materials such as epoxy-aluminum joints.[242] In the case of Si-based film, the stiffer substrate imposed a restriction on the downward flow of the thin film material which lead to stiffer response in the load-displacement curve and formation of pile-up around the indentation site.[243] However, in the case of the more compliant substrate, the film sank-in as the substrate could not support the indentation load imposed by the indenter on the thin film. This lead to substrate deformation once the load was applied.[43] At ultra-low load, there seem to be a region where both films' response to nanoindentation load was similar. The region can be seen in Figure 5.7 For nanoindentation forces less than 0.5 μN, the load-displacement curves for both thin films on Si and PET substrates were found to be close.

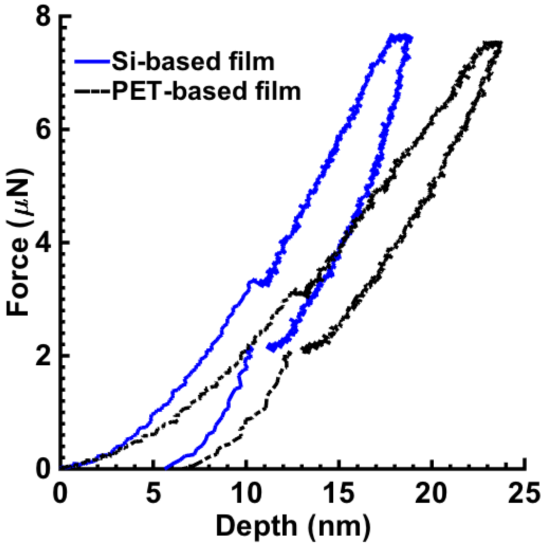

Figure 5.7 Representative shallow load-displacement curves of 8 μN maximum load on Si-based and PET-based films.

The reduced modulus of the silicon substrate ($E_{si} \approx 168.9$ GPa) was much higher than the modulus of the multilayer thin film ($E_{\text{Si-based film}}=12.08$ GPa). The stiffening response for the film could be due to a restriction of polymer chain dynamics near the substrate.[228] However, in the case of PET-based films, the mechanical properties were quickly reduced with depth, therefore the system behaved as a plate on an elastic foundation. The results were influenced by the PET substrate ($E_{PET} \approx 4.2$ GPa) even at very small depths. The indentation response did not represent only the local contact deformation within the film anymore (beneath the indenter), but, it included a global deformation of the entire system.[234] Figure 5.8 illustrates using a schematic the difference in the behavior of the thin films under study having them on stiff and compliant substrates.

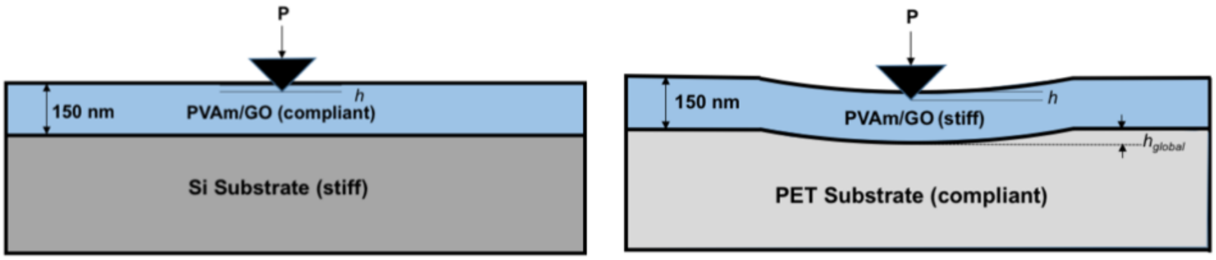

(a) **(b)**

Figure 5.8 The deformation behavior of PVAm/GO film on Si and PET represents (a) compliant film on stiff substrate and (b) stiff film on compliant substrate respectively.

Nanoindentation had a larger influence on the system of stiff film on compliant substrate, as shown in Figure 5.8. If the maximum indentation load was reduced, the global deformation of PET substrate could be reduced. However, even if it was possible to obtain similar load displacement curves at shallower depths, the challenge would be to extract reliable and consistent data due to the roughness effect of the films. Such a nanoindentation depth will be much smaller than the roughness of the films ($R_q \approx 9$ nm).

5.3.2 Raman Spectroscopy

Figure 5.9 shows the Raman spectra for PVAm/GO on both films. In the case of the Si substrate, the peaks appeared at 1339 and 1611 cm^{-1}. While, in the case of PET substrate, the peaks appeared at 1346 and 1611 cm^{-1}. In general, it can be stated that the two films were structurally similar. Particularly, the peak at the low wavenumber corresponded to defective, disordered carbon structure (D band) originating from the defect induced zone boundary phonons, whereas the peak at 1611 cm^{-1} could be attributed to the first order scattering of E_{2g} phonons (in plane optical mode) of sp^2 hybridized carbon atoms (G band), which corresponded to ordered crystalline carbon structures. The position of G band is very sensitive to the number of layers. As the number of layers increases, the band position is shifted to lower energy due to softening of the bonds between the layers. In the particular case where we had alternate layers of PVAm and GO, it seemed that the predominant factors affecting the G band position were the temperature, doping level and strain presence.

Regarding the D band, given that the same excitation laser wavelength was used, the differences in intensity and position were likely due to the different level of disorder in the two films. Quantitatively the I_D/I_G ratio is an index of the quality of the carbon material. For the films on PET substrate, the I_D/I_G ratio was 0.94, whereas the Si-based film had a ratio of 1.019, thus implying a lower defect concentration for the film grown on the PET. This could be explained based on the different initial treatment of the PET and Si substrates. Corona treatment of the PET led to the formation of many functional groups such as carboxylic (COOH), aldehydes (C=O), alcohols (C-OH), esters (C-COO-C) on the surface of the film. Most of these groups were participating with primary bonding with the PVAm layer. In the case of Si, with air plasma oxidation, it was possible that not all the groups were participating in the bonding with the PVAm thus leaving functional groups oriented outwards of the film, causing an increase in the disordering of the upper GO layer.

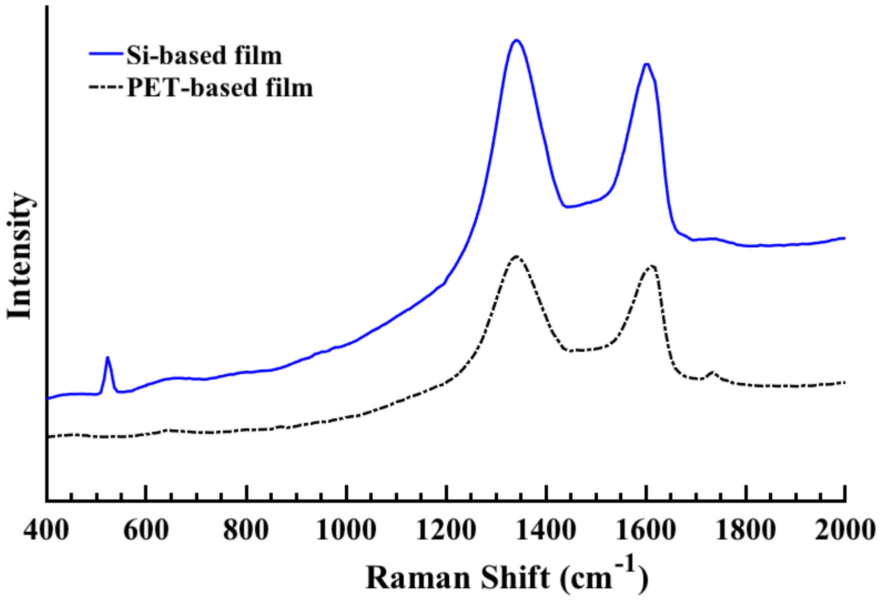

Figure 5.9 Raman spectra of PVAm/GO on Si and PET

5.3.3 Nanoscratch

To gain further insight into the film/substrate system behavior against scratch, constant and ramp load scratch experiments were carried out. Tables 5.3 and 5.4 provides the scratch results of constant normal loads of 25 and 100 μN respectively. Similar to nanoindentation, low and high load experiments were performed to evaluate the influence of the substrate on the scratch behavior of the film. At low loads of 25 μN, the Si-based film exhibited higher friction coefficient than PET-based film. At this load, the scratch represented the adhesive part of the friction. The plowing or deformation friction was not observed here due to both small load and complete elastic recovery. Even though, the films were scratched with low load of 25 μN, the in-situ scratch depth of PET-based film was deeper than silicon-based film showing global deformation of the substrate even at small loads. Similar results were observed with Au on fused quartz substrate (soft film on hard substrate system) and SiO_2 on Al substrate (hard film on soft substrate system).[43]

At a normal scratch loads of 100 μN, the friction coefficient of the Si-based film was slightly lower than the PET-based film. However, the Si-based film experienced more plastic deformation, and it also had a small residual depth resulting in a slightly visible scratch on the surface. The higher friction coefficient of PET could be attributed to the plowing effect of the slightly rougher surface than the Si based film. The scratch behavior of the PET-based film remained elastic and the in-situ scratch depth reached 60% of the film thickness. The PET showed similar COF for both scratch experiments with 25 and 100 μN loads.

Table 5.3 25μN constant load scratch tests summary on Silicon and PET.

Film	Scratch Depth (nm)	Residual depth (nm)	Scratch Visibility	Recovery	Friction Coefficient
Si-based film	27	N	N	100%	0.50
PET-based film	44	N	N	100%	0.25

Table 5.4 100μN constant load scratch tests summary on Silicon and PET.

Film	Scratch Depth (nm)	Residual depth (nm)	Scratch Visibility	Recovery	Friction Coefficient
Si-based film	35	3	Y	94%	0.25
PET-based film	95	N	N	100%	0.30

Scratch ramp load experiments up to a maximum load of 300 μN were conducted to measure transitions in the scratch behavior and film failure analysis. The load was increased linearly with a rate of 20 μN/s. Figure 5.10 shows the AFM images for the residual scratch profiles for both films. The Si-based film experienced more material flow as the scratch load increased.

Also, it showed side surface raptures and widening of the scratch due to low elastic recovery, as the normal scratch force increased. This could be due to the stress being localized within the film due to the stiffer substrate, which did not yield under these scratch loads. As a result, more confinement forced the Si-based film to flow to the side of the scratch and ahead of the indenter. On the other hand, the PET-based film exhibited higher elastic recovery with no material pile-up and more sink-in behavior due to the deformation of the substrate even at small loads as shown by the nanoindentation experiments. As a system, the PVAm/GO on PET was able to accommodate the scratch and maintained the film without failure.

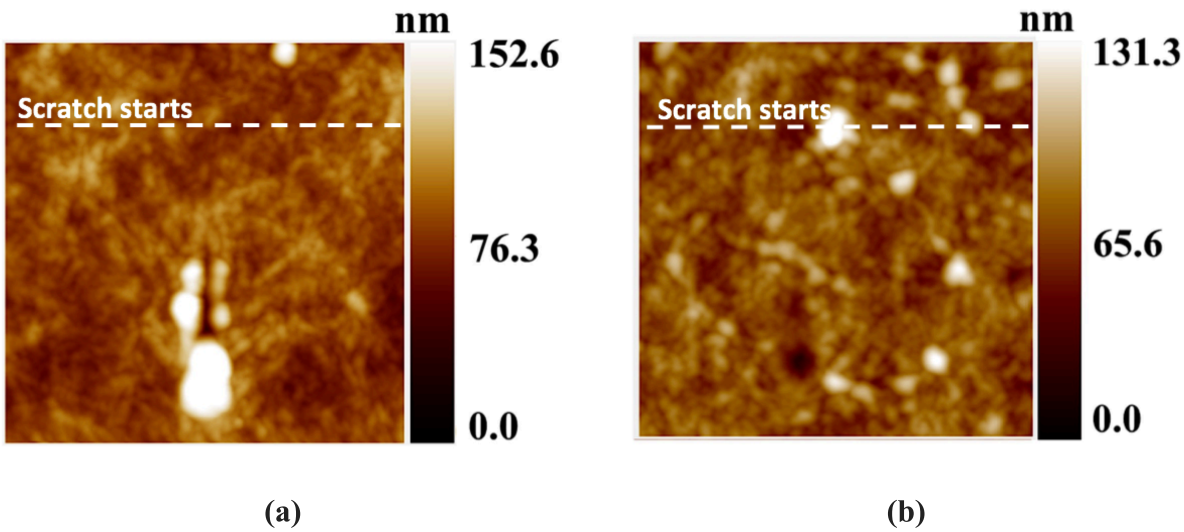

(a) (b)

Figure 5.10 AFM residual scratch images (10x10 μm) for PVAm/ GO on (a) Si and (b) PET under a ramp load from 0 to 300 μN (dashed lines show the start of the scratch).

The in-situ normal depth and COF as a function of scratch normal force up to 300 μN for both thin films are provided in Figure 5.11. Figure 5.11(a) shows that the in-situ depth for PET-based film was larger than the film thickness for loads higher than 100 μN due to the substrate sink-in. While, the indenter remained within the thickness of the Si-based film for the whole experiment. Figure 5.11(b) shows distinct frictional behavior for both films. At small loads, the

Si-based film maintained lower friction coefficient than PET-based film. However, as scratch normal load was ramped up, the friction coefficient increased due to the higher plowing friction and the material pile-up as the indenter penetrated deeper. The PET-based film maintained a stable COF of 0.3 for loads higher than 100 μN.

Another interesting observation was the stick−slip motion in the COF profile, which was observed for the Si-based film (also known in the literature as Schallamach waves).[148] This phenomenon is due to the competition of adhesive interfacial behavior and the relaxation process due to the viscoelastic behavior of the polymer. Since Si-based film showed higher adhesion part of the friction as measured by the nanoscratch, it was expected to show more stick-slip motion. Such waves can reduce the reliability of the coating/substrate system, since it is known to cause buckling and potential delamination of the film. On the other hand, PET-based film did not show pronounced stick-slip motion.

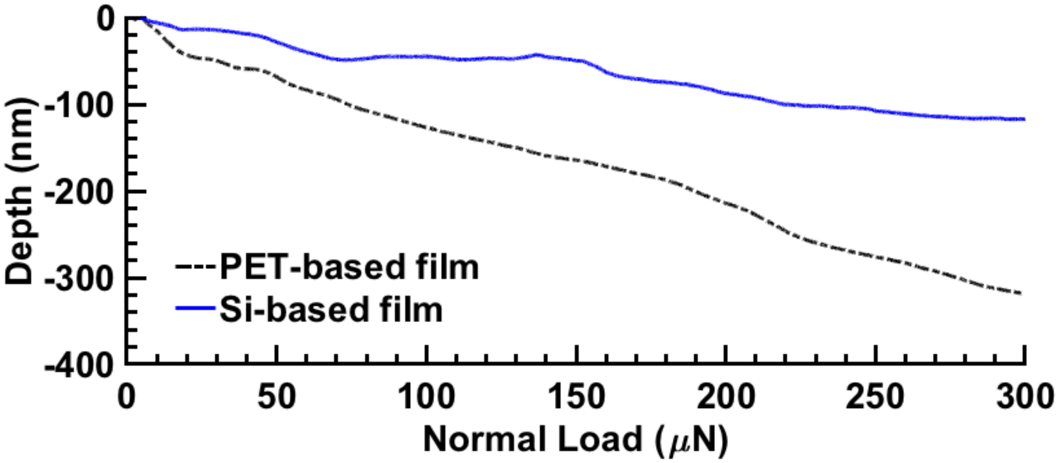

(a)

Figure 5.11 (a) In-situ normal displacement and (b) coefficient of friction as a function of scratch normal force up to 300 μN for both thin films.

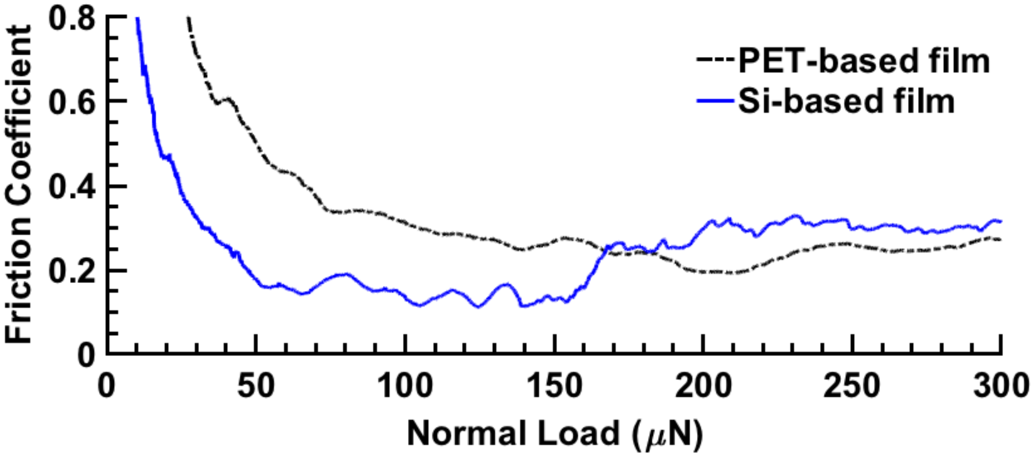

(b)

Figure 5.11 Continued.

While the Si-based film showed lower scratch resistance, the PET-based film maintained higher performance against scratch loading. To evaluate the durability of the PET-based films, it was subjected to scratch conditions at the same location with two passes. Figure 5.12 shows the residual scratch images after each pass. The film sustained similar frictional behavior against multiple scratches showing high durability. For the application of gas barrier, as an example, this is advantageous, since it showed more durability of the film once deposited on PET substrate. The findings here showed the importance of studying thin films on the same substrate as they will be used in the application. Herein, the behavior of the thin film especially the scratch behavior was influenced by the substrate, and it could be different for different substrates.

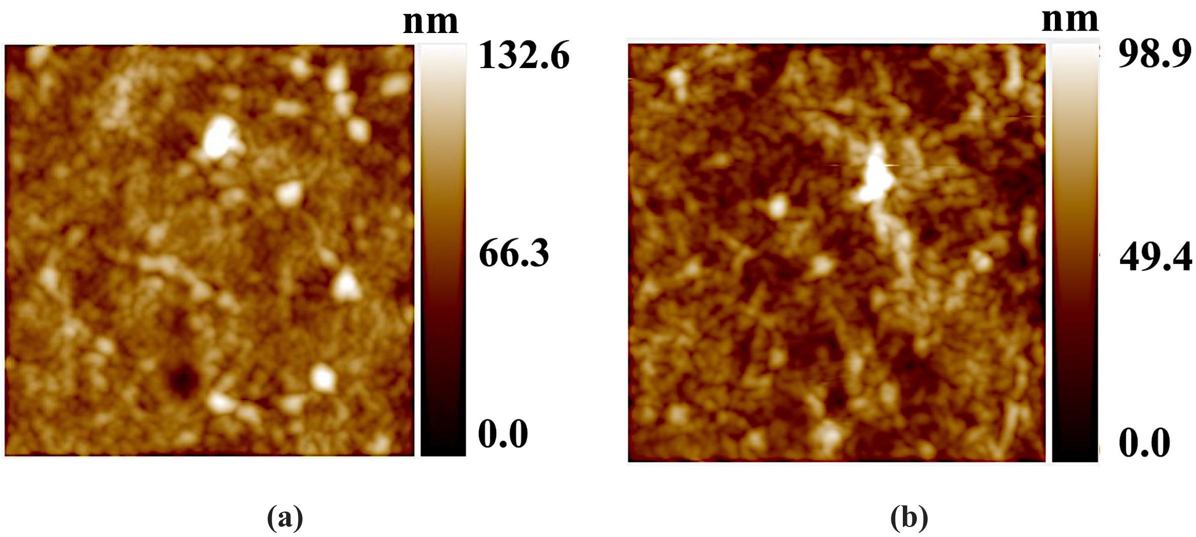

(a) (b)

Figure 5.12 AFM residual scratch images for PVAm/ GO on PET with (a) first pass and (b) second pass.

5.3.4 *Finite Element analysis*

FEA was carried out to better understand the observed phenomena above with nanoscratch experiments, and the reasons for the difference in the scratch behavior for each film/substrate systems. Also, FEA can help to gain some insights in the stress/strain distribution in the film, substrate and interface under scratch loading. Table 5.5 summarizes the properties of the films and substrates used in the FE modelling. The Young modulus (E) was calculated using the equation of the reduced modulus of elasticity (E_r), which was extracted using the nanoindentation experiments. It is defined based on both the elastic modulus of the indenter (E_i) and sample (E_s) and Poisson's ratio of both indenter (v_i) and sample (v_s). The properties of the Si and PET were adopted from the literature.[244]

$$\frac{1}{E_r} = \left(\frac{1 - {v_i}^2}{E_i} + \frac{1 - {v_s}^2}{E_s}\right) \tag{2}$$

First, the FEA was verified with the scratch experiments with a ramp load of 100 μN. The maximum scratch depth of the Si and PET-based films was found to be 27 and 97 nm using the FEA model, which was close to the findings of the experiments (35 and 95 nm for Si- and PET-based films).

Table 5.5 Material properties of film and substrate for FEA.

Material	E_y (GPa)	v	μ
PVAm/GO on Si	10	0.40	0.25
PVAm/GO on PET	10	0.40	0.30
Si	127	0.28	-
PET	3	0.41	-

Figure 5.13(a, b) shows the stress distribution for the PVAm/GO film on Si and PET. For the Si-based film, since the yield stress of Si is 7 GPa, a maximum von Mises stress of 1.8 GPa would result only in elastic deformation in the Si. Therefore, the higher stresses would be confined in the film and the interface. On the other hand, the PET has a yield strength less than 100 MPa. The maximum stress in the PET substrate was about 800 GPa. Therefore, the substrate would yield under this scratch load under the assumption of elastic contact. For the films, the maximum stress distribution was within the Si-based film reaching the surface, while the maximum von Mises stress was on the interface for the PET-based film. The surface of PET-based film did not experience high stresses on the surface. This explained the higher scratch visibility for the Si-based film, compared to the PET-based film.

Figure 5.13 (c, d) illustrates the strain distribution under normal scratch load. For the Si-based film, the strains were on the surface under the indenter. However, for the PET-based film, the indenter was sinking-in under this load due to the deformation of the substrate. This global deformation of the substrate resulted in a lower contact pressure for PET-based film as compared to the Si-based film as shown in Figure 5.13 (e, f). The Si-based film had higher localized contact pressure resulting in significant plastic deformation and pile-up around the scratch area. For the PET-based film, it showed lower contact pressure, but larger contact area due to the deformation of the substrate. Figure 5.13 (g, h) shows the shear strength (S_{12}) for both systems. Si-based film experienced higher shear stress on the surface and across the film ahead of the indenter as compared to PET-based film. Thus, it suffered from more film delimination and material transfer ahead of the tip as Figure 5.10(a) shows.

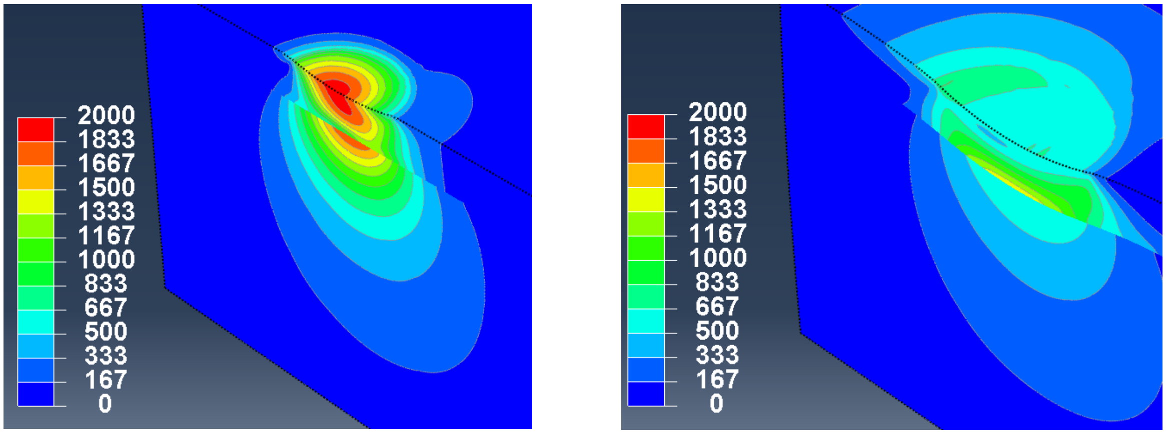

(a) **(b)**

Figure 5.13 FEA contour plots of von Mises stress distribution (MPa), elastic strain, contact pressure (MPa) and shear stress (S_{12}) (MPa) for (a, c, e, g) Si and (b, d, f, h) PET.

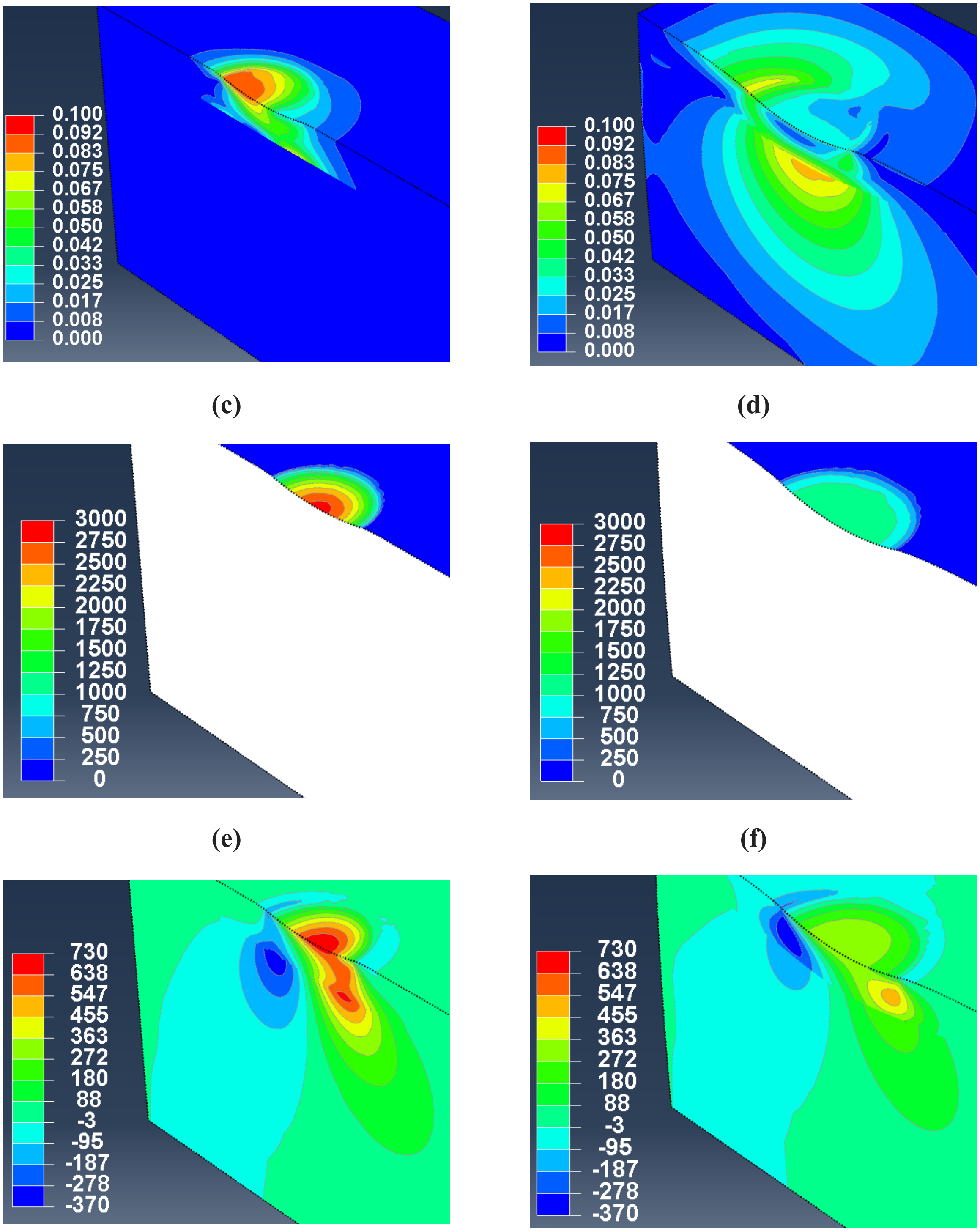

(c) **(d)**

(e) **(f)**

(g) **(h)**

Figure 5.13 Continued.

5.3.5 Film delamination and Adhesive Strength:

It is possible to obtain the interfacial behavior between the film and the substrate if the film delamination is to be induced. To do so, a higher ramp load scratch up to 1 mN was carried out. The adhesive (σ_a) strength was calculated using methods developed Laugier as shown in Equation 3.[125]

$$\text{Adhesive Strength } (\sigma_a) = \frac{2P_c}{\pi d_c^2}\left[(4+\nu_s)\frac{3\pi\mu}{8} - (1-2\nu_s)\right] \tag{3}$$

Where σ_a is a function of the critical contact pressure/load, which was needed for film delamination (P_c), residual scratch width (d_c), coefficient of friction measured during the experiment (μ) at the onset of delamination, and the substrate Poisson's ratio (ν_s).

Figure 5.14 (a, b) shows the SEM residual images for Si and PET-based films. The Si-based film experienced earlier delamination and wider scratch groove. While, PET-based film underwent delayed delamination with slightly narrower scratch width. At the maximum scratch load, both films showed different behaviors. Si-based film showed ductile failure with film rapture at interface, which then transferred and piled up ahead of the indenter. On the other hand, PET-based film experienced brittle fracture with no material pile-up/transfer.

Table 5.6 summarized the properties extracted from the 1 mN scratch experiments. The critical delamination load for PET-based film is nearly twice larger than the Si-based film, and the calculated σ_a for PET-based film is 4.6 times higher than Si-based film. The low adhesive strength explained why Si-based film had a film rapture at the interface followed by pile-up. In case of PET-based film, the higher adhesive strength resulted in more of fracture of the film under high contact forces.

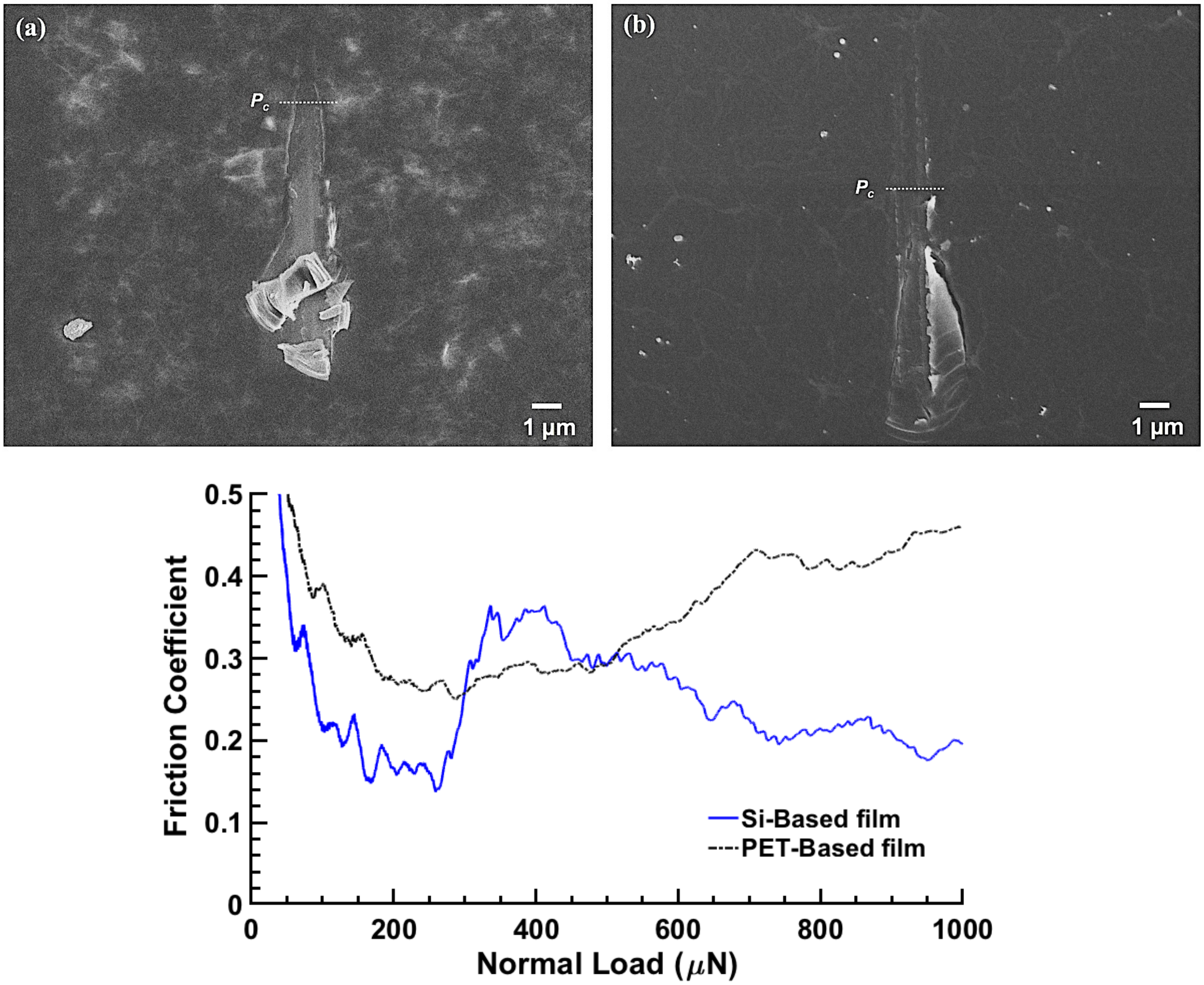

(c)

Figure 5.14 SEM residual scratch images for (a) Si-based film and (b) PET-based film, and (c) coefficient of friction as a function of scratch normal force up to 1 mN.

Table 5.6 Failure properties measured at the onset of delamination.

Sample	Critical load (P_c) (μN)	Friction Coefficient (μ)	Scratch width (d_c) (μm)	Adhesive Strength (σ_a) (GPa)
Si-based film	260	0.35	1.20	0.15
PET-based film	500	0.45	1.00	0.69

5.4 Summary of Chapter 5

Multilayer thin film, PVAm/GO, was deposited on both Si and PET substrates in order to understand the influence of two distinct substrates on the mechanical properties of the thin film. The film on both Si and PET represented two different systems: stiff film on compliant substrate and stiff film on compliant substrate respectively. The “10% of film thickness” rule was shown to hold for compliant film on stiff substrate. However, measuring the properties of the stiff film on the compliant substrate was more challenging. This system behaved as a plate on an elastic foundation with two components of deformations: local within the film, and global for the film/substrate system. To reduce the substrate effects of the compliant PET substrate, higher-resolution force transducer was recommended to be used. Scratch experiments reveled different behaviors for the PVAm/GO thin film once deposited on different substrates. The Si-based film suffered from more plastic deformation and pileup due to stress and strain distributions being confined close to the surface of the film. On the other hand, the PET-based film experienced elastic deformation on the surface due to the global deformation and potentially yielding of the PET substrate. The FEA revealed that the highest von Mises stress for the PET-based film is on the interface between the film and the substrate. Such a finding highlighted the importance of having a strong interfacial bonding between the film and the substrate in order to maintain a reliable operation of these coatings once deposited on PET for the gas barrier applications. While using a rigid substrate such as silicon is useful to extract the intrinsic mechanical properties of unknown films without having a significant substrate effect, it is important to study as well the behavior of these thin films on the same substrate where they will be deposited on in their real-life applications.

6 FABRICATION AND DEFORMATION OF THREE-DIMENSIONAL MULTILAYERED KIRIGAMI MICRO-STRUCTURES*

6.1 Introduction

Mechanically-guided three-dimensional (3D) micro-assembly with controlled compressive buckling represents a promising emerging route to 3D mesostructures in a broad range of advanced materials, including single-crystalline silicon (Si), of direct relevance to microelectronic devices. During practical applications, the assembled 3D mesostructures and micro-devices usually undergo external mechanical loading such as out-of-plane compression, which can induce damage in or failure of the structures/devices. Here, the mechanical responses of a few mechanically-assembled 3D kirigami mesostructures under flat-punch compression are studied through combined experiment and finite element analyses (FEA). These 3D kirigami mesostructures consisting of a bilayer of Si and SU-8 epoxy are formed through integration of patterned 2D precursors with a pre-stretched elastomeric substrate at pre-defined bonding sites to allow controlled buckling that transforms them into desired 3D configurations. In situ SEM measurement enables detailed studies of the mechanical behavior of these structures. Analysis of the load-displacement curves allows the measurement of the effective stiffness and elastic recovery of various 3D structures. The compression experiments indicate distinct regimes in the compressive force/displacement curves, and reveals different geometry-dependent deformation for the

---

*Reprinted with permissions from "Fabrication and Deformation of 3D Multilayered Kirigami Microstructures" by Humood, M.; Shi, Y.; Han, M.; Lefebvre, J.; Yan, Z.; Pharr, M.; Zhang, Y.; Huang, Y.; Rogers, J. A.; Polycarpou, A. A. *Small* 2018, 14, 1703852.

structures. Complementary computational modeling supports our experimental findings and further explains the geometry-dependent deformation.

Biology is inherently based on three-dimensional (3D) designs, optimized for performance through billions of years of survival in challenging environments.[245] These biological structures span length scales from the nanoscale level, such as DNA,[246] to the macroscale, such as shark skin.[247] Additionally, these 3D structures often consist of various levels of hierarchy, as exemplified in geckos' feet.[248] If the advantages of these fascinating 3D structures can be realized in man-made devices, tremendous advances in capabilities of material systems and architectures will occur, overcoming the inherent limitations of 2D microsystems. For example, 3D micoelectromechanical systems (MEMS) offer vastly improved bandwidth and frequency tunability over conventional 2D MEMS structures, such as cantilevered beams and doubly clamped bridges.[8]

Indeed, various shapes and scales of 3D structures have been successfully implemented in a number of applications such as wearable electronics,[249] robotics,[250] solar systems,[251] energy storages,[252] optoelectronics,[253] optomechanical devices,[254] and near-field communication (NFC) devices.[11] The incorporation of 3D structures has improved performance and extended capabilities in these applications. Different fabrication techniques have been developed to form various 3D structures, including 3D printing,[255] two photon/multiphoton lithography,[256] and self-assembly.[257] However, these methods cannot produce inorganic semiconductors such as silicon.[258] Alternatively, mechanically-driven assemblies such as strain-induced bending or folding and compressive buckling have the potential to extend the range of materials, including silicon.[259] of these options, compressive buckling offers advantages compared to strain-induced deformation in terms of possible 3D geometries.[260] Indeed, in the literature one can find a few hundred different

3D mesostructures with different combinations of materials (polymers, metals, and semiconductors). These structures scale from the sub-micrometer to centimeter scale, thus revealing the scalability of the process.[261,262]

The compressive buckling process begins with planar microfabrication of various 2D precursor patterns, consisting of multilayer thin membranes. Next, lithography defines a set of chemically active bonding sites, while reactive ion etching produces patterned cuts in the membrane. Such structures are known as kirigami as their fabrication concept is based on the Japanese art of paper folding and cuts. Transfer printing enables integration of these structures with a pre-stretched elastomeric substrate.[263] Although a variety of 3D mesostructures have been fabricated previously using mechanically guided assembly, their mechanical response to applied loads is still unknown. Thus, in this work we use in situ compression inside the scanning electron microscope (SEM) to investigate their deformation behavior.

The in situ SEM flat punch compression provides capabilities to simultaneously measure load vs. displacement and observe deformation in real time.[264,265] Thus, this technique can uncover detailed information on material behavior during both compression and post-compression. Numerous 3D structures have been studied using in situ compression, including individual and arrays/foams of carbon nanotubes,[266] metals[267] and hierarchical structures of ceramics/polymers.[268] However, no reports exist in the literature on the compression of origami- or kirigami-inspired structures.

Herein, we report on the compression of kirigami-inspired structures, which consist of a bilayer of Si and SU-8 (thickness = 200 and 2000 nm respectively). SU-8 is an epoxy-based photoresist, which is a material commonly used in microfabrication capable of yielding a high aspect ratio even in thick coatings. The SU-8 can be deposited using simple spin casting and has favorable mechanical properties.[269] During in situ compression testing of these kirigami structures, the geometry was found to play a critical role in their flexibility and stretchability. Indeed, we found that structural design enables intrinsically stiff and brittle bulk materials such as Si and SU-8 (~2-3% and 10-12% tensile strain to fracture, respectively) to undergo large deformation.[270] This results in an overall deformable and compliant structure, which can sustain large-scale deformation, including twisting and bending. In light of these experimental findings, a finite element analysis (FEA) model was developed to provide further insight into the maximum stress/strain of kirigami structures during compression.

6.2 Experimental Section

6.2.1 Materials & Fabrication

Preparation of 2D precursors of silicon and epoxy (SU8) bilayers exploited photolithography and reactive ion etching to pattern a thin layer of silicon (200 nm in thickness) using silicon on insulator (SOI) wafer. Wet etching by hydrofluoric acid (HF) fully dissolved the exposed silicon dioxide (1 μm in thickness) on the SOI wafer. The following spin coating and photolithography steps defined the pattern of the epoxy (SU8) layer (2 μm in thickness) on top of the silicon layer. Another spin coated and lithographically defined photoresist layer (AZ 5214, 4 μm in thickness) covered the silicon and epoxy (SU8) patterns but left the bonding regions exposed. Wet etching in HF fully removed all the silicon dioxide underneath the patterns, thereby facilitating the transfer printing process. Deposition of titanium (5 nm in thickness) and silicon dioxide (50 nm) through electron beam evaporation promoted the adhesion of the bonding regions.

Transfer printing of the 2D precursors began with retrieving the patterns from SOI wafer to a PDMS stamp. Laminating water soluble tape onto the PDMS surface enabled the transfer of 2D precursors from PDMS stamp to water soluble tape. The buckling process utilized silicone elastomer (Dragon Skin, 600 μm in thickness) as the assembly substrate. Ultraviolet ozone treatment of the silicone elastomer and 2D precursors on water soluble tape induced hydroxyl termination for strong bonding. The silicone elastomer was then stretched to carry the 2D precursors along with the water-soluble tape. Heating at 70 °C for 8 min formed strong chemical bonding between the bonding regions of the 2D precursors and silicone elastomer. After dissolving water soluble tape with water and AZ 5214 as acetone, releasing the prestrain applied to the silicone elastomer enabled out-of-plane translations of the non-bonding regions.

6.2.2 Mechanical characterization

A PI 88 SEM PicoIndenter (Bruker Nano Surfaces, Eden Prairie, MN) was used to perform the in situ compression experiments. An extended range (xR) transducer allowed for large displacement up to 150 μm. The indenter itself consisted of a diamond flat punch with a 100 μm diameter. The experiments utilized a displacement-controlled mode at a loading rate of 1 μm/s. The samples were coated with 5 nm of Pt/Pd to provide charge dissipation during SEM observation.

6.2.3 Finite Element Analysis

Three-dimensional (3D) finite element analysis (FEA) simulated the final configurations and strain distributions of the 3D structures using the commercial software ABAQUS. The kirigami structures consisted of four-node shell elements, and the elastomer substrates consisted of eight-node 3D stress elements. Surface Contact is applied between the structure and substrate with friction coefficient of 0.3 (“penalty” setting for tangential behavior and “hard contact” for normal behavior in ABAQUS). Convergence of mesh sizes ensured computational accuracy. The elastomer substrate was modeled using a hyperelastic constitutive relation (Mooney-Rivlin model) with parameters C_{10}=0.06757 MPa, C_{01}=0.01689 MPa and D_1=0.48 MPa^{-1} in ABAQUS. The elastic moduli (E) and Poisson's ratios (v) for SU-8 and silicon were $E_{SU\text{-}8} = 4.02$ GPa, $v_{SU\text{-}8} = 0.22$, $E_{Si} = 130$ GPa, and $v_{Si} = 0.27$.

6.3 Results

Figure 6.1 illustrates the 2D design patterns and the transformation into 3D structures using compressive buckling. Four different kirigami structures were made using a fixed pre-strain of 65%. The red color represents the bonding region to the elastomer substrate. Silicone was used as a platform for the assembly of these structures. SEM images were taken before the start of the in situ compression experiments (see Figure 6.1b). A 12 μm diameter fiber is seen in front of the table structure and provides a perception about the size of these structures.

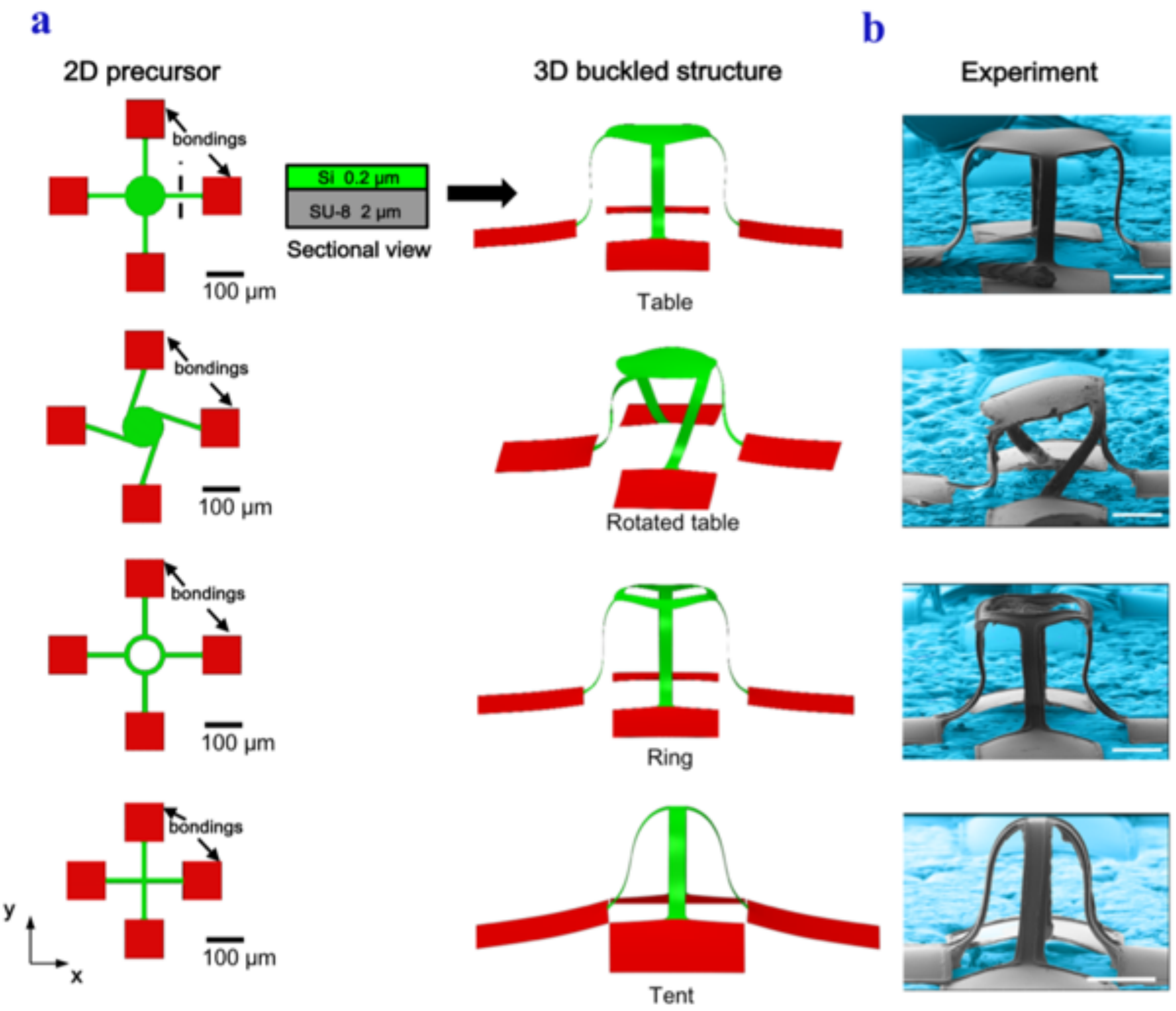

Figure 6.1 (a) Conceptual illustration of the 3D kirigami structures, which were assembled from 2D precursors by compressive bukling using FEA results (scale bar is 100 μm) (b) corresponding SEM images for the 3D structures (scale bar is 30 μm).

Precise height measurements for the four fabricated structures were taken using a profilometer. The height was found to be 75 μm for the table and ring structures and 70 μm for the tent and rotated table structures. For the rotated table, due to the inclined top surface, the height was averaged. The in situ compression was carried out in two steps. In this study, we defined the percentage of compression based on the height measurement for each structure. For example, 50% compression refers to 35 μm of vertical displacement of the flat punch, while 70 μm displacement represents 100% compression of the rotated table sturcture. All structures, except the tent, were compressed to ~50% of their initial height followed by a complete unloading of the flat-punch. Five minutes was set as a wait time to allow relaxation of the structure and substrate before carrying out the next experiment of 100% compression. Both the 50% and 100% compression experiments were performed on the same structure except for the tent structure. These two experiments were repeated on a second sample for each structure to assess repeatability. The first tent was compressed to 30% while the second tent was compressed to 100%.

Figure 6.2 shows typical load-displacement curves for the four structures. The recorded videos for the compression experiments are provided in the supporting information (movies 6.1-6.8). The load-displacement curves demonstrated three regions in the compression of kirigami structures: linear deformation, rapid buckling, and stiffening behavior. The three regions are marked in Figure 6.2a and are similar to those identified in other 3D structures, such as foam-like arrays of carbon nanotubes.[271] The deformation was linear and nearly recoverable from the point of contact to 50% compression. For the second region, the reduction in the slope of the load-displacement plot indicates rapid buckling, i.e., large displacements produce small increases in force. Once approaching a compression of 100%, the stiffness increased due to the nonlinear compression of the legs of the structures accompanied by deformation of the substrate.

Similarly, unloading the structures showed the substrate effect. All structures showed the unloading curve with two different slopes, except the tent structure. The change in the slope took place around 50 μm displacement. This indicated two distinct unloading behaviors after removal of the flat punch. First, the substrate recovered quickly followed by a mixed relaxation of both the structure and the substrate. Indeed, this could be seen in the sumpplementary movies 6.1, 6.2 and 6.3. The tent structure showed a drop in the load at ~100% compression, which correlated with a twisting of the structure in the recorded video (supplementary movie 6.4).

The load-displacement curves highlight different levels of energy dissipation for each kirigami structure based on the area under the load displacement curve. The rotated table structure had the lowest energy dissipation, followed by the ring, and finally the table and the tent structures. The elastic recovery followed the same order, i.e., the rotated table structures showed the highest elastic recovery. The energy dissipation is due to viscoelastic/plastic effects and possible fracture events. Therefore, structures with lower energy dissipation exhibited higher elastic recovery. Table 6.1 shows the response to mechanical compression for all the structures as a function of the load carrying capability, elastic recovery, and unloading stiffness. Both the maximum load and stiffness were calculated using 50% compression experiments to avoid substrate effects. The elastic recovery was calculated using the 100% compression experiments. A correlation exists between the stiffness and recoverability, where a stiffer structure exhibits less elastic recovery.

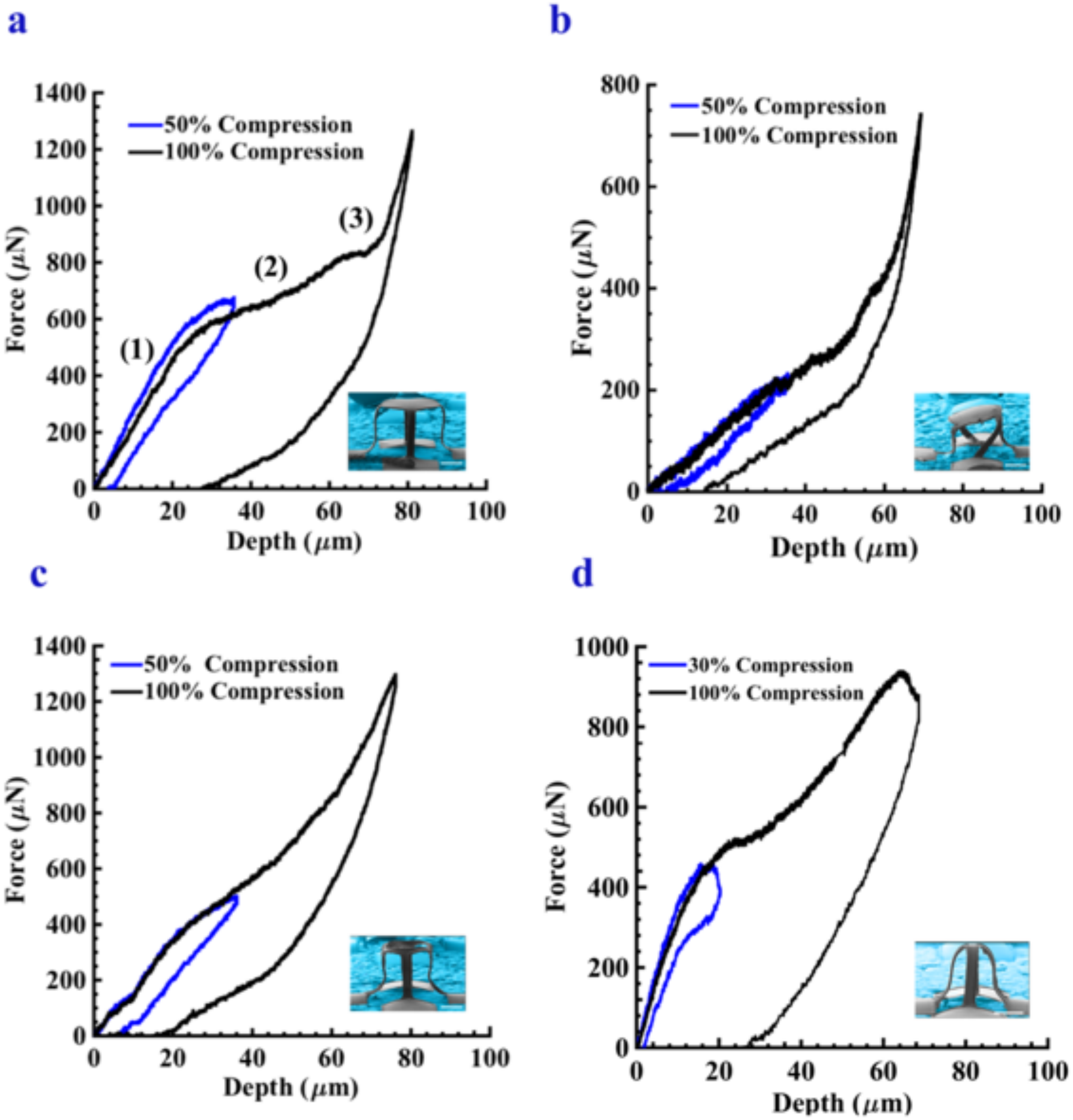

Figure 6.2 Load versus displacement data for flat-punch compression of (a) Table (b) Rotated Table (c) Ring, and (d) Tent structures.

Table 6.1 Comparison between kirigami structures in terms of response to mechanical deformation

Structure	Maximum Load Bearing [μN] [a)]	Max Compression Depth [μm] [a)]	Elastic Recovery [%]	Unloading Stiffness [N/m][a)]
Rotated table	220	36.1	89.5	6.1
Ring	500	36.2	84.2	13.9
Table	670	35.6	77.7	18.1
Tent	450	20.4	70.2	23.7

[a)] Properties measured at 50% compression experiments to avoid substrate effects.

Figure 6.3 provides further insight into the deformation of each structure by taking snapshots from each movie during compression. The snapshots were taken at intervals of 0, 25, 50, and 100% compression. The structures experienced either one-fold bending, two-fold bending, or bending and twisting. The deformation in the table structure took place both inward (towards SU-8) and outward (towards Si), as illustrated by the arrows in Figure 6.3. That is, some regions of the Si thin film experienced tension while others experienced compression. These images help explain the rapid buckling or softening of the table structure, as they undergo larger elongation in the legs in the form of two-fold bending. Due to the rotated arrangement of the legs, the rotated table structure deformed by both bending and twisting. Finally, both the ring and tent structures experienced one-fold bending. Additionally, the tent structure exhibited slight twisting upon reaching close to 100% compression. The arrows in Figure 6.3 provide an illustration of the deformation direction. For example, the double arrows for the table structure show two-fold bending. Corresponding FEA simulations were carried out using the commercial software (ABAQUS) and the distributions of maximum principal strain in the Si layer under different stages of compression were also shown in Figure 6.3. Good agreements of the deformation patterns can be observed between FEA and experiment, for all of the examples studied here. The FEA results indicated strain concentrations at the ribbon-membrane connection regions in the table and rotated-table structures, as well as the ribbon-ribbon connection regions in ring and tent structures. This is in accordance with the relatively small radius of curvature at these regions. The FEA predicts slight twisting of the tent structures once reaching 100% compression, as revealed by experiment.

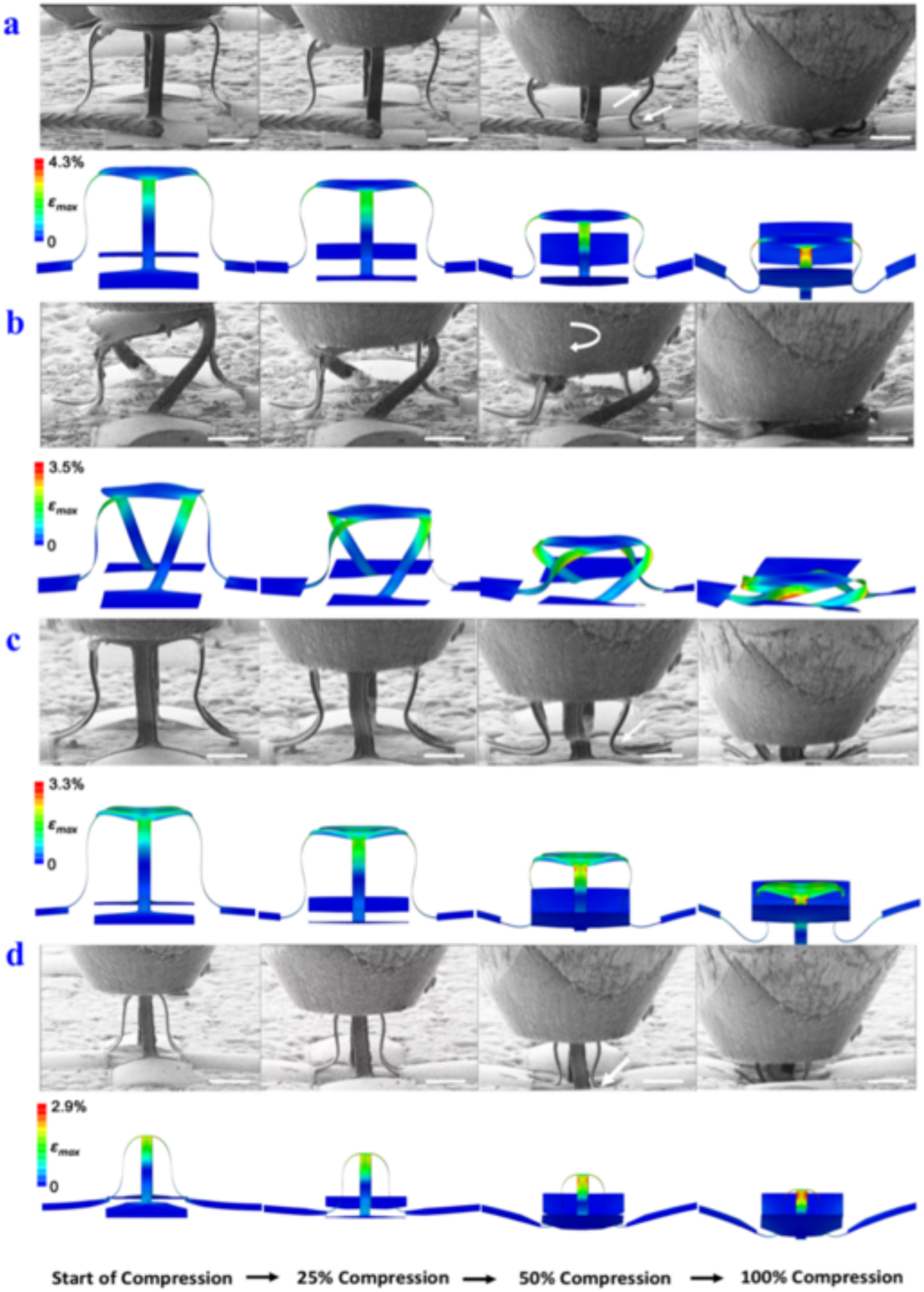

Figure 6.3 Snapshots taken from the recorded movies at the start of the compression, 25%, 50%, and 100% compression for the (a) Table (b) Rotated table (c) Ring (d) Tent structures. (scale bar is 30 μm).

While Figure 6.3 provides in situ snapshots from the recorded movies, Figure 6.4 shows the SEM images at higher resolution, taken before and after each experiment. The 50% compression experiments were nearly recoverable, and there was no change in the shape of the legs. However, the 100% compression experiments yielded observable plastic deformation in all structures except the rotated table structure, which recovered to the initial height. The three other structures had similar residual deformation in the legs in a form of a sharp curvature towards the SU-8 layer. Even though the table structure had two-fold bending, the bottom bending toward the SU-8 layer was larger and left larger residual curvature likely revealing possible plastic deformation or fracture in the SU-8 layer. If the SU-8 film yielded and the maximum strain was higher than the fracture threshold of SU-8 (~10-12%),[272] the SU-8 will not recover fully and elastically. If SU-8 experiences elastic behavior before this threshold, then it will break without a plastic domain.[273] Fracture events might explain the softening (rapid buckling) for the structures above 50% compression. Since the thickness of the Si layer is 10% of the SU-8 layer, fracture events are expected to be experienced by the thicker SU-8 epoxy layer first.

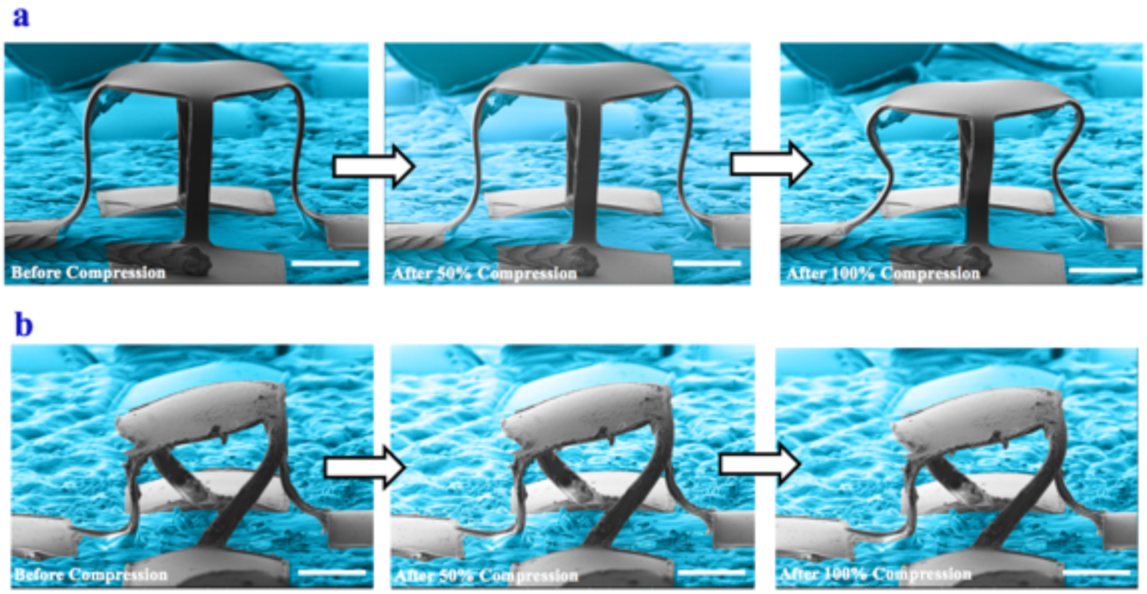

Figure 6.4 SEM images taken before the start of compression, after 30-50%, and after 100% compression for the (a) Table (b) Rotated table (c) Ring (d) Tent. (scale bar is 30 μm)

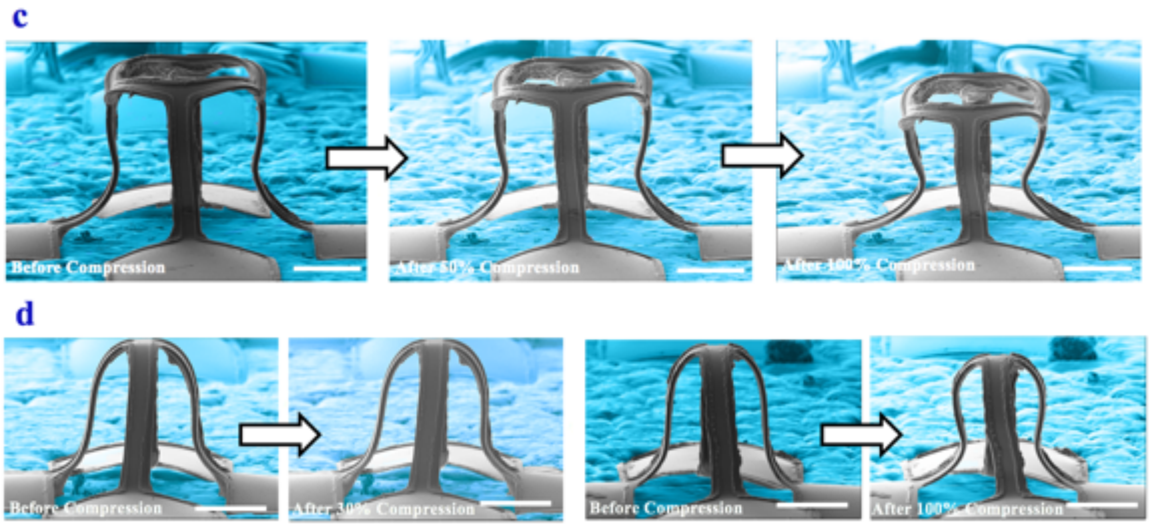

Figure 6.4 Continued.

To better understand the residual curvatures in the legs of the structures, FEA was carried out to calculate the von Mises stress and maximum principal strains. The von Mises stress is used to predict the yielding of a material once subjected to a complex loading, while the maximum principal strain provides the largest normal strain, which is of interest to understand the deformation and/or fracture in the SU-8 layer under compression. Similar contours are provided in the supporting information for the Si layer under compression.

Figure 6.5b revealed insights about the maximum strain experienced by the structures under 100% compression. Only the rotated table structure had a maximum principal strain (~8.0%) lower than 10%, therefore it maintained an elastic deformation. Other structures experienced strains higher than the fracture strain threshold of SU-8, which led to the residual change in the curvature of the legs and potentially fracture events. In terms of stress, structures with bending-dominated deformation experienced high stresses in the bottom of the legs. On the other hand, the rotated table structure had higher stresses in the top part of the legs due to the combined bending/twisting deformations.

Figure 6.6 shows contours of von Mises stress and maximum principal strain in the Si layer only for all the fully compressed structures. The maximum strain (stress) is mainly located at the ribbon-ribbon (or ribbon-membrane) connections, which means the compression loading is mainly taken by these regions. The maximum principal strain for the Si layer is about 4.3% for the table structure, and in the range of 2.9-3.5 % for the other structures. Even though the maximum strain is slightly higher than the maximum tensile strain to fracture for bulk Si (2-3%), others reported that nanoscale silicon structures can reach higher tensile strains of ~5-7% without fracture.[274] Indeed, yielding does not occur in single crystalline silicon until fracture takes place. The yield strength is 7000 MPa,[275] and only the table structure approached this limit. Therefore, there is no any indication of fracture or crack in the silicon layer. We anticipate that the fracture could have occurred in the thicker SU-8 layer for the table, ring and tent structures where the strain was higher than the fracture threshold of SU8 (~10%).

6.4 Summary of Chapter 6

This chapter discussed the fabrication and deformation of 3D Si/SU-8 kirigami structures, which have potential applications in 3D NFC devices and 3D MEMS. The operation of these devices requires a high level of mechanical reliability of their components. In addition, for example, MEMS are made of silicon and its oxides, which is inherently stiff and brittle, and can undergo only 2-3% tensile strain to fracture in 2D configurations. However, silicon can undergo larger deformations without fracture once fabricated in 3D configurations as shown herein and by others in the literature.

Multilayered 2D precursors of brittle Si and SU-8 buckled up to create functional flexible 3D structures. In situ flat punch compression provided insight into the deformation mechanics of kirigami structures. In particular, during 50% compression, the structures recovered elastically back to their initial heights. By comparison, 100% compression produced permanent changes and possible micro-fracture events in the curvature of the legs of the structures. Still, no experimental evidence of the micro-cracks/delamination were observed in the structures, even up to 100% compression, thereby highlighting the flexibility of these structures. Computational modeling supported the experimental findings and provided further insight into the dependence of deformation on the geometry of the structures. The mechanical and geometric properties (such as bending stiffness) at the connections play an important role during the deformation (compression, bending or twisting) of the structures and influence the final configurations of the kirigami structures, which should be considered during the design of the kirigami structures.

In addition, the energy dissipated by these structures is important as it indicates if they will be durable against repeated deformations and maintain stable hysteretic cycling. The future works need to focus in addressing how these structures behave under repeated compressive load. The energy dissipation is due to viscoelastic/plastic effects. Therefore, the strain rate and other time-dependent properties need to be explored as well for both the structures and the substrate. Besides geometry and time-dependent properties, the thickness of each of the Si and SU8 layer, which is not studied here, can be a variable to reduce the maximum strain (stress) in the structure. The agreement between the computational and experimental results suggests the possibility for future computational simulations to optimize pre-cursor design for load bearing, energy dissipation, and elastic recovery capabilities.

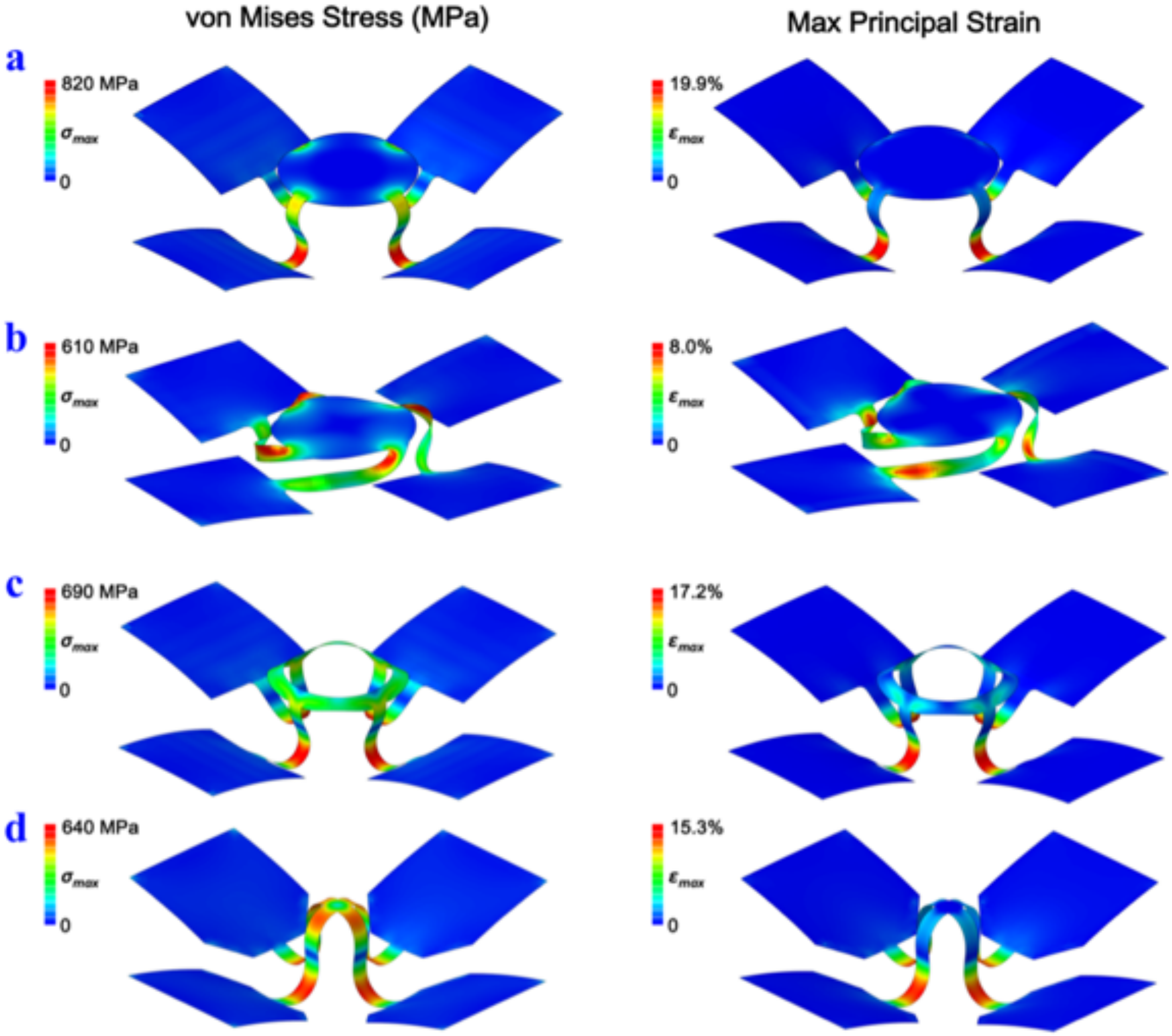

Figure 6.5 FEA results for the compression of SU-8 layer in the kirigami structures (under 100% compression) showing von Mises stress (MPa, left column) and maximum principal strain (right column) for the (a) Table (b) Rotated table (c) Ring (d) Tent. The substrate and punch were removed to allow visual observation of the stress and strain contours in the structures.

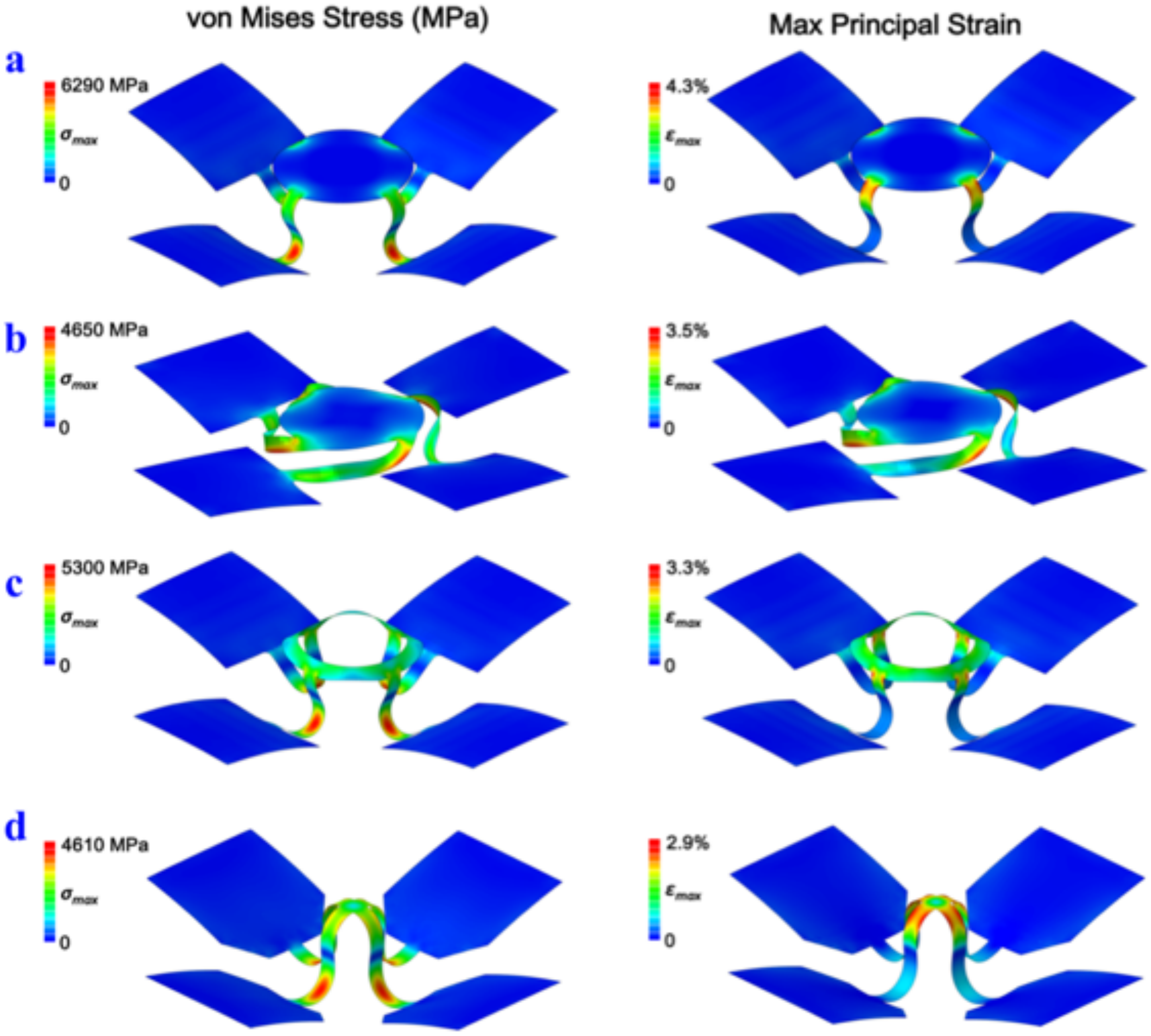

Figure 6.6 FEA results for the compression of Si layer in the kirigami structures (up to 100% height compression) showing von Mises stress (MPa, left column) and maximum principal strain (right column) for the (a) Table (b) Rotated table (c) Ring (d) Tent. The substrate and punch were removed to allow visual observation of stress and strain contours in the structures.

6.5 Supplementary movie legends

- Movie 6.1:100% compression of Table structure
- Movie 6.2: 100% compression of Rotated table structure.
- Movie 6.3: 100% compression of Ring structure.
- Movie 6.4: 100% compression of Tent structure.

- Movie 6.5: 50% compression of Table structure.
- Movie 6.6: 50% compression of Rotated table structure.
- Movie 6.7: 50% compression of Ring structure.
- Movie 6.8: 30% compression of Tent structure.

7 NEW RIENFORCMENT FOR COMPOSITES: 2D ALB$_2$ FLAKES*

7.1 Introduction

Since the discovery of the first graphene flake in 2004 through the mechanical cleavage of highly ordered pyrolytic graphite, two-dimensional (2D) nanomaterials has attracted more attention due to their potential use in a range of applications such as catalysis, electronic and optoelectronic devices, electrodes for energy storages, and nanocomposites.[276,277] 2D Materials such as graphene have versatile and enhanced mechanical, chemical and electrical properties.[278,279] The success of 2D graphene has motivated scientists in the last years to pursue the search for 3D materials that can be exfoliated by separating a 3D compound into single or few 2D layers.[280] These efforts successfully have led to the discovery of promising new 2D materials beyond graphene such as hexagonal boron nitride and transition metal dichalcogenides (TMDs).[281,282] Therefore, the space of 2D materials is expanding and getting more mature as a distinct class of materials bringing new capabilities, functionalities and technologies, which were not attainable with their parent 3D materials.

Layered metal oxides, nitrides and carbides are already being explored and were found to be promising 2D materials for different electronic devices.[283] To date, there is no literature about 2D materials based on metal borides, while there are many advantages of pursuing metal borides as 2D materials such as low temperature synthesis, especially aluminum. Aluminum diboride (AlB_2) has the unique properties of boron, and more cost-effective and practical to produce than

---

*Reprinted with permissions from "2D AlB2 Flakes for Epitaxial Thin Film Growth" by Humood, M.; Meyer, J. L.; Verkhoturov, S. V; Ozkan, T.; Eller, M.; Schweikert, E. A.; Economy, J.; Polycarpou, A. A. *J. Mater. Res.* **2018**, 1–9.

pure boron, which is similar to graphene oxide, as compared to graphene.[284] AlB_2 single crystals show metallic conductivity in the axis parallel to the basal hexagonal plane.[285] In addition, AlB_2 flakes were found to be a very effective reinforcement for polymer composites such as epoxies, with outstanding mechanical performance.[286,287] Therefore, AlB_2 flakes can be utilized for applications, which require conductive polymer composites. Due to the hexagonal structure, thermal and chemical stability, and electrical conductivity, metal borides have been used as substrates or barrier layers for heteroepitaxial growth of semiconductor devices.[288,289]

The hexagonal crystal structure of AlB_2 is one of the simplest inorganic structure types: a simple hexagonal cell of aluminum atoms with two boron atoms occupying the trigonal prismatic sites. The boron atoms form graphite-like sheets with the layers arranged into honeycomb-like structures separated by a lattice parameter (c) of 3.25 Å. AlB_2 is a MB_2 type material where M is for metals, and it has a metastable phase at room temperature.[290,291]

Two morphologies of AlB_2 crystallites have previously been identified – a low aspect ratio (LAR) equiaxed form of micron length, commonly used in grain refining of aluminum alloys, and a high aspect ratio (HAR) flake of up to a centimeter in width.[292–295] Growth of HAR AlB_2 single crystal flakes within an aluminum melt was demonstrated starting with a master alloy containing low aspect ratio AlB_2, which was heated above the Al-B liquidus region followed by various heat treatments.[287,296] Work by Hall and Economy showed that HAR flakes could be synthesized by heating merely above the $Al_{(L)}+AlB_{12}\leftrightarrow AlB_2$ peritectic transition temperature, which is permitted by the lengthy growth time of AlB_{12} from the Al-B melt.[297] In addition, aluminothermic processes have also been used to synthesize HAR AlB_2 flakes.[298]

The growth of high quality and uniform epitaxial thin films requires substrates with both atomically ultra-smooth roughness and flat surfaces. This is necessary to prevent fluctuation in the electrical properties of the deposited electronic devices due to the quantum effect of electron.[299] The ultra-smooth surface roughness allows the continuous efforts towards the miniaturization of electronic devices, and result into a more uniform thin film growth. In addition, the surface flatness is important since oxidation proceeds in a layer-by-layer manner. Therefore, reducing fluctuating in heights such as surface atomic steps will reduce the thickness of the surface oxide layer. In other words, it will be possible to achieve a thinner complete oxide layer. This was successfully achieved here using the mechanical cleavage of the substrate without the need for any extra polishing or etching of the substrate's surface, which simplifies the fabrication process. Once this new atomically smooth and flat surface is achieved, its stability against oxidation and surface reconstructions over short time in air is another critical requirement.[300] Rapid oxidation after cleavage can result on roughening of the surface.[301] Therefore, a low oxidation degree of the substrate is favorable for epitaxial thin film growth.

Here, we show that millimeter-scale HAR AlB_2 crystals grown in situ in an aluminum melt are cleavable via dry mechanical exfoliation resulting in 2D AlB_2.[302–304] This is potentially of interest with respect to ongoing investigations towards low-dimensional boron phases,[305–307] as a surface for epitaxial growth experiments, as well as the relatively high p-type conductivity (7.5 μΩ·cm) of the AlB_2 phase in the basal plane.[291] We monitored the surface of cleaved AlB_2 in terms of roughness and oxidation using AFM and SIMS respectively. The 2D cleaved flakes were found to be stable under ambient conditions for enough time to carry on the subsequent thin film growth of TiO_2 using ALD.

7.2 Experimental Details

7.2.1 Fabrication of HAR Flakes

Initially, an aluminum-boron (5 wt%) master alloy (KB Alloys) was alloyed with a 99.99% pure aluminum ingot (Alcoa) by heating to 750°C in an alumina crucible under flowing argon atmosphere and then cast in a cylindrical graphite mold. To produce the high aspect ratio (HAR) flakes in an aluminum solution, a cast ingot was then heated to 1360°C (above liquidus temperature) under flowing argon in an alumina crucible and then cooled to 900°C (below peritectic temperature) for one hour after which the sample was allowed to cool to room temperature at a rate of 0.2°C/min. HAR AlB_2 flakes were then extracted by etching away the aluminum matrix by 37% hydrochloric acid (Fisher Scientific), which yielded aluminum chloride ($AlCl_3$) precipitates and hydrogen gas. HAR AlB_2 flakes were separated from liquid phase by vacuum filtration using a Buchner funnel. Wet residue, composed of aluminum chloride powder and HAR AlB_2 flakes, was then washed with copious deionized water followed by isopropanol and dried in a convection oven at 110°C. Flakes were then separated from the powder by gentle sieving by hand with a 90 μm mesh sieve. This was followed by gentle flush with isopropanol and subsequent drying at 110°C for 2 hours. The as-grown flakes did not form an oxide layer during synthesis, because they were protected from oxygen by 1) the argon atmosphere but more importantly 2) the aluminum melt. The native oxide formed during and after the extraction and drying process from exposure to atmospheric oxygen rather than the free oxygen in the aluminum melt.

7.2.2 Atomic Force Microscopy (AFM)

The AFM images were scanned using a Cypher AFM instrument (Asylum Research, Santa Barbara, CA). The scans were carried out using non-contact mode and with 8 nm diameter silicon tip, and a scan rate of 0.5 Hz and 512 samples per line.

7.2.3 Nanoindentation

The mechanical properties were measured using a commercial indenter, TI Premier (Bruker, Minneapolis, MN), and the experiments were carried out using load-control mode. A cube corner probe was used (tip radius of 40 nm) to maintain shallow indentation depths. For all experiments, 5 s time periods for loading and unloading and 2 s dwell time at maximum nanoindentation load were used. The hardness (H) and reduced elastic modulus (E_r) were obtained from the first one-third of the unloading curve according to the Oliver and Pharr method [29]. The indenter probe was calibrated using a standard fused quartz (FQ) sample.

7.2.4 X-ray diffraction (XRD)

A Siemens/Bruker D-5000 XRD system (Radiation is Cu K-alpha and wavelength is 0.15418 nm) is used to obtain crystallographic structure determination.

7.2.5 Secondary Ion Mass Spectrometry (SIMS)

A CAMECA 4f SIMS was used in dynamic mode, for the measurement of the thickness of the oxide layers. The profiling was done with 14.5 keV Cs^+ ion beam (raster 500x500 μm^2, image collimation diameter 50 µm, sputtering rate 0.01 nm/s).

7.2.6 Atomic Layer Deposition (ALD)

An Ultratech / Cambridge NanoTech Savannah S200 ALD System is used to deposit TiO_2. ALD allows atomic-level control for the growth, which results in an epitaxial growth of the film.

7.3 Results and Discussion

7.3.1 Nanomechanical properties

Flakes were secured on AFM metal disks using an adhesive, and left to dry overnight in a well-ventilated room. Mechanical cleavage was then performed using mechanical exfoliation (3M scotch tape) inside a glove box filled with Argon gas. The scotch tape, was pressed on the flake and gently peeled up. This exposed the ultra-smooth pristine interior with an extremely flat surface. Figure 7.1(a-b) shows the SEM cross-sectional view of both as-grown and cleaved flakes. The thickness values were 6 and 10 μm for cleaved and as-grown flakes, respectively. The mechanical cleavage removed about 4 μm thick layer of the as-grown flake and was facilitated by the Kirkendall void formed due to diffusion rate differences and compositional gradients encountered during the synthesis of AlB_2 flakes. The cross-sectional SEM image in Figure 7.1(a) shows the length scale and orientation of these voids pointing to morphological origins of the flake formation above the liquidus temperature. Similar Kirkendall voids were observed with other binary alloy systems of Al, specifically Ti-Al and Ni-Al systems.[308] However, to the best of our knowledge, this is the first scientific study reporting the presence of planar Kirkendall voids in AlB_2 flakes.

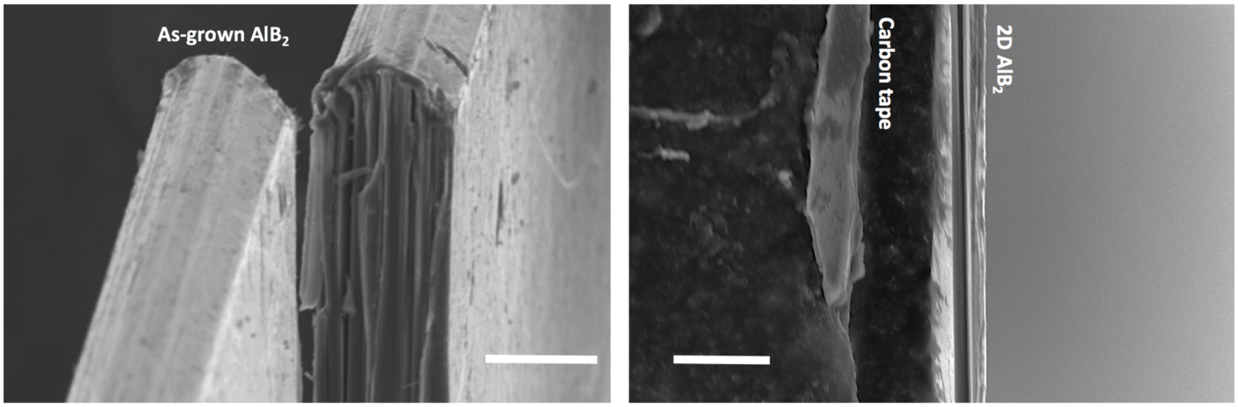

(a) **(b)**

Figure 7.1 Cross sectional SEM images for (a) as-grown and (b) cleaved AlB_2 surfaces. Scale bar is 10 μm.

Figure 7.2(a) shows a step between the as-grown and cleaved surface. Figure 7.2(c) shows the cleaved surface over a large area (10,000 Å x 10,000 Å) with R_q roughness of 1.07 Å and a z-height noise floor of 0.5 Å. The unit cell, $c_{o,}$ is found to be 3.01 Å. The cleaved flake has 80 times lower R_q roughness than the as-grown flake, which has significant defects and intermetallic formations (see Figure 7.2(b)).

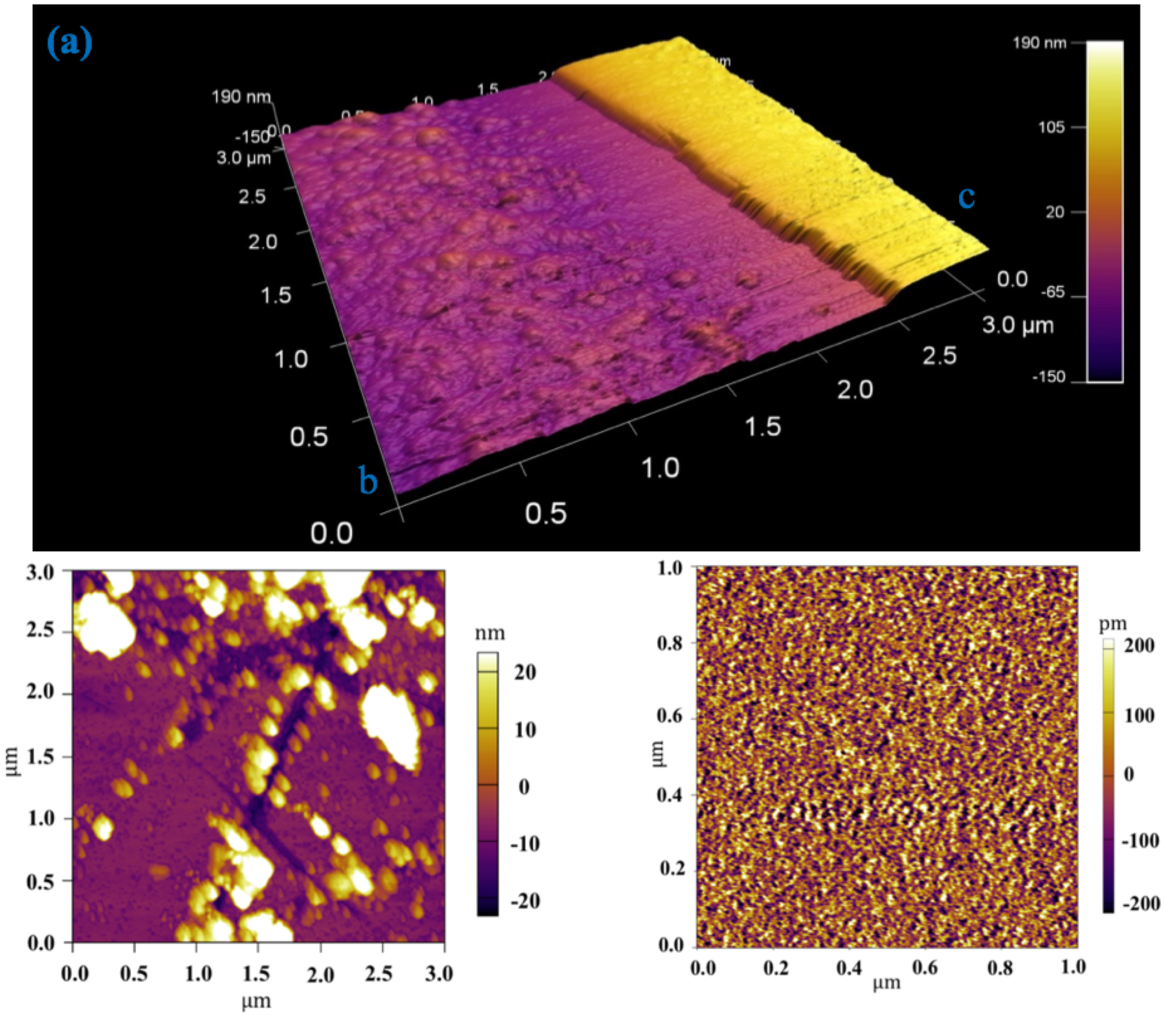

(b) **(c)**

Figure 7.2 (a) AFM of the AlB_2 flake showing a step generated after cleavage, (b) as-grown and (c) cleaved surfaces.

The nanoindentation probe was calibrated according to the Oliver-Pharr method between contact depths of 3-65 nm.[64] Figure 7.3(a) shows the residual image of a 150 µN peak load indentation, measured on the cleaved surface. The cross-section profile shows atomic-scale topography in Figure 7.3(a), where 3 Å height accounts for an atomic step height. There is no clear pile-up under this indentation load. For a higher indentation load of 720 µN, Figure 7.3(b) illustrates a significant pile-up around the indentation mark. The pile-up phenomenon shows highly crystallographic localized material flow.[309]

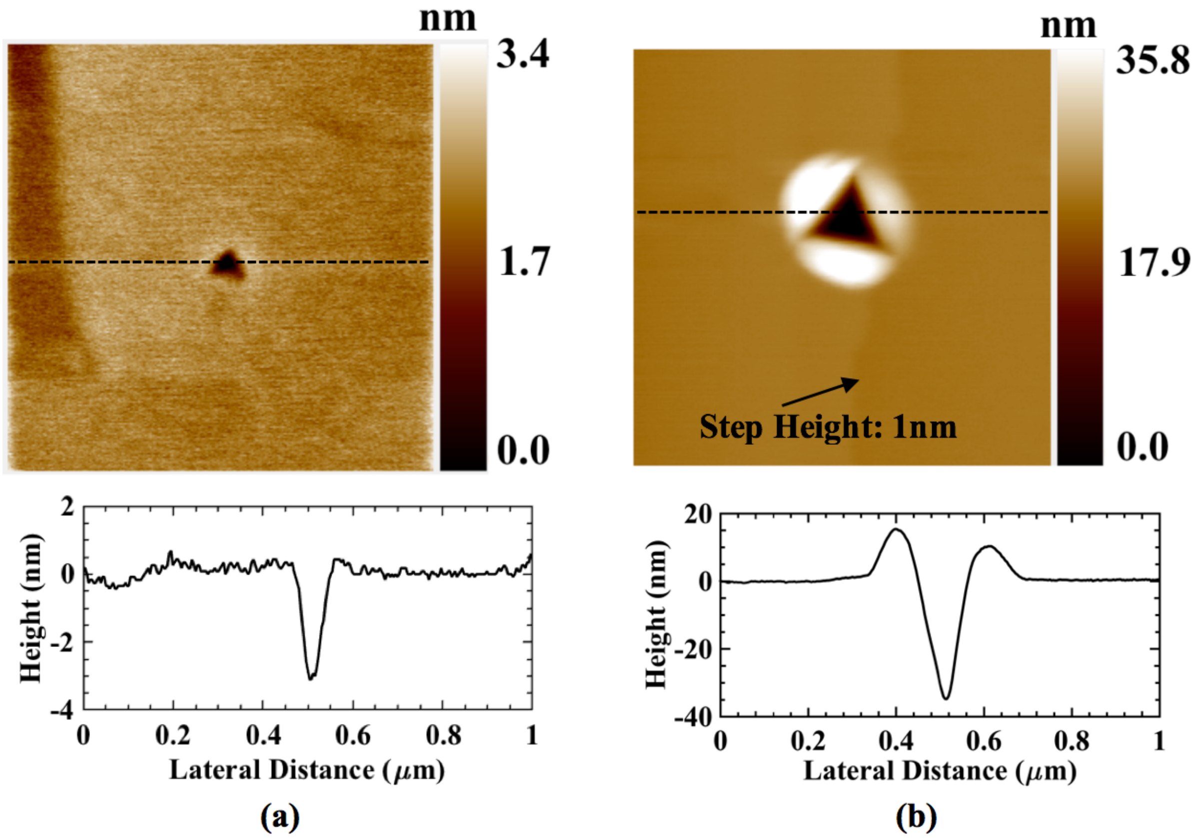

Figure 7.3 Residual indentation images and cross-section profiles (1x1 µm) after (a) 150 µN and (b) 720 µN indentation load on the cleaved sample under ambient dry conditions.

Table 7.1 provides the extracted nanomechanical properties of both samples: as-grown AlB_2 and cleaved AlB_2. The cleaved sample had higher elastic modulus and hardness. The reduced elastic modulus value (~174 GPa) was close to the bulk modulus measurement available both as a simulated/ calculated value provided by Duan et al.[310], Shein and Ivanovskii[311] and Gaillac et al.[312] Figure 7.4(a) and Figure 7.4(b) show representative load/displacement curves for both samples for indentation loads of 150 and 720 μN respectively. There were discrete fracture events in both samples, being more pronounced in the cleaved sample. The first fracture event in the cleaved sample took place in depths of 3-5 nm where the tip broke through a specific number of layers, where c = 3.25 Å. Therefore, for such nanoindentation depths, it was about 10-15 layers. These pop-in events in the loading part of the load-displacement curve of the cleaved sample were attributed to transverse cracking due to relatively lower incompressibility of AlB_2 on the plane of hexagonal symmetry.[296] This response is further amplified by the high Zener anisotropy as shown through first-principles calculations.[310] Through the introduction of freshly cleaved surface, we eliminated the inherent structural compliance of the flake originating from the Kirkendall void, which clearly manifested itself through the increase in reduced modulus as indicated by Table 7.1.

Table 7.1 Nanomechanical properties of as-grown and cleaved AlB_2 flakes.

Specimen	E_r (GPa)	H (GPa)	R_q (Å)
AlB_2 as-grown	174.36±8.33	22.00±2.16	81.1
AlB_2 cleaved	183.92±9.00	28.72±1.99	1.1

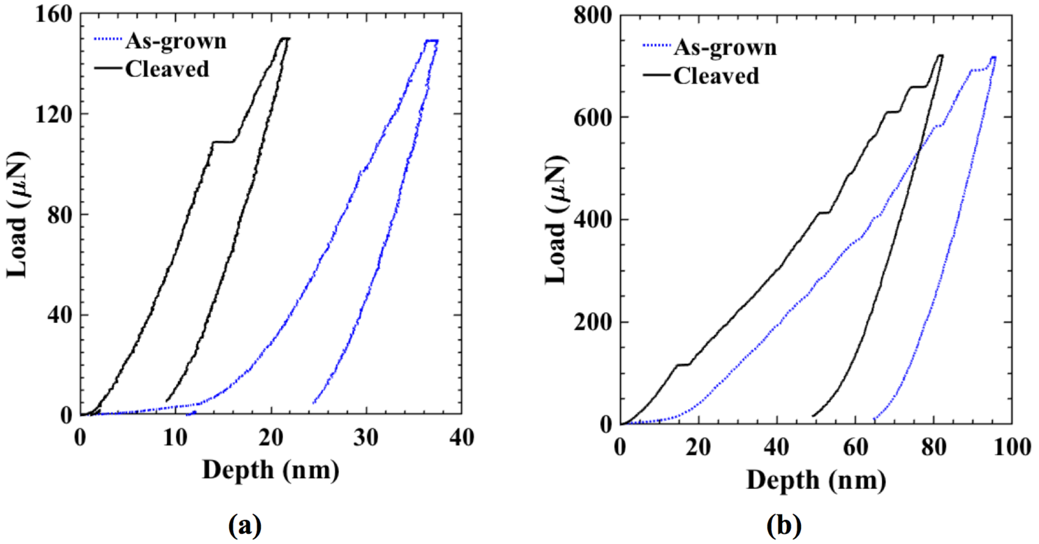

Figure 7.4 Representative load-displacement curves for peak indentation loads of (a) 150 μN and (b) 720 μN, for the as-grown and cleaved samples.

The freshly cleaved AlB_2 exhibits a harder and more brittle response. This experimental observation is in agreement with the findings of the first-principles calculations study, which assigned the highest brittleness among all metal diborides to AlB_2 based on bulk to shear moduli ratio.[310] The lack of structural compliance due to the removal of Kirkendall void combined with the intrinsically higher incompressibility of AlB_2 normal to the hexagonal symmetry plane, explain the hardness increase with the freshly cleaved samples.

In the case of as-grown flake, there is a thick superficial oxide layer, which provides a compliant response for penetration depths less than 10 nm. For the same sample, the lower frequency of fracture events even at higher loads points to a more uniform distribution of applied stress onto the underlying AlB_2 through the conformal oxide. A further insight concerning the native oxide is provided below using SIMS depth profiling. This surface layer was determined to be a conformal oxide consisting of Al_2O_3 and B_2O_3.

7.3.2 The surface chemistry of cleaved AlB_2

7.3.2.1 XRD

Figure 7.5(a) presents the XRD patterns obtained over the as-grown and cleaved AlB_2 flakes. Figure 7.5(b) shows more single-crystalline surface for the cleaved flake, as seen by the sharper peak. Figure 7.5(c) shows a semi-log scale for the cleaved surface with different crystallographic planes, which are labeled in the figure. The blue dashed lines represent the relative normalized polycrystalline peak intensities of AlB_2, which are extracted from the literature.[313] The cleaved plane showed only the diffraction peaks corresponding to the basal plane.

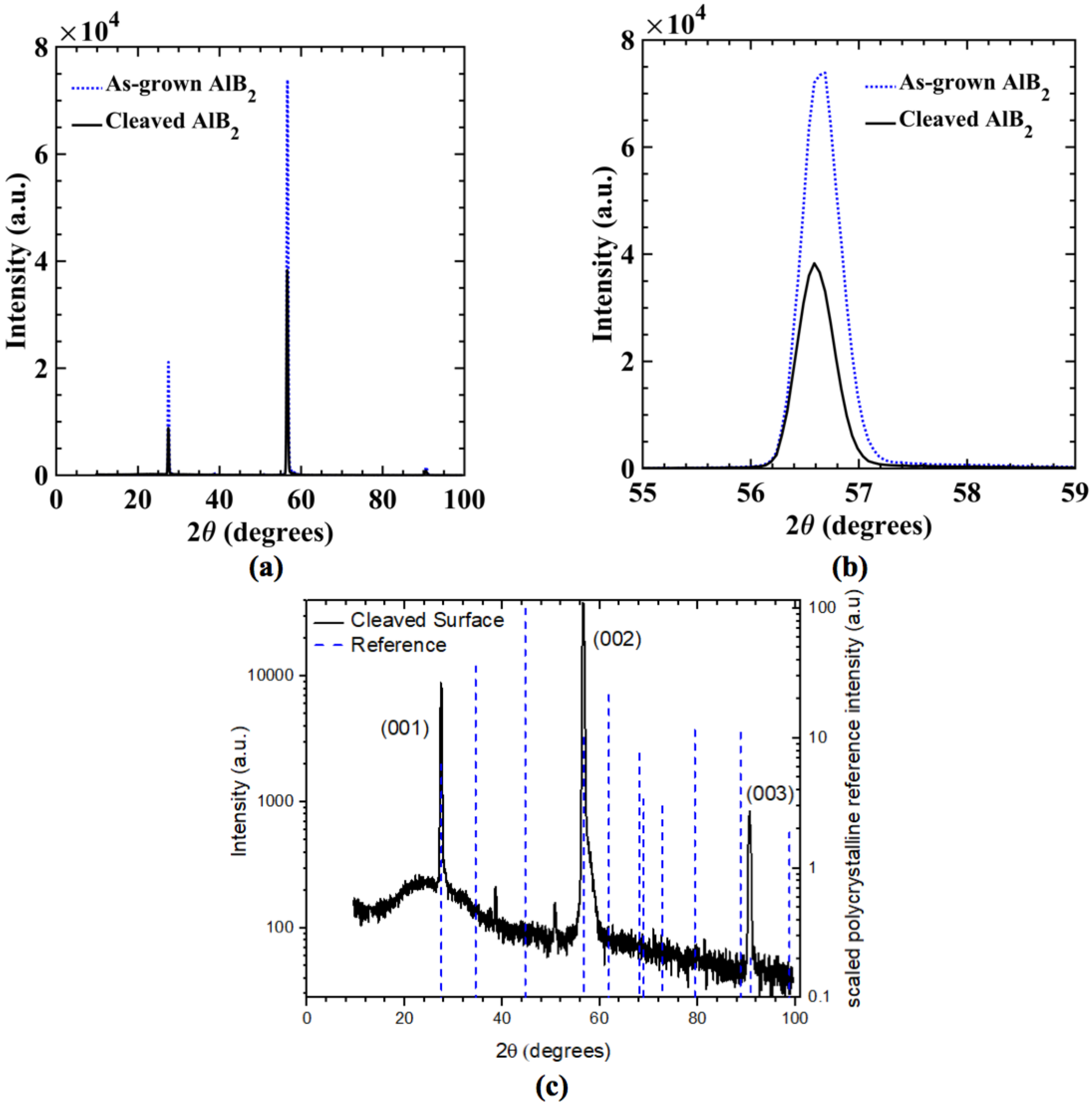

Figure 7.5 XRD for as-grown and cleaved AlB_2 flakes in (a-b) linear scale, and (c) log scale for cleaved sample.

7.3.2.2 SIMS depth profiling

The oxidation of AlB_2 via exposure in dry air or oxygen was investigated for the samples with main attention on the kinetics of oxidation and its growth rate. For the case of air exposure of the cleaved surface of AlB_2 mono-crystal, there is an important question concerning the oxide layers, which need to be addressed, such as: How does the few nm thickness of the oxide layer change with the time of oxidation? The kinetics of oxidation growth rate is important to ensure stability of cleaved surface before the successive chemistry on surface such as the deposition of epitaxial thin films.

To gain further insight about the compositional analysis of AlB_2 as a function of depth, SIMS CAMECA 4F was used for depth profiling. The angle of incidence of the beam was 26°. The measured secondary ions were negatively charged. Three different areas of each sample were probed. The profiles for these areas were very similar and shown in Figure 7.6. The SIMS characterization included both the as-grown and cleaved flakes. The purpose of characterizing the as-grown flake as well was to show the effect of cleavage on the surface roughness and the oxidation layer of the surface of the flake.

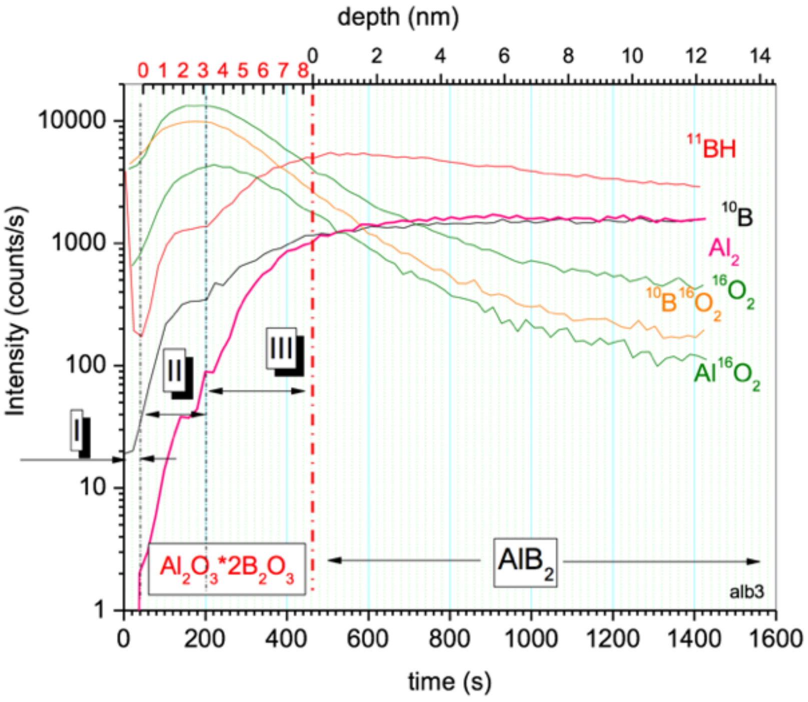

(a)

Figure 7.6 Quantitative SIMS depth profiles of (a) as-grown AlB_2 and (b) cleaved AlB_2 flakes.

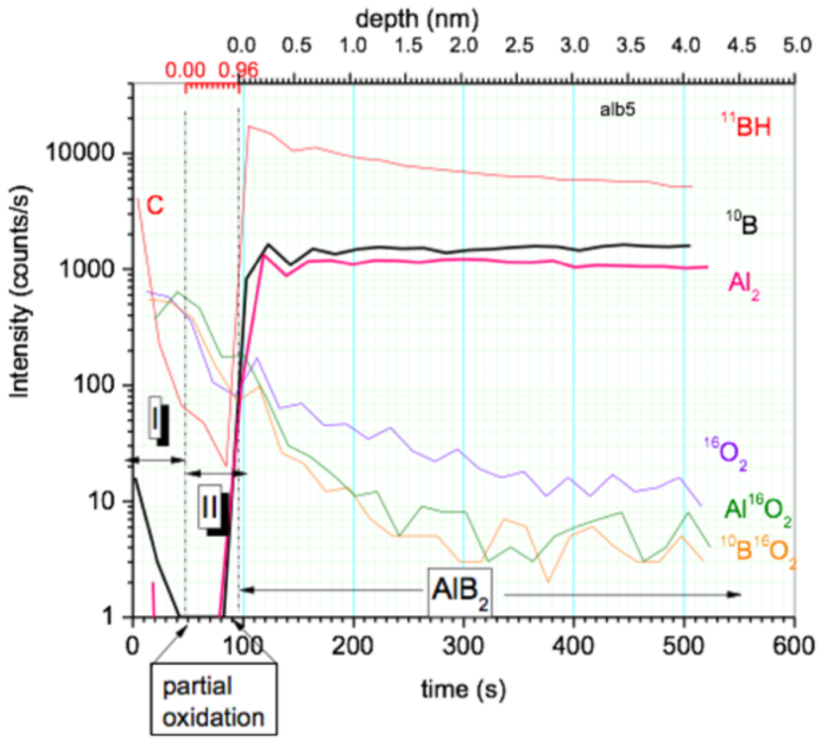

(b)

Figure 7.6 Continued.

Within the first 35 s of profiling the as-grownAlB$_2$ sample shown in Figure 7.6(a), the surface contamination was removed (Zone I). The transition zone II was characterized by increasing concentration of Cs (delivered from the beam), which increased the ionization probability of the emitted ions. It means that increasing of the signals of ions in this zone did not match with the increasing concentration of the corresponding oxides. Zone III showed decreasing concentration of oxides, with increasing B and Al. The next zone was the profiling of the bare AlB$_2$ (the signals of B and Al are steady).

The observed high signals of AlO$_2$ and BO$_2$ indicated strong oxidation, thus the topmost layer likely consisted of oxidation states for Al and B such as Al$_2$O$_3$ and B$_2$O$_3$. Previously, the oxidation kinetics of AlB$_2$ was investigated for the powders which were heated in air (10° C/min).[314] It was found that at the temperatures >600° C, the oxide products Al$_2$O$_3$ and B$_2$O$_3$ form

$Al_4B_2O_9$ ($2Al_2O_3*B_2O_3$) due to strong removing of B_2O_3. For the case presented here, the temperature of drying in air was 110° C only, thus likely, the products of oxidation Al_2O_3 and B_2O_3 form $Al_2O_3*2B_2O_3$. Referring to Figure 7.6, the top x-coordinate shows the profiling depth, which is calculated with the TRIM code, commonly used for sputtering (http://www.srim.org/). The profile shows that the native oxide layer was grown via exposure to atmospheric oxygen during the drying of manufactured sample, which was inserted into a convection oven at 110°C for 120 min. The depth profile showed that the thickness of the oxide layer was ~8nm. An interesting feature was the observation of the signal of BH. This signal was notable even at a depth of ~15 nm in the bulk AlB_2. Perhaps hydrogenation occurred at the time of synthesis of AlB_2.

Now we consider the cleaved 2D AlB_2, which was exposed in air for 5 min after the mechanical cleavage. The profile of this sample was different. Within the first 40 s of profiling the cleaved sample shown in Figure 7.6(b), the surface contamination (carbon, "natural boron") were removed (Zone I). Zone II showed the decreasing concentration of oxides, with increasing B and Al. The next zone was the profiling of the bare AlB_2 (the signals of B and Al are steady). The observed signals of AlO_2 and BO_2 indicated that the topmost molecular layer consisted of Al_2O_3 and B_2O_3 similar to the as-grown flake before the cleavage. However, the rapid decreasing of the signals of AlO_2 and BO_2 (~ 5 times within 1 nm of profiling) showed that the degree of oxidation was reduced with the depth. The total thickness of the oxide layer was less than 1 nm (Figure 7.6b). One should note that the extended low intensity signals of Al_2O_3 and B_2O_3 (intensities decrease 100 times) at the depth of > 2 nm were due to the common diffusion effect stimulated by the beam of primary ions of 14.5 keV Cs^+. Similar to the sample with a native oxide layer, an interesting feature was the observation of the signal of BH. This signal was notable even at a depth of ~5 nm in the bulk AlB_2. The sudden increase of signals of Al_2 and ^{10}B showed that the surface was very flat at the probing area which is of 500x500 μm^2. Therefore, the results of SIMS depth profiling support the findings of AFM roughness imaging.

7.3.3 Epitaxial thin film growth

To demonstrate the superior surface of cleaved AlB_2, ALD was used to deposit a TiO_2 film with a thickness of 10 nm. Also, silicon on insulator (SOI) is used for TiO_2 deposition, for comparison. Silicon is a common substrate for the growth of epitaxial thin films especially in semiconductor manufacturing. SOI refers to a layered structure of thin silicon film (~200 nm), top of insulator (1000 nm thick SiO_2 layer) and finally the micro-thick silicon wafer substrate. The silicon wafer was cleaned with acetone and methanol successively using ultrasonic cleaner. A hot air was used to dry the Si between both solutions. The silicon was used for deposition herein without any further etching of the native SiO_2 oxide. The aim of this experiment was to understand how the superficial oxide layer of cleaved 2D AlB2 and Si would influence the growth of epitaxial thin film.

To evaluate the quality of the epitaxial growth of TiO_2 film on both AlB_2 and Si, SIMS depth profiling and AFM topography imaging were used, as shown in Figures 7.7 and 7.8 respectively. SIMS showed four distinct layers for the TiO_2/Si sample, where two of them were titanium oxide layers. The first layer (area I) was the pure TiO_2 film, while the second layer (area II) consisted of titanium oxide with a strong content of the carbon (perhaps hydrocarbons). The third layer was the silicon oxide with a strong content of the carbon as well. The fourth layer (area IV) is the pure Si film. The estimated thicknesses of the layers are presented as the X coordinate at the top of the graph. On the other hand, three notable profile areas were observed for the TiO_2/AlB_2 sample. Area I showed the TiO_2 layer of thickness ~9 nm. The second area was the thin natural oxide layer of AlB_2 with thickness of ~3.7 nm. Area III was the body of the AlB_2 substrate.

The AFM images were used to measure the R_q roughness (see Figure 7.8). The roughness was 2.6 and 5.4 Å for the TiO_2 thin film on both AlB_2 and Si substrates, respectively. The TiO_2 thin film grown on AlB_2 was smoother as compared to the one grown on silicon. This was due to two reasons (a) the cleaved AlB_2 had smaller surface roughness than Si and (b) cleavage removed the majority of AlB_2 surface defects. Therefore, cleavage improved the conditions of AlB_2 surface for epitaxial thin film growth.

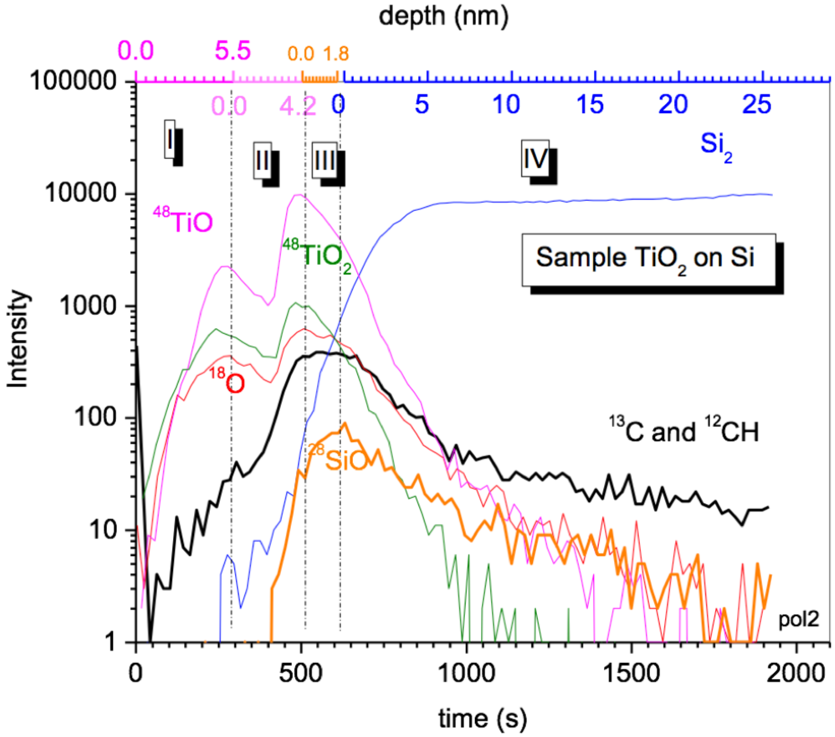

(a)

Figure 7.7 Quantitative SIMS depth profile and AFM roughness images of epitaxial grown (a) TiO_2/Si and (b) TiO_2/cleaved AlB_2.

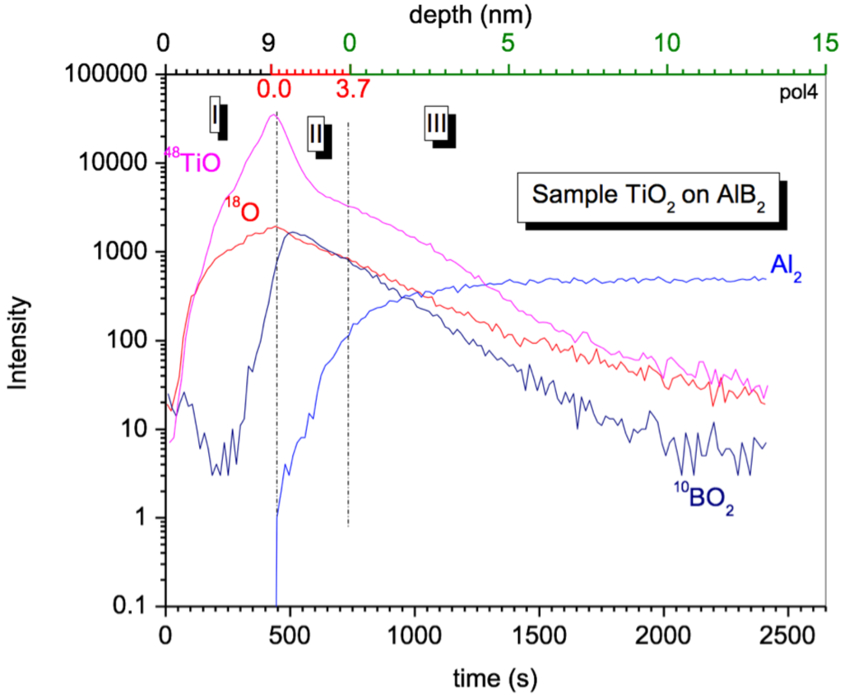

(b)

Figure 7.7 Continued.

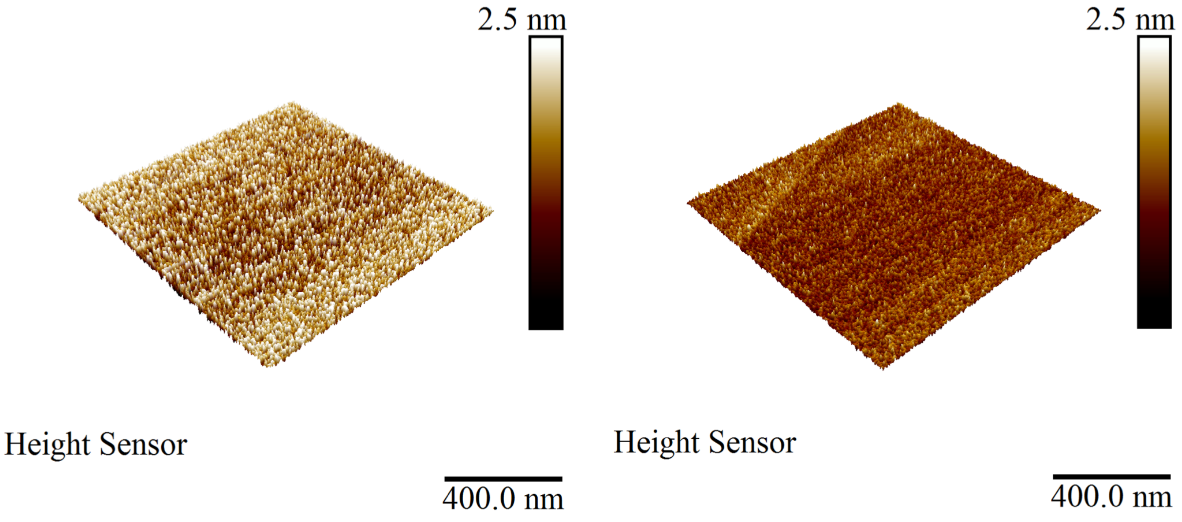

(a) **(b)**

Figure 7.8 AFM roughness images of the TiO$_2$ film deposited on (a) silicon substrate and (b) cleaved AlB$_2$ surface.

7.4 Summary of Chapter 7

To achieve the growth of high quality epitaxial thin film, the substrate needs to be atomically ultra-smooth and flat, highly single crystalline and has a stable and low degree of oxidation. The cleaved AlB_2 was found to successfully attain all these requirements. The as-grown AlB_2 surface layer had substantial defects and evidence of intermetallic formation. The cleavage of AlB_2 flake yielded the surface layer more single crystalline. In addition, the cleaved AlB_2 flakes had a surface roughness that was lower than the lattice parameter *c* of the AlB_2 phase and showed enhanced mechanical properties. Using atomic ion SIMS, we were able to characterize the oxide surface and subsurface of AlB_2 at the nanoscale. The as-grown flake had a native oxide layer with a thickness of ~8 nm. This oxide layer consisted of Al_2O_3 and B_2O_3. The cleavage resulted on a 2D AlB_2 with a superficial oxide layer with an average thickness of ~1 nm. The oxide layer was stable after cleavage as shown by AFM and SIMS, providing enough time to carry on the thin film deposition taking advantage of the atomic scale ultra-smooth and flat surface. TiO_2 thin film deposition showed that the cleaved AlB_2 can be a promising 2D material for thin film epitaxial growth.

8 SUMMARY OF THESIS RESEARCH AND RECOMMENDATION FOR FUTURE WORK

8.1 Summary of the thesis

Nanoindentation, micro-compression and nanoscratch experiments were performed in this thesis on thin multilayer nanocomposites in order to understand their mechanics and behavior against normal and sliding contact. Present work dedicates to investigating the nanomechanics and nanotribology, and their connection to the fabrication of flexible nanocomposites. Contributions and new findings of the investigation can be summarized as below:

(1) In Chapter 2, the 2D multilayer thin films were manufactured using the LbL assembly technique. These films are known to exhibit high gas barrier, but little was known about their durability, which is an important feature for various packaging applications (e.g., food and electronics). Films were prepared from bilayer and quadlayer sequences, with varying thickness and composition. In an effort to evaluate multilayer thin film surface and mechanical properties, and their resistance to failure and wear, a comprehensive range of experiments were conducted: low and high load indentation, low and high load scratch. some of the thin films were found to have exceptional mechanical behavior and exhibit excellent scratch resistance.

Specifically, nanobrick wall structures, comprised of montmorillonite (MMT) clay and polyethylenimine (PEI) bilayers, are the most durable coatings. PEI/MMT films exhibit high hardness, large elastic modulus, high elastic recovery, low friction, low scratch depth and a smooth surface. When combined with the low oxygen permeability and high optical transmission of these thin films, these excellent mechanical properties make them good candidates for hard coating surface-sensitive substrates, where polymers are required to sustain long-term surface aesthetics and quality.

(2) In case of graphene-based films, one main drawback was the weak interfacial bonding, which resulted in a weak adhesion to substrates and low scratch resistance. Typically, this is overcome by adding polymer layers to have stronger adherence to the substrate and between graphene sheets. Yet, these multilayer thin films were found to have lower resistance to lateral scratch forces, when compared to other reinforcements such as polymer/clay nanocomposites. Graphene is a versatile composite reinforcement candidate due to its strong mechanical, tunable electrical and optical properties, and chemical stability.

To solve this issue, two additional processing steps were suggested in Chapter 3 here to improve the scratch resistance of these films: graphene reduction and polymer crosslinking. Graphene/polymer nanocomposites consisting of polyvinylamine (PVAm) and graphene oxide (GO) were fabricated using Layer-by-Layer assembly (LbL) technique. The reduced elastic modulus and hardness of PVAm/GO films were measured using nanoindentation. Reducing GO enhances mechanical properties by 60-70% while polymer crosslinking maintains this enhancement. Both, graphene reduction and polymer crosslinking shows significant improvement to scratch resistance. Particularly, polymer crosslinking leads to films with higher elastic recovery, 50% lower adhesive and plowing friction coefficient, 140 and 50% higher adhesive and shear strength values respectively, and lower material pile-up and scratch width/depth.

(3) In case of all-polymeric multilayer thin films, they were found to be the least appealing, when it comes to scratch and wear resistance, especially when compared to clay and graphene-reinforced polymer nanocomposites. However, these films are favorable due to their ability to self-heal damages. In Chapter 4, Self-healing of mechanical damages was triggered in polymeric

multilayer films of polyethylenimine/ polyacrylic acid (PEI/PAA) by exposure to high humidity conditions such as immersion in deionized (DI) water. In situ wet nanoindentation was carried out to demonstrate the swelling behavior of thin films in high humidity. Once immersed in DI water, the film became softer, where roughness, modulus and hardness were reduced by about 100%. Once the film was dried, its mechanical properties were restored but not its morphology.

In this work, Heating was found to be required to promote the evaporation of immobilized water molecules, which bonds with the polymer once being immersed in DI water. When heating above glass transition temperature (Tg) was introduced, a formation of new bonding between both PEI and PAA took place leading to the formation of new topographical features similar to the as-deposited film. This reconstruction under high temperature (HT) was accompanied by more than 50% increase in the mechanical properties, which were measured using in situ HT nanoindentation. Multiple stimuli were required to achieve complete self-healing. The molecular mechanisms of these stimuli were determined using X-ray photoelectron spectroscopy (XPS) and Fourier transform infrared spectroscopy (FTIR).

(4) Chapter 5 discussed the role of substrate in the behavior of the multilayer thin films, which were deposited on these substrates. The mechanical properties of thin films are typically measured using nanoindentation and nanoscratch. Due to the cost and certain requirements such as improving functionality, the thin films need to be thinner than 200 nm. This can make the measurements more complicated due to the increase of substrate effects. The elastic response of nanoindentation in this case is a combination of film and substrate. Keeping nanoindentation depths within the “10% of film thickness” is a widely-used rule to reduce the effect of substrate effects. This rule tends to hold when the substrate is stiffer than the thin film. However, there are

more challenges to obtain reliable nanoindentation measurements, when the substrate is more compliant.

Therefore, typically, coatings with unknown mechanical properties are deposited on stiffer substrate for nanomechanical testing to avoid issues with having an inelastic response by a more compliant substrate, which influences the extraction of intrinsic properties of a thin film. But, in many cases, it is more realistic to obtain the properties of a film/substrate system as it is used in real-life application. For example, gas barriers coatings are deposited on a compliant substrate such as poly(ethylene terephthalate) (PET). In this study, experiments represented two composites systems: a stiff film on compliant substrate and a compliant film on stiff substrate. The film remained the same in both systems, while the substrates were varied. Nanoindentation and nanoscratch were carried out in both systems. Challenges and recommendations were discussed based on the findings and whether having the film on a stiff substrate resemble the true behavior of polymer nanocomposites in real applications.

(5) Chapters 2-5 discussed how to improve nanocomposites by optimizing the material selection and further processing steps such as reduction and crosslinking. Chapter 6 provided an alternative choice for the optimization of nanocomposites through geometry/shape. Mechanically-guided three-dimensional (3D) micro-assembly with controlled compressive buckling represents a promising emerging route to 3D mesostructures in a broad range of advanced materials, including single-crystalline silicon (Si), of direct relevance to microelectronic devices. During practical applications, the assembled 3D mesostructures and micro-devices usually undergo external mechanical loading such as out-of-plane compression, which can induce damage in or failure of the structures/devices.

Here, the mechanical responses of a few mechanically-assembled 3D kirigami mesostructures under flat-punch compression are studied through combined experiment and finite element analyses (FEA). These 3D kirigami mesostructures consisting of a bilayer of Si and SU-8 epoxy are formed through integration of patterned 2D precursors with a pre-stretched elastomeric substrate at pre-defined bonding sites to allow controlled buckling that transforms them into desired 3D configurations. In situ SEM measurement enables detailed studies of the mechanical behavior of these structures. Analysis of the load-displacement curves allows the measurement of the effective stiffness and elastic recovery of various 3D structures. The compression experiments indicate distinct regimes in the compressive force/displacement curves, and reveals different geometry-dependent deformation for the structures. Complementary computational modeling supports our experimental findings and further explains the geometry-dependent deformation.

(6) Last but not least, a new electrically-conductive reinforcement for polymer-based nanocomposites was discussed in Chapter 7. I reported on the mechanical cleavage of conductive metal-based aluminum diboride (AlB_2) flakes. The cleavage resulted in a 2D material, which is highly single crystalline, and had an atomically flat and smooth surface as shown by atomic force microscopy (AFM) and secondary ion mass spectrometry (SIMS). Nanoindentation and AFM imaging of freshly cleaved specimens revealed sub-nm roughness and 30% improvement in the nanomechanical properties as compared to the original flakes. Once exposed to ambient air, the cleaved AlB_2 flakes formed a superficial oxidation layer of less than 1 nm thickness within 5 minutes.

Owing to atomically smooth surface roughness, ultra-thin and stable oxide layer and excellent mechanical and electrical characteristics of AlB_2, the exfoliated flakes present an ideal 2D material for emerging applications in microfabrication such as the growth of epitaxial thin films and as reinforcement for polymer nanocomposites. To prove the sub-nm surface characteristics of exfoliated AlB_2, a 10-nm thick TiO_2 film was deposited on freshly cleaved AlB_2 using atomic layer deposition. Surface roughness and compositional consistency of this film was compared with a control sample deposited on Si. The TiO_2 film on AlB_2 showed a distinct thin interface layer with less defects than TiO_2 on Si and superior flatness. This superior flatness is excepted to result on a strong interfacial bonding to the polymeric matrix.

8.2 Recommendations for future work

As seen in chapter 3 and 5, the mechanical behavior of a nanocomposite can be dominated by the interface between the filler and the polymer matrix in case of 2D PNC. Similarly, the bonding between the structure and the substrate in case of 3D PNC is crucial. Future studies need to be carried out in order to understand the mechanics and physics of these interfaces, which is not well understood. For example, time-dependent viscoelastic properties and thermomechanical response can varies widely based on the nature of this interface. The FEA models discussed in this thesis had fully-bonded condition between substrate and PNC. As a continuation of the work presented by this thesis, one path for future work is to characterize the mechanical properties near the interface and understand the bonding at the interface. The extraction of viscoelastic properties is important as well to be able to model the contact mechanics near the interface and predict the behavior of these PNC. Once such properties are extracted, they can be added as inputs to the FEA to achieve a better modelling response of these nanocomposites under deformation.

Additionally, a fruitful continuation of this work is to understand the behavior of 3D nanocomposites particularly under cyclic loading. Fatigue resistance is important for the application of these nanocomposites: 3D flexible MEMS, which will be used as biosensors. Biology is inherently three-dimensional complex designs. In addition to the geometric complexity, some biological systems as human skin undergo large elastic deformation due to their huge compliance. These geometrical and mechanical properties have introduced challenges for designing biosensors and bioelectronics. To overcome these challenges, we have fabricated microscale (3D) polymer-based kirigami architectures using patterning cuts on 2D thin layers of silicon and photodefinable epoxy (SU8), which is deposited on elastomer substrates to mimic the properties of the skin. The 2D layers are patterned using photolithography and reactive ion etching (RIE) in stretched elastomer substrate such as silicone to a certain prestrain. The transformation from 2D patterns into 3D engineered structures is carried out using compressive buckling. Studies of the compressive response, cycling and viscoelasticity of these structures will be done using in-situ SEM flat-punch compression. The effect of strain rate is explored as well to understand creep behavior and energy dissipation.

BIBLIOGRAPHY

(1) Decher, G.; Schlenoff, J. B. *Multilayer Thin Films: Sequential Assembly of Nanocomposite Materials*; Wiley, 2006.

(2) Kumar, S. K.; Benicewicz, B. C.; Vaia, R. A.; Winey, K. I. 50th Anniversary Perspective: Are Polymer Nanocomposites Practical for Applications? *Macromolecules* **2017**, *50*, 714–731.

(3) Priolo, M. a.; Gamboa, D.; Holder, K. M.; Grunlan, J. C. Super Gas Barrier of Transparent Polymer-Clay Multilayer Ultrathin Films. *Nano Lett.* **2010**, *10*, 4970–4974.

(4) Xu, L.; Gutbrod, S. R.; Bonifas, A. P.; Su, Y.; Sulkin, M. S.; Lu, N.; Chung, H.-J.; Jang, K.-I.; Liu, Z.; Ying, M.; *et al.* 3D Multifunctional Integumentary Membranes for Spatiotemporal Cardiac Measurements and Stimulation across the Entire Epicardium. *Nat. Commun.* **2014**, *5*, 3329.

(5) Winey, K. I.; Vaia, R. A. Polymer Nanocomposites. *MRS Bull.* **2007**, *32*, 314–322.

(6) Fu, S.-Y.; Feng, X.-Q.; Lauke, B.; Mai, Y.-W. Effects of Particle Size, Particle/Matrix Interface Adhesion and Particle Loading on Mechanical Properties of Particulate–Polymer Composites. *Compos. Part B Eng.* **2008**, *39*, 933–961.

(7) Kojima, Y.; Usuki, A.; Kawasumi, M.; Okada, A.; Fukushima, Y.; Kurauchi, T.; Kamigaito, O. Mechanical Properties of Nylon 6-Clay Hybrid. *J. Mater. Res.* **1993**, *8*, 1185–1189.

(8) Ning, X.; Wang, H.; Yu, X.; Soares, J. A. N. T.; Yan, Z.; Nan, K.; Velarde, G.; Xue, Y.; Sun, R.; Dong, Q.; *et al.* 3D Tunable, Multiscale, and Multistable Vibrational Micro-Platforms Assembled by Compressive Buckling. *Adv. Funct. Mater.* **2017**, *27*, 1605914.

(9) Po-Yen, C.; Muchun, L.; Zhongying, W.; H., H. R.; Y., W. I. From Flatland to Spaceland: Higher Dimensional Patterning with Two-Dimensional Materials. *Adv. Mater.* **2017**, *29*, 1605096.

(10) Xu, B.; Rogers, J. A. Mechanics-Driven Approaches to Manufacturing—A Perspective. *Extrem. Mech. Lett.* **2016**, *7*, 44–48.

(11) Yan, Z.; Zhang, F.; Liu, F.; Han, M.; Ou, D.; Liu, Y.; Lin, Q.; Guo, X.; Fu, H.; Xie, Z.; *et al.* Mechanical Assembly of Complex, 3D Mesostructures from Releasable Multilayers of

Advanced Materials. *Sci. Adv.* **2016**, *2*.

(12) Ariga, K.; Yamauchi, Y.; Rydzek, G.; Ji, Q.; Yonamine, Y.; Wu, K. C.-W.; Hill, J. P. Layer-by-Layer Nanoarchitectonics: Invention, Innovation, and Evolution. *Chem. Lett.* **2014**, *43*, 36–68.

(13) Joseph, N.; Ahmadiannamini, P.; Hoogenboom, R.; Vankelecom, I. F. J. Layer-by-Layer Preparation of Polyelectrolyte Multilayer Membranes for Separation. *Polym. Chem.* **2014**, *5*, 1817–1831.

(14) Sung, C.; Vidyasagar, A.; Hearn, K.; Lutkenhaus, J. L. Effect of Thickness on the Thermal Properties of Hydrogen-Bonded LbL Assemblies. *Langmuir* **2012**, *28*, 8100–8109.

(15) Allen, A. L.; Tan, K. J.; Fu, H.; Batteas, J. D.; Bergbreiter, D. E. Solute- and Temperature-Responsive “Smart” Grafts and Supported Membranes Formed by Covalent Layer-by-Layer Assembly. *Langmuir* **2012**, *28*, 5237–5242.

(16) Sato, M.; Sano, M. Van Der Waals Layer-by-Layer Construction of a Carbon Nanotube 2D Network. *Langmuir* **2005**, *21*, 11490–11494.

(17) Ferreira, M.; Rubner, M. F. Molecular-Level Processing of Conjugated Polymers. 1. Layer-by-Layer Manipulation of Conjugated Polyions. *Macromolecules* **1995**, *28*, 7107–7114.

(18) Irigoyen, J.; Han, L.; Llarena, I.; Mao, Z. W.; Gao, C. Y.; Moya, S. E. Responsive Polyelectrolyte Multilayers Assembled at High Ionic Strength with an Unusual Collapse at Low Ionic Strength. *Macromol. Rapid Commun.* **2012**, *33*, 1964–1969.

(19) Shimazaki, Y.; Nakamura, R.; Ito, S.; Yamamoto, M. Molecular Weight Dependence of Alternate Adsorption through Charge-Transfer Interaction. *Langmuir* **2001**, *17*, 953–956.

(20) Hagen, D. A.; Foster, B.; Stevens, B.; Grunlan, J. C. Shift-Time Polyelectrolyte Multilayer Assembly: Fast Film Growth and High Gas Barrier with Fewer Layers by Adjusting Deposition Time. *ACS Macro Lett.* **2014**, 663–666.

(21) Ariga, K.; Hill, J. P.; Ji, Q. Layer-by-Layer Assembly as a Versatile Bottom-up Nanofabrication Technique for Exploratory Research and Realistic Application. *Phys. Chem. Chem. Phys.* **2007**, *9*, 2319–2340.

(22) Caruso, R. A.; Susha, A.; Caruso, F. Multilayered Titania, Silica, and Laponite Nanoparticle Coatings on Polystyrene Colloidal Templates and Resulting Inorganic

Hollow Spheres. *Chem. Mater.* **2001**, *13*, 400–409.

(23) Podsiadlo, P.; Michel, M.; Lee, J.; Verploegen, E.; Kam, N. W. S.; Ball, V.; Qi, Y.; Hart, A. J.; Hammond, P. T.; Kotov, N. A. Exponential Growth of LBL Films with Incorporated Inorganic Sheets. *Nano Lett.* **2008**, *8*, 1762–1770.

(24) Zou, Y.; Xie, L. X.; Carroll, S.; Muniz, M.; Gibson, H.; Wei, W. Z.; Liu, H. P.; Mao, G. Z. Layer-by-Layer Films with Bioreducible and Nonbioreducible Polycations for Sequential DNA Release. *Biomacromolecules* **2014**, *15*, 3965–3975.

(25) Dreaden, E. C.; Morton, S. W.; Shopsowitz, K. E.; Choi, J. H.; Deng, Z. J.; Cho, N. J.; Hammond, P. T. Bimodal Tumor-Targeting from Microenvironment Responsive Hyaluronan Layer-by-Layer (LbL) Nanoparticles. *ACS Nano* **2014**, *8*, 8374–8382.

(26) Costa, R. R.; Mano, J. F. Polyelectrolyte Multilayered Assemblies in Biomedical Technologies. *Chem. Soc. Rev.* **2014**, *43*, 3453–3479.

(27) Manabe, K.; Nishizawa, S.; Kyung, K. H.; Shiratori, S. Optical Phenomena and Antifrosting Property on Biomimetics Slippery Fluid-Infused Antireflective Films via Layer-by-Layer Comparison with Superhydrophobic and Antireflective Films. *ACS Appl. Mater. Interfaces* **2014**, *6*, 13985–13993.

(28) Fukada, K.; Shiratori, S. Gradient Functional Characteristic of Polymer/Nanoparticle Stacks on a Polyethylene Naphthalate Film. *Ind. Eng. Chem. Res.* **2015**, *54*, 979–986.

(29) Pan, H.; Wang, W.; Pan, Y.; Song, L.; Hu, Y.; Liew, K. M. Formation of Layer-by-Layer Assembled Titanate Nanotubes Filled Coating on Flexible Polyurethane Foam with Improved Flame Retardant and Smoke Suppression Properties. *ACS Appl. Mater. Interfaces* **2015**, *7*, 101–111.

(30) Patra, D.; Vangal, P.; Cain, A. A.; Cho, C.; Regev, O.; Grunlan, J. C. Inorganic Nanoparticle Thin Film That Suppresses Flammability of Polyurethane with Only a Single Electrostatically-Assembled Bilayer. *ACS Appl. Mater. Interfaces* **2014**, *6*, 16903–16908.

(31) Priolo, M. A.; Holder, K. M.; Guin, T.; Grunlan, J. C. Recent Advances in Gas Barrier Thin Films via Layer-by-Layer Assembly of Polymers and Platelets. *Macromol. Rapid Commun.* **2015**, *36*, 866–879.

(32) Tzeng, P.; Lugo, E. L.; Mai, G. D.; Wilhite, B. A.; Grunlan, J. C. Super Hydrogen and Helium Barrier with Polyelectolyte Nanobrick Wall Thin Film. *Macromol. Rapid Commun.* **2015**, *36*, 96–101.

(33) Chatham, H. Oxygen Diffusion Barrier Properties of Transparent Oxide Coatings on Polymeric Substrates. *Surf. Coatings Technol.* **1996**, *78*, 1–9.

(34) Holder, K. M.; Spears, B. R.; Huff, M. E.; Priolo, M. a.; Harth, E.; Grunlan, J. C. Stretchable Gas Barrier Achieved with Partially Hydrogen-Bonded Multilayer Nanocoating. *Macromol. Rapid Commun.* **2014**, *35*, 960–964.

(35) Guin, T.; Krecker, M.; Hagen, D. A.; Grunlan, J. C. Thick Growing Multi Layer Nanobrick Wall Thin Films: Super Gas Barrier with Very Few Layers. *Langmuir* **2014**, *30*, 7057–7060.

(36) Holder, K. M.; Spears, B. R.; Huff, M. E.; Priolo, M. A.; Harth, E.; Grunlan, J. C. Stretchable Gas Barrier Achieved with Partially Hydrogen- Bonded Multilayer Nanocoating. *Macromol. Rapid Commun.* **2014**, *35*, 960–964.

(37) Priolo, M. a.; Gamboa, D.; Grunlan, J. C. Transparent Clay-Polymer Nano Brick Wall Assemblies with Tailorable Oxygen Barrier. *ACS Appl. Mater. Interfaces* **2010**, *2*, 312–320.

(38) Yeo, S. M.; Polycarpou, A. A. Micromechanical Properties of Polymeric Coatings. *Tribol. Int.* **2013**, *60*, 198–208.

(39) Klapperich, C.; Komvopoulos, K.; Pruitt, L. Nanomechanical Properties of Polymers Determined From Nanoindentation Experiments. *J. Tribol.* **2000**, *123*, 624–631.

(40) Geng, K.; Yang, F.; Druffel, T.; Grulke, E. A. Nanoindentation Behavior of Ultrathin Polymeric Films. *Polymer (Guildf).* **2005**, *46*, 11768–11772.

(41) WANG, M. Nanoindentation of Polymeric Thin Films with an Interfacial Force Microscope. *J. Mech. Phys. Solids* **2004**, *52*, 2329–2354.

(42) Saha, R.; Nix, W. D. Effects of the Substrate on the Determination of Thin Film Mechanical Properties by Nanoindentation. *Acta Mater.* **2002**, *50*, 23–38.

(43) Tayebi, N.; Polycarpou, A. a.; Conry, T. F. Effects of Substrate on Determination of Hardness of Thin Films by Nanoscratch and Nanoindentation Techniques. *J. Mater. Res.* **2004**, *19*, 1791–1802.

(44) Yu, N.; Bonin, W. A.; Polycarpou, A. A. High-Resolution Capacitive Load-Displacement Transducer and Its Application in Nanoindentation and Adhesion Force Measurements. *Rev. Sci. Instrum.* **2005**, *76*.

(45) Yeo, C.-D.; Polycarpou, A. a.; Kiely, J. D.; Hsia, Y.-T. Nanomechanical Properties of

Sub-10 Nm Carbon Film Overcoats Using the Nanoindentation Technique. *J. Mater. Res.* **2007**, *22*, 141–151.

(46) Yang, Y.-H.; Haile, M.; Park, Y. T.; Malek, F. A.; Grunlan, J. C. Super Gas Barrier of All-Polymer Multilayer Thin Films. *Macromolecules* **2011**, *44*, 1450–1459.

(47) Yang, Y. H.; Bolling, L.; Priolo, M. A.; Grunlan, J. C. Super Gas Barrier and Selectivity of Graphene Oxide-Polymer Multilayer Thin Films. *Adv. Mater.* **2013**, *25*, 503–508.

(48) Jaber, J. A.; Schlenoff, J. B. Recent Developments in the Properties and Applications of Polyelectrolyte Multilayers. *Curr. Opin. Colloid Interface Sci.* **2006**, *11*, 324–329.

(49) Schmidt, D. J.; Cebeci, F. Ç.; Kalcioglu, Z. I.; Wyman, S. G.; Ortiz, C.; Vliet, K. J. Van; Hammond, P. T. Electrochemically Controlled Swelling and Mechanical Properties of a Polymer Nanocomposite. *ACS Nano* **2009**, *3*, 2207–2216.

(50) Qi, W.; Xue, Z.; Yuan, W.; Wang, H. Layer-by-Layer Assembled Graphene Oxide Composite Films for Enhanced Mechanical Properties and Fibroblast Cell Affinity. *J. Mater. Chem. B* **2014**, *2*, 325–331.

(51) Lehaf, A. M.; Hariri, H. H.; Schlenoff, J. B. Homogeneity, Modulus, and Viscoelasticity of Polyelectrolyte Multilayers by Nanoindentation: Refining the Buildup Mechanism. *Langmuir* **2012**, *28*, 6348–6355.

(52) Dominique Collin, †; Philippe Lavalle *, ‡; Juan Méndez Garza ‡, §; Jean-Claude Voegel, ‡; Pierre Schaaf, ⊥; and Philippe Martinoty†. Mechanical Properties of Cross-Linked Hyaluronic Acid/Poly-(l-Lysine) Multilayer Films. *Macromolecules* **2004**, *37*, 10195–10198.

(53) Conghua Lu; Ingo Dönch; Marc Nolte; and Andreas Fery*. Au Nanoparticle-Based Multilayer Ultrathin Films with Covalently Linked Nanostructures: Spraying Layer-by-Layer Assembly and Mechanical Property Characterization. *Chem. Mater.* **2006**, *18*, 6204–6210.

(54) Prem V. Pavoor, †; Anuj Bellare, ‡; Andrew Strom, §; Dehua Yang, §; and Robert E. Cohen*, †. Mechanical Characterization of Polyelectrolyte Multilayers Using Quasi-Static Nanoindentation. *Macromolecules* **2004**, *37*, 4865–4871.

(55) Ozzy Mermut; Julie Lefebvre; Derek G. Gray; and Christopher J. Barrett*. Structural and Mechanical Properties of Polyelectrolyte Multilayer Films Studied by AFM. *Macromolecules* **2003**, *36*, 8819–8824.

(56) Ploehn, H. J.; Liu, C. Quantitative Analysis of Montmorillonite Platelet Size by Atomic Force Microscopy. *Ind. Eng. Chem. Res.* **2006**, *45*, 7025–7034.

(57) Paul Podsiadlo, †; Zhiyong Tang, ‖; Bong Sup Shim, †; and Nicholas A. Kotov* †, ‡ §. Counterintuitive Effect of Molecular Strength and Role of Molecular Rigidity on Mechanical Properties of Layer-by-Layer Assembled Nanocomposites. *Nano Lett.* **2007**, *7*, 1224–1231.

(58) Zhang, X.; Hu, L.; Sun, D. Nanoindentation and Nanoscratch Profiles of Hybrid Films Based on (γ-Methacrylpropyl)Trimethoxysilane and Tetraethoxysilane. *Acta Mater.* **2006**, *54*, 5469–5475.

(59) Han, B.; Chery, D. R.; Yin, J.; Lu, X. L.; Lee, D.; Han, L. Nanomechanics of Layer-by-Layer Polyelectrolyte Complexes: A Manifestation of Ionic Cross-Links and Fixed Charges. *Soft Matter* **2016**, *12*, 1158–1169.

(60) Li, Y. C.; Schulz, J.; Grunlan, J. C. Polyelectrolyte/Nanosilicate Thin-Film Assemblies: Influence of PH on Growth, Mechanical Behavior, and Flammability. *ACS Appl. Mater. Interfaces* **2009**, *1*, 2338–2347.

(61) Jang, W. S.; Grunlan, J. C. Robotic Dipping System for Layer-by-Layer Assembly of Multifunctional Thin Films. *Rev. Sci. Instrum.* **2005**, *76*.

(62) Gamboa, D.; Priolo, M. A.; Ham, A.; Grunlan, J. C. Note: Influence of Rinsing and Drying Routines on Growth of Multilayer Thin Films Using Automated Deposition System. *Rev. Sci. Instrum.* **2010**, *81*.

(63) Yu, N.; Polycarpou, A. a.; Conry, T. F. Tip-Radius Effect in Finite Element Modeling of Sub-50 Nm Shallow Nanoindentation. *Thin Solid Films* **2004**, *450*, 295–303.

(64) Oliver, W. C.; Pharr, G. M. An Improved Technique for Determining Hardness and Elastic Modulus Using Load and Displacement Sensing Indentation Experiments. *J. Mater. Res.* **1992**, *7*, 1564–1583.

(65) Chatterjee, A.; Kumar, N.; Abelson, J. R.; Bellon, P.; Polycarpou, A. A. Nanoscratch and Nanofriction Behavior of Hafnium Diboride Thin Films. *Wear* **2008**, *265*, 921–929.

(66) G. Ladam †, ‡; P. Schaad, §; J. C. Voegel *, ‡; P. Schaaf †, ⊥; G. Decher, †; and F. Cuisinier‡. In Situ Determination of the Structural Properties of Initially Deposited Polyelectrolyte Multilayers. *Langmuir* **2000**, *16*, 1249–1255.

(67) Tzeng, P.; Maupin, C. R.; Grunlan, J. C. Influence of Polymer Interdiffusion and Clay

Concentration on Gas Barrier of Polyelectrolyte/Clay Nanobrick Wall Quadlayer Assemblies. *J. Memb. Sci.* **2014**, *452*, 46–53.

(68) Stevens, B.; Dessiatova, E.; Hagen, D. A.; Todd, A. D.; Bielawski, C. W.; Grunlan, J. C. Low-Temperature Thermal Reduction of Graphene Oxide Nanobrick Walls: Unique Combination of High Gas Barrier and Low Resistivity in Fully Organic Polyelectrolyte Multilayer Thin Films. *ACS Appl. Mater. Interfaces* **2014**, *6*, 9942–9945.

(69) Guin, T.; Stevens, B.; Krecker, M.; D'Angelo, J.; Humood, M.; Song, Y.; Smith, R.; Polycarpou, A.; Grunlan, J. C. Ultrastrong, Chemically Resistant Reduced Graphene Oxide-Based Multilayer Thin Films with Damage Detection Capability. *ACS Appl. Mater. Interfaces* **2016**, *8*, 6229–6235.

(70) Tzeng, P.; Stevens, B.; Devlaming, I.; Grunlan, J. C. Polymer–Graphene Oxide Quadlayer Thin-Film Assemblies with Improved Gas Barrier. *Langmuir* **2015**, *31*, 5919–5927.

(71) Okonkwo, A. O.; Jagadale, P.; García Herrera, J. E.; Hadjiev, V. G.; Muñoz Saldaña, J.; Tagliaferro, A.; Robles Hernandez, F. C. High-Toughness/Low-Friction Ductile Epoxy Coatings Reinforced with Carbon Nanostructures. *Polym. Test.* **2015**, *47*, 113–119.

(72) Godara, A.; Raabe, D.; Green, S. The Influence of Sterilization Processes on the Micromechanical Properties of Carbon Fiber-Reinforced PEEK Composites for Bone Implant Applications. *Acta Biomater.* **2007**, *3*, 209–220.

(73) Mohimi, E.; Ozkan, T.; Babar, S.; Polycarpou, A. A.; Abelson, J. R. Conformal Growth of Low Friction HfBxCy Hard Coatings. *Thin Solid Films* **2015**, *592*, 182–188.

(74) Kim, D.; Tzeng, P.; Barnett, K. J.; Yang, Y. H.; Wilhite, B. a.; Grunlan, J. C. Highly Size-Selective Ionically Crosslinked Multilayer Polymer Films for Light Gas Separation. *Adv. Mater.* **2014**, *26*, 746–751.

(75) Charitidis, C. A. Probing Mechanical Properties of Thin Film and Ceramic Materials in Micro- and Nano-Scale Using Indentation Techniques. *Appl. Surf. Sci.* **2010**, *256*, 7583–7590.

(76) Charitidis, C.; Gioti, M.; Logothetidis, S. Nanomechanical and Optical Studies on Polymeric Membranes. *Macromol. Symp.* **2004**, *205*, 239–250.

(77) Charitidis, C.; Logothetidis, S. Nanoscale Effects on the Nanomechanical Properties of Multifunctional Materials. *Comput. Mater. Sci.* **2005**, *33*, 296–302.

(78) Strojny, A.; Xia, X.; Tsou, A.; Gerberich, W. W. Techniques and Considerations for

Nanoindentation Measurements of Polymer Thin Film Constitutive Properties. *J. Adhes. Sci. Technol.* **1998**, *12*, 1299–1321.

(79) Früh, J.; Köhler, R.; Möhwald, H.; Krastev, R. Changes of the Molecular Structure in Polyelectrolyte Multilayers under Stress. *Langmuir* **2010**, *26*, 15516–15522.

(80) S. Gaidukov, I. Danilenko, G. G. Characterization of Strong and Crystalline Polyvinyl Alcohol/Montmorillonite Films Prepared by Layer-by-Layer Deposition Method. *Int. J. Polym. Sci.* **2015**.

(81) Rajini, N.; Jappes, J. T. W.; Suresha, B.; Rajakarunakaran, S.; Siva, I.; Azhagesan, N. Effect of Organically Modified Montmorillonite Clay on Wear Behavior of Naturally Woven Coconut Sheath/Polyester Composite. *Proc. Inst. Mech. Eng. Part J J. Eng. Tribol.* **2014**.

(82) Dibaei, A. H.; Abdouss, M.; Torabi, A. M.; Haji, A. Surface and Mechanical Properties of Polypropylene/Clay Nanocomposite. *Chem. Ind. Chem. Eng. Q.* **2013**, *19*, 441–448.

(83) Cao, J.; Zhang, Y.; Men, C.; Sun, Y.; Wang, Z.; Zhang, X.; Li, Q. Programmable Writing of Graphene Oxide/Reduced Graphene Oxide Fibers for Sensible Networks with in Situ Welded Junctions. *ACS Nano* **2014**, *8*, 4325–4333.

(84) Lee, C.; Wei, X.; Kysar, J. W.; Hone, J. Measurement of the Elastic Properties and Intrinsic Strength of Monolayer Graphene. *Science (80-.).* **2008**, *321*, 385–388.

(85) Seol, J. H.; Jo, I.; Moore, A. L.; Lindsay, L.; Aitken, Z. H.; Pettes, M. T.; Li, X.; Yao, Z.; Huang, R.; Broido, D.; *et al.* Two-Dimensional Phonon Transport in Supported Graphene. *Science (80-.).* **2010**, *328*, 213–216.

(86) Hong, T.-K.; Lee, D. W.; Choi, H. J.; Shin, H. S.; Kim, B.-S. Transparent, Flexible Conducting Hybrid Multilayer Thin Films of Multiwalled Carbon Nanotubes with Graphene Nanosheets. *ACS Nano* **2010**, *4*, 3861–3868.

(87) Nair, R. R.; Wu, H. A.; Jayaram, P. N.; Grigorieva, I. V; Geim, A. K. Unimpeded Permeation of Water Through Helium-Leak–Tight Graphene-Based Membranes. *Science (80-.).* **2012**, *335*, 442–444.

(88) Luo, Z.; Yang, D.; Qi, G.; Yuwen, L.; Zhang, Y.; Weng, L.; Wang, L.; Huang, W. Preparation of Highly Dispersed Reduced Graphene Oxide Decorated with Chitosan Oligosaccharide as Electrode Material for Enhancing the Direct Electron Transfer of Escherichia Coli. *ACS Appl. Mater. Interfaces* **2015**, *7*, 8539–8544.

(89) Yoon, J.; Park, W.; Bae, G.-Y.; Kim, Y.; Jang, H. S.; Hyun, Y.; Lim, S. K.; Kahng, Y. H.; Hong, W.-K.; Lee, B. H.; *et al.* Highly Flexible and Transparent Multilayer MoS2 Transistors with Graphene Electrodes. *Small* **2013**, *9*, 3295–3300.

(90) Lee, T.; Min, S. H.; Gu, M.; Jung, Y. K.; Lee, W.; Lee, J. U.; Seong, D. G.; Kim, B.-S. Layer-by-Layer Assembly for Graphene-Based Multilayer Nanocomposites: Synthesis and Applications. *Chem. Mater.* **2015**, *27*, 3785–3796.

(91) Goh, K.; Heising, J. K.; Yuan, Y.; Karahan, H. E.; Wei, L.; Zhai, S.; Koh, J.-X.; Htin, N. M.; Zhang, F.; Wang, R.; *et al.* Sandwich-Architectured Poly(Lactic Acid)–Graphene Composite Food Packaging Films. *ACS Appl. Mater. Interfaces* **2016**, *8*, 9994–10004.

(92) Cohen-Tanugi, D.; Lin, L.-C.; Grossman, J. C. Multilayer Nanoporous Graphene Membranes for Water Desalination. *Nano Lett.* **2016**, *16*, 1027–1033.

(93) Banszerus, L.; Schmitz, M.; Engels, S.; Dauber, J.; Oellers, M.; Haupt, F.; Watanabe, K.; Taniguchi, T.; Beschoten, B.; Stampfer, C. Ultrahigh-Mobility Graphene Devices from Chemical Vapor Deposition on Reusable Copper. *Sci. Adv.* **2015**, *1*.

(94) Zou, X.; Zhang, L.; Wang, Z.; Luo, Y. Mechanisms of the Antimicrobial Activities of Graphene Materials. *J. Am. Chem. Soc.* **2016**, *138*, 2064–2077.

(95) Weatherup, R. S.; D'Arsié, L.; Cabrero-Vilatela, A.; Caneva, S.; Blume, R.; Robertson, J.; Schloegl, R.; Hofmann, S. Long-Term Passivation of Strongly Interacting Metals with Single-Layer Graphene. *J. Am. Chem. Soc.* **2015**, *137*, 14358–14366.

(96) Agostini, M.; Brutti, S.; Hassoun, J. High Voltage Li-Ion Battery Using Exfoliated Graphite/Graphene Nanosheets Anode. *ACS Appl. Mater. Interfaces* **2016**, *8*, 10850–10857.

(97) Li, Y.; Samad, Y. A.; Polychronopoulou, K.; Alhassan, S. M.; Liao, K. Highly Electrically Conductive Nanocomposites Based on PolymerInfused Graphene Sponges. *Sci. Rep.* **2014**, *4*, 4652.

(98) Siemann, U. Solvent Cast Technology – a Versatile Tool for Thin Film Production. In *Scattering Methods and the Properties of Polymer Materials SE - 1*; Progress in Colloid and Polymer Science; Springer Berlin Heidelberg, 2005; Vol. 130, pp. 1–14.

(99) Kim, S.-S.; Na, S.-I.; Jo, J.; Tae, G.; Kim, D.-Y. Efficient Polymer Solar Cells Fabricated by Simple Brush Painting. *Adv. Mater.* **2007**, *19*, 4410+.

(100) Vak, D.; Kim, S.-S.; Jo, J.; Oh, S.-H.; Na, S.-I.; Kim, J.; Kim, D.-Y. Fabrication of

Organic Bulk Heterojunction Solar Cells by a Spray Deposition Method for Low-Cost Power Generation. *Appl. Phys. Lett.* **2007**, *91*.

(101) Aernouts, T.; Aleksandrov, T.; Girotto, C.; Genoe, J.; Poortmans, J. Polymer Based Organic Solar Cells Using Ink-Jet Printed Active Layers. *Appl. Phys. Lett.* **2008**, *92*, 33306.

(102) Hall, D. B.; Underhill, P.; Torkelson, J. M. Spin Coating of Thin and Ultrathin Polymer Films. *Polym. Eng. Sci.* **1998**, *38*, 2039–2045.

(103) Huang, J.; Juszkiewicz, M.; de Jeu, W. H.; Cerda, E.; Emrick, T.; Menon, N.; Russell, T. P. Capillary Wrinkling of Floating Thin Polymer Films. *Science (80-.).* **2007**, *317*, 650–653.

(104) Norton, D. P. Pulsed Laser Deposition of Complex Materials: Progress Toward Applications. In *Pulsed Laser Deposition of Thin Films*; John Wiley & Sons, Inc., 2006; pp. 1–31.

(105) Jiang, C.; Liu, X.; Luo, C.; Zhang, Y.; Shao, L.; Shi, F. Controlled Exponential Growth in Layer-by-Layer Multilayers Using High Gravity Fields. *J. Mater. Chem. A* **2014**, *2*, 14048.

(106) Aboutalebi, S. H.; Gudarzi, M. M.; Zheng, Q. Bin; Kim, J.-K. Spontaneous Formation of Liquid Crystals in Ultralarge Graphene Oxide Dispersions. *Adv. Funct. Mater.* **2011**, *21*, 2978–2988.

(107) Zhao, X.; Zhang, Q.; Hao, Y.; Li, Y.; Fang, Y.; Chen, D. Alternate Multilayer Films of Poly(Vinyl Alcohol) and Exfoliated Graphene Oxide Fabricated via a Facial Layer-by-Layer Assembly. *Macromolecules* **2010**, *43*, 9411–9416.

(108) Chen, L.; Huang, Z.; Kumar, S. Impact of Bonding at Multi-Layer Graphene/Metal Interfaces on Thermal Boundary Conductance. *RSC Adv.* **2014**, *4*, 35852–35861.

(109) Roy, S.; Tang, X.; Das, T.; Zhang, L.; Li, Y.; Ting, S.; Hu, X.; Yue, C. Y. Enhanced Molecular Level Dispersion and Interface Bonding at Low Loading of Modified Graphene Oxide To Fabricate Super Nylon 12 Composites. *ACS Appl. Mater. Interfaces* **2015**, *7*, 3142–3151.

(110) Zhang, M.; Li, Y.; Su, Z.; Wei, G. Recent Advances in the Synthesis and Applications of Graphene-Polymer Nanocomposites. *Polym. Chem.* **2015**, *6*, 6107–6124.

(111) Humood, M.; Chowdhury, S.; Song, Y.; Tzeng, P.; Grunlan, J. C.; Polycarpou, A. A.

Nanomechanical Behavior of High Gas Barrier Multilayer Thin Films. *ACS Appl. Mater. Interfaces* **2016**, *8*, 11128–11138.

(112) Sinha, S. K.; Lim, D. B. J. Effects of Normal Load on Single-Pass Scratching of Polymer Surfaces. *Wear* **2006**, *260*, 751–765.

(113) Thuyavan, Y. L.; Anantharaman, N.; Arthanareeswaran, G.; Ismail, A. F. Impact of Solvents and Process Conditions on the Formation of Polyethersulfone Membranes and Its Fouling Behavior in Lake Water Filtration. *J. Chem. Technol. Biotechnol.* **2016**, n/a--n/a.

(114) Yan, C.; Kim, K.-S.; Lee, S.-K.; Bae, S.-H.; Hong, B. H.; Kim, J.-H.; Lee, H.-J.; Ahn, J.-H. Mechanical and Environmental Stability of Polymer Thin-Film-Coated Graphene. *ACS Nano* **2012**, *6*, 2096–2103.

(115) Pei, S.; Cheng, H.-M. The Reduction of Graphene Oxide. *Carbon N. Y.* **2012**, *50*, 3210–3228.

(116) Krumova, M.; López, D.; Benavente, R.; Mijangos, C.; Pereña, J. . Effect of Crosslinking on the Mechanical and Thermal Properties of Poly(Vinyl Alcohol). *Polymer (Guildf).* **2000**, *41*, 9265–9272.

(117) Ligot, S.; Bousser, E.; Cossement, D.; Klemberg-Sapieha, J.; Viville, P.; Dubois, P.; Snyders, R. Correlation Between Mechanical Properties and Cross-Linking Degree of Ethyl Lactate Plasma Polymer Films. *Plasma Process. Polym.* **2015**, *12*, 508–518.

(118) Richert, L.; Engler, A. J.; Discher, D. E.; Picart, C. Elasticity of Native and Cross-Linked Polyelectrolyte Multilayer Films. *Biomacromolecules* **2004**, *5*, 1908–1916.

(119) Wang, F.; Zhang, Y.; Zhang, B. B.; Hong, R. Y.; Kumar, M. R.; Xie, C. R. Enhanced Electrical Conductivity and Mechanical Properties of ABS/EPDM Composites Filled with Graphene. *Compos. Part B Eng.* **2015**, *83*, 66–74.

(120) Yousefi, N.; Gudarzi, M. M.; Zheng, Q.; Lin, X.; Shen, X.; Jia, J.; Sharif, F.; Kim, J.-K. Highly Aligned, Ultralarge-Size Reduced Graphene Oxide/Polyurethane Nanocomposites: Mechanical Properties and Moisture Permeability. *Compos. Part A Appl. Sci. Manuf.* **2013**, *49*, 42–50.

(121) Wu, F.; Li, J.; Su, Y.; Wang, J.; Yang, W.; Li, N.; Chen, L.; Chen, S.; Chen, R.; Bao, L. Layer-by-Layer Assembled Architecture of Polyelectrolyte Multilayers and Graphene Sheets on Hollow Carbon Spheres/Sulfur Composite for High-Performance Lithium–Sulfur Batteries. *Nano Lett.* **2016**, *16*, 5488–5494.

(122) Su, Y.; Kravets, V. G.; Wong, S. L.; Waters, J.; Geim, A. K.; Nair, R. R. Impermeable Barrier Films and Protective Coatings Based on Reduced Graphene Oxide. *Nat Commun* **2014**, *5*.

(123) Bhattacharya, M. Polymer Nanocomposites—A Comparison between Carbon Nanotubes, Graphene, and Clay as Nanofillers. *Materials (Basel).* **2016**, *9*, 262.

(124) Chen, J.; Gao, Y.; Liu, W.; Shi, X.; Li, L.; Wang, Z.; Zhang, Y.; Guo, X.; Liu, G.; Li, W.; *et al.* The Influence of Dehydration on the Interfacial Bonding, Microstructure and Mechanical Properties of Poly(Vinyl Alcohol)/Graphene Oxide Nanocomposites. *Carbon N. Y.* **2015**, *94*, 845–855.

(125) Laugier, M. T. An Energy Approach to the Adhesion of Coatings Using the Scratch Test. *Thin Solid Films* **1984**, *117*, 243–249.

(126) Lee, J.; Polychronopoulou, K.; Cloud, A. N.; Abelson, J. R.; Polycarpou, A. A. Shear Strength Measurements of Hafnium Diboride Thin Solid Films. *Wear* **2014**, *318*, 168–176.

(127) Mallikarjunachari, G.; Ghosh, P. Analysis of Strength and Response of Polymer Nano Thin Film Interfaces Applying Nanoindentation and Nanoscratch Techniques. *Polymer (Guildf).* **2016**, *90*, 53–66.

(128) Kalbasi, R. J.; Kolahdoozan, M.; Rezaei, M. Synthesis and Characterization of Polyvinyl Amine–SiO2–Al2O3 as a New and Inexpensive Organic–Inorganic Hybrid Basic Catalyst. *J. Ind. Eng. Chem.* **2012**, *18*, 909–918.

(129) Panagopoulos, C.; Georgiou, E.; Tradas, G.; Gianakopoulos, K. Wear Behaviour of Nanostructured Polymer-Based Safety Films on Soda-Lime Glass. *Coatings* **2016**, *6*, 26.

(130) Lin, L.; Schlarb, A. K. Effect of the Varied Load Conditions on the Tribological Performance and the Thermal Characteristics of PEEK-Based Hybrid Composites. *Tribol. Int.* **2016**, *101*, 218–225.

(131) Ashcroft, I. A.; Derby, B. Adhesion Testing of Glass-Ceramic Thick Films on Metal Substrates. *J. Mater. Sci.* **1993**, *28*, 2989–2998.

(132) Dolbow, J.; Gosz, M. Effect of Out-of-Plane Properties of a Polyimide Film on the Stress Fields in Microelectronic Structures. *Mech. Mater.* **1996**, *23*, 311–321.

(133) Wortman, J. J.; Evans, R. A. Young's Modulus, Shear Modulus, and Poisson's Ratio in Silicon and Germanium. *J. Appl. Phys.* **1965**, *36*.

(134) Pergande, S. R.; Polycarpou, A. A.; Conry, T. F. Nanomechanical Properties of Aluminum 390-T6 Rough Surfaces Undergoing Tribological Testing. *J. Tribol.* **2004**, *126*, 573–582.

(135) Potts, J. R.; Lee, S. H.; Alam, T. M.; An, J.; Stoller, M. D.; Piner, R. D.; Ruoff, R. S. Thermomechanical Properties of Chemically Modified Graphene/Poly(Methyl Methacrylate) Composites Made by in Situ Polymerization. *Carbon N. Y.* **2011**, *49*, 2615–2623.

(136) You, F.; Wang, D.; Cao, J.; Li, X.; Dang, Z. M.; Hu, G. H. In Situ Thermal Reduction of Graphene Oxide in a Styrene-Ethylene/Butylene-Styrene Triblock Copolymer via Melt Blending. *Polym. Int.* **2014**, *63*, 93–99.

(137) Xu, Z.; Sun, H.; Zhao, X.; Gao, C. Ultrastrong Fibers Assembled from Giant Graphene Oxide Sheets. *Adv. Mater.* **2013**, *25*, 188–193.

(138) Ferrari, A. C.; Robertson, J. Interpretation of Raman Spectra of Disordered and Amorphous Carbon. *Phys. Rev. B* **2000**, *61*, 14095–14107.

(139) Guo, Y.; Sun, X.; Liu, Y.; Wang, W.; Qiu, H.; Gao, J. One Pot Preparation of Reduced Graphene Oxide (RGO) or Au (Ag) Nanoparticle-RGO Hybrids Using Chitosan as a Reducing and Stabilizing Agent and Their Use in Methanol Electrooxidation. *Carbon N. Y.* **2012**, *50*, 2513–2523.

(140) Shin, H.-J.; Kim, K. K.; Benayad, A.; Yoon, S.-M.; Park, H. K.; Jung, I.-S.; Jin, M. H.; Jeong, H.-K.; Kim, J. M.; Choi, J.-Y.; *et al.* Efficient Reduction of Graphite Oxide by Sodium Borohydride and Its Effect on Electrical Conductance. *Adv. Funct. Mater.* **2009**, *19*, 1987–1992.

(141) Bai, H.; Li, C.; Wang, X.; Shi, G. On the Gelation of Graphene Oxide. *J. Phys. Chem. C* **2011**, *115*, 5545–5551.

(142) National Institute of Standards and Technology (NIST) Material Measurement Laboratory (MML). NIST X-ray Photoelectron Spectroscopy Database http://srdata.nist.gov/xps/Default.aspx (accessed Aug 28, 2016).

(143) Ni, B. Y.; Faou, A. Le. Scratching Behaviour of Polymer Films Using Blunt Spherical Styli. *J. Mater. Sci.* **1996**, *31*, 3955–3963.

(144) Halling, J. *Principles of Tribology*; Macmillan: London, 1975.

(145) Yusoh, K.; Jin, J.; Song, M. Subsurface Mechanical Properties of

Polyurethane/Organoclay Nanocomposite Thin Films Studied by Nanoindentation. *Prog. Org. Coatings* **2010**, *67*, 220–224.

(146) Yousefi, N.; Lin, X.; Zheng, Q.; Shen, X.; Pothnis, J. R.; Jia, J.; Zussman, E.; Kim, J.-K. Simultaneous in Situ Reduction, Self-Alignment and Covalent Bonding in Graphene Oxide/Epoxy Composites. *Carbon N. Y.* **2013**, *59*, 406–417.

(147) Yang, X.; Tu, Y.; Li, L.; Shang, S.; Tao, X. Well-Dispersed Chitosan/Graphene Oxide Nanocomposites. *ACS Appl. Mater. Interfaces* **2010**, *2*, 1707–1713.

(148) Barquins, M. Sliding Friction of Rubber and Schallamach Waves — A Review. *Mater. Sci. Eng.* **1985**, *73*, 45–63.

(149) Diesendruck, C. E.; Sottos, N. R.; Moore, J. S.; White, S. R. Biomimetic Self-Healing Angewandte. **2015**, 10428–10447.

(150) Hager, M. D.; Greil, P.; Leyens, C.; van der Zwaag, S.; Schubert, U. S. Self-Healing Materials. *Adv. Mater.* **2010**, *22*, 5424–5430.

(151) Zhao, Y.; Wei, J.; Li, H.; Yan, Y.; Zhou, W.; Yu, D.; Zhao, Q. A Polymer Scaffold for Self-Healing Perovskite Solar Cells. *Nat. Commun.* **2016**, *7*, 10228.

(152) Sun, W.; Wang, L.; Wu, T.; Zhu, T.; Xie, H.; Pan, Y.; Liu, G. A Catalyst-Based Self-Sufficient System with Durable Self-Healing Functionality . *Adv. Eng. Mater.* **2016**, *18*, 923–931.

(153) Song, Y.; Meyers, K. P.; Gerringer, J.; Ramakrishnan, R. K.; Humood, M.; Qin, S.; Polycarpou, A. A.; Nazarenko, S.; Grunlan, J. C. Fast Self-Healing of Polyelectrolyte Multilayer Nanocoating and Restoration of Super Oxygen Barrier. *Macromol. Rapid Commun.* **2017**, 1700064–n/a.

(154) Wu, S.; Li, J.; Zhang, G.; Yao, Y.; Li, G.; Sun, R.; Wong, C.-P. Ultrafastly Self-Healing Nanocomposites via Infrared Laser and Its Application in Flexible Electronics. *ACS Appl. Mater. Interfaces* **2017**.

(155) Getachew, B. A.; Kim, S.-R.; Kim, J.-H. Self-Healing Hydrogel Pore-Filled Water Filtration Membranes. *Environ. Sci. Technol.* **2017**.

(156) Kongparakul, S.; Kornprasert, S.; Suriya, P.; Le, D.; Samart, C.; Chantarasiri, N.; Prasassarakich, P.; Guan, G. Self-Healing Hybrid Nanocomposite Anticorrosive Coating from Epoxy/Modified Nanosilica/Perfluorooctyl Triethoxysilane. *Prog. Org. Coatings* **2017**, *104*, 173–179.

(157) Kang, S.; Yang, K.; White, S. R.; Sottos, N. R. Silicon Composite Electrodes with Dynamic Ionic Bonding. *Adv. Energy Mater.* **2017**, 1700045.

(158) Thakur, V. K.; Kessler, M. R. Self-Healing Polymer Nanocomposite Materials: A Review. *Polymer (Guildf).* **2015**, *69*, 369–383.

(159) Li, B.; Zhang, J. Durable and Self-Healing Superamphiphobic Coatings Repellent Even to Hot Liquids. *Chem. Commun.* **2016**, *52*, 2744–2747.

(160) Skorb, E. V.; Andreeva, D. V. Layer-by-Layer Approaches for Formation of Smart Self-Healing Materials. *Polym. Chem.* **2013**, *4*, 4834.

(161) Scheiner, M.; Dickens, T. J.; Okoli, O. Progress towards Self-Healing Polymers for Composite Structural Applications. *Polymer (Guildf).* **2016**, *83*, 260–282.

(162) Taylor, D. L.; In Het Panhuis, M. Self-Healing Hydrogels. *Adv. Mater.* **2016**, *28*, 9060–9093.

(163) Christogianni, P.; Moniruzzaman, M.; Kister, G. Light-Triggered Enhancement of Mechanical Properties and Healing Effect in Azobenzene-Based Polymer Films. *Polymer (Guildf).* **2015**, *77*, 272–277.

(164) Wang, X.; Wang, Y.; Bi, S.; Wang, Y.; Chen, X.; Qiu, L.; Sun, J. Optically Transparent Antibacterial Films Capable of Healing Multiple Scratches. *Adv. Funct. Mater.* **2014**, *24*, 403–411.

(165) Ahn, B. K.; Lee, D. W.; Israelachvili, J. N.; Waite, J. H. Surface-Initiated Self-Healing of Polymers in Aqueous Media. *Nat Mater* **2014**, *13*, 867–872.

(166) Nakahata, M.; Mori, S.; Takashima, Y.; Yamaguchi, H.; Harada, A. Self-Healing Materials Formed by Cross-Linked Polyrotaxanes with Reversible Bonds. *Chem* **2016**, *1*, 766–775.

(167) Kang, S.; Baginska, M.; White, S. R.; Sottos, N. R. Core–Shell Polymeric Microcapsules with Superior Thermal and Solvent Stability. *ACS Appl. Mater. Interfaces* **2015**, *7*, 10952–10956.

(168) Schlaich, C.; Cuellar Camacho, L.; Yu, L.; Achazi, K.; Wei, Q.; Haag, R. Surface-Independent Hierarchical Coatings with Superamphiphobic Properties. *ACS Appl. Mater. Interfaces* **2016**, *8*, 29117–29127.

(169) Liu, F.; Urban, M. W. Recent Advances and Challenges in Designing Stimuli-Responsive Polymers. *Prog. Polym. Sci.* **2010**, *35*, 3–23.

(170) Chen, D.; Wu, M.; Li, B.; Ren, K.; Cheng, Z.; Ji, J.; Li, Y.; Sun, J. Layer-by-Layer-Assembled Healable Antifouling Films. *Adv. Mater.* **2015**, *27*, 5882–5888.

(171) Abu-Thabit, N. Y.; Hamdy, A. S. Stimuli-Responsive Polyelectrolyte Multilayers for Fabrication of Self-Healing Coatings – A Review. *Surf. Coatings Technol.* **2016**, *303*, *Part*, 406–424.

(172) Wang, Z.; Zuilhof, H. Self-Healing Superhydrophobic Fluoropolymer Brushes as Highly Protein-Repellent Coatings. *Langmuir* **2016**, *32*, 6310–6318.

(173) Zhao, J.; Xu, R.; Luo, G.; Wu, J.; Xia, H. Self-Healing Poly(Siloxane-Urethane) Elastomers with Remoldability, Shape Memory and Biocompatibility. *Polym. Chem.* **2016**, *7*, 7278–7286.

(174) Ji, S.; Cao, W.; Yu, Y.; Xu, H. Visible-Light-Induced Self-Healing Diselenide-Containing Polyurethane Elastomer. *Adv. Mater.* **2015**, *27*, 7740–7745.

(175) Binder, W. H. Self-Healing Polymers. *Polymer (Guildf).* **2015**, *69*, 215.

(176) Constantinides, G.; Kalcioglu, Z. I.; McFarland, M.; Smith, J. F.; Van Vliet, K. J. Probing Mechanical Properties of Fully Hydrated Gels and Biological Tissues. *J. Biomech.* **2008**, *41*, 3285–3289.

(177) Li, J.; Ejima, H.; Yoshie, N. Seawater-Assisted Self-Healing of Catechol Polymers via Hydrogen Bonding and Coordination Interactions. *ACS Appl. Mater. Interfaces* **2016**, *8*, 19047–19053.

(178) Merindol, R.; Diabang, S.; Felix, O.; Roland, T.; Gauthier, C.; Decher, G. Bio-Inspired Multiproperty Materials: Strong, Self-Healing, and Transparent Artificial Wood Nanostructures. *ACS Nano* **2015**, *9*, 1127–1136.

(179) Altaf, K.; Ashcroft, I. A.; Hague, R. Modelling the Effect of Moisture on the Depth Sensing Indentation Response of a Stereolithography Polymer. *Comput. Mater. Sci.* **2012**, *52*, 112–117.

(180) Benítez, A. J.; Torres-Rendon, J.; Poutanen, M.; Walther, A. Humidity and Multiscale Structure Govern Mechanical Properties and Deformation Modes in Films of Native Cellulose Nanofibrils. *Biomacromolecules* **2013**, *14*, 4497–4506.

(181) Amuzu, J. K. A. The Effect of Humidity on Friction and Shear Strength of Nylon. *J. Mater. Sci. Lett.* **1984**, *3*, 291–292.

(182) Bell, G. A.; Bieliński, D. M.; Beake, B. D. Influence of Water on the Nanoindentation

Creep Response of Nylon 6. *J. Appl. Polym. Sci.* **2008**, *107*, 577–582.

(183) Merindol, R.; Diabang, S.; Felix, O.; Roland, T.; Gauthier, C.; Decher, G. Bio-Inspired Multiproperty Materials: Strong, Self-Healing, and Transparent Artificial Wood Nanostructures. *ACS Nano* **2015**, *9*, 1127–1136.

(184) Humood, M.; Qin, S.; Song, Y.; Polychronopoulou, K.; Zhang, Y.; Grunlan, J. C.; Polycarpou, A. A. Influence of Graphene Reduction and Polymer Cross-Linking on Improving the Interfacial Properties of Multilayer Thin Films. *ACS Appl. Mater. Interfaces* **2017**, *9*, 1107–1118.

(185) Wang, K.; Gao, W.; Wang, X.; He, H. Quasi-Static and Dynamic Nanoindentation of Particle-Reinforced Soft Composites. *J. Appl. Polym. Sci.* **2017**, *134*.

(186) Du, Y.; Qiu, W.-Z.; Wu, Z. L.; Ren, P.-F.; Zheng, Q.; Xu, Z.-K. Water-Triggered Self-Healing Coatings of Hydrogen-Bonded Complexes for High Binding Affinity and Antioxidative Property. *Adv. Mater. Interfaces* **2016**, *3*, 1600167.

(187) Wang, X.; Liu, F.; Zheng, X.; Sun, J. Water-Enabled Self-Healing of Polyelectrolyte Multilayer Coatings. *Angew. Chemie - Int. Ed.* **2011**, *50*, 11378–11381.

(188) Sun, Y.; Ren, K.; Wang, J.; Chang, G.; Ji, J. Electrochemically Controlled Stiffness of Multilayers for Manipulation of Cell Adhesion. *ACS Appl. Mater. Interfaces* **2013**, *5*, 4597–4602.

(189) Hariri, H. H.; Lehaf, A. M.; Schlenoff, J. B. Mechanical Properties of Osmotically Stressed Polyelectrolyte Complexes and Multilayers: Water as a Plasticizer. *Macromolecules* **2012**, *45*, 9364–9372.

(190) Calabri, L.; Pugno, N.; Valeri, S. AFM Nanoindentation Method: Geometrical Effects of the Indenter Tip BT - Applied Scanning Probe Methods XI: Scanning Probe Microscopy Techniques. In; Bhushan, B.; Fuchs, H., Eds.; Springer Berlin Heidelberg: Berlin, Heidelberg, 2009; pp. 139–164.

(191) Ferencz, R.; Sanchez, J.; Blümich, B.; Herrmann, W. AFM Nanoindentation to Determine Young's Modulus for Different EPDM Elastomers. *Polym. Test.* **2012**, *31*, 425–432.

(192) Nestler, P.; Block, S.; Helm, C. A. Temperature-Induced Transition from Odd–Even to Even–Odd Effect in Polyelectrolyte Multilayers Due to Interpolyelectrolyte Interactions. *J. Phys. Chem. B* **2012**, *116*, 1234–1243.

(193) Secrist, K. E.; Nolte, A. J. Humidity Swelling/Deswelling Hysteresis in a Polyelectrolyte

Multilayer Film. *Macromolecules* **2011**, *44*, 2859–2865.

(194) Song, Y.; Meyers, K. P.; Gerringer, J.; Ramakrishnan, R. K.; Humood, M.; Qin, S.; Polycarpou, A. A.; Nazarenko, S.; Grunlan, J. C. Fast Self-Healing of Polyelectrolyte Multilayer Nanocoating and Restoration of Super Oxygen Barrier. *Macromol. Rapid Commun.* **2017**, 1700064–n/a.

(195) Bai, N.; Li, Q.; Dong, H.; Tan, C.; Cai, P.; Xu, L. A Versatile Approach for Preparing Self-Recovering Superhydrophobic Coatings. *Chem. Eng. J.* **2016**, *293*, 75–81.

(196) Song, Y.; Tzeng, P.; Grunlan, J. C. Super Oxygen and Improved Water Vapor Barrier of Polypropylene Film with Polyelectrolyte Multilayer Nanocoatings. *Macromol. Rapid Commun.* **2016**, *37*, 963–968.

(197) Gu, Y.; Huang, X.; Wiener, C. G.; Vogt, B. D.; Zacharia, N. S. Large-Scale Solvent Driven Actuation of Polyelectrolyte Multilayers Based on Modulation of Dynamic Secondary Interactions. *ACS Appl. Mater. Interfaces* **2015**, *7*, 1848–1858.

(198) Salamone, J. C. *Concise Polymeric Materials Encyclopedia*; Polymeric Materials Encyclopedia; Taylor & Francis, 1998.

(199) Yang, Y.-H.; Bolling, L.; Haile, M.; Grunlan, J. C. Improving Oxygen Barrier and Reducing Moisture Sensitivity of Weak Polyelectrolyte Multilayer Thin Films with Crosslinking. *RSC Adv.* **2012**, *2*, 12355–12363.

(200) Köhler, R.; Dönch, I.; Ott, P.; Laschewsky, A.; Fery, A.; Krastev, R. Neutron Reflectometry Study of Swelling of Polyelectrolyte Multilayers in Water Vapors: Influence of Charge Density of the Polycation. *Langmuir* **2009**, *25*, 11576–11585.

(201) Gu, Y.; Zacharia, N. S. Self-Healing Actuating Adhesive Based on Polyelectrolyte Multilayers. *Adv. Funct. Mater.* **2015**, *25*, 3785–3792.

(202) Zhang, D.-D.; Ruan, Y.-B.; Zhang, B.-Q.; Qiao, X.; Deng, G.; Chen, Y.; Liu, C.-Y. A Self-Healing PDMS Elastomer Based on Acylhydrazone Groups and the Role of Hydrogen Bonds. *Polymer (Guildf).* **2017**, *120*, 189–196.

(203) Pramanik, N. B.; Mondal, P.; Mukherjee, R.; Singha, N. K. A New Class of Self-Healable Hydrophobic Materials Based on ABA Triblock Copolymer via RAFT Polymerization and Diels-Alder "Click Chemistry." *Polymer (Guildf).* **2017**, *119*, 195–205.

(204) Kim, B.-S.; Park, S. W.; Hammond, P. T. Hydrogen-Bonding Layer-by-Layer-Assembled Biodegradable Polymeric Micelles as Drug Delivery Vehicles from Surfaces. *ACS Nano*

2008, *2*, 386–392.

(205) Nolte, A. J.; Treat, N. D.; Cohen, R. E.; Rubner, M. F. Effect of Relative Humidity on the Young's Modulus of Polyelectrolyte Multilayer Films and Related Nonionic Polymers. *Macromolecules* **2008**, *41*, 5793–5798.

(206) Frontini, P.; Lotfian, S.; Monclús, M. A.; Molina-Aldareguia, J. M. High Temperature Nanoindentation Response of RTM6 Epoxy Resin at Different Strain Rates. *Exp. Mech.* **2015**, *55*, 851–862.

(207) Ling, G. C. and Z. Z. and W. Z. and S. Y. and J. D. and Z. Nanoindentation in a Wetting Environment: The Coupling Effect of Liquid and Surface Roughness on Mechanical Calibration. *J. Phys. D. Appl. Phys.* **2015**, *48*, 15302.

(208) Mubashar, A.; Ashcroft, I. A.; Critchlow, G. W.; Crocombe, A. D. Moisture Absorption–Desorption Effects in Adhesive Joints. *Int. J. Adhes. Adhes.* **2009**, *29*, 751–760.

(209) Zerball, M.; Laschewsky, A.; von Klitzing, R. Swelling of Polyelectrolyte Multilayers: The Relation Between, Surface and Bulk Characteristics. *J. Phys. Chem. B* **2015**, *119*, 11879–11886.

(210) Harris, J. J.; Bruening, M. L. Electrochemical and in Situ Ellipsometric Investigation of the Permeability and Stability of Layered Polyelectrolyte Films. *Langmuir* **2000**, *16*, 2006–2013.

(211) Chung, C.-M.; Roh, Y.-S.; Cho, S.-Y.; Kim, J.-G. Crack Healing in Polymeric Materials via Photochemical [2+2] Cycloaddition. *Chem. Mater.* **2004**, *16*, 3982–3984.

(212) Tuncaboylu, D. C.; Argun, A.; Algi, M. P.; Okay, O. Autonomic Self-Healing in Covalently Crosslinked Hydrogels Containing Hydrophobic Domains. *Polymer (Guildf).* **2013**, *54*, 6381–6388.

(213) Mangun, C. L.; Mader, A. C.; Sottos, N. R.; White, S. R. Self-Healing of a High Temperature Cured Epoxy Using Poly(Dimethylsiloxane) Chemistry. *Polymer (Guildf).* **2010**, *51*, 4063–4068.

(214) Das, P.; Thomas, H.; Moeller, M.; Walther, A. Large-Scale, Thick, Self-Assembled, Nacre-Mimetic Brick-Walls as Fire Barrier Coatings on Textiles. *Sci. Rep.* **2017**, *7*, 39910.

(215) Das, S.; Kumar, S.; Samal, S. K.; Mohanty, S.; Nayak, S. K. A Review on Superhydrophobic Polymer Nanocoatings: Recent Development and Applications. *Ind. Eng. Chem. Res.* **2018**, *57*, 2727–2745.

(216) Jurin, F. E.; Buron, C. C.; Clément, S.; Mehdi, A.; Viau, L.; Lakard, B.; Martin, N.; Filiâtre, C. Flexible and Conductive Multilayer Films Based on the Assembly of PEDOT:PSS and Water Soluble Polythiophenes. *Org. Electron.* **2017**, *46*, 263–269.

(217) Qin, S.; Song, Y.; Floto, M. E.; Grunlan, J. C. Combined High Stretchability and Gas Barrier in Hydrogen-Bonded Multilayer Nanobrick Wall Thin Films. *ACS Appl. Mater. Interfaces* **2017**, *9*, 7903–7907.

(218) Humood, M.; Polychronopoulou, K.; Song, Y.; Grunlan, J. C.; Polycarpou, A. A. In Situ Nanomechanical Behavior and Self-Healing Response of Polymeric Multilayer Thin Films. *Polym. (United Kingdom)* **2017**, *131*, 169–178.

(219) Vadivel, H. S.; Golchin, A.; Emami, N. Tribological Behaviour of Carbon Filled Hybrid UHMWPE Composites in Water. *Tribol. Int.* **2018**, *124*, 169–177.

(220) Chen, W.-H.; Luo, G.-F.; Qiu, W.-X.; Lei, Q.; Liu, L.-H.; Wang, S.-B.; Zhang, X.-Z. Mesoporous Silica-Based Versatile Theranostic Nanoplatform Constructed by Layer-by-Layer Assembly for Excellent Photodynamic/Chemo Therapy. *Biomaterials* **2017**, *117*, 54–65.

(221) Shojaeiarani, J.; Bajwa, D. S.; Stark, N. M. Spin-Coating: A New Approach for Improving Dispersion of Cellulose Nanocrystals and Mechanical Properties of Poly (Lactic Acid) Composites. *Carbohydr. Polym.* **2018**, *190*, 139–147.

(222) Vandenbossche, M.; Bernard, L.; Rupper, P.; Maniura-Weber, K.; Heuberger, M.; Faccio, G.; Hegemann, D. Micro-Patterned Plasma Polymer Films for Bio-Sensing. *Mater. Des.* **2017**, *114*, 123–128.

(223) Cai, C.; Zhang, Y.; Song, R.; Peng, Z.; Xia, L.; Wu, M.; Xiong, K.; Wang, B.; Lin, Y.; Xu, X.; *et al.* Polymer Solar Cells Spray Coated with Non-Halogenated Solvents. *Sol. Energy Mater. Sol. Cells* **2017**, *161*, 52–61.

(224) Kim, H.; Fernando, T.; Li, M.; Lin, Y.; Tseng, T.-L. B. Fabrication and Characterization of 3D Printed BaTiO3/PVDF Nanocomposites. *J. Compos. Mater.* **2017**, *52*, 197–206.

(225) Culebras, M.; Cho, C.; Krecker, M.; Smith, R.; Song, Y.; Gómez, C. M.; Cantarero, A.; Grunlan, J. C. High Thermoelectric Power Factor Organic Thin Films through Combination of Nanotube Multilayer Assembly and Electrochemical Polymerization. *ACS Appl. Mater. Interfaces* **2017**, *9*, 6306–6313.

(226) Kotov, N. A. Layer-by-Layer Self-Assembly: The Contribution of Hydrophobic

Interactions. *Nanostructured Mater.* **1999**, *12*, 789–796.

(227) Kim, J.-H.; Nizami, A.; Hwangbo, Y.; Jang, B.; Lee, H.-J.; Woo, C.-S.; Hyun, S.; Kim, T.-S. Tensile Testing of Ultra-Thin Films on Water Surface. *Nat. Commun.* **2013**, *4*, 2520.

(228) Xia, W.; Song, J.; Hsu, D. D.; Keten, S. Understanding the Interfacial Mechanical Response of Nanoscale Polymer Thin Films via Nanoindentation. *Macromolecules* **2016**, *49*, 3810–3817.

(229) Dai, L.; Long, Z.; Chen, J.; An, X.; Cheng, D.; Khan, A.; Ni, Y. Robust Guar Gum/Cellulose Nanofibrils Multilayer Films with Good Barrier Properties. *ACS Appl. Mater. Interfaces* **2017**, *9*, 5477–5485.

(230) Park, J. J.; Hyun, W. J.; Mun, S. C.; Park, Y. T.; Park, O. O. Highly Stretchable and Wearable Graphene Strain Sensors with Controllable Sensitivity for Human Motion Monitoring. *ACS Appl. Mater. Interfaces* **2015**, *7*, 6317–6324.

(231) Haile, M.; Fomete, S.; Lopez, I. D.; Grunlan, J. C. Aluminum Hydroxide Multilayer Assembly Capable of Extinguishing Flame on Polyurethane Foam. *J. Mater. Sci.* **2016**, *51*, 375–381.

(232) Di, J.; Yao, S.; Ye, Y.; Cui, Z.; Yu, J.; Ghosh, T. K.; Zhu, Y.; Gu, Z. Stretch-Triggered Drug Delivery from Wearable Elastomer Films Containing Therapeutic Depots. *ACS Nano* **2015**, *9*, 9407–9415.

(233) Evans, C. M.; Narayanan, S.; Jiang, Z.; Torkelson, J. M. Modulus, Confinement, and Temperature Effects on Surface Capillary Wave Dynamics in Bilayer Polymer Films Near the Glass Transition. *Phys. Rev. Lett.* **2012**, *109*, 38302.

(234) Argatov, I. I.; Sabina, F. J. Small-Scale Indentation of an Elastic Coated Half-Space: The Effect of Compliant Substrate. *Int. J. Eng. Sci.* **2016**, *104*, 87–96.

(235) Ma, Y.; Xue, Y.; Jang, K.-I.; Feng, X.; Rogers, J. A.; Huang, Y. Wrinkling of a Stiff Thin Film Bonded to a Pre-Strained, Compliant Substrate with Finite Thickness. *Proc. R. Soc. A Math. Phys. Eng. Sci.* **2016**, *472*.

(236) Humood, M.; Qin, S.; Song, Y.; Polychronopoulou, K.; Zhang, Y.; Grunlan, J. C.; Polycarpou, A. A. Influence of Graphene Reduction and Polymer Cross-Linking on Improving the Interfacial Properties of Multilayer Thin Films. *ACS Appl. Mater. Interfaces* **2017**, *9*, 1107–1118.

(237) Martinet, C.; Devine, R. A. B.; Brunel, M. Oxidation of Crystalline Si in an O2 Plasma:

Growth Kinetics and Oxide Characterization. *J. Appl. Phys.* **1997**, *81*, 6996–7005.

(238) Kakiuchi, H.; Ohmi, H.; Harada, M.; Yasutake, K. Formation of Silicon Dioxide Layers at Low Temperatures (150—400°C) by Atmospheric Pressure Plasma Oxidation of Silicon. *Sci. Technol. Adv. Mater.* **2007**, *8*, 137–141.

(239) Polychronopoulou, K.; Lee, J.; Tsotsos, C.; Demas, N. G.; Meschewski, R. L.; Rebholz, C.; Polycarpou, A. A. Deposition and Nanotribological Characterization of Sub-100-Nm Thick Protective Ti-Based Coatings for Miniature Applications. *Tribol. Lett.* **2011**, *44*, 213.

(240) Xu, D.; Liechti, K. M. Bulge Testing Transparent Thin Films with Moiré Deflectometry. *Exp. Mech.* **2010**, *50*, 217–225.

(241) Tvergaard, V.; Needleman, A. Effect of Properties and Turgor Pressure on the Indentation Response of Plant Cells. *J. Appl. Mech.* **2018**, *85*, 61007–61008.

(242) Drelich, J.; Mittal, K. L. *Atomic Force Microscopy in Adhesion Studies*; CRC Press, 2005.

(243) Tsui, T. Y.; Pharr, G. M. Substrate Effects on Nanoindentation Mechanical Property Measurement of Soft Films on Hard Substrates. *J. Mater. Res.* **1999**, *14*, 292–301.

(244) Chatterjee, A.; Polycarpou, A. A.; Abelson, J. R.; Bellon, P. Nanoscratch Study of Hard HfB2 Thin Films Using Experimental and Finite Element Techniques. *Wear* **2010**, *268*, 677–685.

(245) Wegst, U. G. K.; Bai, H.; Saiz, E.; Tomsia, A. P.; Ritchie, R. O. Bioinspired Structural Materials. *Nat Mater* **2015**, *14*, 23–36.

(246) Zhang, F.; Hong, F.; Yan, H. DNA Origami Tiles: Nanoscale Mazes. *Nat Nano* **2017**, *12*, 189–190.

(247) Wen, L.; Weaver, J. C.; Lauder, G. V. Biomimetic Shark Skin: Design, Fabrication and Hydrodynamic Function. *J. Exp. Biol.* **2014**, *217*, 1656 LP-1666.

(248) Zhang, C.; Mcadams, D. A.; Grunlan, J. C. Nano/Micro-Manufacturing of Bioinspired Materials: A Review of Methods to Mimic Natural Structures. *Adv. Mater.* **2016**, *28*, 6292–6321.

(249) Su, Y.; Ping, X.; Yu, K. J.; Lee, J. W.; Fan, J. A.; Wang, B.; Li, M.; Li, R.; Harburg, D. V.; Huang, Y.; *et al.* Stretchable Electronics: In-Plane Deformation Mechanics for Highly Stretchable Electronics (Adv. Mater. 8/2017). *Adv. Mater.* **2017**, *29*.

(250) Breger, J. C.; Yoon, C.; Xiao, R.; Kwag, H. R.; Wang, M. O.; Fisher, J. P.; Nguyen, T. D.;

Gracias, D. H. Self-Folding Thermo-Magnetically Responsive Soft Microgrippers. *ACS Appl. Mater. Interfaces* **2015**, *7*, 3398–3405.

(251) Lamoureux, A.; Lee, K.; Shlian, M.; Forrest, S. R.; Shtein, M. Dynamic Kirigami Structures for Integrated Solar Tracking. *Nat. Commun.* **2015**, *6*, 8092.

(252) Song, Z.; Ma, T.; Tang, R.; Cheng, Q.; Wang, X.; Krishnaraju, D.; Panat, R.; Chan, C. K.; Yu, H.; Jiang, H. Origami Lithium-Ion Batteries. **2014**, *5*, 3140.

(253) Kim, J.; Salvatore, G. A.; Araki, H.; Chiarelli, A. M.; Xie, Z.; Banks, A.; Sheng, X.; Liu, Y.; Lee, J. W.; Jang, K.-I.; *et al.* Battery-Free, Stretchable Optoelectronic Systems for Wireless Optical Characterization of the Skin. *Sci. Adv.* **2016**, *2*.

(254) Tang, Y.; Lin, G.; Yang, S.; Yi, Y. K.; Kamien, R. D.; Yin, J. Programmable Kiri-Kirigami Metamaterials. *Adv. Mater.* **2017**, *29*, 1604262.

(255) Lin, D.; Nian, Q.; Deng, B.; Jin, S.; Hu, Y.; Wang, W.; Cheng, G. J. Three-Dimensional Printing of Complex Structures: Man Made or toward Nature? *ACS Nano* **2014**, *8*, 9710–9715.

(256) Yee, D. W.; Schulz, M. D.; Grubbs, R. H.; Greer, J. R. Functionalized 3D Architected Materials via Thiol-Michael Addition and Two-Photon Lithography. *Adv. Mater.* **2017**, *29*, 1605293.

(257) Zadegan, R. M.; Jepsen, M. D. E.; Thomsen, K. E.; Okholm, A. H.; Schaffert, D. H.; Andersen, E. S.; Birkedal, V.; Kjems, J. Construction of a 4 Zeptoliters Switchable 3D DNA Box Origami. *ACS Nano* **2012**, *6*, 10050–10053.

(258) Kang, S. H.; Dickey, M. D. Patterning via Self-Organization and Self-Folding: Beyond Conventional Lithography. *MRS Bull.* **2016**, *41*, 93–96.

(259) Xu, S.; Yan, Z.; Jang, K.-I.; Huang, W.; Fu, H.; Kim, J.; Wei, Z.; Flavin, M.; McCracken, J.; Wang, R.; *et al.* Assembly of Micro/Nanomaterials into Complex, Three-Dimensional Architectures by Compressive Buckling. *Science (80-.).* **2015**, *347*, 154–159.

(260) Shi, Y.; Zhang, F.; Nan, K.; Wang, X.; Wang, J.; Zhang, Y.; Zhang, Y.; Luan, H.; Hwang, K.-C.; Huang, Y.; *et al.* Plasticity-Induced Origami for Assembly of Three Dimensional Metallic Structures Guided by Compressive Buckling. *Extrem. Mech. Lett.* **2017**, *11*, 105–110.

(261) Zhang, Y.; Zhang, F.; Yan, Z.; Ma, Q.; Li, X.; Huang, Y.; Rogers, J. A. Printing, Folding and Assembly Methods for Forming 3D Mesostructures in Advanced Materials. **2017**, *2*,

17019.

(262) Yan, Z.; Han, M.; Yang, Y.; Nan, K.; Luan, H.; Luo, Y.; Zhang, Y.; Huang, Y.; Rogers, J. A. Deterministic Assembly of 3D Mesostructures in Advanced Materials via Compressive Buckling: A Short Review of Recent Progress. *Extrem. Mech. Lett.* **2017**, *11*, 96–104.

(263) Kim, S.; Wu, J.; Carlson, A.; Jin, S. H.; Kovalsky, A.; Glass, P.; Liu, Z.; Ahmed, N.; Elgan, S. L.; Chen, W.; *et al.* Microstructured Elastomeric Surfaces with Reversible Adhesion and Examples of Their Use in Deterministic Assembly by Transfer Printing. *Proc. Natl. Acad. Sci.* **2010**, *107*, 17095–17100.

(264) Hutchens, S. B.; Hall, L. J.; Greer, J. R. In Situ Mechanical Testing Reveals Periodic Buckle Nucleation and Propagation in Carbon Nanotube Bundles. *Adv. Funct. Mater.* **2010**, *20*, 2338–2346.

(265) Delaine-Smith, R. M.; Burney, S.; Balkwill, F. R.; Knight, M. M. Experimental Validation of a Flat Punch Indentation Methodology Calibrated against Unconfined Compression Tests for Determination of Soft Tissue Biomechanics. *J. Mech. Behav. Biomed. Mater.* **2016**, *60*, 401–415.

(266) Ozden, S.; Yang, Y.; Tiwary, C. S.; Bhowmick, S.; Asif, S.; Penev, E. S.; Yakobson, B. I.; Ajayan, P. M. Indentation Tests Reveal Geometry-Regulated Stiffening of Nanotube Junctions. *Nano Lett.* **2016**, *16*, 232–236.

(267) Chen, L.-Y.; Xu, J.-Q.; Choi, H.; Pozuelo, M.; Ma, X.; Bhowmick, S.; Yang, J.-M.; Mathaudhu, S.; Li, X.-C. Processing and Properties of Magnesium Containing a Dense Uniform Dispersion of Nanoparticles. *Nature* **2015**, *528*, 539–543.

(268) Meza, L. R.; Zelhofer, A. J.; Clarke, N.; Mateos, A. J.; Kochmann, D. M.; Greer, J. R. Resilient 3D Hierarchical Architected Metamaterials. *Proc. Natl. Acad. Sci.* **2015**, *112*, 11502–11507.

(269) Lorenz, H.; Despont, M.; Fahrni, N.; Brugger, J.; Vettiger, P.; Renaud, P. High-Aspect-Ratio, Ultrathick, Negative-Tone near-UV Photoresist and Its Applications for MEMS. *Sensors Actuators A Phys.* **1998**, *64*, 33–39.

(270) Das, A.; Sinha, A.; Rao, V. R.; Jonnalagadda, K. N. Fracture in Microscale SU-8 Polymer Thin Films. *Exp. Mech.* **2017**, *57*, 687–701.

(271) Maschmann, M. R.; Zhang, Q.; Wheeler, R.; Du, F.; Dai, L.; Baur, J. In Situ SEM Observation of Column-like and Foam-like CNT Array Nanoindentation. *ACS Appl.*

Mater. Interfaces **2011**, *3*, 648–653.

(272) Lu, T. X. and J. H. Y. and S. B. and S. R. and J.-B. L. and H. Characterization of the Mechanical Behavior of SU-8 at Microscale by Viscoelastic Analysis. *J. Micromechanics Microengineering* **2016**, *26*, 105001.

(273) Chollet, F. SU-8: Thick Photo-Resist for MEMS http://memscyclopedia.org/su8.html (accessed Aug 8, 2017).

(274) Zhang, H.; Tersoff, J.; Xu, S.; Chen, H.; Zhang, Q.; Zhang, K.; Yang, Y.; Lee, C.-S.; Tu, K.-N.; Li, J.; *et al.* Approaching the Ideal Elastic Strain Limit in Silicon Nanowires. *Sci. Adv.* **2016**, *2*.

(275) Petersen, K. E. Silicon as a Mechanical Material. *Proceedings of the IEEE*, 1982, *70*, 420–457.

(276) Novoselov, K. S.; Geim, A. K.; Morozov, S. V; Jiang, D.; Zhang, Y.; Dubonos, S. V; Grigorieva, I. V; Firsov, A. A. Electric Field Effect in Atomically Thin Carbon Films. *Science (80-.).* **2004**, *306*, 666 LP-669.

(277) Novoselov, K. S.; Jiang, D.; Schedin, F.; Booth, T. J.; Khotkevich, V. V; Morozov, S. V; Geim, A. K. Two-Dimensional Atomic Crystals. *Proc. Natl. Acad. Sci. U. S. A.* **2005**, *102*, 10451 LP-10453.

(278) Pan, W. Y.; Bao, Q. W.; Mao, Y. J.; Liu, B. H.; Li, Z. P. Low-Temperature Synthesis of Nanosized Metal Borides through Reaction of Lithium Borohydride with Metal Hydroxides or Oxides. *J. Alloys Compd.* **2015**, *651*, 666–672.

(279) Sun, X.; Liu, X.; Yin, J.; Yu, J.; Li, Y.; Hang, Y.; Zhou, X.; Yu, M.; Li, J.; Tai, G.; *et al.* Two-Dimensional Boron Crystals: Structural Stability, Tunable Properties, Fabrications and Applications. *Adv. Funct. Mater.* **2016**.

(280) Mounet, N.; Gibertini, M.; Schwaller, P.; Campi, D.; Merkys, A.; Marrazzo, A.; Sohier, T.; Castelli, I. E.; Cepellotti, A.; Pizzi, G.; *et al.* Two-Dimensional Materials from High-Throughput Computational Exfoliation of Experimentally Known Compounds. *Nat. Nanotechnol.* **2018**, *13*, 246–252.

(281) Marrazzo, A.; Gibertini, M.; Campi, D.; Mounet, N.; Marzari, N. Prediction of a Large-Gap and Switchable Kane-Mele Quantum Spin Hall Insulator. *Phys. Rev. Lett.* **2018**, *120*, 117701.

(282) Pacilé, D.; Meyer, J. C.; Girit, Ç. Ö.; Zettl, A. The Two-Dimensional Phase of Boron

Nitride: Few-Atomic-Layer Sheets and Suspended Membranes. *Appl. Phys. Lett.* **2008**, *92*, 133107.

(283) Gupta, A.; Sakthivel, T.; Seal, S. Recent Development in 2D Materials beyond Graphene. *Prog. Mater. Sci.* **2015**, *73*, 44–126.

(284) Thakur, S.; Karak, N. Alternative Methods and Nature-Based Reagents for the Reduction of Graphene Oxide: A Review. *Carbon N. Y.* **2015**, *94*, 224–242.

(285) Burkhardt, U.; Gurin, V.; Haarmann, F.; Borrmann, H.; Schnelle, W.; Yaresko, A.; Grin, Y. On the Electronic and Structural Properties of Aluminum Diboride Al0.9B2. *J. Solid State Chem.* **2004**, *177*, 389–394.

(286) Savaş, Ö.; Kayikci, R. Production and Wear Properties of Metal Matrix Composites Reinforced with Boride Particles. *Mater. Des.* **2013**, *51*, 641–647.

(287) Deppisch, C.; Liu, G.; Hall, A.; Xu, Y.; Zangvil, A.; Shang, J. K.; Economy, J. The Crystallization and Growth of AlB2 Single Crystal Flakes in Aluminum. *J. Mater. Res.* **1998**, *13*, 3485–3498.

(288) Suda, J.; Matsunami, H. Heteroepitaxial Growth of Group-III Nitrides on Lattice-Matched Metal Boride ZrB2 (0 0 0 1) by Molecular Beam Epitaxy. *J. Cryst. Growth* **2002**, *237–239*, *P*, 1114–1117.

(289) Yamada-Takamura, Y.; Wang, Z. T.; Fujikawa, Y.; Sakurai, T.; Xue, Q. K.; Tolle, J.; Liu, P.-L.; Chizmeshya, A. V. G.; Kouvetakis, J.; Tsong, I. S. T. Surface and Interface Studies of GaN Epitaxy on Si(111) via ${\mathrm{ZrB}}_{2}$ Buffer Layers. *Phys. Rev. Lett.* **2005**, *95*, 266105.

(290) Hoffmann, R.-D.; Pöttgen, R. AlB2-Related Intermetallic Compounds – a Comprehensive View Based on Group-Subgroup Relations. *Zeitschrift für Kristallographie - Crystalline Materials*, 2001, *216*, 127.

(291) Loa, I.; Kunc, K.; Syassen, K.; Bouvier, P. Crystal Structure and Lattice Dynamics of AlB2 under Pressure and Implications for MgB2. *Phys. Rev. B* **2002**, *66*, 134101.

(292) Matkovich, V. I.; Economy, J.; Giese, R. F. Presence of Carbon in Aluminum Borides. *J. Am. Chem. Soc.* **1964**, *86*, 2337–2340.

(293) Kisly, P. S.; Prikhna, T. A.; Golubyak, L. S. Properties of High-Temperature Solution-Grown Aluminium Borides. *J. Less Common Met.* **1986**, *117*, 349–353.

(294) Samsonov, G. V; Neronov, V. A.; Lamikhov, L. K. The Conditions, Structure and Some

Properties of Phases in the Al-B System. *J. Less Common Met.* **1979**, *67*, 291–296.

(295) Serebryanskii, V. T.; Epel'baum, V. A. Phase Diagram of the Aluminum — Boron System. *J. Struct. Chem.* **1961**, *2*, 692–694.

(296) Deppisch, C.; Liu, G.; Shang, J. K.; Economy, J. Processing and Mechanical Properties of AlB2 Flake Reinforced Al-Alloy Composites. *Mater. Sci. Eng. A* **1997**, *225*, 153–161.

(297) Hall, A.; Economy, J. The Al(L) + AlB12 ↔ AlB2 Peritectic Transformation and Its Role in the Formation of High Aspect Ratio AlB2 Flakes. *J. Phase Equilibria* **2000**, *21*, 63.

(298) Hall, A. C.; Economy, J. Preparing High- and Low-Aspect Ratio AlB2 Flakes from Borax or Boron Oxide. *JOM* **2000**, *52*, 42–44.

(299) Yamabe, R. H. and J. O. and N. T. and K. Nonuniformity in Ultrathin SiO 2 on Si(111) Characterized by Conductive Atomic Force Microscopy. *Jpn. J. Appl. Phys.* **2004**, *43*, 7861.

(300) Lay, P. D. P. and C. O. and C. Q. and B. O. and P. I. and E. S. and T. A. and L. Q. and C. R. and A. V. and M. M.-M. and A. G. and B. P. 24 h Stability of Thick Multilayer Silicene in Air. *2D Mater.* **2014**, *1*, 21003.

(301) Yamabe, K. O. and Y. H. and R. H. and K. Roughness Increase on Surface and Interface of SiO 2 Grown on Atomically Flat Si (111) Terrace. *J. Phys. Conf. Ser.* **2009**, *191*, 12031.

(302) Kim, J.; Kim, F.; Huang, J. Seeing Graphene-Based Sheets. *Mater. Today* **2010**, *13*, 28–38.

(303) Zhu, J. Graphene Production: New Solutions to a New Problem. *Nat Nano* **2008**, *3*, 528–529.

(304) Li, H.; Lu, G.; Wang, Y.; Yin, Z.; Cong, C.; He, Q.; Wang, L.; Ding, F.; Yu, T.; Zhang, H. Mechanical Exfoliation and Characterization of Single-and Few-Layer Nanosheets of WSe2, TaS2, and TaSe2. *Small* **2013**, *9*, 1974–1981.

(305) Mannix, A. J.; Zhou, X.-F.; Kiraly, B.; Wood, J. D.; Alducin, D.; Myers, B. D.; Liu, X.; Fisher, B. L.; Santiago, U.; Guest, J. R.; *et al.* Synthesis of Borophenes: Anisotropic, Two-Dimensional Boron Polymorphs. *Science (80-.).* **2015**, *350*, 1513 LP-1516.

(306) Zhang, Z.; Mannix, A. J.; Hu, Z.; Kiraly, B.; Guisinger, N. P.; Hersam, M. C.; Yakobson, B. I. Substrate-Induced Nanoscale Undulations of Borophene on Silver. *Nano Lett.* **2016**, *16*, 6622–6627.

(307) Feng, B.; Zhang, J.; Zhong, Q.; Li, W.; Li, S.; Li, H.; Cheng, P.; Meng, S.; Chen, L.; Wu, K. Experimental Realization of Two-Dimensional Boron Sheets. *Nat Chem* **2016**, *8*, 563–568.

(308) Paul, A.; van Dal, M. J. H.; Kodentsov, A. A.; van Loo, F. J. J. The Kirkendall Effect in Multiphase Diffusion. *Acta Mater.* **2004**, *52*, 623–630.

(309) Wang, Y.; Raabe, D.; Klüber, C.; Roters, F. Orientation Dependence of Nanoindentation Pile-up Patterns and of Nanoindentation Microtextures in Copper Single Crystals. *Acta Mater.* **2004**, *52*, 2229–2238.

(310) Duan, Y. H.; Sun, Y.; Guo, Z. Z.; Peng, M. J.; Zhu, P. X.; He, J. H. Elastic Constants of AlB2-Type Compounds from First-Principles Calculations. *Comput. Mater. Sci.* **2012**, *51*, 112–116.

(311) Shein, I. R.; Ivanovskii, A. L. Elastic Properties of Mono- and Polycrystalline Hexagonal AlB 2 -like Diborides of s, p and d Metals from First-Principles Calculations. *J. Phys. Condens. Matter* **2008**, *20*, 415218.

(312) Coudert, R. G. and P. P. and F.-X. ELATE: An Open-Source Online Application for Analysis and Visualization of Elastic Tensors. *J. Phys. Condens. Matter* **2016**, *28*, 275201.

(313) Die Struktur von Aluminiumborid AlB2 . *Zeitschrift für Physikalische Chemie* , 1936, *31B*, 214.

(314) Whittaker, M. L.; Sohn, H. Y.; Cutler, R. A. Oxidation Kinetics of Aluminum Diboride. *J. Solid State Chem.* **2013**, *207*, 163–169.

(315) Holmberg, K.; Erdemir, A. Global Impact of Friction on Energy Consumption, Economy and Environment. *FME Trans.* **2015**, *43*, 181–185.

(316) Donnet, C.; Erdemir, A. Historical Developments and New Trends in Tribological and Solid Lubricant Coatings. *Surf. Coatings Technol.* **2004**, *180–181*, 76–84.

(317) De Barros Bouchet, M. I.; Martin, J. M.; Avila, J.; Kano, M.; Yoshida, K.; Tsuruda, T.; Bai, S.; Higuchi, Y.; Ozawa, N.; Kubo, M.; *et al.* Diamond-like Carbon Coating under Oleic Acid Lubrication: Evidence for Graphene Oxide Formation in Superlow Friction. *Sci. Rep.* **2017**, *7*, 46394.

(318) Richard, C. Tribological Coatings for High-Temperature Applications BT - Encyclopedia of Tribology. In; Wang, Q. J.; Chung, Y.-W., Eds.; Springer US: Boston, MA, 2013; pp.

3778–3787.

(319) Naujoks, D.; Eggeler, Y. M.; Hallensleben, P.; Frenzel, J.; Fries, S. G.; Palumbo, M.; Koßmann, J.; Hammerschmidt, T.; Pfetzing-Micklich, J.; Eggeler, G.; *et al.* Identification of a Ternary μ-Phase in the Co-Ti-W System – An Advanced Correlative Thin-Film and Bulk Combinatorial Materials Investigation. *Acta Mater.* **2017**, *138*, 100–110.

(320) Abadias, G.; Ivashchenko, V. I.; Belliard, L.; Djemia, P. Structure, Phase Stability and Elastic Properties in the Ti1–XZrxN Thin-Film System: Experimental and Computational Studies. *Acta Mater.* **2012**, *60*, 5601–5614.

(321) Dearnley, P. A.; Schellewald, M.; Dahm, K. L. Characterisation and Wear Response of Metal-Boride Coated WC–Co. *Wear* **2005**, *259*, 861–869.

(322) Parthasarathy, T. A.; Rapp, R. A.; Opeka, M.; Kerans, R. J. A Model for the Oxidation of ZrB2, HfB2 and TiB2. *Acta Mater.* **2007**, *55*, 5999–6010.

(323) Zapata-Solvas, E.; Jayaseelan, D. D.; Lin, H. T.; Brown, P.; Lee, W. E. Mechanical Properties of ZrB2- and HfB2-Based Ultra-High Temperature Ceramics Fabricated by Spark Plasma Sintering. *J. Eur. Ceram. Soc.* **2013**, *33*, 1373–1386.

(324) Chatterjee, A.; Jayaraman, S.; Gerbi, J. E.; Kumar, N.; Abelson, J. R.; Bellon, P.; Polycarpou, A. A.; Chevalier, J. P. Tribological Behavior of Hafnium Diboride Thin Films. *Surf. Coatings Technol.* **2006**, *201*, 4317–4322.

(325) Yu, J.; Dong, L.; Li, C.; Pan, Y.; Wan, R.; Gu, H.; Li, D. The Influence of Modulation Periods on the Evolution of Microstructure and Mechanical Properties of Nanoscale HfN/HfB2 Multilayers. *Surf. Coatings Technol.* **2017**, *326*, 368–374.

(326) Jayaraman, S.; Gerbi, J. E.; Yang, Y.; Kim, D. Y.; Chatterjee, A.; Bellon, P.; Girolami, G. S.; Chevalier, J. P.; Abelson, J. R. HfB2 and Hf–B–N Hard Coatings by Chemical Vapor Deposition. *Surf. Coatings Technol.* **2006**, *200*, 6629–6633.

(327) Teghil, R.; Santagata, A.; Zaccagnino, M.; Barinov, S. M.; Marotta, V.; De Maria, G. Hafnium Carbide Hard Coatings Produced by Pulsed Laser Ablation and Deposition. *Surf. Coatings Technol.* **2002**, *151–152*, 531–533.

(328) Chowdhury, S.; Polychronopoulou, K.; Cloud, A.; Abelson, J. R.; Polycarpou, A. A. Nanomechanical and Nanotribological Behaviors of Hafnium Boride Thin Films. *Thin Solid Films* **2015**, *595*, *Part*, 84–91.

(329) Karabacak, T.; Lu, T.-M. Enhanced Step Coverage by Oblique Angle Physical Vapor

Deposition. *J. Appl. Phys.* **2005**, *97*, 124504.

(330) Colinet, C.; Tedenac, J.-C. Enthalpies of Formation of Transition Metal Diborides: A First Principles Study. *Crystals* , 2015, *5*.

(331) Kornilov, A. N.; Chelovskaya, N. V; Zhelankin, V. I.; Shveikin, G. P. Enthalpies of Formation of Hafnium Carbides. *J. Chem. Thermodyn.* **1977**, *9*, 629–642.

(332) Chase, M. W. NIST-JANAF Themochemical Tables, 4th Edition.

(333) Rogl, P.; Bittermann, H. On the Ternary System Hafnium–Boron–Carbon. *J. Solid State Chem.* **2000**, *154*, 257–262.

(334) Rodenbücher, C.; Hildebrandt, E.; Szot, K.; Sharath, S. U.; Kurian, J.; Komissinskiy, P.; Breuer, U.; Waser, R.; Alff, L. Hafnium Carbide Formation in Oxygen Deficient Hafnium Oxide Thin Films. *Appl. Phys. Lett.* **2016**, *108*, 252903.

(335) Chatterjee, A.; Kumar, N.; Abelson, J. R.; Bellon, P.; Polycarpou, A. A. Nanoscratch and Nanofriction Behavior of Hafnium Diboride Thin Films. *Wear* **2008**, *265*, 921–929.

(336) Kolakieva, L.; Kakanakov, R. *Nanostructured Materials, Thin Films and Hard Coatings for Advanced Applications: Selected, Peer Reviewed Papers from the 2nd International Conference on Nanostructured Materials, Thin Films and Hard Coatings for Advanced Applications, Sozopol, Bulgaria,* ; Diffusion and defect data, solid state data. Part B, Solid state phenomena; Trans Tech, 2010.

(337) Johnson, L. J. S.; Rogström, L.; Johansson, M. P.; Odén, M.; Hultman, L. Microstructure Evolution and Age Hardening in (Ti,Si)(C,N) Thin Films Deposited by Cathodic Arc Evaporation. *Thin Solid Films* **2010**, *519*, 1397–1403.

(338) Pal, R. Porosity-Dependence of Effective Mechanical Properties of Pore-Solid Composite Materials. *J. Compos. Mater.* **2005**, *39*, 1147–1158.

(339) Ozkan, T.; Demirkan, M. T.; Walsh, K. A.; Karabacak, T.; Polycarpou, A. A. Density Modulated Nanoporous Tungsten Thin Films and Their Nanomechanical Properties. *J. Mater. Res.* **2016**, *31*, 2011–2024.

(340) Zeng, Q.; Peng, J.; Oganov, A. R.; Zhu, Q.; Xie, C.; Zhang, X.; Dong, D.; Zhang, L.; Cheng, L. Prediction of Stable Hafnium Carbides: Stoichiometries, Mechanical Properties, and Electronic Structure. *Phys. Rev. B* **2013**, *88*, 214107.

(341) McClellan, K. J.; Chu, F.; Roper, J. M.; Shindo, I. Room Temperature Single Crystal Elastic Constants of Boron Carbide. *J. Mater. Sci.* **2001**, *36*, 3403–3407.

(342) He, C.; Zhong, J. X. Structures, Stability, Mechanical and Electronic Properties of α-Boron and A*-Boron. *AIP Adv.* **2013**, *3*, 42138.

(343) Bower, A. F. *Applied Mechanics of Solids*; CRC Press, 2009.

(344) Johnson, K. L. The Correlation of Indentation Experiments. *J. Mech. Phys. Solids* **1970**, *18*, 115–126.

(345) Erdemir, A.; Bindal, C.; Fenske, G. R. Formation of Ultralow Friction Surface Films on Boron Carbide. *Appl. Phys. Lett.* **1996**, *68*, 1637–1639.

(346) Shuo, W.; Kan, Z.; Tao, A.; Chaoquan, H.; Qingnan, M.; Yuanzhi, M.; Mao, W.; Weitao, Z. Structure, Mechanical and Tribological Properties of HfCx Films Deposited by Reactive Magnetron Sputtering. *Appl. Surf. Sci.* **2015**, *327*, 68–76.

(347) Bao, Y. W.; Wang, W.; Zhou, Y. C. Investigation of the Relationship between Elastic Modulus and Hardness Based on Depth-Sensing Indentation Measurements. *Acta Mater.* **2004**, *52*, 5397–5404.

(348) Charitidis, C.; Logothetidis, S.; Douka, P. Nanoindentation and Nanoscratching Studies of Amorphous Carbon Films. *Diam. Relat. Mater.* **1999**, *8*, 558–562.

(349) Charitidis, C. A. Nanomechanical and Nanotribological Properties of Carbon-Based Thin Films: A Review. *Int. J. Refract. Met. Hard Mater.* **2010**, *28*, 51–70.

(350) Freund, L. B.; Suresh, S. *Thin Film Materials: Stress, Defect Formation and Surface Evolution*; Cambridge University Press: Cambridge, 2004.

(351) Monteverde, F.; Bellosi, A.; Scatteia, L. Processing and Properties of Ultra-High Temperature Ceramics for Space Applications. *Mater. Sci. Eng. A* **2008**, *485*, 415–421.

(352) Charitidis, C. A.; Koumoulos, E. P.; Dragatogiannis, D. A. Nanotribological Behavior of Carbon Based Thin Films: Friction and Lubricity Mechanisms at the Nanoscale. *Lubricants* **2013**, *1*, 22–47.

(353) Charitidis, C. A.; Koumoulos, E. P.; Dragatogiannis, D. A. Nanotribological Behavior of Carbon Based Thin Films: Friction and Lubricity Mechanisms at the Nanoscale. *Lubricants* **2013**, *1*, 22–47.

(354) Zhang, S. *Thin Films and Coatings: Toughening and Toughness Characterization*; Advances in Materials Science and Engineering; CRC Press, 2015.

APPENDIX

A FRAMEWORK FOR MODELLING THE NANOMECHANICAL PROPERTIES OF HIGH TEMPERATURE HFBXCY COATINGS

A.1 Introduction

Friction reduction is often required to lower the energy consumption and increase the lifetime of moving mechanical components.[315] Liquid lubricants are often used to reduce friction and contact between surfaces. However, under extreme conditions such as elevated temperature and pressure, which is often experienced in aerospace or nuclear applications, the usage of these liquid lubricants is limited. Alternatively, solid lubricants such as molybdenum disulfide (MoS_2) and boron nitride (BN) in the form of coatings have been adopted.[316] Particularly, coatings, which can achieve very low friction coefficient ($\mu \approx 0.01$-0.001) are advantageous due to the potential impact on the economy and the environment. Such an ultra-low μ is known as superlubricity. For example, DLC exhibits superlubricity, when it runs against graphene.[317] But, there are shortcomings of C-based coatings such as a-C and DLC at elevated temperatures (above 350 ˚C) due to the graphitization and oxidative degradation under tribological contact. Therefore, there is a need to find alternatives for high temperature tribological applications such as nuclear energy generation, combustion technology and contact surfaces of hypervelocity reentry vehicles. Such applications require mechanically durable coatings with high-temperature resistance ($T_{service} > 400$ ˚C).[318] One of the promising alternatives is ultra-high temperature ceramic (UHTCs) coatings [319,320].

Transition metal borides such as hafnium diboride (HfB_2) are among UHTCs, and it has been shown to be a promising choice for the aforementioned applications.[318] Transition metal borides have unique tribological properties such as high melting point ($T_m > 3000$ ˚C), high thermal conductivity and ultra-high hardness.[321,322] This is due to the unique bonding of boron, which forms a strong hexagonal AlB_2-type layered structure.[323] Specifically, HfB_2 thin solid films are shown to be an excellent protective friction and wear coatings in applications ranging from traditional tribological surfaces such as wear-resistant applications to conformal coatings for miniaturized systems such as microelectromechanical systems, cutting tools and packaging components.[126,324] This is due to the unique properties of HfB_2 such as high modulus and hardness, highly dense structure, oxidation resistance and low wear.

Tribological thin films based on hafnium and boron are deposited using different methods such as sputtering,[325] chemical vapor deposition (CVD)[326] and pulsed laser deposition.[327] Particularly, thin films deposited by the CVD method have the advantage of achieving high conformality. The cold wall CVD approach has been shown to be a versatile deposition method to achieve stoichiometric and pure HfB_2 using a single source precursor, $Hf(BH_4)_4$.[326] In addition, HfB_2 nanoscale thin films with improved tribological properties were developed by incorporating nitrogen and carbon on the coatings.[73,328] In the specific case of carbon containing variants of hafnium and boron based nanoscale thin films (HfB_xC_y), the films have high hardness, low friction coefficient with excellent conformality attributes and inherently superior high temperature resistance (up to 3250 C°).[329] The annealed HfB_xC_y films in particular were found to exhibit very high hardness and shear strength rendering them feasible for very demanding tribological applications.

From the film growth physicochemistry perspective, the comparison of standard condition formation enthalpies for HfB_2 (~106.6 kJ/mol),[330] HfC (~209.4 kJ/mol),[331] and B_4C (~62.7

kJ/mol)[332] and the phase diagrams for these systems would indicate that the balance of the localized formation reactions during deposition would shift to the B_4C side, whenever there is no depletion of boron or carbon in the aggregate. Since, hafnium systems require higher formation enthalpies and their stoichiometric compounds provide the path of least resistance among possible synthesis routes, the likelihood of bond forming probabilistic random encounters would be the highest for the boron-carbon pairs during the growth of the aggregate.[333,334] Conversely, the lower carbon contents would have a higher tendency to undergo suppressed diffusion-governed kinetics, namely formation reactions of B_4C and its non-stoichiometric variants, since higher hafnium and boron fractions would favor the kinetics leading to higher encounter rate for hafnium-boron or hafnium-carbon pairs with inherently larger enthalpies for resulting compounds. Based on these considerations, it can be hypothesized that the effective properties of the HfB_xC_y film would not only depend on the absolute amounts of hafnium, boron and carbon atoms, but also on their respective ratios.

The primary intent herein is to formulate a predictive framework based on a quantitative experimental characterization of the mechanical and tribological properties of carbon containing variants of hafnium and boron-based nanoscale thin films, as a function of constituent compositions. This can lead to thorough mechanical/tribological optimization schemes for composition dependent properties of these thin films, which is of paramount importance for durable coatings. Specifically, the correlation between intermixed phases of stoichiometric and non-stoichiometric binary compounds of hafnium, boron, and carbon within the thin film aggregate and their mechanical response is essential for understanding the deposition kinetics related evolution of the film so that potential optimization avenues can be identified. It should be mentioned that in our analysis, we deliberately made the choice of taking only the stoichiometric compounds into account. This choice is supported by two arguments: First, the phase diagrams for binary Hf-B, Hf-C and B-C systems indicate that the stoichiometric compounds indeed represent the most energy efficient synthesis routes. Second, from the mechanical point of view, the widest range of possible elastic constants can be covered if stoichiometric compounds are taken as the limit values for the accompanying analysis. Furthermore, the nanostructural effects due to nanoporosity represent an unexplored research frontier, where the optimum film behavior is intertwined with growth kinetics during deposition and resulting micro-/nanostructural characteristics determining mechanical and tribological properties.

To date, no descriptive framework or model has been suggested for the ternary nanofilms such as HfB_xC_y to link the atomic fractions of constituent species to quasi-equilibrium cluster distributions of stoichiometric HfB_2, HfC, and B_4C nanophases and their impact on global thin film characteristics. To generate adequate experimental data for the formulation of the modeling framework, we measured the contact mechanical and tribological responses of these thin films through high fidelity nanoindentation and nanoscratch techniques. Subsequently, we compare the experimental data with reaction kinetic theoretical estimates generated by taking all possible stoichiometric compounds within the aggregate into account. This effort provides a predictive analytical framework model for design and optimization of HfB_xC_y hard thin films for technologically important applications.

A.2 Methods

A.2.1 Synthesis

A modification of common CVD methods, the cold wall CVD enables wafer-level fabrication of HfB_xC_y thin films with nanoscale thickness. This particular modification capitalizes on the versatility of vapor-based deposition methods implemented for other nanoscale hard thin film materials and provides superior conformality due to optimized control of thin film growth kinetics, unique to the combination of precursor material and carbon source selected for the HfB_xC_y system. Deposition conditions corresponding to a temperature range of 250–600 °C and regulated flux of a non-halogenated precursor and olefinic carbon source, 3,3-dimethyl-1-butene (DMB), provide a step coverage above 90% at a depth to width ratio of 30:1 in a deep trench.[73] Increasing the carbon source (DMB) pressure yielded thin films with higher carbon contents. The carbon content was found to influence the mechanical and tribological properties. Therefore, HfB_xC_y thin films with different carbon concentration of 5-35 at.% were deposited. After annealing for an hour at 700°C, the transition from amorphous to nanocrystalline grain structure is expected to take place.

A.2.2 Nanoindentation

The mechanical properties were measured using a commercial indenter, TI 950 (Bruker, Minneapolis, US), and the experiments were carried out using load-control mode. Due to the small thickness of the films, a sharp cube corner probe was used (tip radius ~ 40 nm). For all experiments, 5 s time periods for loading and unloading and 2 s dwell time at maximum nanoindentation load were used. The hardness (H) and reduced elastic modulus (E_r) were obtained from the first one-third of the unloading curve according to the Oliver and Pharr method.[64] The indenter probe was calibrated using a standard fused quartz (FQ) sample.

A.2.3 Nanoscratch

The nanoscratch experiments were carried out using the same commercial indenter to study the nanotribological and nanofriction behavior of HfB_xC_y. A conospherical probe with a tip radius of ~ 870 nm was used. Scratch experiments were performed under various constant normal loads of 100, 200, 350 and 500 μN similar to previous studies to allow comparison of performance.[335]

The scratch length was kept to 6 μm. At the end of each scratch experiment, a height scan was performed using the same tip to measure the residual scratch depth. The coefficient of friction (μ) is recorded for each experiment by dividing the lateral load over the normal load. Also, the elastic recovery (ER) is defined as the ratio of residual penetration depth divided by the maximum penetration depth and multiplied by 100. In addition, multiple-pass scratch experiments were performed on the HfB_xC_y coating as shown in the schematic of Figure 9.1.

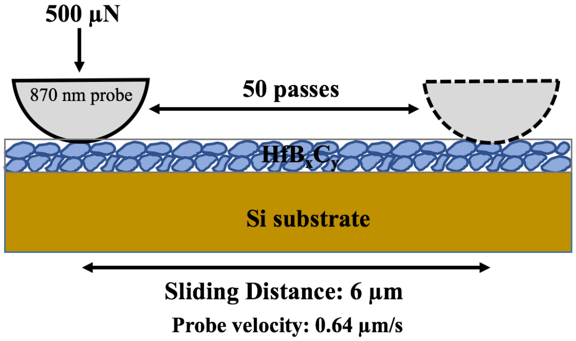

Figure A.1 Schematic for the multiple-pass scratch experiments on HfB_xC_y coating. The tip was moved back and forth.

A.2.4 Analytical framework model

During the CVD process, the equilibrium distribution of species deposited on the Si substrate experience a competition between energetically favorable formation reactions such that the growth of stable stoichiometric HfB_2, HfC, B_4C nanophases and their metastable non-stoichiometric derivatives. It would be confined to certain clusters and directions governed by atomic diffusion and nucleation kinetics.[336] This non-ergodic competition between surface-confined diffusion and atomic intermixing dominated nucleation mechanisms control the type and fraction of nanophases present within the growing film, which, in turn, determine the effective film properties. The cold wall CVD method enables nanoscale HfB_xC_y thin films within a deposition temperature range of 250-600˚C. Shown in Figure 9.2 is a representative schematic of quasi-equilibrium cluster distributions of stoichiometric HfB_2, HfC, and B_4C nanophases and their non-stoichiometric variants. Conversion of amorphous clusters into nanocrystalline grains and increase in the overall stoichiometric content of the aggregate occur after annealing at 700°C.

In this work, the semi-empirical framework was formulated by considering the two extremes: Diffusion controlled growth (that maximizes HfC) vs. nucleation controlled growth (that maximizes B_4C). We used the experimental nanoindentation data to verify the framework and predict which scenario dominates for different samples, as the amount of carbon increases. Once this was done, we were able to calculate the Young's modulus, yield strength, Poisson's ratio, and adhesive and shear strengths. The measured properties provided a better insight into the mechanical underpinnings of the tribological behavior of HfB_xC_y thin films.

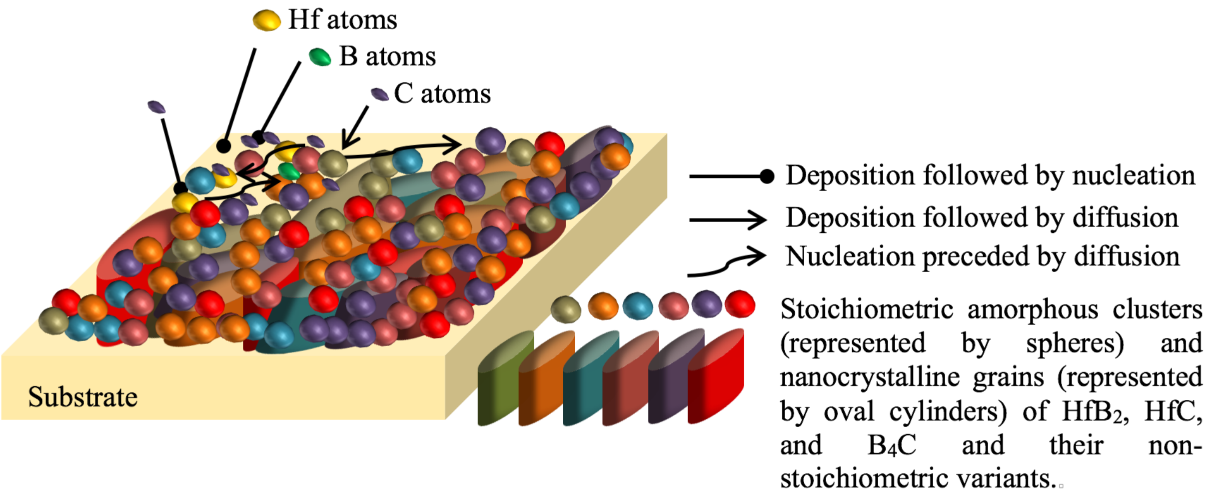

Stoichiometric amorphous clusters (represented by spheres) and nanocrystalline grains (represented by oval cylinders) of HfB_2, HfC, and B_4C and their non-stoichiometric variants.

Figure A.2 Schematic of quasi-equilibrium cluster distributions of stoichiometric HfB_2, HfC, and B_4C nanophases and their non-stoichiometric variants.

A fundamental assumption of the proposed framework is that the annealing temperature would drive the thin film closer to the meta-stable and equilibrium phases via internal stress increase and grain boundary diffusion. Therefore, it is assumed herein that the annealed samples would have predominantly stoichiometric phases. Indeed, annealing treatment was found to bring $Ti_{1-x}Si_xC_yN_{1-y}$ system, closer to stoichiometric distribution. A similar trend was observed for molybdenum nitride thin films, which are another ultra-high melting point ceramics categorically. Therefore, phase transformations and metastable and equilibrium phase formations at similar annealing temperature ranges as the HfB_xC_y thin films were observed.[337]

Figure 9.3a shows a schematic explaining how the mechanical properties are obtained using the semi-empirical framework for HfB_xC_y thin films. For example, sample 1 has 28 Hf, 56 B and 5 C atomic weights (at.%). To follow the first scenario, which would maximize the HfC phase, all C will be used to form the HfC phase first. The rest of the Hf will participate in HfB_2 and the extra boron will remain in elemental form. This distribution of atomic weights into different phases is used to calculate the weight and volume fractions of each phase. The elastic constants, atomic weight (wt.) and density (ρ) of each element/compound are reported in the literature and provided herein in Table 9.1. With the knowledge of elastic constants and volume fractions, the Voigt model can be used to obtain the elastic modulus, shear modulus, and Poisson's ratio of the aggregate. The Pal model is used to correct for porosity in the thin films, which was found to predict well the mechanical properties for nanoporous thin film structures.[338,339] Last, the reduced modulus of elasticity (E_r) is found for the material combination of the tip and the sample. It is defined based on the known elastic modulus of both the diamond indenter (E_i) and the sample (E_s), and the Poisson's ratio for the indenter (v_i) and sample (v_s). The E_s *and* v_i are reported for diamond probes in the literature (E_s= 1140 GPa and v_i= 0.07). E_r is used to verify the framework with the experimental measurements, which are obtained from nanoindentation. A schematic for the second scenario is provided as well in Figure 9.3b.

Table A.1 Elastic constants and properties of the elements and compounds in HfB_xC_y.

Element/ Compound	*E* *(GPa)*	*G* *(GPa)*	*A*tomic Weight (g/mol)	*Density* *(g/cm^3)*
HfB_2 [311]	584	243	200.11	10.50
HfC [340]	498	278	190.50	12.20
B_4C [341]	460	196	55.26	2.52
B [342]	460	202	10.81	2.37
Hf [343]	163	52	178.49	13.20

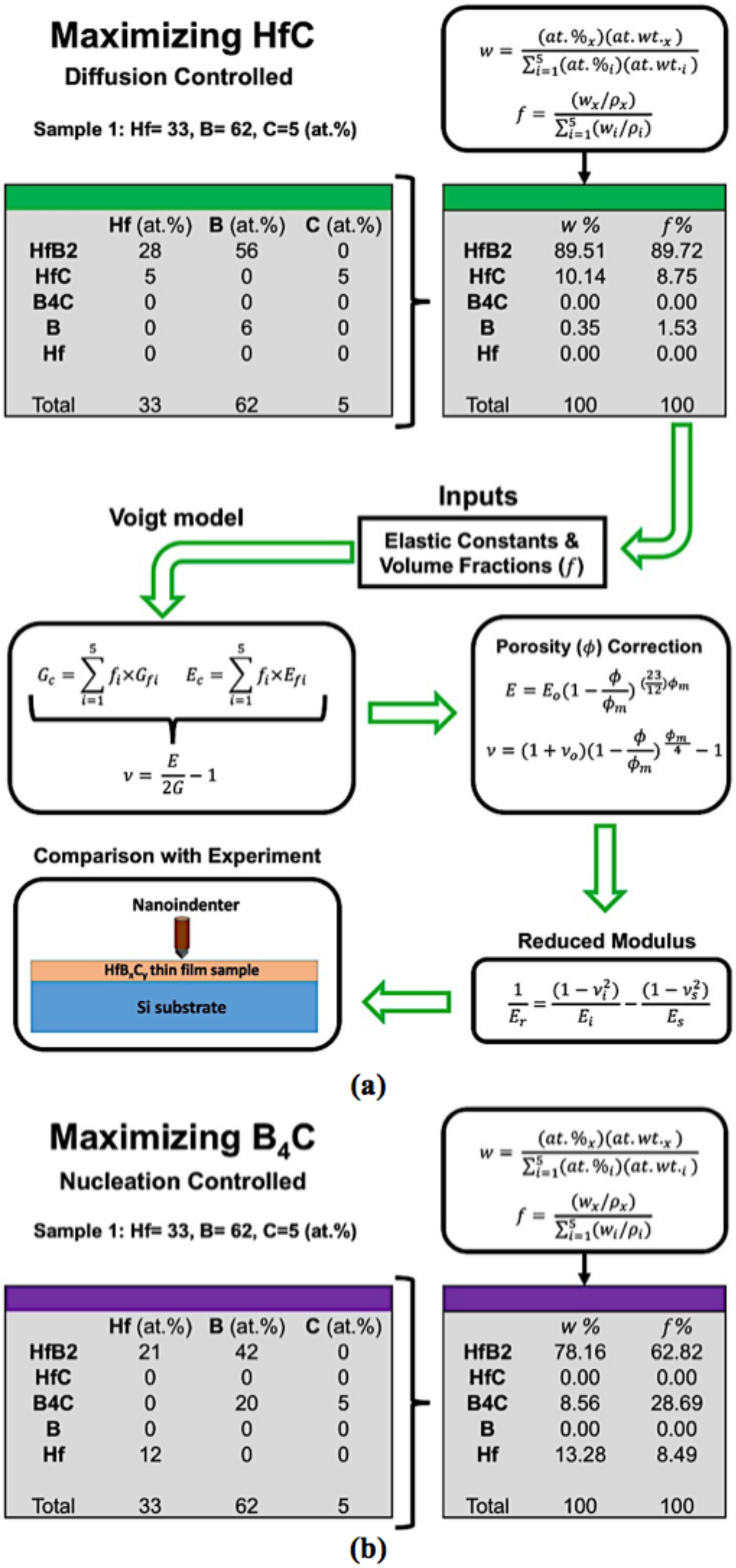

$$w = \frac{(at.\%_x)(at.wt._x)}{\sum_{i=1}^{5}(at.\%_i)(at.wt._i)}$$

$$f = \frac{(w_x/\rho_x)}{\sum_{i=1}^{5}(w_i/\rho_i)}$$

	Hf (at.%)	B (at.%)	C (at.%)
HfB2	28	56	0
HfC	5	0	5
B4C	0	0	0
B	0	6	0
Hf	0	0	0
Total	33	62	5

	w %	*f* %
HfB2	89.51	89.72
HfC	10.14	8.75
B4C	0.00	0.00
B	0.35	1.53
Hf	0.00	0.00
Total	100	100

$$\underbrace{G_c = \sum_{i=1}^{5} f_i \times G_{fi} \quad E_c = \sum_{i=1}^{5} f_i \times E_{fi}}_{\nu = \frac{E}{2G} - 1}$$

$$E = E_o\left(1 - \frac{\phi}{\phi_m}\right)^{\left(\frac{23}{12}\right)\phi_m}$$

$$\nu = (1 + \nu_o)\left(1 - \frac{\phi}{\phi_m}\right)^{\frac{\phi_m}{4}} - 1$$

$$\frac{1}{E_r} = \frac{(1 - \nu_i^2)}{E_i} - \frac{(1 - \nu_s^2)}{E_s}$$

$$w = \frac{(at.\%_x)(at.wt._x)}{\sum_{i=1}^{5}(at.\%_i)(at.wt._i)}$$

$$f = \frac{(w_x/\rho_x)}{\sum_{i=1}^{5}(w_i/\rho_i)}$$

	Hf (at.%)	B (at.%)	C (at.%)
HfB2	21	42	0
HfC	0	0	0
B4C	0	20	5
B	0	0	0
Hf	12	0	0
Total	33	62	5

	w %	*f* %
HfB2	78.16	62.82
HfC	0.00	0.00
B4C	8.56	28.69
B	0.00	0.00
Hf	13.28	8.49
Total	100	100

Figure A.3 Schematic for the semi-empirical mixing framework using (a) the first scenario (maximizing HfC), and (b) the second scenario (maximizing B_4C).

A.3 Results & Discussion

A.3.1 Nanomechanical Properties

The nanoindentation measurements are reported in Table 9.2, and were kept within 10-15% of the film thickness to avoid substrate effects. The reduced modulus and hardness are extracted from the measured nanoindentation data according to the Oliver-Pharr method. Nanoindentation tests revealed that for the low temperature (i.e., 250-300°C) deposited HfB_xC_y thin films, hardness and reduced modulus decrease almost linearly with increasing carbon content from 5 at.% to 21 at.%. The highest values were measured for 5% C containing films, which had a hardness of 34 GPa and reduced modulus of 250 GPa. The nanoindentation data shows a jump in the mechanical properties for thin films with carbon contents higher than 21 at.%. This is due to the higher density for the films due to the higher temperature growth of 600 °C.

Table A.2 Nanomechanical properties of HfB_xC_y thin films measured using nanoindentation.

Sample	Composition of thin films			Film thickness (nm)	*Er* (GPa)	*H* (GPa)
	C (at.%)	B (at.%)	Hf (at.%)			
A	5	62	33	200	247.7±8.5	33.8±1.8
B	8	59	33	180	226.8±8.2	28.1±1.2
C	15	49	36	180	184.4±4.5	21.9±0.6
D	21	46	33	150	157.2±7.1	16.7±0.4
E	28	38	34	200	196.0±4.0	23.4±1.2
F	35	33	32	260	187.6±3.3	19.5±0.7

In the next step, the reduced modulus is computed using the proposed semi-empirical framework, which was explained in Figure 9.3. Figure 9.4a-b provides a comparison between the computed reduced modulus for each scenario using the framework and the measured reduced modulus obtained by the nanoindentation experiments, for each sample. The modeled results were corrected for a wide range of porosity (ϕ = 5-20%).

Maximizing HfC resulted in good agreement with the experimental nanoindentation data for low carbon content (C ≤ 8 at.%), while the assumption of maximizing B_4C matched well the higher carbon content samples (C ≥ 8 at.%). That is, the experimental data agrees with the diffusion-controlled scenario for low C content and with the nucleation-controlled scenario at higher C content. To shed light on the growth kinetics of these thin films and their mechanical properties in Figure 9.4, the percentage of all possible five stoichiometric phases, which are anticipated to be in this aggregate, are monitored as a function of carbon content in Figure 9.5. For zero carbon content (not shown here), HfB_2 will be 100%. HfB_2 drops fast reaching zero at C=15 at.% as the formation of carbides dominates. The presence of B in elemental form is low for all samples, and the elemental Hf increase up to C=15 at.%. Then, the presence of Hf element decreased substantially as the growth favored the formation of HfC instead at higher carbon contents.

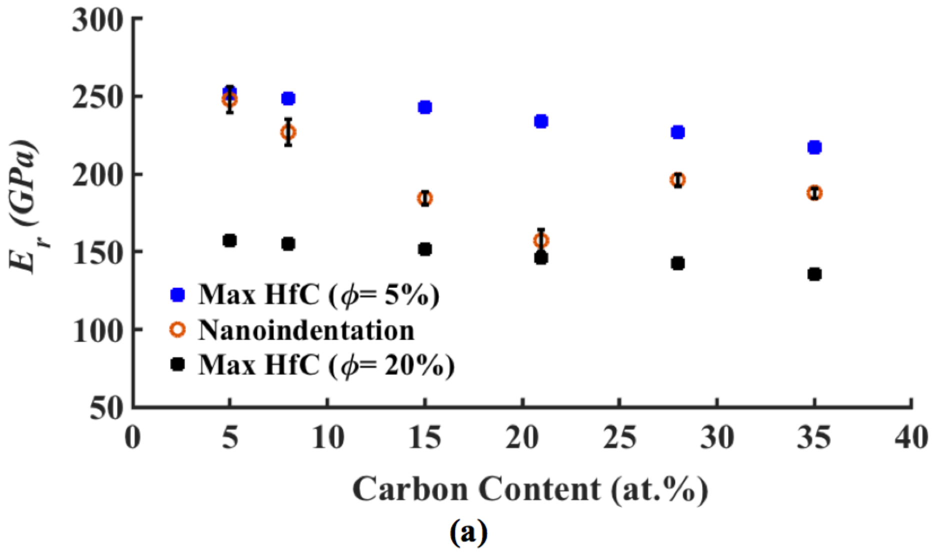

Figure A.4 Computed reduced modulus using the semi-empirical framework for the scenarios of maximizing (a) HFC and (b) B4C, and comparison with the nanoindentation results.

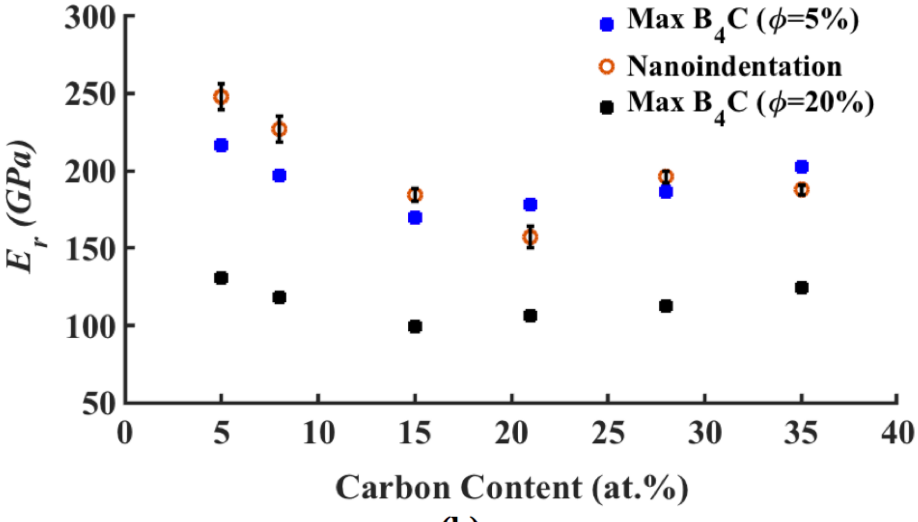

(b)

Figure A.4 Continued.

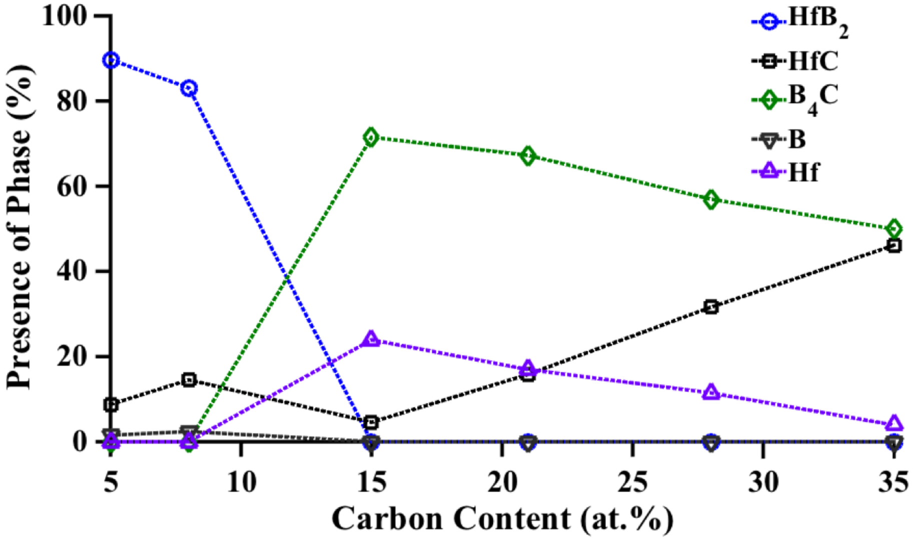

Figure A.5 Modeled results of phase percentages, which are made of different compounds/ elements in the aggregate as a function of carbon content based on their volume fractions.

Figure 9.6 shows a combination of both scenarios, where diffusion-controlled mode (max HfC) dominates at low carbon content and nucleation-controlled mode (max B_4C) at higher carbon content. The range of porosity is restricted to 5-10%, because it was found to best fit the experimental data. For the rest of the study, the diffusion-controlled mode is used to calculate the properties for films with carbon content less than 10%. Alternatively, the nucleation-controlled mode is chosen. After the framework was verified via comparisons with the nanoindentation experiments, its predictive capability was established, granting further optimization capabilities for improved nanomechanical and tribological properties through compositional control. In addition, the framework can be utilized to find other properties of interest such as Young modulus (*E*), Poisson's ratio and yield strength (*Ys*). The Poisson's ratio is calculated according to Figure 9.3 using the Voigt model and porosity corrected Pal method. The yield strength is calculated based on the assumption of elastic-perfectly plastic response. The hardness (*H*), yield strength and Young modulus are related based on the work of Johnson as shown in Equation 1.[344] Parameter β is the half angle of the tip, and equals 35.26° for an ultra-sharp cube corner probe.

$$\frac{H}{Ys} = \frac{2}{3}[1 + \ln(\frac{1}{3}\frac{E}{Ys}\tan\beta)] \qquad (1)$$

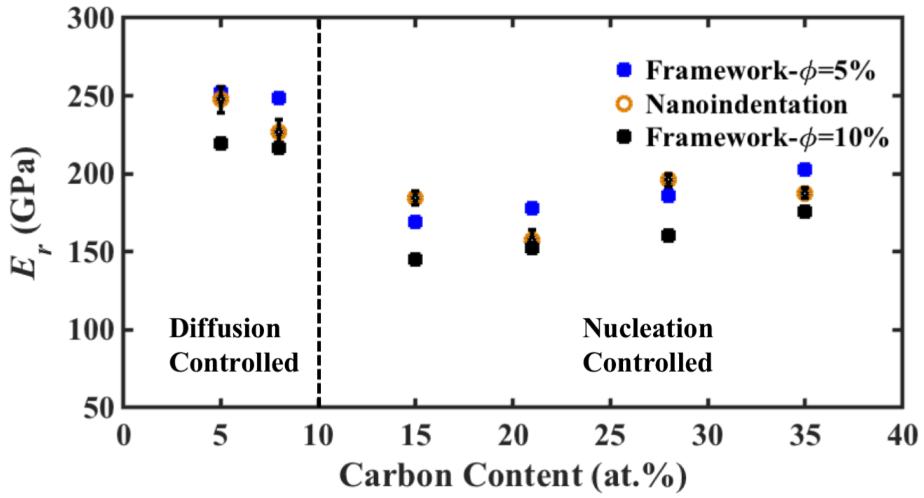

Figure A.6 E_r for HfBxCy thin films with different compositions computed and measured using the framework and nanoindentation experiments.

The calculation of both Poisson’s ratio and yield strength provides a more complete picture of the mechanical behavior of these thin films. Typically, the extraction of these properties is not a straightforward calculation using experimental nanoindentation data, as it involves fittings using analytical models or finite element analysis. Figure 9.7a-b shows the Poisson's ratio and yield strength, which were obtained using the proposed modeling framework. The Poisson's ratio varies from 0.334 to 0.087 for thin films with 5% nanoporosity. The aggregates with carbon content of 15 and 35 at.% show the highest and lowest Poisson's ratio, receptively. These two thin films are expected to have different mechanical behavior under deformation due to the large difference in Poisson's ratio. The yield strength shows a fluctuating trend, with decreasing trend for thin films with carbon content from 5% to 35%. The reason for these non-uniform changes in the yield strength is attributed to the dependence on both hardness and elastic modulus.

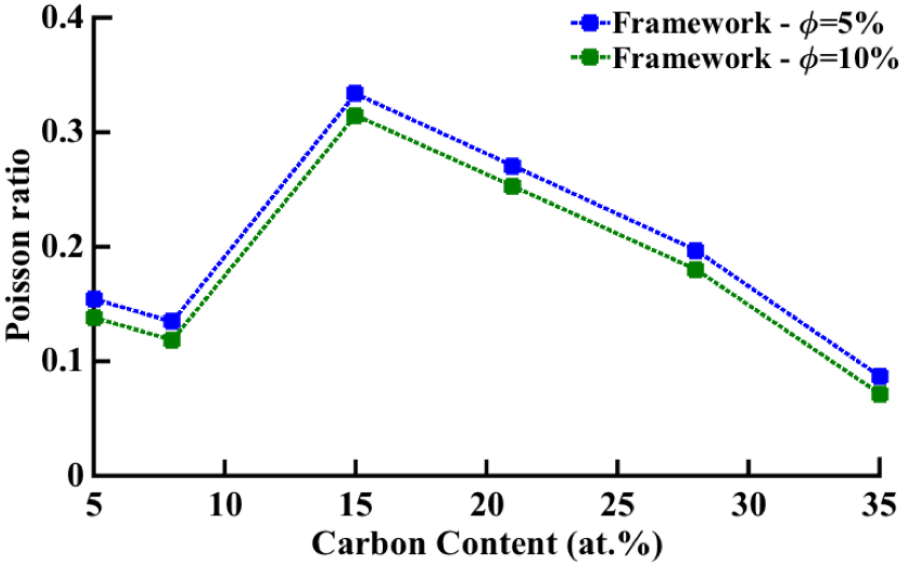

(a)

Figure A.7 Poisson's ratio and Yield Strength computed using the semi-empirical framework as a function of carbon content.

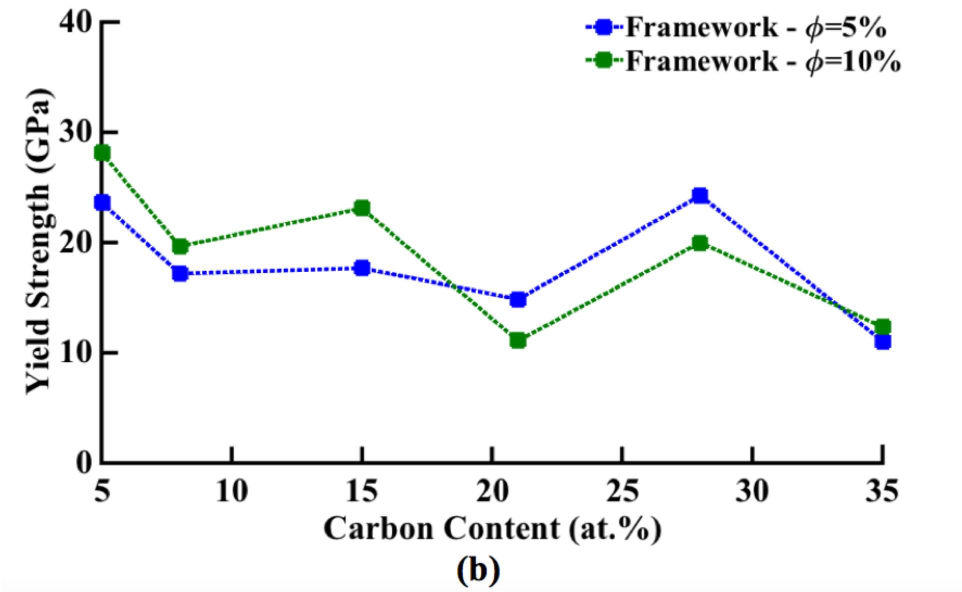

Figure A.7 Continued.

A.3.2 Nanoscratch experiments

Based on the findings of Figure 9.6 and Figure 9.7, the thin films with carbon content of 5, 15 and 35 at.% were chosen for detailed nanotribological experiments, using nanoscratch. The friction coefficient (μ) and elastic recovery (*ER*) were extracted from the scratch experiments and they are provided in Figure 9.8. The scratch behavior was found to be different for each of the three films. The hardest/stiffest coating (5 at.% carbon content) showed an increasing trend for μ as normal load increases, and it maintained a high and stable elastic recovery. For the thin film with 15 at.% carbon content, which had the lowest E_r and H, the average μ was the highest. However, it had the highest elastic recovery. On the other hand, the thin film with 35 at.% carbon content showed the lowest μ and ER. The friction coefficient of this thin film approached the superlubricity regime ($\mu \leq 0.05$), but it suffered from a decreasing low elastic recovery with increasing normal load. The ultra-low friction coefficient is due the dominant presence of boron and hafnium carbides in the composition of aggregate (see Figure 9.5), which are known to have such ultralow friction behavior.[345,346] Particularly, the results of the thin film with carbon contents of 5 and 35 at.% showed a lower μ as compared to the μ of HfB_2 thin films, reported in.[335]

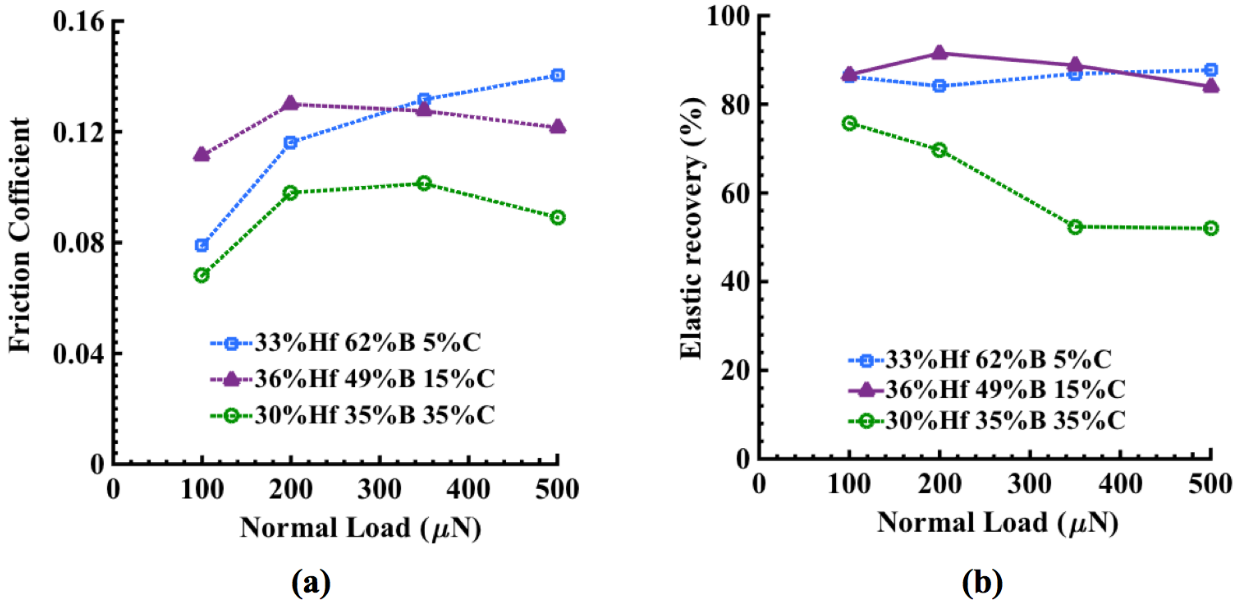

Figure A.8 (a) Friction coefficient an (b) elastic recovery of different HfB_xC_y thin films as a function of normal load obtained from nanoscratch experiments.

A.3.3 Nanotribological Properties

To elucidate the tribological behavior of these films, further analysis is conducted and used to guide the optimization efforts of the HfB_xC_y thin films to achieve the best tribological behavior. It starts with establishing a theoretical relationship between different parameters such as scratch displacement, nanoindentation hardness, modulus and maximum applied load. The goal of this analysis is to calculate the contact depth, area and pressure during scratch experiments in order to evaluate the deconvoluted scratch resistance of the thin films.

Equation 2 decomposes the maximum scratch displacement (h_m) into the sum of both contact depth (h_c) and elastic surface displacement (h_s), which is defined in Equation 5. The h_s measures how far the surface is displaced at the perimeter of the contact.[347] Equation 3 defines the elastic recovery resistance (R_s) as a function of hardness and reduced modulus. Also, R_s can be defined in terms of the maximum contact load (F_N) and h_s as in Equation 4. The elastic recovery is an indication of the dissipated energy during the scratch experiments.

$$h_m = h_c + h_s \tag{2}$$

$$R_s = 2.263\frac{E_r^2}{H} \tag{3}$$

$$R_s = \frac{F_N}{h_s^2} \tag{4}$$

Therefore, Equation 4 can be rearranged to compute h_s (See Equation 5). Since h_m is measured from the experiment, h_c can be found from Equation 2. Equations 6 and 7 define the contact area and pressure.

$$h_s = \left(\frac{F_N H}{2.263 \times E_r^2}\right)^{1/2} \tag{5}$$

$$A_c = ((2Rh_c) - h_c^2)^{1/2} \tag{6}$$

$$P = \frac{F_N}{\pi(A_c^2)} \tag{7}$$

Nanoscratch properties of HfB_xC_y thin films are provided in Tables 9.3, 9.4 and 9.5 for different carbon content values. h_m, h_s, h_c and A_c were found to increase with increasing normal load. The numbers in the parentheses indicate which equation is used to calculate each property. P is the maximum contact pressure, which was experienced by the film under deformation. The ratio of $\frac{P}{Ys}$ provides an indication of the extent of yielding zone. The HfB_xC_y film (5% carbon content) experienced the highest contact pressure close to yielding (see Table 9.3). Since the thin film had the highest E_r and H, the contact area was smaller than the other films especially at low scratch normal loads. This resulted in a higher contact pressure. In addition, with increasing normal loads, the contact pressure dropped for this thin film compared to the other two films in Tables 9.4 and 9.5 where the contact pressure increased with increasing normal load. $\frac{H^3}{E^2}$ is typically used as a metric to assess the scratch/ wear resistance for ultra-hard coatings,[348] and is known as the plastic resistance parameter. The higher the value, the more elastic is the behavior of the film under contact. Thin films with $\frac{H^3}{E^2} \geq 0.235$ largely exhibit elastic behavior. Otherwise, they exhibit a fairly plastic behavior.[349] The data are again provided as a range for thin films with porosities of 5% and 10% for $\frac{P}{Ys}$, $\frac{H^3}{E^2}$ and $\frac{P}{Ys}\Big/\frac{H^3}{E^2}$ since Ys and E were calculated using the semi-empirical framework. The H is extracted from the nanoindentation experiments while F_N, μ and h_m were measured using the scratch data.

Table A.3 Nanoscratch properties of HfB_xC_y thin films (carbon content = 5%).

F_N (μN)	μ	h_m (nm)	$h_c^{(2)}$ (nm)	$h_s^{(5)}$ (nm)	$A_c^{(6)}$ (nm^2)	$P^{(7)}$ (GPa)	$\frac{P}{Ys}$	$\frac{H^3}{E^2}$ (GPa)	$\frac{P}{Ys}\Big/\frac{H^3}{E^2}$ (GPa^{-1})
100	0.08	5.80	0.86	4.93	38.73	21.22	0.75-0.90	0.39-0.54	1.39-2.31
200	0.12	8.92	1.94	6.98	58.07	18.88	0.67-0.80	0.39-0.54	1.24-2.05
350	0.13	13.81	4.58	9.23	89.14	14.02	0.50-0.59	0.39-0.54	0.93-1.52
500	0.14	17.09	6.06	11.03	102.53	15.14	0.54-0.64	0.39-0.54	1.00-1.64

Table A.4 Nanoscratch properties of HfB_xC_y thin films (carbon content = 15%).

F_N (μN)	μ	h_m (nm)	$h_c^{(2)}$ (nm)	$h_s^{(5)}$ (nm)	$A_c^{(6)}$ (nm^2)	$P^{(7)}$ (GPa)	$\frac{P}{Ys}$	$\frac{H^3}{E^2}$ (GPa)	$\frac{P}{Ys}\Big/\frac{H^3}{E^2}$ (GPa^{-1})
100	0.11	9.23	3.89	5.33	82.20	4.71	0.20-0.27	0.34-0.47	0.43-0.78
200	0.13	15.30	7.75	7.54	115.90	4.74	0.21-0.27	0.34-0.47	0.45-0.79
350	0.13	22.53	12.54	9.98	147.21	5.14	0.22-0.29	0.34-0.47	0.47-0.86
500	0.12	25.00	13.07	11.93	150.25	7.05	0.31-0.40	0.34-0.47	0.66-1.17

Table A.5 Nanoscratch properties of HfB_xC_y thin films (carbon content = 35%).

F_N (μN)	μ	h_m (nm)	$h_c^{(2)}$ (nm)	$h_s^{(5)}$ (nm)	$A_c^{(6)}$ (nm^2)	$P^{(7)}$ (GPa)	$\frac{P}{Ys}$	$\frac{H^3}{E^2}$ (GPa)	$\frac{P}{Ys} \Big/ \frac{H^3}{E^2}$ (GPa^{-1})
100	0.07	10.55	5.61	4.95	98.61	3.27	0.27-0.30	0.12-0.17	1.59-2.47
200	0.10	17.21	10.22	7.00	132.93	3.60	0.29-0.33	0.12-0.17	1.71-2.72
350	0.10	26.72	17.46	9.26	173.44	3.70	0.30-0.34	0.12-0.17	1.77-2.79
500	0.09	30.78	19.72	11.06	184.17	4.69	0.38-0.42	0.12-0.17	2.24-3.54

Another useful parameter underlying the tribological behavior is the normalized ER, which is defined as the multiplication of $\frac{P}{Ys}$ and ER. It suggests an interesting way to compare the three thin films with different C content when it comes to the transition from elastic response to plastic response. Furthermore, it shows how the film behaves under increasing scratch normal loads. Figure 9.9 shows the average normalized ER versus the average $\frac{H^3}{E^2}$. The average Poisson's ratio for each data cluster is provided in this figure, because it provides additional insights about the deformation behavior of these films under contact.

Based on Figure 9.9, the HfB_xC_y thin films' response can be divided into two categories, elastic or plastic behavior dominated. The arrows illustrate how the average normalized ER changes with increasing contact load. Even though the thin film with carbon content of 35 at.% had the lowest friction coefficient approaching the superlubricity regime, it had the lowest $\frac{H^3}{E^2}$ and normalized ER. Thus, it is expected to experience more plastic deformation compared to the other HfB_xC_y thin films. Furthermore, the very low v for this film indicates lower transverse film rigidity providing more free volume under contact. Thus, it was easier to be compressed than sheared, which could result in the growth of sub-surface cracks at high contact loads.

On the other hand, the HfB_xC_y thin films with higher v resisted compression and favored shear. Thus, they had higher normalized ER. Particularly the thin film with carbon content of 15 at.% had a high v of 0.32. Therefore, it demonstrated an increasing normalized ER with increasing scratch normal loads (see arrows). On the other hand, the normalized ER dropped fast for the thin film with carbon content of 5 at.% once the load was increased. This explains the elastic recovery behavior, which is shown in Figure 9.9 for the three films.

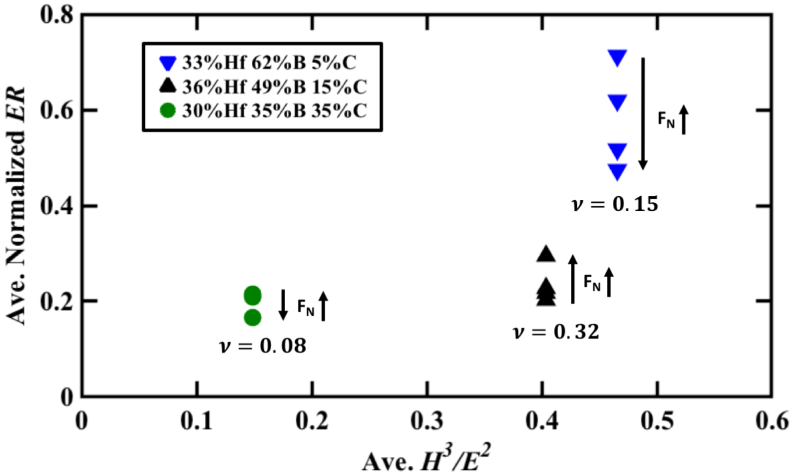

Figure A.9 Average normalized ER versus average $\frac{H^3}{E^2}$ for HfB_xC_y thin films.

To evaluate the durability of these thin films, multiple scratch experiments were carried out over the same area. Figure 9.10 a-b show the friction coefficient and contact depth as a function of number of passes or cycles. The three films maintained fairly constant friction coefficient after the first few cycles with $\mu \leq 0.1$. This is an improved performance, as compared to annealed HfB_2 which showed an increasing trend in the friction coefficient in a previous study under the same experimental conditions.[65] Particularly, the HfB_xC_y thin film (35 at.% carbon content) maintained the lowest friction coefficient of about 0.05. But, it experienced pronounced plastic response as the contact depth increased faster, after the tenth cycle.

Alternatively, the HfB_xC_y thin film (15 at.% carbon content) experienced the highest friction coefficient among the three films, but it maintained the lowest contact depth and highly elastic response. The HfB_xC_y thin film (5 at.% carbon content) exhibited an average performance of both films with an elastic-plastic behavior. The HfB_xC_y thin film with 5 at.% carbon content exhibited lower contact depths than the HfB_xC_y thin film with 15 at.% carbon content in the first few passes due to the slightly higher resistance to plasticity, $\frac{H^3}{E^2}$. However, due to increasing normalized ER trend with increasing number of passes and the highest v among these films, the HfB_xC_y thin film with 15 at.% carbon content managed to keep the contact depth lowest after many passes. Note that a lower elastic modulus and higher v will lead to more compliant elastic response, which in general would enable a thin film's better accommodation of superficial strains.[350] Even though, the E and H for the thin film with carbon content of 15 at.% is much lower than the one with carbon content of 5 at.%, their $\frac{H^3}{E^2}$ ratios are fairly close. This finding indicates that having higher H and E_r is not always advantageous for hard protective coatings. The plastic resistance parameter is clearly more useful. In addition, the elastic parameters such as Poisson's ratio can be significant as well to achieve a high scratch/wear resistance.

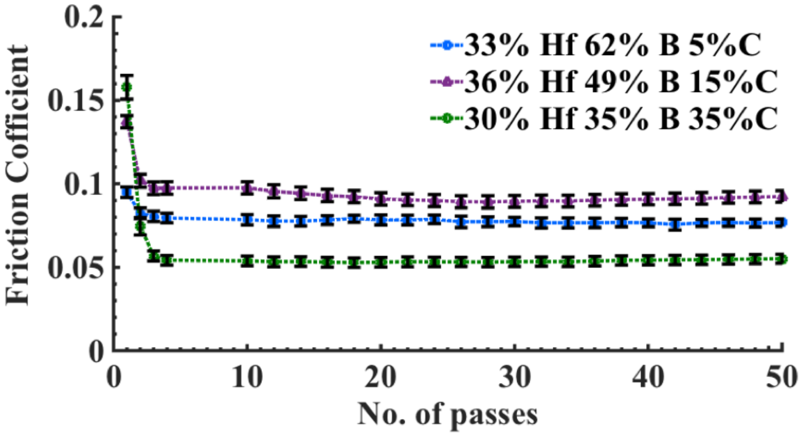

(a)

Figure A.10 (a) Friction coefficient and (b) contact depth as a function of the number of scratch passes using nanoscratch experiments.

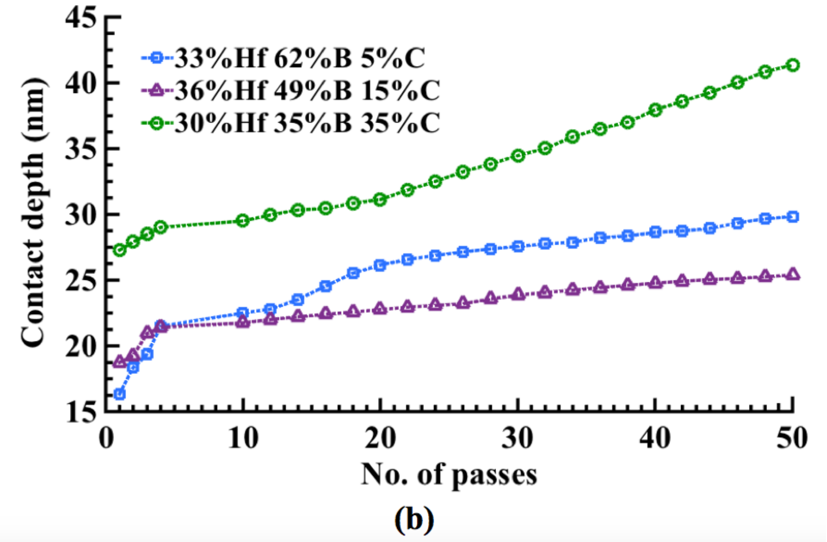

Figure A.10 Continued.

To summarize, Table 9.6 provides a comparison between HfB_xC_y thin films and different hard coatings, which have been used in tribological applications. At room temperature, diamond-like coating (DLC) is the best candidate as a protective coating, because it has the highest *H/E* and $\frac{H^3}{E^2}$ and the lowest μ. However, if the need arises to have excellent tribological coatings for high temperature applications, such as nuclear reactor contact surfaces or advanced engine systems, conventional coating solutions exhibit major shortcomings. Diamond will graphitize above 350 ℃, and the service temperature for other carbon-based coatings such as DLC and amorphous carbon (a-C) are limited to 400-600 ℃, as shown in Table 9.6. Transition metal borides such as hafnium diboride with carbon alloying has the potential for use in high temperature tribological applications. Hafnium diboride belongs to the UHTCs and has shown enhanced resistance to oxidation up to 1600 °C.[351] In addition, HfB_xC_y thin films achieved very high conformality. This is especially important for aerospace applications, because it would be possible to deposit coatings with innate compatibility with aerodynamic shapes. The HfB_xC_y films with carbon content of 5-15 at.% were revealed to be the most tribologically promising candidates.

Table A.6: Comparison of HfB_xC_y with other hard tribological coatings.

	a-C 352	**DLC** 353	**BN** 354	**TiN** 244	**HfB_2** 244	**HfB_xC_y (C=5%)**	**HfB_xC_y (C=15%)**	**HfB_xC_y (C=35%)**
t (nm)	274	250	170	300	150	200	180	260
H/E	0.123	0.163	0.076	0.037	0.091	0.11-0.13	0.12-0.15	0.08-0.09
H^3/E^2 (GPa)[a]	0.440	0.687	0.109	0.020	0.355	0.39-0.54	0.34-0.47	0.12-0.17
μ[b]	0.05-0.30	0.05-0.30	0.05-0.30	0.16-0.24	0.07-0.15	0.08-0.14	0.10 -0.13	0.05-0.09
T[c] (°C)	600	≤400	>1000	<600	>1000	>1000	>1000	>1000

[a] H^3/E^2 =1.0 for diamond, [b] Experiments done at RT and in air

[c] Maximum service temperature

A.4 Conclusion

High aspect ratio conformal HfB_xC_y coatings were grown using low-temperature CVD. The aggregates were annealed at a temperature of 700 ℃. Once annealed, depending on the C and B content, different compositions of HfB_2, HfC, B_4C, B and Hf were expected to be present in the film. The composition of these phases had a strong influence on the mechanical and tribological properties. The compositional evolution was controlled by the growth conditions and kinetics. To predict the mechanical and tribological behavior, a semi-empirical framework was developed herein. The modeling framework was verified using instrumented nanoindentation experimental data and exhibited excellent match with the experiments. Furthermore, scratch experiments revealed that HfB_xC_y thin films could attain very low coefficient of friction values, approaching the super lubricity regime (i.e., less than 0.05 in dry conditions) for the 35 at.% carbon content. The effective reduction in the μ without major sacrifice in mechanical properties was a critical attribute of these films. Mechanically and tribologically DLC appeared to be the main competitor for HfB_xC_y at room and low temperature conditions, whereas for elevated temperatures beyond 600°C, HfB_xC_y will be superior to many existing coating solutions considering its anticipated low reactivity in air. Carbon-based HfB_xC_y thin films can be used for transformative technological applications in several strategic fields, such as high temperature protective tribological coatings, wear and scratch resistant thermal shields, and diffusion barriers in the microelectronic, nuclear and aerospace industries.